

# **USCIPI REPORT #970**

## **High Resolution Digital Radar Imaging of Rotating Objects**

**by**

**Yeh-Hua Peter Chuan**

**June 1980**

**Signal and Image Processing Institute  
UNIVERSITY OF SOUTHERN CALIFORNIA  
Department of Electrical Engineering-Systems  
3740 McClintock Avenue, Room 404  
Los Angeles, CA 90089-2564 U.S.A.**

## ACKNOWLEDGEMENTS

I would like to express my gratitude to Professor A.A. Sawchuk for all the guidance and concern I received over the years at USC. I am even more grateful to him for his assistance in both encouragement and providing the computer account during the final phase of completing this thesis. Without his contribution this thesis may not have been completed in any reasonable amount of time.

I am also greatly indebted to Professor I.S. Reed for his careful review of the initial few chapters of this thesis. Through his expert criticism a great deal of improvement became possible in the quality of this thesis. I would further like to acknowledge his invaluable suggestions in the pursuit of the research on polar sampling effects.

For all the guidance attended to me during the initial period of this research, and for the experimental data I was able to use, I am grateful to Dr. H.C. Andrews. Without his counseling I would probably not have chosen this interesting and rewarding topic.

It is a pleasure to acknowledge my appreciation to Dr. C.C. Chen for many helpful discussions concerning the research.

I would also like to acknowledge Professors E.K. Blum and O.D. Faugeras for serving on my guidance committee.

Finally, special thanks to Sau-Wah my fiancée. Her inspiration throughout the years has made the pursuit of this thesis a successful task.

## ABSTRACT.

This dissertation is devoted to the imaging aspect of the problem of obtaining high resolution images of practical radar targets with digital processing techniques. The motion compensation aspect of the problem is also briefly described. A multi-frequency stepped (MFS) radar is assumed and the Fourier transform relationship between the data (dimensioned in aspect angle and signal frequency) and the target reflectivity function is derived in both 2-D and 3-D forms. Assuming that the data is available for  $360^\circ$  aspect angle and using wideband radar, a coherent digital processing method is developed which will give the best possible resolution. Such a situation occurs when the target makes a complete turn. It is found that for such an imaging system the resolution is inversely proportional to the mean carrier frequency if such frequency is large compared to the signal bandwidth. In the case when the data is undersampled in range or aspect angle or both, a modified coherent digital signal processing technique is described that will get around such difficulty. It is found that the modified processing method gives poorer resolution but is better than either



the mixed processing method or the incoherent processing method. The latter two processing techniques are also described in this dissertation. Experimental results are also presented and problems with real targets such as shadowing, glint and scintillation are discussed.

In the 2-D case, the radar data are sampled in polar coordinate format. The sampling requirements in this sampling scheme are discussed in great detail. Results from Doppler processing and Degrees of Freedom concepts both show that polar coordinate sampling in the Fourier domain is adequate if the inverse of the greatest sampling interval (in either radial or cross-radial dimension) in the Fourier domain covers the entire linear extent of interest in the real domain. Analytical methods using Poisson's summation formula show the same results in more detail especially in predicting undersampling effects. The results on polar coordinate sampling can be applied to other systems in which polar format sampling is a natural setting.

## TABLE OF CONTENTS

	<u>Page</u>
ACKNOWLEDGEMENTS	ii
ABSTRACT	iv
LIST OF FIGURES	ix
LIST OF TABLES	xiii
Chapter	
1 PREAMBLE	1
1.1 Background	1
1.2 Problem Description	4
1.3 Approach to the Problem and Thesis Outline	10
2 RADAR SYSTEM AND DATA REPRESENTATION	13
2.1 Multi-Frequency Radar System	13
2.2 Interpretation of Target Data	22
2.3 Generalized Three Dimensional Formula	31
3 POINT SPREAD FUNCTION, SYSTEM RESOLUTION	40
3.1 Spatial Frequency Units	40
3.2 Point Spread Function in the Continuous Domain	47
3.3 Point Spread Function from a Different Point of View	52
3.4 Resolution of the Imaging System	58
3.5 Resolution from Doppler Bandwidth of the Signal	62
	vi

4	DISCRETE PSF AND SAMPLING REQUIREMENTS	67
4.1	Discrete PSF	67
4.2	Sampling Requirements	77
4.3	Sampling Requirements from the DOF Point of View	83
4.4	Conclusion	86
5	ERRORS IN POLAR COORDINATE SAMPLING	88
5.1	Poisson's Summation Formula	90
5.2	Angular Sampling	92
5.3	Radial Sampling	98
5.4	Simultaneous Radial and Angular Sampling	109
5.5	Conclusion	127
6	RECONSTRUCTION METHODS	131
6.1	Coherent Processing	133
6.2	Incoherent Processing	148
6.3	Mixed Processing	154
6.4	Digital Implementation	155
	APPENDIX 6A	165
	APPENDIX 6B	166
	APPENDIX 6C	168
7	SOME PRACTICAL CONSIDERATIONS AND EXPERIMENTAL RESULTS	170
7.1	RAT SCAT (Radar Target SCATtering site) Data	170
7.2	Range Compression	174
7.3	Azimuth Compression, Coherent Processing	179

7.4	Incoherent Processing	197
7.5	Mixed Processing	200
7.6	Comparison of the Three Techniques	201
8	INVERSE SYNTHETIC APERTURE RADAR	203
8.1	The General ISAR Doppler	203
8.2	Linear Trajectory	210
8.3	Circular Trajectory	216
8.4	Conclusion	231
	APPENDIX 8A	234
	APPENDIX 8B	235
9	EXTENSION TO FURTHER STUDIES AND CONCLUSION	236
9.1	Extension to Further Studies- Motion Compensation	236
9.2	Conclusion	242
	REFERENCES	250

## LIST OF FIGURES

<u>Figures</u>	<u>Page</u>
1.1 Measurement of echo phase from a rotating target.	5
2.1.1 Signal format for the MFS radar with $t_i = 0$ .	15
2.1.2 Block diagram of the MFS radar data gathering system.	16
2.2.1 2-D Imaging geometry and the pupil function.	24
2.2.2 Distorted data sampling pattern in the Fourier domain for large values of $\omega T_2$ vs. undistorted sampling pattern in the Fourier transform domain for small values of $\omega T_2$ .	25
2.3.1 3-D radar target model for Bojarski's identity.	38
2.3.2 3-D data in Fourier domain showing data confined in concentric spheres of radii $k_{\min}$ and $k_{\max}$ .	38
3.1.1 Doppler geometry for Strip mode SAR.	43
3.2.1 Point spread function of the radar imaging system.	49
3.2.2 Approximate PSF of the MFS radar imaging system.	51
3.3.1 Projected distance onto the LOS of point P is $\rho \cos(\theta - \phi)$ , and of point $P_0$ is $\rho_0 \cos(\theta)$ .	57
3.4.1 Comparison of point spread functions for the annula ring ( $k_0 = 10k_B$ ) and disk ( $k_0 = 1/2k_B$ ) pupil functions.	60
3.5.1 Figure showing the distance of $P_0$ along the LOS (range) from the initial point at aspect $\theta = 0$ .	64
4.1.1 PSF of discrete pupil of the imaging system.	72

4.1.2	Difference of the PSF in Fig. 4.1.1a and the PSF in Fig. 4.1.1b.	75
4.1.3	PSF for the discrete pupil $N=256$ , $K=1$ .	76
4.2.1	$\ell = a \cos(\theta - \phi_0)$ is the contour of the signal from a point target $\sigma(a, \phi_0)$ projected onto the line-of-sight as it rotates.	82
4.2.2	Regions of $(N, K)$ which illustrate the sampling requirements. $N, K$ are integers greater than 0.	84
5.2.1	Angular sampling on a unit circle.	93
5.2.2	Fourier Bessel transform of a unit circle and its angular sampling effects.	99
5.3.1	Full disc pupil function, discrete in radial dimension but continuous in angular dimension.	101
5.3.2	Convolution of $\hat{e}_n(\rho, x)$ with $w(\frac{n(K-1)}{k_B} - x)$ .	107
5.3.3	An annula ring pupil function, discretely sampled in radial dimension, but continuously sampled in angular dimension.	108
5.3.4	Fourier Bessel transform of a radially sampled disc function and its sampling effect.	110
5.3.5	Fourier Bessel transform of a radially sampled annula ring pupil function ( $k_0 = 10k_B$ ).	111
5.4.1	Polar format sampling in both radial and angular dimensions.	114
5.4.2	Integration process for the system angular sampling clutter $A_n(\rho)$ .	119
5.4.3	Plot of $\hat{C}_n(\rho, x)$ for $n=1$ , $N=0, 2, 4, 6, 8, 10, 100$ , and $\rho=0.1$ .	122
5.4.4	Integration interval for the annula ring case.	126
6.1.1	Range compression for MFS radar.	136
6.1.2	Phase and Doppler vs. aspect angle for point target at $(\phi, \rho)$ .	137

6.1.3	Angular (azimuth) partitioning of the radar data and the change in variables in coherent processing and mixed processing methods.	140
6.2.1	The correlation processing of Eq. (6.2.3) for the incoherent PSF.	151
6.2.2	Point spread function of a disc pupil function and a conical pupil function. $\mathcal{B}\{\cdot\}$ represents a Fourier Bessel transform or Hankel transform.	153
6.3.1	Plots of magnitudes of point spread functions related to the three processing techniques.	156
6.4.1	Magnitude of point spread functions with coherence intervals $60^\circ$ and $180^\circ$ . These are normalized such that the total energy is unity.	160
6.4.2	Variation of $\rho_{HP}$ the half power (3dB) width of the point spread function with coherence angle $\theta_c$ .	161
7.1.1	RAT-SCAT site recording geometry.	171
7.2.1	Phase and magnitude of experimental data set 1. The horizontal axis represents frequency in steps of 3.4MHz (9.130MHz to 9.997MHz). The vertical axis represents aspect (azimuth) angles $0^\circ$ (top) to $180^\circ$ (bottom) in increments of a nominal $0.2^\circ$ .	175
7.2.2	Magnitude of phase of the range compressed data. The horizontal axis represents range (0 to 145ft.) and the vertical axis represents aspect angle (azimuth) $0^\circ$ (top) to $180^\circ$ (bottom).	177
7.3.1	Reconstruction by coherent processing technique.	181
7.3.2	Magnitude of the reflectivity of two tail end target points.	184
7.3.3	Reconstruction from experimental data set 1 using unmodified coherent reconstruction technique showing aspect (azimuth) angle undersampling effects due to non-constant target reflectivity function.	186

7.3.4	Images from data set 2, reconstructed from modified range compressed data.	189
7.3.5	Reconstruction with $180^\circ$ aspect (azimuth) angle extent from experimental data set 2, with no target symmetry assumed. The bottom half of the target is in the shadow region.	192
7.3.6	Reconstruction from data set 2, using coherent interval $\theta_c = 47^\circ$ , mean (spatial) frequency $k_0 = 194.478$ but varying center (of rotation) range bin number. One range bin number corresponds to 0.56 ft.	194
7.4.1	Reconstruction from data set 1, using the three reconstruction techniques.	198
7.4.2	Reconstruction from data set 2, using the three reconstruction techniques.	199
8.1.1	Inverse SAR geometry.	205
8.2.1	Linear flight path geometry.	211
8.2.2	Computed flight parameters for linear trajectory vs. distance from the broadside position.	213
8.2.3	Flight parameter variation with time for a linear trajectory, plotted from actual tracking data of a F111 plane.	217
8.3.1	Imaging geometry for the circular trajectory case.	219
8.3.2	Computed time variation of flight parameters for a circular trajectory with values of $\delta (=R/R_0)$ equal to .1, .3, .5, .7, and .9.	222
8.3.3	Computed time variation of flight parameters for a circular trajectory with values of $\delta (=R/R_0)$ equal to .1, .3, .5, .7, and .9.	224
8.3.4	Flight parameters vs. time for a circular trajectory (approximately) plotted from actual tracking data on a F111 plane making a circular turn.	226
8.3.5	Elliptical effective trajectory for small angle of intersection between the circular trajectory plane and the $(\bar{u}_h, \bar{R}_0)$ plane.	232
		xii



## LIST OF TABLES

<u>Tables</u>	<u>Page</u>
3.4.1 Resolution Limit and Sidelobe Levels of Different PSF's.	61
3.4.2 Variation of Sidelobe Level with Bandwidth.	62
4.2.1 Summary of Sampling Requirements in Polar Coordinates.	83
5.2.1 Properties of the First Five Angular Sampling Clutter.	97
5.4.1 The Five Components of the Fourier Bessel Transform of the Discrete Pupil Function.	128
7.1.1 Parameters for Model F102-Plane Data, Model: 0.29 x Actual Plane Dimensions, Plane Dimensions: 68 ft. (Nose-Tail), 38 ft. (Wing-Span), Model Dimensions; 20 ft. (nose-Tail), 11 ft. (Wing-Span).	173

## Chapter 1

### PREAMBLE

#### 1.1 Background

This dissertation addresses the problem of obtaining high resolution images of rotating objects utilizing radar signals. High resolution here refers to resolutions which are a fraction of a wavelength.

The key idea behind the high resolution capability of imaging radars is the ability to record not only the magnitude of an echo but also its phase. In a broad sense, radar receivers that can do this are called coherent radar. The era of coherent radar was inaugurated when stable oscillators became available. Once the phase measuring capability of a radar receiver was realized, it did not take long for Carl Wiley at the Goodyear Aerospace Corporation to initiate the concept of the Synthetic Aperture Radar in 1951 [31].

The Synthetic Aperture Radar (henceforth SAR) in the simplest case achieves high azimuth resolution by making use of the linear motion of the antenna platform with

respect to the earth. The early radar imaging systems were primarily terrain mapping systems. The radar platform was typically airborne. The actual physical antenna aperture was usually small. A bibliography consisting of the articles [8,12,22,35] gives a good review of SAR. The first practical SAR system was demonstrated in 1957 by Cutrona et al. using an optical processor. Since then, a wide range of coherent radar imaging systems have been initiated and developed for many diverse applications.

SAR can in general be classified into two groups based on the geometry of the system. The first group assumes that the target is stationary. This includes the usual SAR modes which depend primarily on optical scattering, namely strip mapping, Doppler Beam Sharpening mapping, and Spotlight mapping [21,6]. Other imaging systems in the group are based on different principles of operation. In particular, there is Interferometer Radar [16] for topographic mapping, Harmonic Radar [17] for in-foliage metallic targets, and Hologram Matrix Radar [19] for ice thickness profile measurement. Members of this group are typically characterized as terrain mappers.

The second group of SAR types is one in which the target is presumed to move along a certain trajectory

while the antenna(e) remains stationary. Inverse SAR is a typical example. Other radar imaging systems in this class exploit a mixture of techniques; namely, frequency diversity (multiple frequency system), spatial diversity (multistatic system), and polarization properties of radar reflections. To analyze this type of SAR, a wide range of scattering models including Rayleigh, physical optics and Geometrical Theory of Diffraction (GTD) are used. Ormsby et al. [25] give a succinct overview of some of the systems. Inverse SAR techniques can be found in Chapter 7 of [10] for airborne targets and in [39] for ships upon the ocean. Strictly speaking, both groups utilize a similar theory but because of the different applications and geometry, the resolution requirements, sampling rate, parameter sensitivity, target model and system geometry will vary. Radio astronomy is an exception because it belongs to both groups.

Interest in SAR in this dissertation lies mainly on the Inverse SAR. Such a system is also called a Range-Doppler Imaging Radar. If the phase differences between the phase of the transmitted waveform and the phase of the received echo of some fixed point of reference on the target are compensated for, the moving target will "appear" as if it were static in translational motion but rotating about the point of reference. Since

the gross overall range to the target does not contribute to the imaging process, inverse SAR is essentially a Range Doppler Imaging system of rotating objects. Except for system geometry, this system is similar in principle to the Spotlight mode SAR [6]. The problem of gross range estimation and the phase compensation associated with it is called motion compensation.

## 1.2. Problem Description

Consider a rigid body as shown in figure 1.1 rotating with its axis normal to the paper. If the illuminating radar is far from the target, then the lines of constant range ( $x$ ) and cross-range ( $y$ ) are rectangular coordinates on the target.

Consider a point reflector at  $(x,y)$  on the target. The two way phase delay of an echo from this point can be measured by a coherent radar as

$$\phi = \frac{4\pi}{\lambda} r(x,y)$$

where  $\lambda$  is the wavelength of the radar signal and  $r(x,y)$  is the antenna to the  $(x,y)$  point distance.  $r_0 \gg |x|$ ,  $r_0 \gg |y|$ . Then

$$\begin{aligned} r(x,y) &= \sqrt{(r_0+x)^2 + y^2} \\ &\approx (x+r_0) + \frac{y^2}{2(r_0+x)} \end{aligned}$$

Radar  
antenna

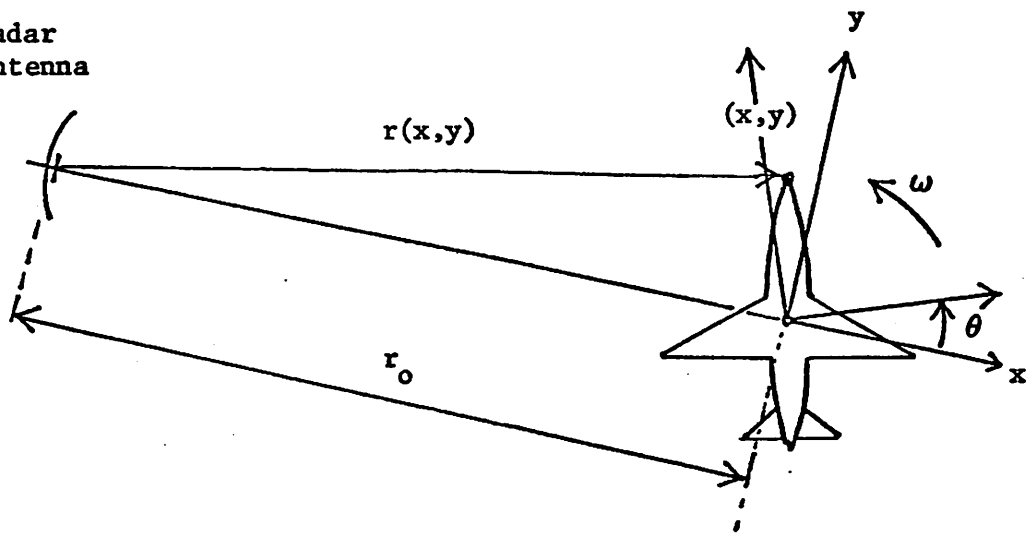


Figure 1.1. Measurement of echo phase from a rotating target.

$$\approx r_0 + x + \frac{y^2}{2r_0}$$

Suppose  $r_0$  is constant. Then the Doppler frequency of the echo is

$$\begin{aligned} f &= \frac{1}{2\pi} \frac{d\phi}{dt} \\ &\approx \frac{2}{\lambda} \left[ \frac{dx}{dt} + \frac{y}{r_0} \frac{dy}{dt} \right] \\ &= \frac{2}{\lambda} \left[ -1 + \frac{x}{r_0} \right] \omega y \end{aligned} \quad (1.2.1)$$

where  $\omega$  is the rotation rate in radians per second, so that  $x = \rho \cos \omega t$ ,  $y = \rho \sin \omega t$  for  $\rho = \sqrt{x^2 + y^2}$ .

Suppose over a small enough time interval, the target rotation is small enough such that  $x$  does not change by more than one range cell width. This means no range migration. In this case the Doppler frequency of the reflected signal is proportional to the cross-range distance  $y$  of the point reflector. Therefore, resolving the Doppler frequencies of two point reflectors will mean resolving them in cross-range.

In attempts to strike a better cross-range resolution, there has been over the years a trend toward processing SAR and Inverse SAR (ISAR) data over wider and

wider time (hence aspect angle) intervals. Over this time interval, the range coordinate  $x$  may migrate through one or more range cells (called range walking). Also, the "constant" of proportionality  $\frac{2}{\lambda} (-1 + \frac{x}{r_0}) \omega$  in Eq. (1.2.1) may not stay constant over the time interval (changing Doppler), resulting in Doppler spread, which translates into poorer cross-range resolution. The latter effect is also called variable range-rate (page 14, [37]).

Processing techniques which partially solve these problems were suggested [7] but in 1974 it was realized [37] that all these problems disappeared if the data were regarded as samples collected over a polar coordinate raster. This idea in principle allowed full Doppler processing and hence full potential resolution. Optical methods were used to show the principle that indeed by physically rearranging the data on the photographic surface of an optical filter in polar format, the conventional problems of range walking, changing Doppler, and higher order terms in the Taylor's series expansion of  $r(x,y)$  disappeared altogether.

In practice, to make the principle work takes more considerations. For one thing, most radar objects that are of interest are three dimensional in nature. Therefore, point scatterers in the shadow region of the



object can get obscured. In other words, some point scatterers will not contribute to the signal return for all aspect angles. This means that one will not be able to fully utilize the data from all aspect angles and therefore not be able to achieve the best resolution from these point scatterers.

A similar problem that is different in origin is that for practical radar objects, signal returns from point scatterers are subject to a great deal of fluctuation, both in amplitude and phase. This phenomenon can be due to either the nature of the target itself or due to atmospheric effects. The important point is that now the original assumption that the target backscatter function is constant with time can no longer hold. These questions are dealt with in Chapters 2 and 7.

In the early years of SAR development, because of the enormous storage and computational load required to reconstruct SAR images, most operational SAR used optical processors. It was not until about 1975 that serious work on SAR digital processing appeared in the literature ([21],[3]). The advent of CCD correlators [2] and new memory technology (page 181,[6]) make the real time SAR digital processor a realizable entity. In fact, the first real time SAR digital system was built into the NASA SEASAT

satellite and launched in early 1979. Therefore it is important that digital processing of ISAR data be studied and well understood.

The main issue in this dissertation will be to study digital reconstruction techniques with ISAR data to obtain as good a resolution as possible. One possibility is to collect and process the data over a wider time interval. This invariably leads to the necessity of having to treat the data as being sampled in polar format. The special case in which the target data is collected over  $360^\circ$  aspect angle is considered.

A question arises from the known fact that a practical processor for such imaging systems has to be digitally implemented [3]. Since data samples are collected in discrete target aspect angle intervals and only discrete range samples can be measured with a radar, the effects of such discrete sampling must be studied first. The important question that needs to be answered is therefore how to determine the sampling requirement for the polar coordinate sampling format. The answer to this question has applications in Tomography, Radio astronomy, and all other systems which collect data in polar format.

In practical ISAR systems, the gross range ( $r_0$ ) of the target is not constant. This will give rise to a

composite Doppler in the reflected signal. It is therefore important to isolate the Doppler component due to  $\frac{dr_0}{dt}$  and subtract it from the composite Doppler. Moreover, since the reconstructed image is a projection of the target onto a plane normal to the target rotation vector, the direction of the rotation vector  $\bar{\omega}$  should be known or estimated apriori so that the image can be scaled correctly. For an arbitrary object flying an arbitrary trajectory,  $\bar{\omega}$  is time varying and difficult to predict.

### 1.3. Approach to the Problem and Thesis Outline

The radar data collecting system cascaded with a signal processor are treated together as an imaging system. A good idea of the resolution provided by the signal processor can be obtained by first computing the point spread function (PSF) of the imaging system. A measure of resolution based on the PSF can be defined by either the Rayleigh criterion or the half power width of the PSF. The PSF and hence the resolution can also be derived from Doppler bandwidth concepts. These are done in Chapter 3.

The polar coordinate sampling requirement issue is dealt with first using the Degrees of Freedom (henceforth DOF) concept [15], then with Doppler bandwidth concepts.

These are studied in detail in Chapter 4. Unfortunately these concepts only provide a method to evaluate the sampling requirement of the system. It does not however, indicate what happens in the event that the sampling requirement(s) is not met. In Chapter 5, Poisson's summation formula [27] is used to study the error incurred in the discrete sampling in polar coordinates. The analytic expressions derived for the sampling error can be used to evaluate the consequences of undersampling. At the same time, Poisson's summation formula is also applied to Tomographic systems. The resulting analytic expressions for the sampling error also allow one to understand the effects of polar coordinate sampling in these systems.

For reasons of available experimental data, a Multiple Frequency Step (MFS) radar is described in Chapter 2. The relation between the data and the target reflectivity function  $\sigma(x,y)$  is derived first for the two dimensional case where  $(x,y)$  are the target coordinates. In this case the target rotation vector is always normal to the line-of-sight (LOS). The three dimensional relation between  $\sigma(\bar{x})$  and the data is also derived with  $\bar{x}$  being the target point vector relative to the rotation center. In this case the LOS is at an arbitrary angle relative to the rotation vector.

The analyses in the subsequent chapters are based on the MFS radar system. Even then, unless otherwise stated the actual analyses can be applied to other high-resolution radar systems.

Digital implementation techniques of the target reconstruction problem are developed in Chapter 6 keeping in mind the computational speed and storage restrictions. These techniques are applied to the experimental data in Chapter 7.

An attempt will be made in Chapter 8 to derive analytically the various Doppler components of an airborne target flying an arbitrary trajectory. The time pattern of these Doppler components is studied for a linear trajectory and a circular trajectory. An understanding of the time pattern of the various Doppler components is an important step before the actual reconstruction techniques can be applied to realistic ISAR data.

Chapter 9 gives a summary of the results in all the previous chapters.

## Chapter 2

### RADAR SYSTEM AND DATA REPRESENTATION

#### 2.1 Multi-Frequency Radar System

The radar transmits a sequence or burst of  $K$  pulses starting at time  $t_i$ . The subscript  $i$  corresponds to the  $i^{\text{th}}$  burst. The transmitted signal is

$$s(t) = \sum_{i=0}^{N-1} x(t-t_i) \quad (2.1.1)$$

where  $N$  = total number of bursts transmitted

$t_i = iT_3$

$T_3$  =burst repetition period

$x(t-t_i)$  is the  $i^{\text{th}}$  burst of pulses defined as

$$x(t) = \sum_{j=0}^{K-1} x_j(t-jT_2), \quad (2.1.2)$$

$x_j(t-jT_2)$  is the  $j^{\text{th}}$  pulse defined as

$$x_j(t) = Ba(t)\cos(2\pi f_j t + \phi_j) \quad (2.1.3)$$
$$a(t) = \begin{cases} 1 & \text{if } t \in [0, T_1] \\ 0 & \text{if } t \notin [0, T_1] \end{cases}$$

$T_2$  =pulse repetition period in seconds

$T_1$  =pulse width in seconds

$f_j$  =frequency of the  $j^{\text{th}}$  pulse carrier

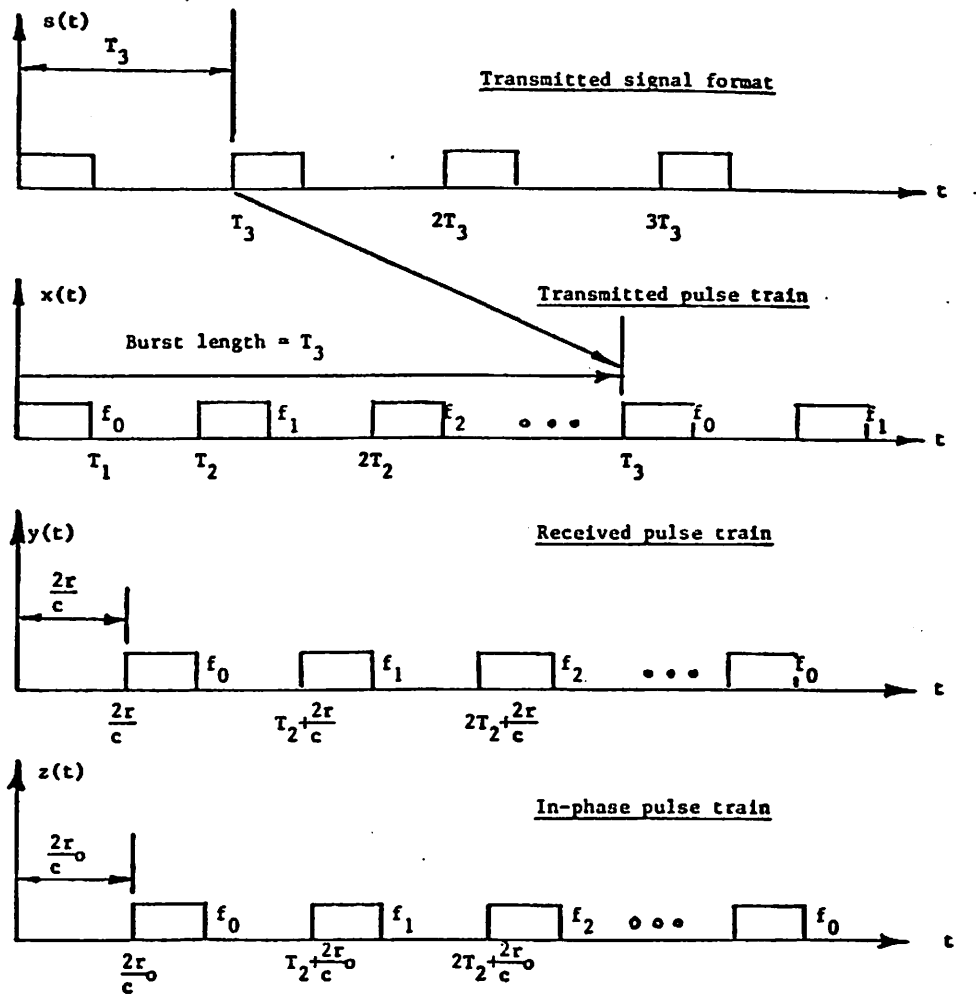
$\phi_j$  = arbitrary but constant phase in the  $j^{\text{th}}$  pulse. It is implicit in Eq. (2.1.1) that the bursts are repeated continuously. For convenience of illustration, the bursts are separated in time. This is depicted in Fig. 2.1.1, with  $T_3 \gg T_2$ . Time separation between bursts may or may not exist depending on the application and design. For example, in designing a "track while scan radar," one may want to separate the bursts and do search scanning between bursts.

Figure 2.1.2 is a functional block diagram of the MFS radar system. It shows the implementation of a matched filter composed of a reference signal generator, a mixer (multiplier) and an integrator. The matched filter is matched to a signal phase corresponding to the two-way propagation delay of a point at some arbitrary but fixed range  $r_0$ . With the return signal as input, the matched filter output will give a composite phase of all scattering centers referenced to the point at range  $r_0$ .

From Eqs. (2.1.1) to (2.1.3) the transmitted signal can be rewritten as

$$s(t) = B \sum_{i=0}^{N-1} \sum_{j=0}^{K-1} a(t-iT_3-jT_2) \cos(2\pi f_j [t-iT_3-jT_2] + \phi_{ij})$$

where  $a(t)=1$  if  $t \in [0, T_1]$ , and where  $\phi_{ij}$  is the arbitrary phase associated with the  $j^{\text{th}}$  pulse in the  $i^{\text{th}}$  burst. For simplicity, suppose there is only one point



Quadrature reference signal  $z'(t) = \text{Hilbert transform of } z(t)$ .  
 Complex reference signal  $R(t) = z(t) + jz'(t)$ .

Figure 2.1.1. Signal format for the MFS radar with  $t_1 = 0$ .



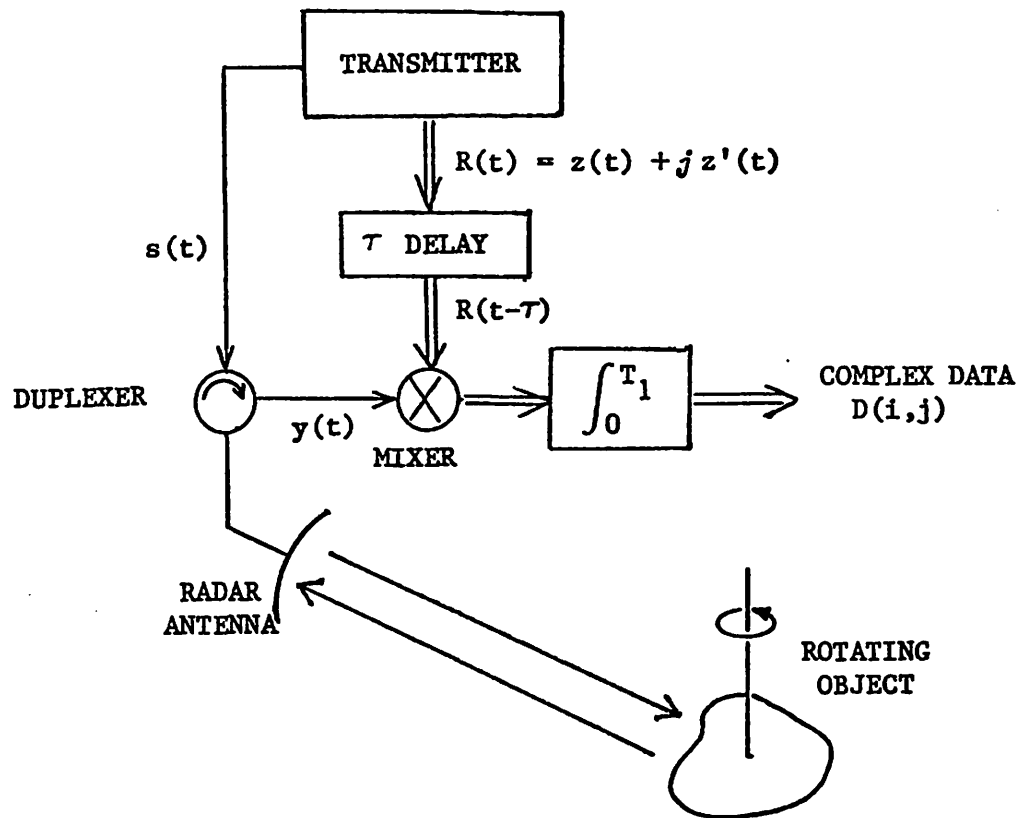


Figure 2.1.2. Block diagram of the MFS radar data gathering system.

scatterer at range  $r(t)$ . Suppose also that the pulse width  $T_1$  is sufficiently small so that the  $j^{\text{th}}$  pulse of the  $i^{\text{th}}$  burst can be considered as hitting the target at time  $t = iT_3 + jT_2 + \tau$ .  $\tau$  is the pulse transit time between the antenna and the point target. Then the complex representation of the received signal is

$$y(t) = B' \sum_i \sum_j a(t - iT_3 - jT_2 - \frac{2r(iT_3 + jT_2 + \tau)}{c}) \cdot \exp\{j2\pi f_j(t - iT_3 - jT_2 - \frac{2r(iT_3 + jT_2 + \tau)}{c} + \phi_{ij})\}$$

where  $j^2 = -1$ .

For simplicity of notation,  $r(iT_3 + jT_2 + \tau)$  will be written as  $r$  unless it is important to show the  $\tau$  dependence explicitly. For the reference signal to the matched filter, let us use the complex representation of the carrier wave in the following.

$$R^*(t_s - t) = B \exp\{-j[2\pi f_j(t - t_s) + \phi_{ij}]\}$$

for  $t \in [iT_3 + jT_2, iT_3 + (j+1)T_2]$ ,  $i=0,1,2,\dots,N-1$ ,  $j=0,1,2,\dots,K-1$ .  $R(t)$  is the impulse response of the matched filter and  $t_s$  is sampling time instant of the matched filter. The matched filter output is thus

$$D_r(t_s) = \int_{t_s - T_1}^{t_s} R^*(t_s - t) y(t) dt$$

$$\begin{aligned}
&= BB' \sum_i \sum_j \int_{t_s - T_1}^{t_s} e^{-j[2\pi f_j(t-t_s) + \phi_{ij}]} \\
&\quad \cdot e^{j[2\pi f_j(t_s - iT_3 - jT_2 - \frac{2r}{c}) + \phi_{ij}]} \\
&\quad \cdot \frac{a(t - iT_3 - jT_2 - \frac{2r}{c}) dt}{a(t - iT_3 - jT_2 - \frac{2r}{c}) dt} \\
&= BB' \sum_i \sum_j \int_{t_s - T_1}^{t_s} e^{j2\pi f_j[t_s - iT_3 - jT_2 - \frac{2r}{c}]} \\
&\quad \cdot \frac{a(t - iT_3 - jT_2 - \frac{2r}{c}) dt}{a(t - iT_3 - jT_2 - \frac{2r}{c}) dt}
\end{aligned}$$

Let  $D_r(t_s)$  be sampled at

$t_s = i_0 T_3 + j_0 T_2 + \frac{2r_0}{c} + T_1$ , for  $i = 0, 1, \dots, N-1$ ,  
 $j = 0, 1, \dots, K-1$ .  $r_0$  is the range at some fixed reference point near the target point. Then, as illustrated in

Fig. 2.1.2, the sampled data will be

$$\begin{aligned}
D_r(i_0, j_0) &= BB' \sum_i \sum_j \int_{i_0 T_3 + j_0 T_2 + \frac{2r_0}{c}}^{i_0 T_3 + j_0 T_2 + \frac{2r_0}{c} + T_1} a(t - iT_3 - jT_2 - \frac{2r}{c}) dt \\
&\quad \cdot \exp\{j2\pi f_j[(i_0 - i)T_3 + (j_0 - j)T_2 - \frac{2}{c}(r - r_0)]\}
\end{aligned}$$

where  $D_r(t_s)$  is now denoted as  $D_r(i_0, j_0)$ . For  $|r - r_0|$  sufficiently small (say  $|r - r_0| \ll T_1 = \text{pulse width}$ ),

$$\begin{aligned}
D_r(i_0, j_0) &= T_1 BB' \sum_i \sum_j \delta(i - i_0) \delta(j - j_0) \\
&\quad \cdot e^{j2\pi f_j[i_0 - i]T_3 + (j_0 - j)T_2 - \frac{2}{c}(r - r_0)} \\
&= BB' T_1 \exp\{-j2\pi f_j(\frac{2}{c})(r - r_0)\}.
\end{aligned}$$

Thus in general

$$D_r(i, j) = T_1 BB' \exp\{j2\pi(\frac{2f_j}{c})(r - r_0)\}.$$

Using a simpler notation

$$k_j = \frac{2f_j}{c}, \text{ then}$$

$$D_r(i, j) = T_1 BB' \exp\{j2\pi k_j (r - r_0)\}. \quad (2.1.5)$$

This matched filter output which corresponds to the  $j^{\text{th}}$  pulse of the  $i^{\text{th}}$  burst is the sample data point corresponding to the  $j^{\text{th}}$  frequency. The output from each pulse is a complex number whose phase corresponds to the two way path difference between the target point and its reference, and whose "amplitude"  $T_1 BB'$  measures the scattering coefficient of the point object. The radar system described will therefore measure the phase differential between a target point and a reference point.

It should also be noted that if  $\{f_j\}$  is arranged so that

$$\begin{aligned} f_j &= f_0 + j\Delta f \\ k_j &= \frac{2f_0}{c} + j\frac{2\Delta f}{c} \end{aligned}$$

where  $\Delta f$  is the temporal frequency step, then  $D_r(i, j)$  represents the spectral signature of the point object at range  $r$  corresponding to the  $i^{\text{th}}$  burst. If one takes the discrete Fourier transformation of  $D_r(i, j)$  over  $j$ , a range profile can be obtained. The above assertion, of course, holds true only if the target range  $r$  does not change significantly over the burst length interval. For a continually moving target (changing  $r$  with motion in translation and rotation), the entire burst must be sampled before the target point moves sufficiently far to

produce appreciable phase shift. The customary criterion is to set the phase shift over half the burst length to be less than  $\pi/2$ . In the worst case, this corresponds to

$$(v_r \cdot \frac{KT_2}{2}) (\frac{2f_B}{c}) \leq \frac{\pi}{2}$$

where  $v_r$  is the range rate,  $f_B$  the signal bandwidth over the entire burst. The pulse repetition period within a burst is therefore governed by

$$T_2 \leq \frac{\pi c}{2Kv_r f_B} \quad (2.1.6)$$

For example, with  $K=256$ ,  $v_r=250$  m/s,  $f_B=500\text{MHz}$ ,  $T_2 \leq 15\mu\text{s}$ . This corresponds to a maximum unambiguous range of only 2.25km.

When the above condition on  $T_2$  is not met, range profile distortion will be one consequence. If the point target were stationary,  $D_r(i,j)$  in Eq. (2.1.5) is an accurate representation of the point target spectrum. The DFT of  $D_r(i,j)$  over  $j$  will give a range profile which is the result of an impulse function convolved with the ambiguity function of the signal  $x(t)$ . If the point target moves in range by some appreciable amount during the entire burst length time, the range profile will be a rectangular (or pulse) function convolved with the signal ambiguity function. This form of distortion is called range profile distortion. For constant  $v$ , range profile distortion (abbreviated rpd) can be eliminated by phase

shift correction on  $D_r(i,j)$  . It has been estimated [40] that

$$D_r(i,j) \Big|_{\substack{\text{rpd} \\ \text{corrected}}} = D_r(i,j) \exp\{-j2\pi(\frac{2f_j}{c})(v_r T_2)\}$$

Burst-to-burst range walking is another consequence of the motion of the object. It means that the target point has moved more than one range resolution cell distance during a burst time interval. In the absence of range profile distortion, the effect of range walking is a shifting in range between two adjacent signatures\*. The moving target point gives rise to a similar linear phase shift error of the data. Range walking (abbreviated rw) is corrected as follows [40]:

$$D_r(i,j) \Big|_{\substack{\text{rw} \\ \text{corrected}}} = D_r(i,j) \exp\{-j2\pi(\frac{2f_j}{c})(v_r i T_3)\}$$

where  $v_r i T_3$  is the distance moved since the first burst.

Range profile distortion due to substantial target point displacement caused by rotation of the vector  $\overline{rr}_0$  is a much more difficult problem. Fortunately target point displacement within a burst length is usually negligibly small and of little consequence. For example say the target rotation rate is  $\omega=0.02(\text{rad/s})$ ,  $\overline{rr}_0 = 30 \text{ m.}$ ; then

---

\*A signature is the set of data associated with a burst either before or after range compression.

the maximum range rate is  $v_r = 0.6$  m/s. For a burst length of  $T_3 = 10^{-2}$  s, the displacement is  $\Delta r = 0.006$  m. For  $f = 500$  MHz, the echo phase shift error is  $\frac{2f}{c} \Delta r = 0.004$  rad ( $0.0006 \lambda$ ).

## 2.2 Interpretation of Target Data

The MFS radar described in section 2.1 can be used as an Inverse SAR (ISAR) system. The reference point will be the center of rotation of the object. Its range  $r_0$  will still be kept constant.  $r_0$  is called here the gross range. The ISAR will be modeled first in two dimensions. This model will be extended later to three dimensions.

In deriving Eq. (2.1.5) for the  $j^{\text{th}}$  pulse in the  $i^{\text{th}}$  burst, the following implicit assumptions are made.

1. The gross range  $r_0$  is either constant or of a known time variation. In practice  $r_0$  is limited to an accuracy of one range resolution cell. It is even more difficult to identify the center of rotation of an airborne target by virtue of its coherent signal reflections.
2. The signal echoes are specular returns. This means that the reflections can be approximated by physical optics. Echoes due to diffraction, reverberative phenomenon, and creeping waves are

considered negligible. The specular assumption holds when signal wavelength  $\lambda \ll 2a$  where  $a$  is the maximum radial extent of the target.

3. There is no atmospheric frequency dispersion. The phase delay from a target at constant range  $r$  is the same at all frequencies.
4. There is no atmospheric propagation phase error. That is, the delay phase error is negligible. This holds for relatively short propagation path lengths in the troposphere.

Instead of a single point scatterer, consider a rotating object ( $\omega$  rad/s) with every point on it being a scattering center as shown in Fig. 2.2.1. Let the rotation vector  $\bar{\omega}$  be normal to the LOS. Suppose the far field assumption ( $r_0 \gg 2a$ ) holds so that there is no range curvature. Let  $(\xi, \eta)$  be rectangular coordinates fixed on the object. Suppose at  $t=0$ , the  $(\xi, \eta)$  axes coincides with the (down-range( $x$ ), cross-range( $y$ )) axes. Also suppose  $t=0$  at the beginning of the first pulse ( $j=0$ ) in the first burst ( $i=0$ ). Here the aspect angle is synonymous to the angle between the  $x$ -axis and some particular fixed axis ( $\xi$ ) on the target. The aspect angle at time  $t$  is equal to  $\omega t$ , where  $\omega$  is assumed to be constant. The  $(x, y)$  coordinates are thus related to the  $(\xi, \eta)$  coordinates by



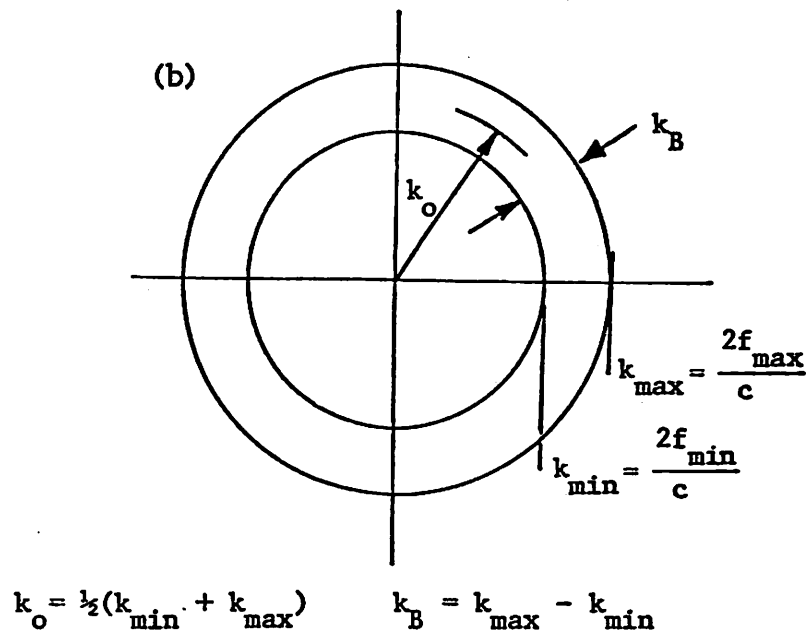
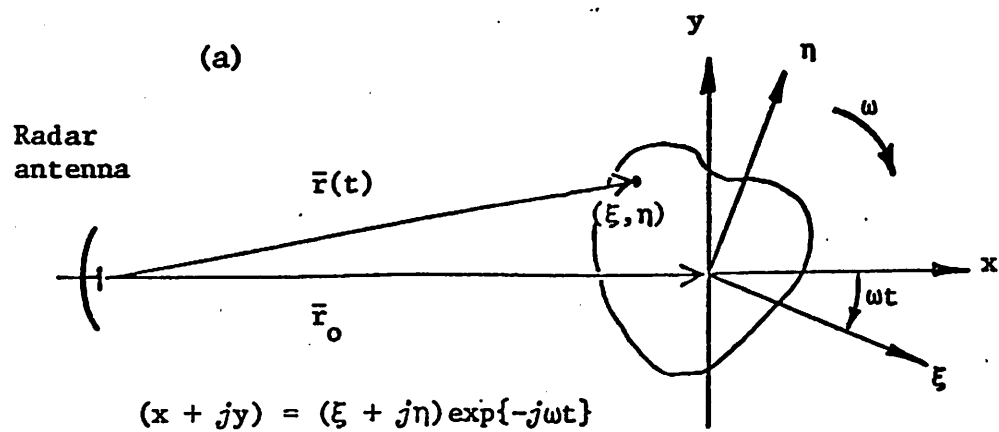
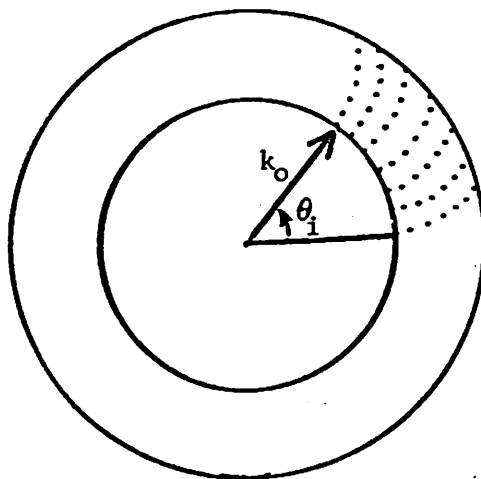
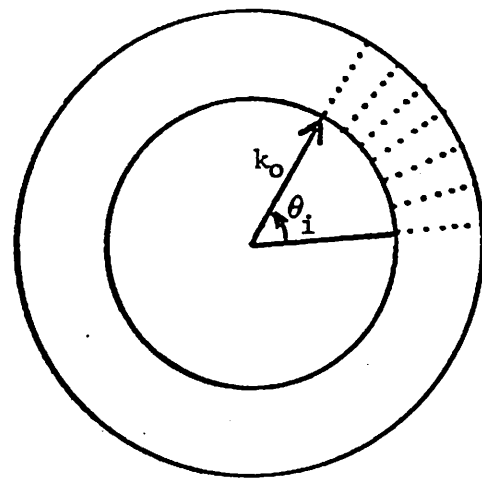


Figure 2.2.1. 2-D Imaging geometry and the pupil function.  
 (a) Two dimensional target coordinates and the rotating object. (b) The resulting 2-D pupil function of the radar imaging system.



With  $\omega T_2$  not sufficiently  
small



With  $\omega T_2$  sufficiently  
small

Figure 2.2.2. Distorted data sampling pattern in the Fourier domain for large values of  $\omega T_2$  vs. undistorted data sampling pattern in the Fourier transform domain for small values of  $\omega T_2$ .

$$(x+jy) = (\xi+j\eta)\exp\{-j\omega t\} \quad (2.2.1)$$

Finally assume that there is no range shadowing\* so that at the  $\omega t$  aspect angle, the reflectivity of any point scatterer at  $(\xi, \eta)$  is  $\sigma(\xi, \eta; \omega t)$ . The point scattering coefficient of the same point scatterer is denoted as  $\sigma(x, y; \omega t)$  where  $(x, y)$  and  $(\xi, \eta)$  are related by Eq. (2.2.1).

The range vector  $\bar{r}$  of the point  $(\xi, \eta)$  at time  $t$  is

$$\bar{r}(t) = \bar{r}_0 + (\xi + j\eta)e^{-j\omega t} \quad (2.2.2)$$

Let  $r(\tau)$  be the initial distance of target point  $(\xi, \eta)$  when the first pulse ( $i=0, j=0$ ) hits the target. The two way transit time for the first pulse is therefore  $2\tau$ . Since the second pulse is transmitted  $T_2$  seconds later, the target point distance when the second pulse hits the target is  $r(\tau + T_2)$ . It is easy to see that the target is illuminated by a pulse only at the discrete times  $t=t_{ij}$  where

$$t_{ij} = iT_3 + jT_2 + \tau \quad (2.2.3)$$

for  $i=0, 1, 2, \dots, K-1$ ;  $j=0, 1, 2, \dots, N-1$ .

\*-----  
For any realistic object, shadowing cannot be avoided. But this assumption must be made for analytical justifications.

Let

$$(\xi + j\eta) = \rho \exp\{j\phi\}.$$

It follows from Eq. (2.2.2) that

$$\begin{aligned} r(t) &= [r_0^2 + \rho^2 + 2r_0\rho \cos(\omega t - \phi)]^{1/2} \\ &= r_0 [1 + (\frac{\rho}{r_0})^2 + 2(\frac{\rho}{r_0}) \cos(\omega t - \phi)]^{1/2} \end{aligned}$$

With the far field assumption,

$$(\frac{\rho}{r_0})^2 < (\frac{2a}{r_0})^2 \ll 1$$

Thus

$$\begin{aligned} r(t) &\approx r_0 [1 + 2(\frac{\rho}{r_0}) \cos(\omega t - \phi)]^{1/2} \\ &= r_0 [1 + \frac{\rho}{r_0} \cos(\omega t - \phi) + 0(\frac{\rho^2}{r_0^2})] \quad (\text{Taylor's expansion}) \\ &\approx r_0 + \rho \cos(\omega t - \phi) \quad (\text{far field assumption}) \quad (2.2.4) \end{aligned}$$

It follows from Eq. (2.1.5) that the data from point target  $(\xi, \eta)$  alone is

$$\begin{aligned} D_r(i, j) &= T_1 BB' \sigma(\xi, \eta; \omega t) e^{j2\pi k_j (r(t) - r_0)} \\ &= T_1 BB' \sigma(\xi, \eta; \omega t) e^{j2\pi k_j \rho \cos(\omega t - \phi)}. \end{aligned}$$

The variable doppler phase shift of the scattering point is thus

$$k \rho \cos(\omega t - \phi)$$

where  $k = k_j$  when  $t \in [iT_3 + jT_2, iT_3 + (j+1)T_2]$  for all values of  $i, j$  defined previously. Since the data is sampled only at  $t = t_{ij} = iT_3 + jT_2 + \tau$ , the sampled data becomes

$$\begin{aligned} D_r(i, j) &= T_1 BB' \sigma(\xi, \eta; \omega t_{ij}) \\ &\quad \cdot e^{j2\pi k_j \rho \cos(i\omega T_3 + j\omega T_2 + \omega \tau - \phi)} \quad (2.2.5) \end{aligned}$$

Let  $\theta_i = i\omega T$ . Typically with  $\omega = 0.02$  rad/s,  $T_2 = 10^{-2}$  s, and with no range ambiguity,

$$\omega T < \omega T_2 = (0.02)(10^{-2}) = 2 \times 10^{-4} \text{ rad.}$$

$\omega T$  can therefore be dropped from Eq. (2.2.5). Then,

$$D_r(i, j) = T_1 B B' \sigma(\xi, \eta; \omega t_{ij}) e^{jkj\rho \cos(\theta - \phi + j\omega T_2)} \quad (2.2.6)$$

Let

$$(x_i + jy_i) = (\xi + j\eta) e^{-j\theta_i} \quad (2.2.7)$$

$x_i$ ,  $y_i$  are therefore respectively the range and cross-range distances of the point  $(\xi, \eta)$  from its reference center at the beginning of the  $i^{\text{th}}$  burst.

$$\begin{aligned} \rho \cos(\theta_i - \phi + j\omega T_2) &= \text{Re}\{(\xi + j\eta) e^{-j(\theta_i + j\omega T_2)}\} \\ &= \text{Re}\{(x_i + jy_i) e^{-j(j\omega T)}\} \\ &= x_i \cos(j\omega T_2) + y_i \sin(j\omega T_2) \quad (2.2.8) \end{aligned}$$

Using the previous example again, but with the number of pulses per burst being  $K=256$ ,

$$j\omega T_2 < K\omega T_2 = (256)(0.02)(10^{-2}) = 5.12 \times 10^{-2} \text{ rad.}$$

Therefore  $j\omega T_2$  can be dropped from Eq. (2.2.7) and the following approximation can be made.

$$\begin{aligned} \rho \cos(\theta_i - \phi + j\omega T_2) &\approx x_i \\ &= \xi \cos \theta_i + \eta \sin \theta_i \quad (2.2.9) \end{aligned}$$

Substituting Eq. (2.2.9) into Eq. (2.2.6)

$$D_r(i,j) = T_1 BB' \sigma(x_i, y_i; \omega t_{ij}) e^{jk_j x_i} \quad (2.2.10)$$

Another way of looking at the problem is that one would like to keep  $j\omega T_2 \ll \pi/2$  by forcing

$$T_2 \ll \frac{\pi}{2\omega K} \quad (2.2.11)$$

such that the approximation in Eq. (2.2.9) still holds. For imaging a seaborne target with  $\omega=0.6$  rad/s and  $K=256$ , one would want to choose the pulse repetition period  $T_2$  such that

$$T_2 \ll \pi / (2 \times 0.6 \times 256) = 10^{-2} \text{ sec}$$

which corresponds to a pulse repetition frequency of at least in the order of 1KHz.

It follows from Eq. (2.2.10) that the composite data from the entire object is

$$D(i,j) = T_1 BB' \iint_{\substack{\text{Target} \\ \text{Area}}} \sigma(x_i, y_i; \omega t_{ij}) e^{j2\pi k_j x_i} dx_i dy_i .$$

Carrying out a coordinate transformation with Eq. (2.2.7),

$$D(i,j) = T_1 BB' \iint_{\substack{\text{Target} \\ \text{Area}}} \sigma(\xi, \eta; \omega t_{ij}) e^{j2\pi k_j (\xi \cos \theta_i + \eta \sin \theta_i)} d\xi d\eta$$

If  $\sigma(\xi, \eta; \omega t_{ij})$  is independent of  $\omega t_{ij}$ , and

$$Z(\theta, f) \triangleq \iint \sigma(\xi, \eta) e^{j\pi f (\xi \cos \theta + \eta \sin \theta)} d\xi d\eta \quad (2.2.12)$$

= 2-D Inverse F.T. of  $\sigma(\xi, \eta)$ .

Then  $T_1 BB' Z(\theta_i, k_j)$

Therefore, for a general object the data collected by the MFS radar can be interpreted approximately as the 2-D Inverse Fourier transform of the target reflectivity function  $\sigma(\xi, \eta)$ .  $i$  corresponds to the aspect angle  $\theta_i$  on the object at the beginning the  $i^{\text{th}}$  burst;  $j^{\text{th}}$  corresponds to the  $j^{\text{th}}$  spatial frequency component  $k_j$  of the object reflectivity function.

For most of the time  $\sigma(\xi, \eta; \omega t_{ij})$  represents the diffraction coefficient of  $(\xi, \eta)$  depending on its neighborhood. According to GTD [20], both the magnitude and the phase of  $\sigma$  will change with  $\theta_i$ .

In the case when  $\omega T_2$  is not sufficiently small to be neglected, one needs to substitute Eq. (2.2.7) into Eq. (2.2.6). Carrying out an analysis similar to the one above will lead to

$$D(i, j) = T_1 B B' Z' (k_j \cos j\omega T_2, k_j \sin j\omega T_2) \quad (2.2.13)$$

where

$$Z'(f_x, f_y) = Z(\tan^{-1}(f_y/f_x), \sqrt{f_x^2 + f_y^2}).$$

Thus even when  $\omega T_2$  cannot be neglected, the data still represents the two dimensional inverse F.T. of  $\sigma(x, y)$  except that now the transform domain sampling follows a curve

$$f_x(j) = k_j \cos(j\omega T_2)$$

$$f_y(j) = k_j \sin(j\omega T_2)$$

where  $f_x(j)$  and  $f_y(j)$  are radial and cross-radial dimensions in the transform domain. Figure 2.2.2 illustrates this distortion in the transform domain sampling.

### 2.3 Generalized Three Dimensional Formula

The three dimensional representation of the scattered wave from a rotating target was formally derived [4] in terms of the wave propagation vector  $\bar{k}$  and scattering point vector  $\bar{x}$ . With reference to Fig. 2.3.1, the far field electromagnetic wave incident on the object can be approximated by a plane wave

$$E_i(t, \bar{x}) = E_0 e^{-j2\pi f t} e^{j\bar{k} \cdot (\bar{x} + \bar{r}_0)} \quad (2.3.1)$$

where  $f$  is the signal frequency,  $E_0$  the field strength of the incident electromagnetic wave. If one uses Kirchhoff's approximation one gets for the backscattered far field  $E_s$  at the receiving antenna [4]

$$E_s = \iint_{\text{Illuminated surface}} E_i(t, \bar{x}) \frac{e^{j\bar{k} \cdot (\bar{x} + \bar{r}_0)}}{j\lambda r_0} \bar{u}_k \cdot d\bar{S}(\bar{x}) \quad (2.3.2)$$

where  $\lambda = c/f$ ,  $d\bar{S}$  is the incremental area vector normal to the target surface, and

$$\bar{u}_k = \bar{k}/|\bar{k}|.$$

Define



$$\bar{p} \triangleq -2\bar{k} \quad (2.3.3)$$

and

$$\rho(\bar{p}) \triangleq \frac{j}{2\sqrt{\pi}} \iint_{\text{illuminated surface}} e^{-j\bar{p} \cdot \bar{x}} \bar{p} \cdot d\bar{S}(\bar{x}). \quad (2.3.4)$$

By substituting Eq. (2.3.1) into Eq. (2.3.2) and using the relations in Eqs. (2.3.3) and (2.3.4) one gets

$$E_s = \frac{E_0}{2\sqrt{\pi}r_0} \rho(\bar{p}) e^{-j(2\pi ft + \bar{p} \cdot \bar{r}_0)} \quad (2.3.5)$$

By restricting the class of targets being observed to only convex objects,  $\rho(\bar{p})$  can be rewritten as

$$\rho(\bar{p}) = \frac{j}{2\sqrt{\pi}} \iint_{\bar{p} \cdot \bar{n} > 0} e^{-j\bar{p} \cdot \bar{x}} \bar{p} \cdot d\bar{S}(\bar{x}) \quad (2.3.6)$$

where  $\bar{n}$  is a unit vector in the direction of  $d\bar{S}$ . By inspecting Eq. (2.3.5) it can be seen that  $\rho(\bar{p})$  is a measureable quantity by homodyning\*  $E_s$  and phase shifting the resulting baseband video by a phase equal to  $\bar{p} \cdot \bar{r}_0$  which can be determined apriori.  $\rho(\bar{p})$  can therefore be treated as the baseband video signal of a coherent radar system except that other than being baseband, it is also

---

\*Homodyning is a demodulation or "mixing down" operation in which the video signal riding on a carrier frequency is mixed with a 180° out-of-phase carrier of the same frequency resulting in a baseband video.

phase shifted by an amount equal to  $\bar{p} \cdot \bar{r}_0$ . Since the video signal can be easily measured by a standard radar system, it is justified to concentrate only on  $\rho(\bar{p})$ . Since  $\rho(\bar{p})$  is the video signal measured off the illuminated side of the object (i.e.  $\bar{p} \cdot \bar{n} > 0$ ), the video signal measured off the non-illuminated "back" side of the object is  $\rho(-\bar{p})$ . It follows from Eq. (2.3.6) that

$$\rho(\bar{p}) + \rho^*(-\bar{p}) = \frac{j}{2\sqrt{\pi}} \int_S e^{-j\bar{p} \cdot \bar{x}} \bar{p} \cdot d\bar{S}(\bar{x}) \quad (2.3.7)$$

where  $S$  is the entire surface of the convex body  $B$ . From the divergence theorem

$$\begin{aligned} \rho(\bar{p}) + \rho^*(-\bar{p}) &= \frac{j}{2\sqrt{\pi}} \int_B \nabla \cdot (\bar{p} e^{-j\bar{p} \cdot \bar{x}}) d\bar{x} \\ &= \frac{\bar{p}^2}{2\sqrt{\pi}} \int_B e^{-j\bar{p} \cdot \bar{x}} d\bar{x} \end{aligned} \quad (2.3.8)$$

$$= \frac{\bar{p}^2}{2\sqrt{\pi}} \int \gamma(\bar{x}) e^{-j\bar{p} \cdot \bar{x}} d\bar{x} \quad (2.3.9)$$

where  $\gamma(\bar{x})$  is the characteristic function of  $B$  defined as

$$\gamma(\bar{x}) = \begin{cases} 1 & \bar{x} \in B \\ 0 & \bar{x} \notin B. \end{cases}$$

If one further defines

$$\Gamma(\bar{p}) \triangleq \frac{2\sqrt{\pi}}{\bar{p}} [\rho(\bar{p}) + \rho^*(-\bar{p})],$$

it follows from Eq. (2.3.9) that  $\Gamma(\bar{p})$  and  $\gamma(\bar{x})$  are Fourier

transform pairs:

$$\Gamma(\bar{p}) = \int \gamma(\bar{x}) e^{-j\bar{p} \cdot \bar{x}} d\bar{x}. \quad (2.3.10)$$

This is Bojarski's identity.

Since  $\rho(\bar{p})$  and  $\rho(-\bar{p})$  are respectively the phase shifted baseband video signal measured off the "front" and "back" of the target,  $\Gamma(\bar{p})$  represents a composite phase shifted baseband video signal measured off the entire target body. The only difference with  $\Gamma(\bar{p})$  is that it is scaled by the propagation vector parameter  $p$ . By the way the characteristic function  $\gamma(\bar{x})$  of the target is defined,  $\gamma(\bar{x})$  represents the spatial distribution of the point scatterers on the surface of the target. Equation (2.3.10) thus shows that by measuring the composite phase shifted baseband video signal  $\Gamma(\bar{p})$  for all values of  $\bar{p}$  (in frequency  $f$  and aspect angles), the characteristic function  $\gamma(\bar{x})$  of the target can be obtained by simply Inverse Fourier transforming  $\Gamma(\bar{p})$ .

Now it will be shown that it is unnecessary to pose the target-data relationship in terms of  $\Gamma(\bar{p})$  and the characteristic function. A direct relationship between the target "reflectivity" function  $\sigma(\bar{x}; \bar{k})$  and the signal return data  $D(\bar{k})$  will be derived in line with the 2-D model used earlier.

Write the transmitted signal (or beam) in vector form

$$\bar{k}_{ij} = (\alpha_i, \epsilon_i, \frac{2f_j}{c}) \quad (2.3.11)$$

where  $\alpha_i$ =beam azimuth at the beginning of the  $i^{\text{th}}$  burst,  
 $\epsilon_i$ =beam elevation at the beginning the  $i^{\text{th}}$  burst,  
 $f_j$ =carrier frequency of the  $j^{\text{th}}$  pulse.

Let  $\bar{r}_0$ =vector from the antenna to the target center or  
point reference,  
=vector from the antenna to a point on the target.

Note that  $\bar{k}_{ij}$  can also be written as

$$\bar{k}_{ij} = \bar{k}/\pi = \frac{2}{\lambda} \bar{u}_k$$

where  $\bar{k}$ =signal wave propagation vector

$$\lambda = \text{signal wavelength } (= \frac{c}{2\pi k})$$

$$\bar{u}_k = \bar{k}/|k|$$

With this new notation, Eq. (2.1.5) can be rewritten as

$$D_r(\bar{k}_{ij}) = T_1 BB' \exp\{j2\pi \bar{k}_{ij} \cdot (\bar{r} - \bar{r}_0)\}.$$

It follows that the point target vector is

$$\bar{x}(t) = \bar{r}(t) - \bar{r}_0. \quad (2.3.12)$$

For the same reason as in the 2-D case, the data are  
sampled at  $t=t_{ij}=iT_3+jT_2+\tau$  as in Eq. (2.2.3). The data  
from a point target  $\bar{x}$  can thus be written as

$$D_r(\bar{k}_{ij}) = T_1 BB' \sigma(x_{ij}; \bar{k}_{ij}) e^{j2\pi \bar{k}_{ij} \cdot \bar{x}_{ij}}$$

where  $\bar{x}_{ij}$  stands for  $\bar{x}(t_{ij})$ . If the scattering

coefficient  $\sigma$  stays constant with aspect change,

$$\sigma(\bar{x}_{ij}; \bar{k}_{ij}) = \sigma(\bar{x}_{ij}).$$

If all the assumptions made for the 2-D model holds, the composite data from the 3-D object is

$$D(\bar{k}_{ij}) = BB' \iint_{\text{Target volume}} \sigma(\bar{x}_{ij}) e^{j2\pi \bar{k}_{ij} \cdot \bar{x}_{ij}} d\bar{x}_{ij} \quad (2.3.13)$$

Let

$$\begin{aligned} Z(\bar{k}) &\triangleq \iiint \sigma(\bar{x}) e^{j2\pi \bar{k} \cdot \bar{x}} d\bar{x} \\ &= \text{3-D Inverse F.T. of } \sigma(\bar{x}). \end{aligned}$$

Then

$$D(\bar{k}_{ij}) = BB' Z(\bar{k}_{ij}) .$$

Again as with the 2-D case,  $D(\bar{k}_{ij})$  can be interpreted as the 3-D spatial frequency spectrum of the target scattering coefficient.

An important result of Eq. (2.3.13) is that the Fourier transform data in the  $\bar{k}$  space of the scattering coefficient function for one signature (say the  $i^{\text{th}}$  signature which corresponds to the  $i^{\text{th}}$  burst) coincides in direction with the actual physical aspect angle direction of the object. One can now directly associate the aspect angle of the object with the angular dimension of the Inverse F.T. data in  $\bar{k}$  space. In practice because the available signal frequency is limited in the lower end ( $f_{\min}$ ) by the scattering model and in the upper end ( $f_{\max}$ )

limited by technology, the available F.T. data is contained in between two concentric spheres. This is illustrated clearly in Fig. 2.3.2.

In the 2-D model of section 2.2, the target is assumed to be rotating on a flat platform (say  $(x_1, x_2)$  plane) with rotation vector  $\bar{\omega}$  in the  $x_3$  direction. Because the incident radar wave is parallel to this plane, one should get the Inverse F.T. data within an annula ring on the  $(x_1, x_2)$  plane as shown in Fig. 2.3.2. However, if the rotation platform is not rotating in the same  $x_3$  direction at all points in time, the scattered data will not all lie on the  $(x_1, x_2)$  plane. This is expected to occur for aircraft, which at any instant in time will have pitch, yaw and roll besides the rotation effect due to translation. A similar situation occurs for seaborne targets in which one has again the roll, pitch and yaw motion besides the rotation effect due to translation. The major difference between an airborne target and a seaborne target is that for most cases the long-term translational-rotation effect would be the predominant rotational motion of an aircraft; meanwhile, it is the shorter term roll, pitch and yaw that would be predominant for a ship target, especially in high sea states.

Now we have a compact model in which all kinds of

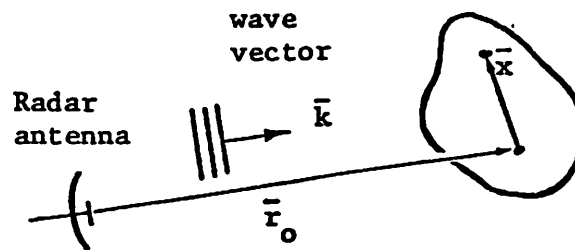


Figure 2.3.1. 3-D radar target model for Bojarski's identity.

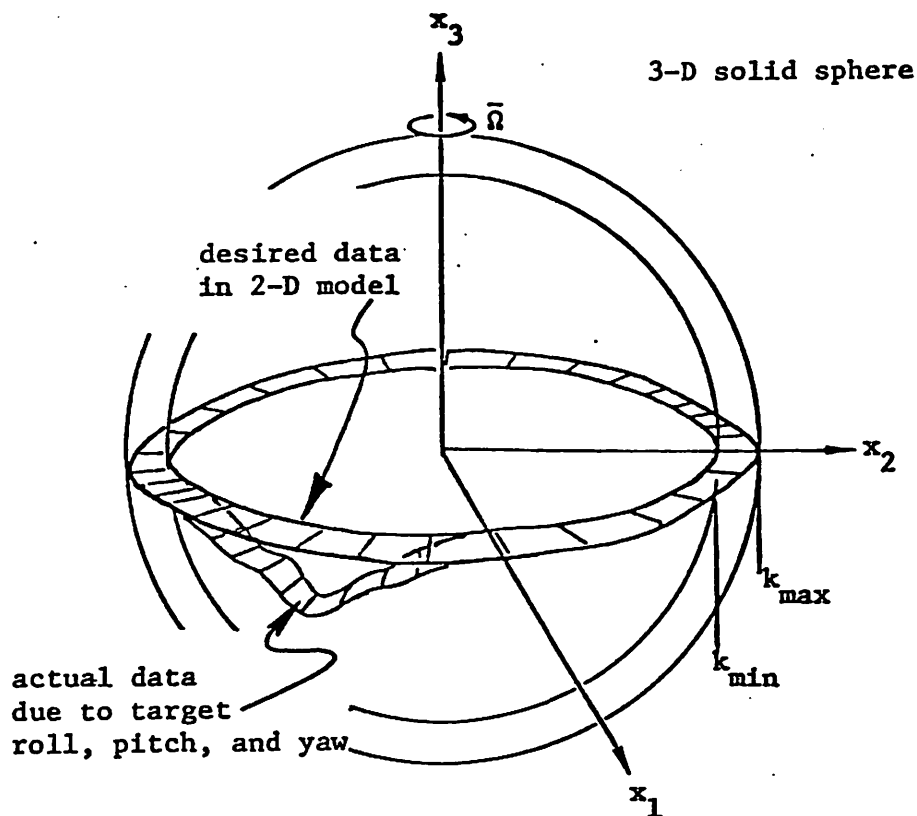


Figure 2.3.2. 3-D data in Fourier domain showing data confined in concentric spheres of radii  $k_{min}$  and  $k_{max}$ . (Note that the deviation of the F.T. data from the planar annula ring due to target rotation vector changes.)

rotational motion with respect to the LOS can be completely accounted for in Fig. 2.3.2. One should keep in mind that this is a direct result of the fact that the propagation vector ( $\bar{k}$ ) direction coincides in direction with the Inverse F.T. vector ( $\bar{p}$ ) in the data. An important point here is to realize that whatever the absolute rotation rate vector  $\bar{\Omega}$  is in the absolute fixed coordinates, only the components of  $\bar{\Omega}$  that are perpendicular to the LOS contribute to the imaging process. Therefore, where the data lie in the 3-D sphere depends only on the aspect angle of the target with respect to the LOS. The component of  $\bar{\Omega}$  that is normal to the LOS determines only the scale along the aspect angle. This is obvious from Fig. 2.3.2.



## Chapter 3

### POINT SPREAD FUNCTION, SYSTEM RESOLUTION

#### 3.1 Spatial Frequency Units

In Eq. (2.1.5)  $k_j$  was used instead of  $\frac{2f_j}{c}$  for the reason of simpler notation. It became clear with this substitution that for a given burst (say the  $i^{\text{th}}$  burst), the measured data given by Eq. (2.1.5) was the spectral signature of a point object. That is, if the target reflectivity and ranges were constant, the data corresponding to signal frequency  $f_j$  was a measure of the  $k_j^{\text{th}}$  spatial frequency component of the point object. By incorporating the assumptions made in section 2.2, it was further concluded that the radar data  $D(i,j)$  represented along the direction of aspect angle  $\theta_i$  the  $k_j^{\text{th}}$  spatial frequency component of the target reflectivity function. This notion was easily extended to the three dimensional model in which the spatial frequency  $(k_j, \theta_i)$  was replaced by a vector  $\bar{k}_{ij}$ .  $k_j$  is therefore a more useful notation when it comes to relating the radar data with the target reflectivity function. One can now measure the  $k_j^{\text{th}}$  spatial frequency component of the target by using a

carrier frequency  $f_j$  such that

$$k_j = \frac{2f_j}{c} = \frac{2}{\lambda_j}$$

where  $\lambda_j$  is the carrier wavelength.

Justification for using spatial units can also be found in SAR. For one thing, equations in SAR have been derived in a variety of ways by many authors. In almost all of the derivations, the time dimension has been an essential part of the formulae being derived, and the meaning of the formula sometimes becomes obscured in the many factors involved in it. Yet, in almost all the applications for which SAR was designed, the spatial distribution of the object is the central objective. It seems reasonable, therefore, to put the equations in spatial units rather than in temporal units. Of course, when one is concerned with implementation then temporal units must be taken in consideration. Another reason for preferring spatial units is the fact that the echo phase is determined by the relative spatial distribution of scattering centers.

The first basic equation relating temporal units to spatial units is

$$x = \int_0^t v dt' \quad (3.1.1)$$

where  $x$  is the spatial distance of an object at instant  $t$ ,

travelling with velocity  $v$  along a linear path.

Next, the Doppler frequency which is usually considered in temporal units, can be expressed in spatial units. Consider for example the strip mode SAR geometry in Fig. 3.1.1 where the aircraft is flying a straight line along the  $x$ -axis with its antenna looking down and forward at squint angle  $\theta_s$ . Consider a point target  $C$ . The aircraft is at point  $A$  at time  $t=0$ , with slant range  $R_0$ .  $B$  is the aircraft position at any other instant  $t$ . Suppose the transmitter temporal frequency is  $f_0$  (wavelength  $\lambda_0$ ), then the phase of the echo from point  $C$  will be

$$\phi(t) = 2\pi f_0 \frac{2R(t)}{c}.$$

After rearrangement,

$$\phi(t) = 2\pi k_0 R(t) \quad (3.1.2)$$

where  $k_0$  is the spatial frequency associated with  $f_0$  given by the conversion equation

$$k_0 \triangleq \frac{2f_0}{c}. \quad (3.1.3)$$

Hence, phases can be written in terms of spatial frequency and spatial distance using the conversion Eq. (3.1.3). This representation is also meaningful from the optical signal processing point of view. If a monochromatic

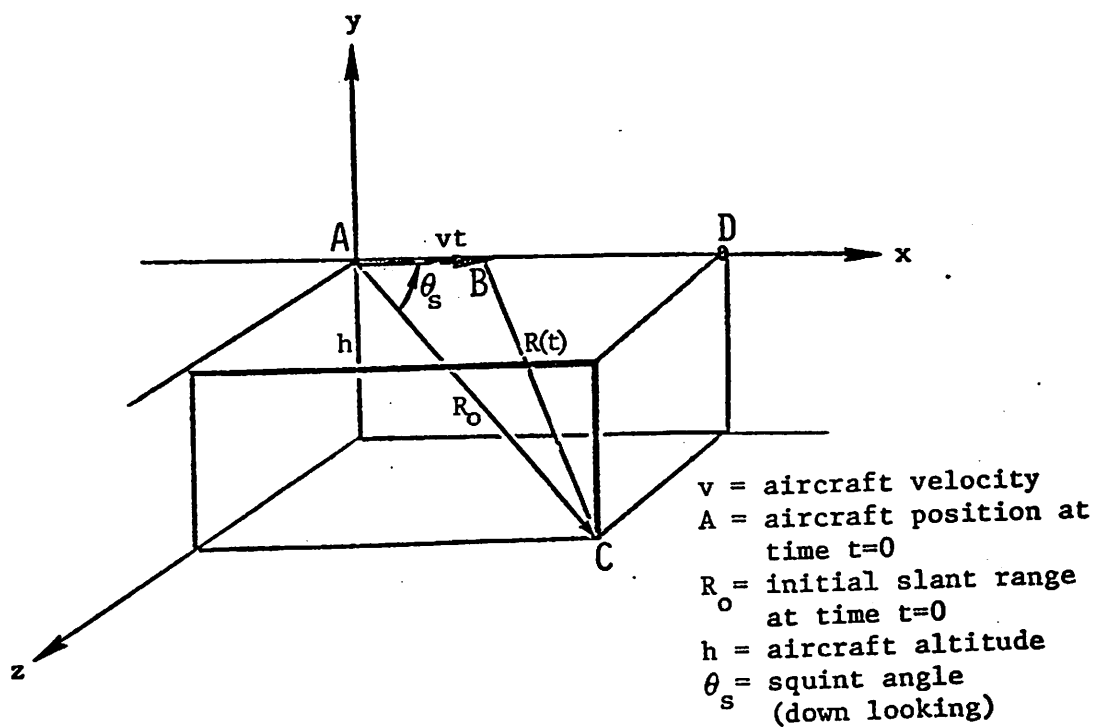


Figure 3.1.1. Doppler geometry for Strip mode SAR.

source at C illuminates the x-axis of Fig. 3.1.1 with wavelength  $c/2f_0$ , the phase of the illumination at any point along the x-axis trajectory relative to the phase at some fixed point on the x-axis (say point A) will be  $\phi(x) = 2\pi k_0 R(x)$ . The instantaneous spatial frequency at any point x due to the phase  $\phi(x)$  measured along the x-axis will in fact be  $\frac{1}{2\pi} \frac{d\phi(x)}{dx} = k_0 \frac{dR(x)}{dx}$ . However, the instantaneous Doppler time frequency is

$$\frac{1}{2\pi} \frac{d\phi(t)}{dt} = k_0 \frac{dR(t)}{dt} = \left[ k_0 \frac{dR(x)}{dx} \right] v.$$

Therefore the instantaneous time Doppler frequency at point x is related to the spatial frequency of the illumination on the x-axis by the velocity v. For this reason, the spatial frequency can be treated as the spatial counterpart of the instantaneous Doppler time frequency with the velocity v as the conversion factor. We will call it the Spatial Doppler frequency.

For another example let us look at the strip mode SAR again as in Fig. 3.1.1. Using the cosine rule on triangle ABC

$$R(t) = \sqrt{R_0^2 + (vt)^2 - 2R_0vt\cos(\theta_s)} \quad (3.1.4)$$

Expanding in Taylor's series, then

$$R(t) \approx R_0 \left[ 1 - \frac{vt \cos \theta_s}{R_0} + \frac{(vt)^2}{2R_0^2} \right] \quad (3.1.5)$$

if one keeps only terms of 2nd order in the Taylor's Series expansion. Substituting Eq. 3.1.4) into Eq. 3.1.2),

$$\phi(t) = 2\pi k_0 R_0 \left[ 1 - \frac{vt \cos \theta_s}{R_0} + \frac{1}{2} \frac{(vt)^2}{R_0^2} \right] \quad (3.1.6)$$

With Eq. (3.1.1)

$$\phi(x) \approx 2\pi k_0 R_0 \left[ 1 - \frac{xc \cos \theta_s}{R_0} + \frac{1}{2} \frac{x^2}{R_0^2} \right] \quad (3.1.7)$$

If the Doppler frequency is defined as

$$f_D \triangleq \frac{1}{2\pi} \frac{d\phi}{dt} \quad (3.1.8)$$

then Eq. (3.1.6) leads to

$$f_D \approx - \frac{2vf_0 \cos \theta_s}{c} + \frac{2v^2 f_0 t}{c}$$

If the spatial Doppler frequency is defined as

$$k_D \triangleq \frac{1}{2\pi} \frac{d\phi(x)}{dx}$$

then Eq. (3.1.7) leads to

$$k_D \approx - k_0 \cos \theta_s + k_0 \left( \frac{x}{R_0} \right) \quad (3.1.9)$$

One now has the Doppler frequency in a very compact form.

$k_D$  is the rate of change of echo phase per unit distance

travelled by the aircraft. This is the actual fundamental doppler which determines the system's imaging ability. Besides,  $k_D$  is a function of the distance  $x$  of the aircraft at point B irrespective of what perturbations might exist on the velocity  $v$ . Notice also that the first Doppler term in Eq. (3.1.9) is due to the relative translational velocity (along the line of sight) between points C and A. This component is called the translational Doppler ( $k_t$ ). It is given here in spatial frequency units, i.e.

$$k_t = -k_0 \cos \theta_s.$$

The translational Doppler is zero for the antenna beam which is directed broadside at  $\theta_s = 90^\circ$ . For more complex trajectories of the aircraft,  $k_t$  is more complicated with the squint  $\theta_s$  being a function of time. This is related to the problem of motion compensation.

The second term  $k_0(\frac{x}{R_0})$  is called the differential Doppler ( $k_d$ ) in spatial frequency units. The differential Doppler is solely responsible for the high resolution imaging property of synthetic aperture radar systems. This is in fact true for all modes of SAR.

$$k_d = k_0(\frac{x}{R_0}).$$

Finally if one compares Eqs. (3.1.8) and (3.1.9), the spatial frequency  $k_D$  can be converted readily to time

frequency  $f_D$  by

$$f_D = vk_D \quad (3.1.10)$$

### 3.2 Point Spread Function in the Continuous Domain

As noted earlier in section 2.3, the Fourier transform (F.T.) data was restricted to two concentric spheres. For the two dimensional model the data was restricted to an annula ring of radii  $\frac{2f_{\min}}{c} = k_{\min}$  and  $\frac{2f_{\max}}{c} = k_{\max}$ . If the data were available for all frequencies and aspect angle, the target can be reconstructed by taking the F.T. of the data.

Since the data represents the 2-D F.T. of the object in the 2-D model, and since the object can be reconstructed by taking another 2-D F.T. on the data, the entire radar system and the reconstruction processor can be lumped together and viewed as an imaging system. As such, the annula ring structure in the F.T. data can be viewed as the pupil function of the imaging system. The F.T. of this pupil function then gives the point spread function (henceforth abbreviated PSF) or impulse response of the imaging system.

Suppose there is no perturbation on the rotation vector of the target. The annula ring pupil function can be written as an isotropic function as follows.



$$G(k) = \text{circ}(k/k_{\max}) - \text{circ}(k/k_{\min}) \quad (3.2.1)$$

where

$$\text{circ}(x) = \begin{cases} 1 & |x| \leq 1 \\ 0 & \text{otherwise} \end{cases}$$

Polar coordinates have been used for convenience. The PSF is thus

$$\begin{aligned} g(\rho) &= \mathcal{B}\{G(k)\} \\ &= k_{\max} \frac{J_1(2\pi k_{\max} \rho)}{\rho} - k_{\min} \frac{J_1(2\pi k_{\min} \rho)}{\rho} \end{aligned} \quad (3.2.2)$$

where  $\mathcal{B}\{\cdot\}$  indicates Fourier Bessel transform,

$\rho$  = radial polar coordinate in the spatial domain,

$J_1(\cdot)$  = Bessel Function of the 1st kind, order 1.

The PSF of the radar imaging system is plotted in Fig. 3.2.1. It is difficult to predict the behavior of the PSF from Eq. (3.2.2). Instead, some approximate forms will be studied.

#### PSF for Small Values of $\rho$

From the relation

$$J_1(x) = \frac{1}{x} \int_0^x \xi J_0(\xi) d\xi \quad (3.2.3)$$

the PSF can be written as

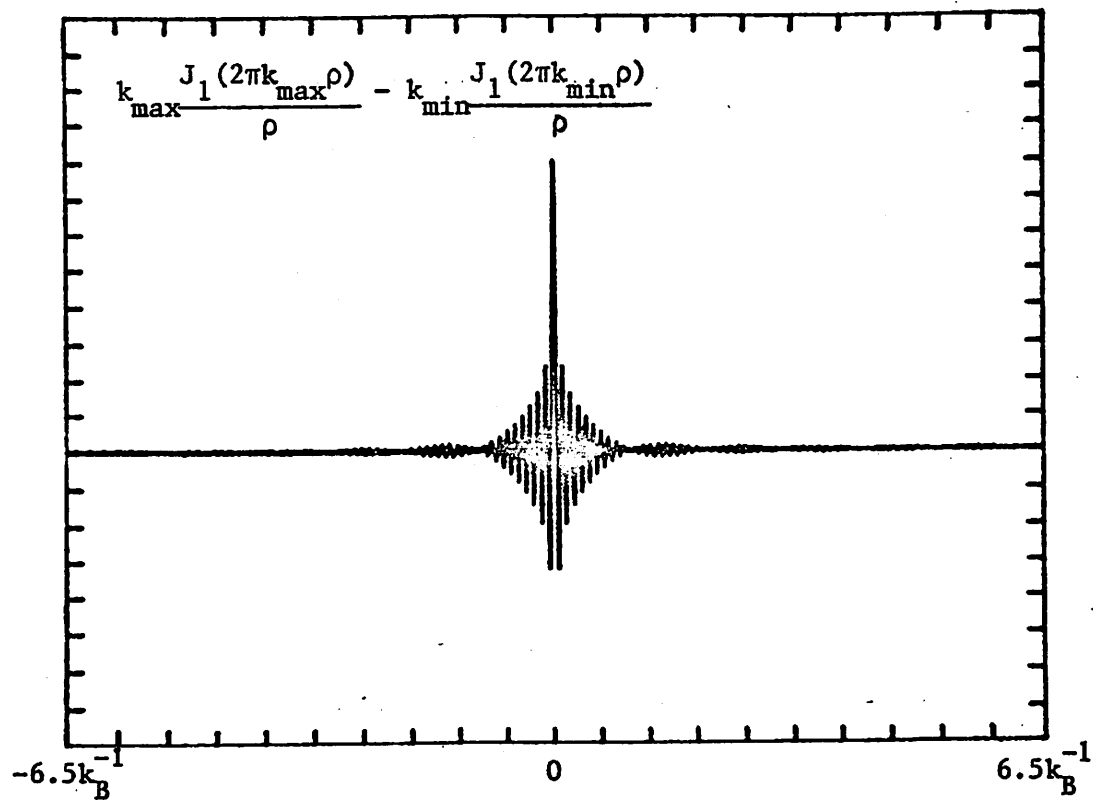


Figure 3.2.1. Point spread function of the radar imaging system.

$$g(\rho) = \frac{1}{2\pi\rho^2} \int_{2\pi\rho k_{\min}}^{2\pi\rho k_{\max}} \xi J_0(\xi) d\xi.$$

Suppose the "narrow" band assumption holds, in which

$$k_0 \gg k_B$$

where

$$k_0 = \frac{1}{2}(k_{\min} + k_{\max})$$

$$k_B = k_{\max} - k_{\min}.$$

Then

$$g(\rho) \approx \frac{k_0}{\rho} \int_{2\pi\rho k_{\min}}^{2\pi\rho k_{\max}} J_0(\xi) d\xi \quad (3.2.4)$$

The integration interval is linearly proportional to  $\rho$ .

Hence for small  $\rho (< \frac{1}{k_B})$ ,  $J_0(\xi)$  is essentially constant.

Thus

$$g(\rho) \approx 2\pi k_0 k_B J_0(2\pi k_0 \rho) \quad (3.2.5)$$

This approximate PSF is plotted in Fig. 3.2.2a with  $k_B = 0.1k_0$ .

#### PSF for Large Values of $\rho$

For large  $\rho$  one can use the following approximation [page 401,38].

$$J_n(\xi) = \sqrt{\frac{2}{\pi\xi}} \cos\left(\xi - \frac{\pi}{4} - \frac{n\pi}{2}\right) \quad (3.2.6)$$

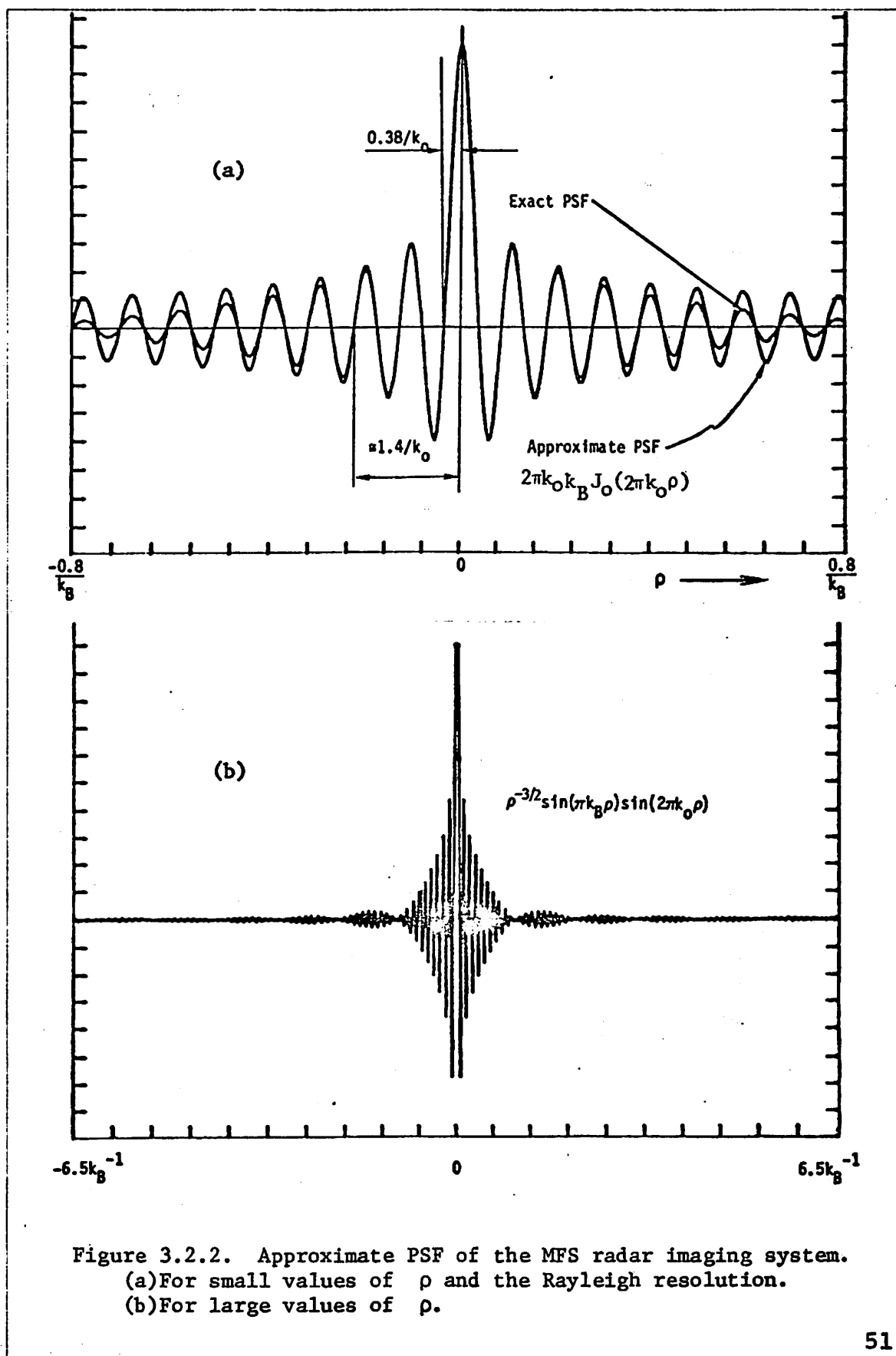


Figure 3.2.2. Approximate PSF of the MFS radar imaging system.  
 (a) For small values of  $\rho$  and the Rayleigh resolution.  
 (b) For large values of  $\rho$ .

Substituting Eq. (3.2.6) into Eq. (3.2.4) and using the narrowband assumption again, one gets by integration

$$g(\rho) \approx \left( \frac{-2k_0^{1/2}}{\pi} \right) \rho^{-3/2} \sin(2\pi\rho \frac{k_B}{2}) \sin(2\pi\rho k_0) \quad (3.2.7)$$

The closeness of these approximations is evident from Figs. 3.2.2a,b. With  $k_0 = 10k_B$ , the approximation for small  $\rho$  in Eq. (3.2.5) is accurate up to about  $1.4k_0^{-1}$ . For large  $\rho$ ,

$$|g(\rho)| \propto \rho^{-3/2}$$

The beating phenomenon for large  $\rho$  which is predicted in Eq. (3.2.7) is also evident in Fig. 3.2.2b.

Even though  $k_B \ll k_0$  for the current system, in practice the temporal frequency corresponding to  $k_B$  can be very wide in bandwidth, for example as high as 1 GHz.

### 3.3 Point Spread Function from a Different Point of View

The point spread function in the previous section was derived as an optical system. Here we will try to understand the system in a different way which will allow us to analyze the system more as a matched filtering problem.

Suppose point object  $P_0$  is located at polar

coordinates  $(\rho_0, 0)$  with constant reflectivity  $\sigma_0$ . From Eq. (2.2.6) the recorded data is proportional to

$$G(\theta, k) = \sigma_0 e^{j2\pi k \rho_0 \cos \theta}$$

where  $(\theta, k)$  are polar coordinates in the F.T. domain.

Let the data  $G$  be processed to be resolved in range first. From the expression above for  $G(\theta, k)$ , one can see that for each point scatter  $P$  at distance  $\ell$  along the LOS from the center of rotation, a linear phase  $\exp\{j2\pi k \ell\}$  will be introduced. Therefore in order to identify a point scatterer at range  $\ell$ ,  $G(\theta, k)$  can be passed through a matched filter corresponding to the linear phase returns from that point scatterer. The weighting (impulse response) for this matched filter will be  $[e^{j2\pi k \ell}]^*$  over all possible values of  $k$ .

Thus the matched filter output is

$$g(\theta, \ell) = \int G(\theta, k) e^{-j2\pi k \ell} dk.$$

This is the one-dimensional Fourier transform of the collected data. Therefore, Fourier transforming the data also corresponds to matched filtering the data to get range compression.

Suppose one has a full range of continuous data for all frequencies between  $k_{\min}$  and  $k_{\max}$  and for all aspect

angles  $\theta \in (0, 2\pi)$  . Taking the 1-dimensional F.T. on  $G$  with respect to  $k$  will lead to

$$\begin{aligned} g(\theta, \ell) &\triangleq \int_{-1/2k_B}^{1/2k_B} G(\theta, k) e^{-j2\pi k \ell} dk \\ &= \sigma_0 S_0 e^{j2\pi k_0 [\rho_0 \cos \theta - \ell]} \end{aligned} \quad (3.3.1)$$

where

$$S_0 = \text{sinc}[k_B(\ell - \rho_0 \cos \theta)]$$

$$\text{sinc}(x) = \sin(\pi x) / \pi x$$

Now the data is resolved in range and the function  $g(\theta, \ell)$  is called the range compressed data. It is obvious from Eq. (3.3.1) that  $g(\theta, \ell)$  peaks at  $\ell = \rho_0 \cos \theta$ . This means that the matched filter response peaks only when the matched filter parameter  $\ell$  matches with the instantaneous range  $\rho_0 \cos \theta$  .

After range compression, the phase of the data  $g(\theta, \ell)$  is proportional to only  $k_0$  and the range differential  $\rho_0 \cos \theta - \ell$  between the point object and the point center  $O$ . The magnitude of the data is proportional to  $S_0(\ell)$  which peaks at  $\ell = \rho_0 \cos \theta$ . However, range compressed data having the same characteristics as  $g(\theta, \ell)$  can also be obtained from a completely different radar system with a completely different signal format. Thus, if the target is rotating slowly enough so that it satisfies the conditions discussed in chapter 2, one has the option of choosing other radar systems to achieve the same imaging property. For example a linear FM signal with signal

bandwidth  $\frac{c}{2}k_B$  and mean frequency  $\frac{c}{2}k_0$  will give essentially the same characteristics as the multifrequency bursts.

In the  $\theta$  dimension, one can again use the matched filtering concept to reconstruct the point image of the point scatterer  $P_0$ . Since the range compressed data from  $P_0$  is proportional to

$$\text{sinc}[k_B(\ell - \rho_0 \cos \theta)] e^{j2\pi k_0[\rho_0 \cos \theta - \ell]},$$

ideally the matched filter is two dimensional.

In the  $\theta$  dimension, one can again use the matched filter concept to reconstruct the point image of the point scatterer  $P_0$ . Since the range compressed data from  $P_0$  is proportional to

$$\text{sinc}[k_B(\ell - \rho_0 \cos \theta)] e^{j2\pi k_0(\rho_0 \cos \theta - \ell)},$$

ideally the matched filter is two dimensional in nature.

The response of the filter matched to  $P(\rho, \phi)$  is

$$\sigma(P) = \frac{1}{2\pi} \int_0^a \int_0^{2\pi} g(\theta, \ell) \text{sinc } k_B[\ell - \rho \cos(\theta - \phi)] e^{-j2\pi k_0 \rho \cos(\theta - \phi)} d\theta d\ell.$$

In practice, this implies that long processing time will be needed to implement the filter. Instead, an approximate filter impulse response function will be used as follows:



$$\text{sinc } k_B (\ell - \rho \cos(\theta - \phi)) \delta(\ell - \rho \cos(\theta - \phi)) e^{-j2\pi k_0 \rho \cos(\theta - \phi)}$$

Using the expression for  $g(\theta, \ell)$  in Eq. (3.3.1) the filter response will be

$$\begin{aligned} \sigma(P) &= \frac{1}{2\pi} \int_0^a \int_0^{2\pi} g(\theta, \ell) \text{sinc}[k_B (\ell - \rho \cos(\theta - \phi))] \delta(\ell - \rho \cos(\theta - \phi)) \\ &\quad \cdot e^{-j2\pi k_0 \rho \cos(\theta - \phi)} d\theta d\ell \\ &= \frac{\sigma_0}{2\pi} \int_0^{2\pi} \text{sinc } k_B (\rho \cos(\theta - \phi) - \rho_0 \cos(\theta - \phi_0)) \\ &\quad \cdot e^{j2\pi k_B [\rho_0 \cos\theta - \rho \cos(\theta - \phi)]} d\theta, \end{aligned}$$

where the  $\ell$  dependent phase term is dropped because only the magnitude of the matched filter response will be of interest here. The above expression for the matched filter can be observed as being a contour integration along the contour

$$\ell = \rho \cos(\theta - \phi).$$

By referring to Fig. 3.3.1 and using the relation

$$\rho' = \rho_0^2 + \rho^2 - 2\rho_0 \rho \cos\phi$$

$$\phi' = \tan^{-1} \left( \frac{\rho \sin\phi}{\rho_0 - \rho \cos\phi} \right), \text{ the following simplification can be made}$$

$$\rho_0 \cos - \rho \cos(\theta - \phi) = \rho' \cos(\theta + \phi'). \quad \text{Therefore}$$

$$\sigma(P) = \frac{\sigma_0}{2\pi} \int_0^{2\pi} \text{sinc}[k_B \rho' \cos(\theta + \phi')] e^{-j2\pi k_0 \rho' \cos(\theta + \phi')} d\theta$$

But  $\rho'$  is the distance  $P_0 P$  between the target points,  $(\theta + \phi')$  is the angle between  $P_0 P$  and the LOS. Therefore  $\rho' \cos(\theta + \phi')$  is the projected length of  $P_0 P$  on the LOS. We can, for convenience, make a change in variable  $\theta' = \theta + \phi'$ . Then the filter response at point P is

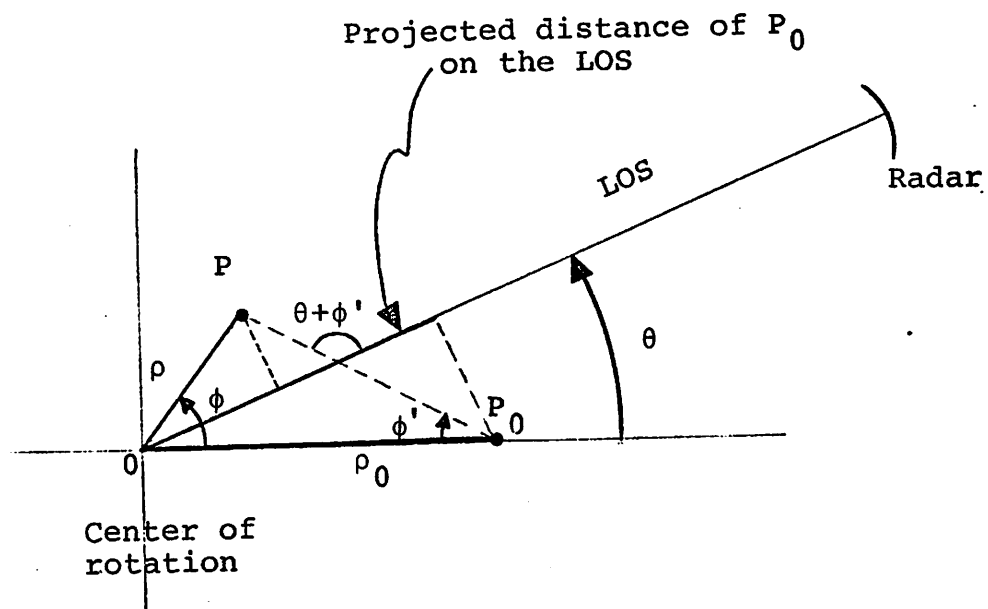


Figure 3.3.1. Projected distance onto the LOS of point P is  $\rho \cos(\theta - \phi)$ , and of point  $P_0$  is  $\rho_0 \cos \theta$ .

$$\sigma(P) = \frac{\sigma_0}{2\pi} \int_0^{2\pi} \text{sinc}[k_B \rho' \cos\theta] e^{-j2\pi k_0 \rho' \cos\theta} d\theta \quad (3.3.2)$$

This means that any target point at distance  $\rho'$  away from  $P_0$  will have a non-zero contribution to the reconstruction of  $P_0$ , proportional to  $\sigma(P)$ .  $\sigma(P)/\sigma_0$  is by definition the point spread function of the imaging system. The PSF in expression (3.3.2) can be rewritten as

$$g(\rho') = \frac{\sigma(P)}{\sigma_0} = \frac{1}{2\pi} \int_0^{2\pi} \int_{k_0-1/2k_B}^{k_0+1/2k_B} e^{-j2\pi k \rho' \cos\theta} dk d\theta \quad (3.3.3)$$

which is exactly the same as Eq. (3.2.2).

Even though we arrive at the same point spread function from both the optical system view point and the matched filter point of view, the latter approach gives us a more intimate understanding of the reconstruction process. In fact it suggests a method to reconstruct the target, which is more suitable on a digital computer. Its further importance will also be obvious when we come to the problem of sampling requirements.

### 3.4 Resolution of the Imaging System

The resolution obtainable from an annula pupil function will be of interest here. Just as in the problem of defining the bandwidth or the time width of one

dimensional signals, we are faced with the problem of defining the resolution of our system. There are two ways of looking at the resolution of the system. One is the usual resolution criterion used in optics. The other is from the signal bandwidth approach.

### Resolution From the Point Spread Function

From section 3.2 we have seen that for small values of  $\rho$ , the PSF can be approximated by  $J_0(2\pi k_0 \rho)$ . With Rayleigh's criterion for resolution,

$$J_0(2\pi k_0 \rho) \Big|_{\rho=\delta} = 0$$

where  $\delta$  is the Raleigh resolution. Therefore  $2\pi k_0 \delta = 2.4048$  and the Rayleigh resolution is

$$\delta = \frac{0.3827}{k_0} \quad (3.4.1)$$

This resolution limit is good at least for  $k_B/k_0$  ratios less than 0.1. The surprising result here is that the bandwidth becomes insignificant with this resolution limit. To show the importance of  $k_0$  in the sharpening of the point spread function and therefore the sharpening of the resolution limit, we will compare two PSF's, one with  $k_0 = 10k_B$  and the other with  $k_0 = \frac{1}{2} k_B$ . The second case represents a disc pupil function  $\text{circ}(k/k_B)$ . The magnitudes of the PSF's are shown in Fig. 3.4.1. The

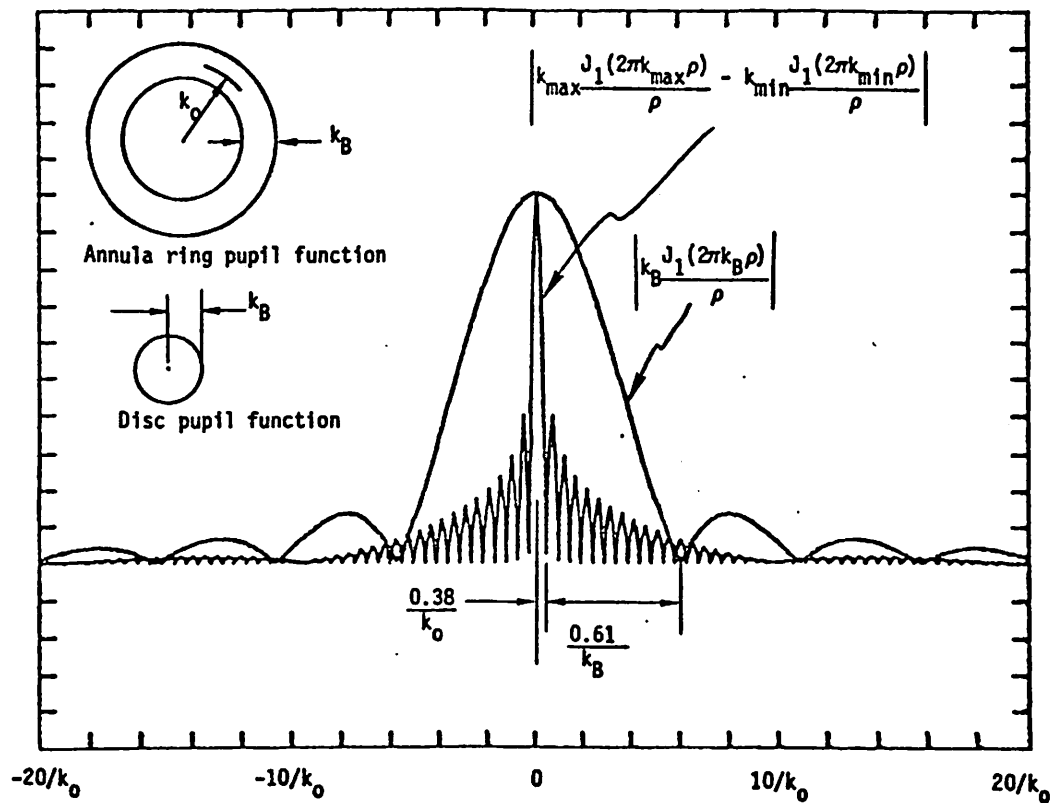


Figure 3.4.1. Comparison of point spread functions for the annula ring ( $k_0 = 10k_B$ ) and the disk ( $k_0 = \frac{1}{2}k_B$ ) pupil functions.

Rayleigh resolution of the disc pupil function is  $0.61/k_B$  compared to  $0.38/k_0$  for the annula pupil function. The improvement in resolution from the disc pupil to the annula pupil is

$$\frac{0.61/k_B}{0.38/k_0} \approx 16 \text{ fold.}$$

Unfortunately, we are getting this resolution improvement by paying a price at the side lobes. The first sidelobe for ring pupil PSF is approximately -4dB (0.4) while that for the disc pupil PSF is approximately -8.7dB (0.135).

Comparing with the PSF of a rectangular pupil function  $\text{rect}(k/2k_B)$  the resolution improvement is even more dramatic, but again with a worse sidelobe level. The resolution and sidelobe levels for the three systems are summarized below:

TABLE 3.4.1  
RESOLUTION LIMIT AND SIDELobe LEVELS OF  
DIFFERENT PSF'S.

Pupil Function	Resolution	Sidelobe Level
Annula Ring ( $k_0=10k_B$ )	$0.38/k_0$	-4.0dB
Disc (radius $k_B$ )	$0.61/k_B$	-8.7dB
Square (length $2k_B$ )	$0.5 /k_B$	-13.4dB

Even though  $k_B$  does not show up in the expression for the resolution limit of the annula pupil PSF,  $k_B$

affects the level of the sidelobes. The effect however, is not significant. The table below shows the change in sidelobe level with respect to  $k_B$ .

TABLE 3.4.2  
VARIATION OF SIDELOBE LEVEL WITH BANDWIDTH

$k_B$	First Sidelobe level
0.1 $k_0$	-4.01 dB
0.2 $k_0$	-4.05 dB
0.4 $k_0$	-4.37 dB

### 3.5 Resolution From the Doppler Bandwidth of the Signal

The resolution of the system can also be obtained from the signal bandwidth of the radar returns. For any constant aspect angle  $\theta$ , let us call the projection space data (range compressed data)  $g(\theta, \ell)$  a range profile. A range profile is therefore the projection of the target onto the LOS and then convolved with the  $\text{sinc}(\ell)$  function due to the narrowband property. From Eq. (3.3.1), the projection of a point target at  $(\rho_0, 0)$  is

$$g(\theta, \ell) = \sigma_0 \text{sinc}[k_B(\ell - \rho_0 \cos \theta)] e^{+j2\pi k_0 \rho_0 \cos \theta} \quad (3.5.1)$$

This can be rewritten as

$$g(\theta, \ell) = \sigma_0 \text{sinc}[k_B(\ell - \rho_0 \cos \theta)] e^{j2\pi k_0 \rho_0} \cdot e^{-j2\pi k_0 \rho_0 (1 - \cos \theta)}$$

As in Fig. 3.5.1 the phase term in the last exponential is the phase due to the distance of the point target from the initial point at  $\theta = 0$ . The relative phase of the signal at aspect angle  $\theta$  is

$$\phi = 2\pi k_0 \rho_0 (1 - \cos\theta)$$

The incremental phase change when the aspect angle makes an incremental change  $\Delta\theta$  is

$$\Delta\phi \approx \frac{\partial\phi}{\partial\theta} \Delta\theta = 2\pi k_0 \rho_0 \sin\theta \Delta\theta$$

This is the phase change along the contour  $\ell = \rho_0 \cos\theta$ . Within this angular increment, the point target traverses an arc of length  $\rho_0 \Delta\theta$ . The spatial Doppler frequency of the signal can be defined as

$$k_d \triangleq \frac{1}{2\pi} \frac{\text{change in signal phase}}{\text{distance travelled by point target}}$$

$$= \lim_{\Delta\theta \rightarrow 0} \frac{\Delta\phi}{2\pi \Delta\theta \rho_0}.$$

Thus

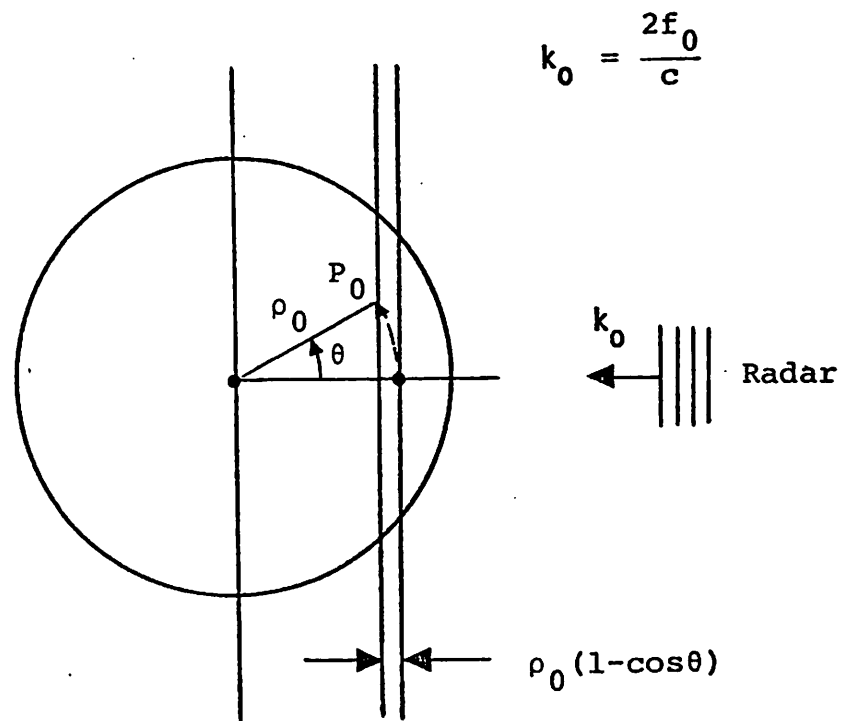
$$\boxed{k_d = k_0 \sin\theta} \quad (3.5.2)$$

The maximum Doppler return therefore occurs at  $\theta = \pi/2$  and minimum occurs at  $\theta = 3\pi/2$ . In particular,

$$\begin{aligned} k_d|_{\max} &= k_0 \\ k_d|_{\min} &= -k_0. \end{aligned}$$

The Doppler bandwidth  $k_{dB} = 2k_0$ . It is well known that the inverse bandwidth is a good measure of the resolution obtained from a signal. The resolution of target points





Phase recorded at aspect angle is

$$\phi \propto 2\pi f_0 \frac{2\rho_0(1-\cos\theta)}{c}$$

$$2\pi k_0 \rho_0(1-\cos\theta).$$

Figure 3.5.1. Figure showing the distance of  $P_0$  along the LOS (range) from the initial point at aspect  $\theta=0$ .

along a circular arc can therefore be taken as

$$\delta_A = \frac{0.5}{k_0} \quad (3.5.3)$$

In other words, any two points sitting on a same circle of radius  $\rho_0$  can be resolved if their arc distance is greater than  $\delta_A$ . Since  $\delta_A$  is independent of the radius  $\rho_0$ , the resolvable distance  $\delta_A$  (which we will call arc resolution for now) is uniform over the entire target.

Since the pupil function is isotropic, the PSF must also be isotropic. Thus, the above arc resolution limit is also a resolution limit in radial distance. The two dimensional resolution can therefore be closely represented by  $\delta_A$ .

The interesting result here is that even though a completely different approach is used, the resolution limit from both the optical system and the bandwidth concept agreed very closely. More importantly, both approaches come to the same conclusion that the bandwidth  $k_B$  (in radial frequency) does not play a dominant role in determining the resolution. This conclusion seems contrary to the fact that for each  $\theta$ , the projection data (range profile) resolution is determined by the inverse bandwidth ( $k_B^{-1}$ ). Because of this we should clarify the relationships between resolution and  $k_0$  and  $k_B$ . If we

consider only one projection data (range profile) from a given aspect angle, the resolution obtainable is only along the line of sight and it is proportional to  $k_B^{-1}$ . On the other hand, if we consider the projection data over the complete set  $[0, 2\pi]$  of aspect angles, the resolution is proportional to  $k_0^{-1}$ . Between the two extremes, both  $k_0$  and  $k_B$  are expected to play an important role. This will not be pursued further here until we come to consider the distortion (aberration) effects in practical situations.

## Chapter 4

### DISCRETE PSF AND SAMPLING REQUIREMENTS

#### 4.1 Discrete PSF

The polar coordinate Fourier transform data in the MFS radar system is available only in discrete frequency steps. The radial frequency sampling interval is  $\Delta k = 2\Delta f/c$ . There the data is discretized radially. In the azimuth direction, data are sampled only over increments of aspect angle  $\Delta\theta = \omega T_3$ . Because of this radial and angular sampling, the PSF is no longer available in a closed form as in Eq. (3.2.2).

In Chapter 2, it was shown that the target reflectivity function  $\sigma$  can be computed by taking the Inverse F.T. on the radar data. In polar coordinates, let  $g(\phi_m, \ell_n)$  be the computed target reflectivity function. Then

$$g(\phi_m, \ell_n) \approx \frac{k_0}{2\pi} \int_{k_{\min}}^{k_{\max}} \int_0^{2\pi} G(\theta, k) e^{j2\pi k \ell_n \cos(\theta - \phi_m)} dk d\theta \quad (4.1.1)$$

In order to compute the PSF, let  $G(\theta, k)$  be the data from a point target at  $(\rho = 0, \phi = 0)$ ; thus

$$G(\theta, k) = \sigma_0 \delta(\theta - \theta_i) \delta(k - k_j)$$

where  $\delta(x)$  is the usual Dirac delta function,

$$k_j = k_{\min} + j\Delta k \text{ for } j=0, 1, 2, \dots, K-1$$

$$\theta_i = i\Delta\theta \text{ for } i=0, 1, 2, \dots, N-1$$

$$\Delta k = 2\Delta f/c \text{ (spatial frequency increments)}$$

$$\Delta\theta = \text{aspect angle increment.}$$

Then  $g(\phi_m, \ell_n)$  can be written as the following linear approximation

$$g(\phi_m, \ell_n) \approx \frac{k_0 k_B}{NK} \sigma_0 \sum_{j=0}^{K-1} \sum_{i=0}^{N-1} e^{j2\pi k_j \ell_n \cos(i\Delta\theta - \phi_n)}$$

Here one is only interested in values of  $g(\theta_m, \ell_n)$  over a discrete angular array of  $\phi_m = m\Delta\theta$ ,  $m=0, 1, \dots, N-1$ . The above equation becomes

$$g(m, \ell_n) \approx \frac{k_0 k_B}{NK} \sigma_0 \sum_{j=0}^{K-1} \sum_{i=0}^{N-1} e^{j2\pi k_j \ell_n \cos(i-m)\Delta\theta} \quad (4.1.2)$$

where  $g(m, \ell_n)$  now denotes  $g(\phi_m, \ell_n)$ .

Integrating over  $k$  first, the expression can be simplified to

$$g(m, \ell_n) = \frac{k_0 k_B}{NK} \sigma_0 \sum_{i=0}^{N-1} \frac{\sin(\pi K \ell_n \Delta k \cos(i-m)\Delta\theta)}{\sin(\pi \ell_n k \cos(i-m)\Delta\theta)} \cdot e^{j2\pi k_0 \ell_n \cos(i-m)\Delta\theta}$$

If one discretizes  $\ell_n$  by setting  $\ell_n = sn/k_B$  where  $s$  is a scaling factor  $\hat{k}_0 = k_0/k_B$ , then

$$g(m,n) = \frac{k_0 k_B}{NK} \sigma_0 \sum_{i=0}^{N-1} \frac{\sin(\pi s n \cos(i-m)\Delta\theta)}{\sin(\pi \frac{sn}{K} \cos(i-m)\Delta\theta)} e^{j2\pi k_0 s n \cos(i-m)\Delta m} \quad (4.1.3)$$

Where  $g(m,n)$  denotes  $g(\phi_m, \ell_n)$ . The exact equality is used in Eq. (4.1.3) because  $g(m,n)$  is the linear approximation of  $g(\phi_m, \ell_n)$ .

Statement:  $g(m,n) = g(0,n) \quad \forall m,n$   
i.e.  $g(m,n) = g(n)$  is isotropic

Proof:

$$g(m,n) = \frac{k_0 k_B}{NB} \sigma_0 \sum_{j=0}^{K-1} \sum_{i=0}^{N-1} e^{j2\pi k_j \ell_n \cos(i-m)\Delta\theta}$$

By changing variable,  $i' = (i-m)$

$$g(m,n) = \frac{k_0 k_B}{NK} \sigma_0 \sum_{j=0}^{K-1} \left[ \sum_{i'=-m}^{-1} + \sum_{i'=0}^{N-m-1} \right] e^{j2\pi k_j \ell_n \cos(i'\Delta\theta)}$$

Note that  $N\Delta\theta = 2\pi$ ; the cyclic property of  $\cos(i'\Delta\theta)$  gives

$$\cos(-m\Delta\theta) = \cos((N-m)\Delta\theta)$$

Hence

$$\begin{aligned} g(m,n) &= \frac{k_0 k_B}{NK} \sigma_0 \sum_{j=1}^{K-1} \left[ \sum_{i'=N-M}^{N-1} + \sum_{i'=0}^{N-m-1} \right] e^{j2\pi k_j \ell_n \cos(i'\Delta\theta)} \\ &= g(0,n) \end{aligned}$$

We conclude from the above statement that the discrete point spread function is isotropic if we discretize the angle  $\phi_m$  with the same increment  $\Delta\theta$  and starting from the same initial angle. Because of this, the PSF in Eq. (4.1.3) will be plotted in one dimension only, viz., in the radial dimension  $n$ . The figures in Fig. 4.1.1 are plots of  $g(0,n)$  versus  $n$  for  $k_0 = 10k_B$ . Figure 4.1.1a is plotted for  $N = 256$ ,  $K = 40$ ; Fig. 4.1.1b is plotted for  $N = 512$ ,  $K = 40$ ; Fig. 4.1.1c is plotted for  $N = 512$ ,  $K = 20$  except for a change in scale on  $n$ .

The most salient difference between the discrete pupil PSF and the continuous pupil PSF is in the presence of "periodic" clutters for the discrete case. The function  $g(n)$  is "periodic" in the sense that the relatively significant values of the function occur at periodic intervals. Moreover, the period  $P$  of such repetitive structures is approximately

$$P = \frac{N}{2\pi} k_0^{-1} \quad (4.1.4)$$

The empirical relation in Eq. (4.1.4) also indicates that the period is independent of the range sampling rate ( $K$ ). By doubling  $N$  from 256 to 512 while keeping  $K$  constant at 40, the "period" of the clutters increases twofold as shown in Figs. 4.1.1a and b. A different kind of clutter that does not obey Eq. (4.1.4) appears beyond  $\rho = 20/k_B$

for  $K = 20$ ,  $N = 512$ . This fluctuating clutter seems to be a result of  $K$  value because it shifts with  $K$ . Another point of interest is that while the peak of the clutter decreases monotonically with its order, the "width" increases. In the actual 2-dimensional plots for the PSF, these clutter will show up as concentric annula rings with the radii being approximately  $jN/2\pi$  (in  $k_0^{-1}$  units).

Figures 4.1.1a,b,c also show that the PSF  $g(n)$  is pretty "badly behaved" beyond the first clutter. It also seems like that the clutters are additive in nature. Therefore if the PSF for  $N = 512$  is subtracted from the PSF for  $N = 256$  with  $K = 40$  in both cases, the first clutter should be pretty well isolated. Figure 4.1.2 shows the difference between the two PSF's. Surprisingly enough, the first clutter does appear to be isolated because it looks much more like some "well behaved" function. Note that  $\rho$  ranges from 0 to  $10/k_B$  in this figure. The peak of the first clutter occurs at about  $P = \frac{256^{-1}}{2\pi k_0} = 40.744k_0^{-1}$ . As a further illustration,  $g(n)$  is plotted for the special case in which there is only one range sample, i.e.  $K = 1$ . In this case the PSF for the continuous pupil becomes  $J_0(2\pi k_0 n)$ . This is shown in Fig. 4.1.3a. Again notice that the first clutter appears at around  $P = 40.744k_0^{-1}$ . This further supports the conjecture that it is caused by azimuth (angle)



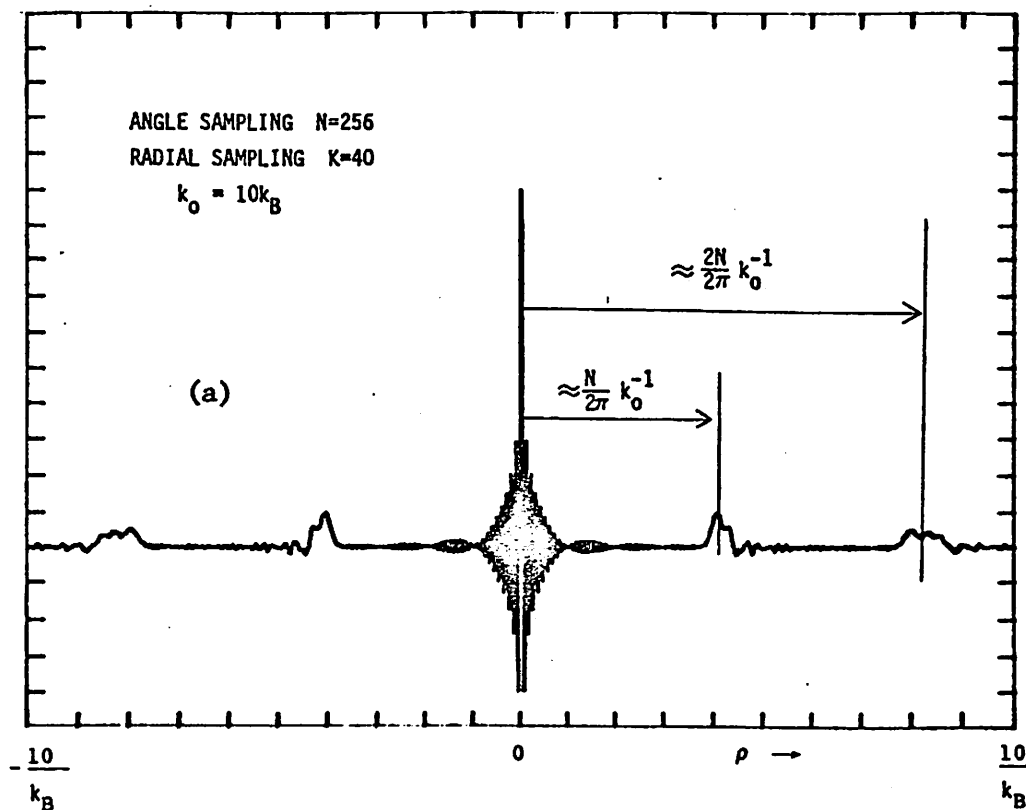


Figure 4.1.1. PSF of discrete pupil of the imaging system.  
 (K is the number of radial samples;  
 N is the number of angular samples.)  
 (a)  $K=40$ ,  $N=256$   
 (b)  $K=40$ ,  $N=512$   
 (c)  $K=20$ ,  $N=512$

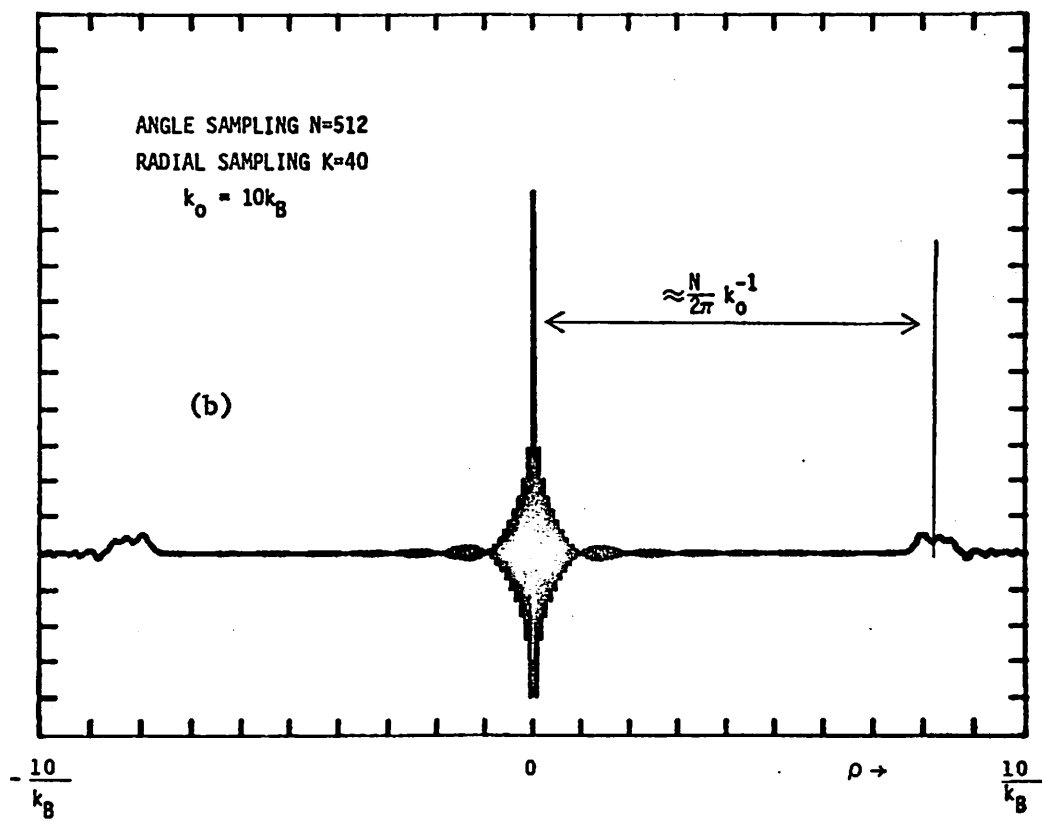


Figure 4.1.1 continued

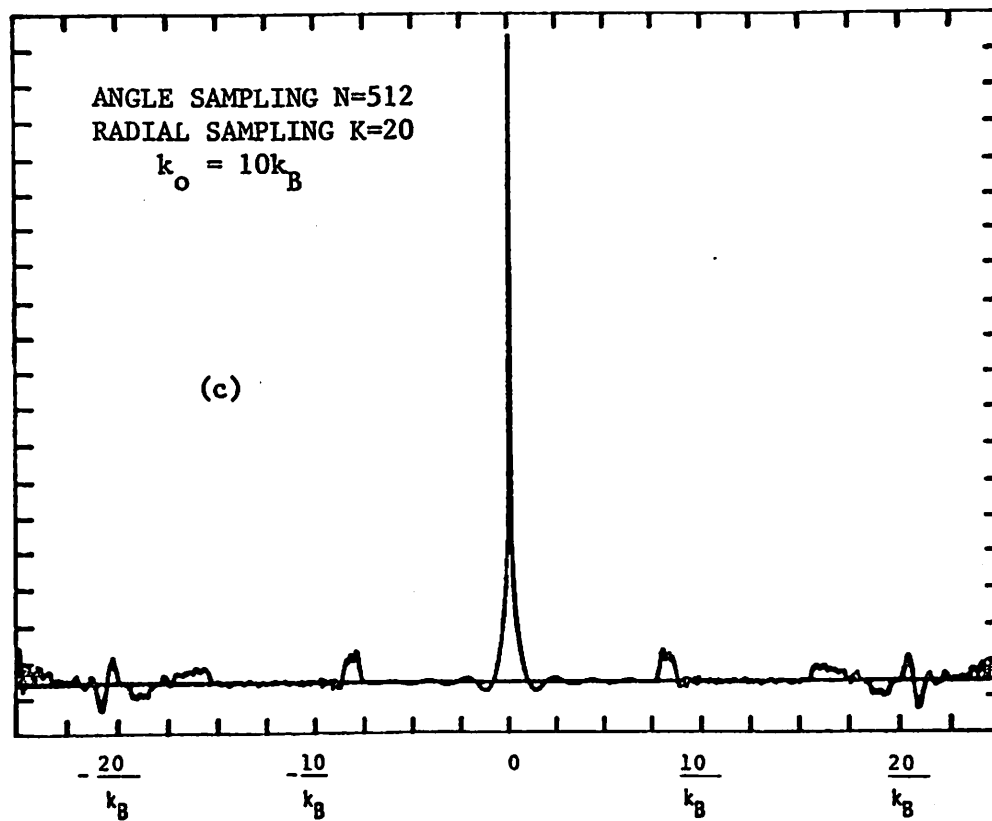


Figure 4.1.1 continued

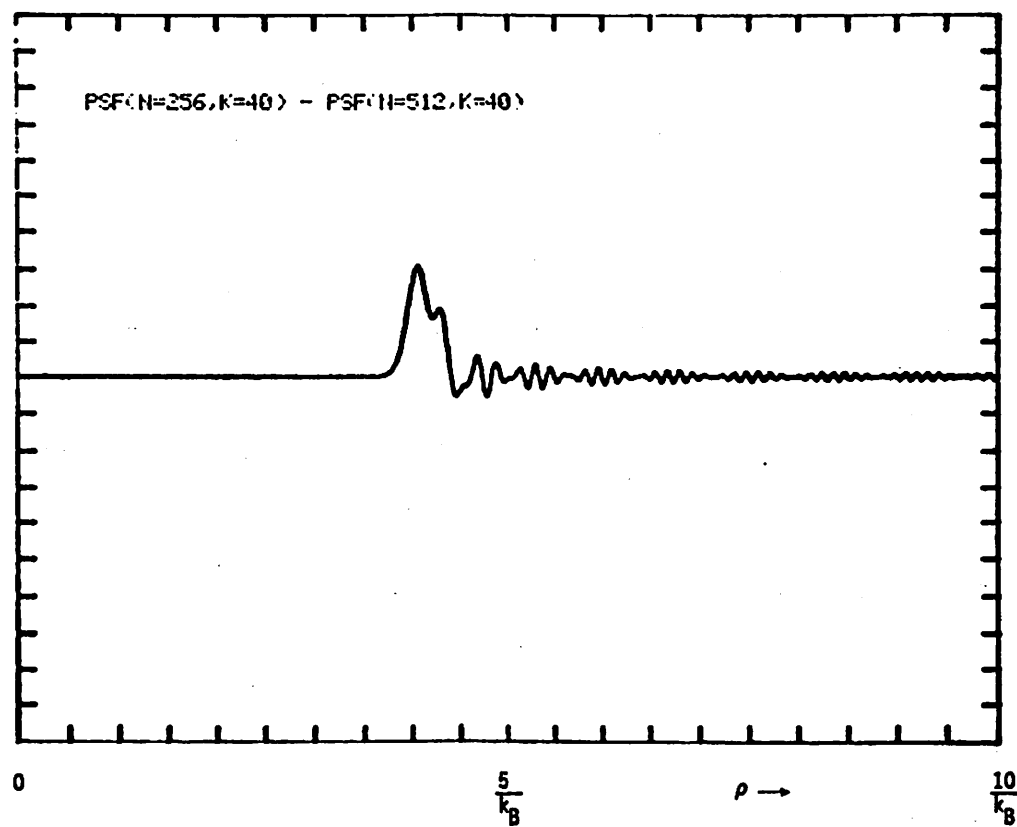
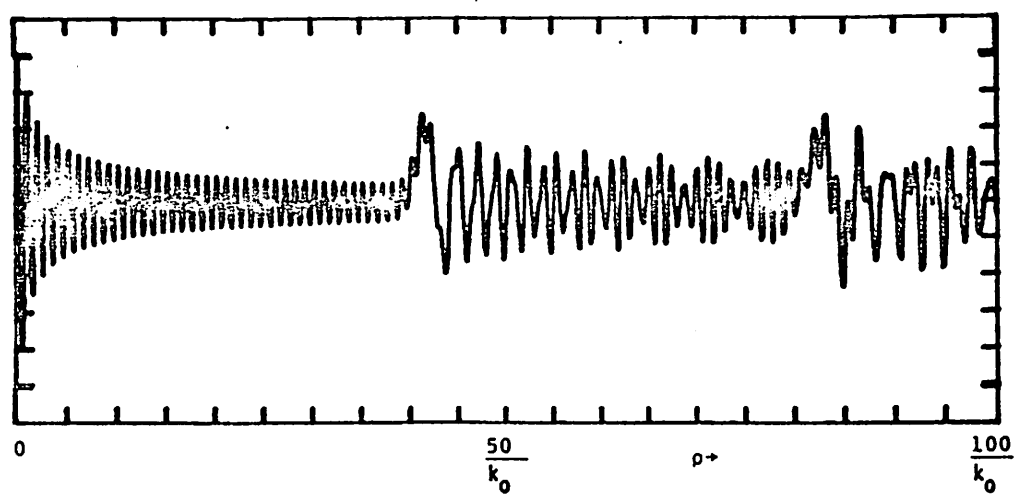
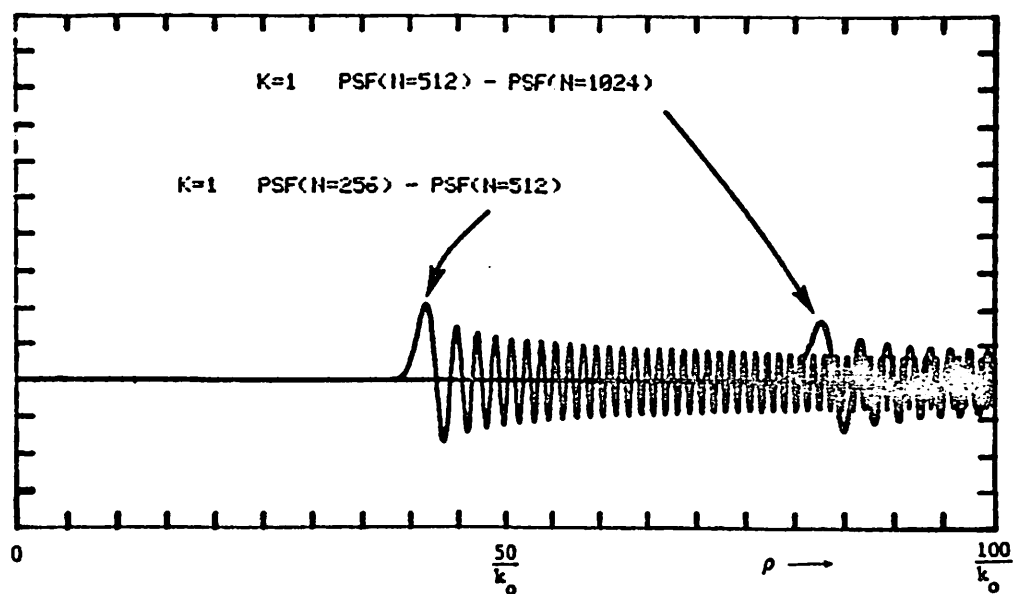


Figure 4.1.2. Difference of the PSF in Fig. 4.1.1a and the PSF in Fig. 4.1.1b.



(a)



(b)

Figure 4.1.3. PSF for the discrete pupil  $N=256$ ,  $K=1$ .  
 (a) The PSF. (b) The isolated first and second  
 order clutter term computed from taking the  
 difference of two PSF's.

undersampling. In Fig. 4.1.3b the 1st and 2nd clutter are obtained as before by taking the difference of two PSF's.

$$\text{First clutter } e_1(n) = g(n) \Big|_{N=256} - g(n) \Big|_{N=512} \quad (4.1.5)$$

$$\text{Second clutter } e_2(n) = g(n) \Big|_{N=512} - g(n) \Big|_{N=1024} \quad (4.1.6)$$

Again one sees that the clutter terms are some well behaved functions. These clues provide us with some interesting guides into solving the problem analytically.

#### 4.2 Sampling Requirements

We have found some clues in the previous section on the effect of undersampling in both azimuth and range dimensions of the PSF. One obvious conclusion from these is that the sampling rates are extremely important parameters for the design of a radar imaging system. Here we will try to solve the problem of defining what is considered sufficient sampling and what are the barest necessary sampling rates so that the data can still be used to reconstruct the target. The importance of this problem is also underscored by the fact that the narrowband assumption can be relaxed into a full disc plane and thereby give a concrete understanding to the polar coordinate sampling requirements in tomographic systems.

The key idea here is to 1-D Fourier transform the data into range profiles which is also called projection data, and then carry out analysis in that domain. Another important concept that will be utilized here is the degrees of freedom (DOF) concept [15].

(A) Range Sampling - Number of Frequency Steps (K)

Since the DFT in the radial frequency dimension is carried out to convert the data into range profiles (in so called "projection space"), the DFT property gives the unambiguous range

$$\frac{1}{\Delta k} = \frac{K}{k_B} \text{ for } K > 1.$$

For sufficient sampling in radial (range) dimension, the following criterion must be met.

Criterion 1: The projection data must unambiguously cover the whole target of maximum extent  $2a$ , i.e.,

$$\frac{K}{k_B} \geq 2a.$$

Hence

$$K \geq 2ak_B$$

(B) Azimuth Sampling - Aspect Angle Sample (N)

Depending on which aspect of the imaging system we are emphasizing on, the sampling rate in this dimension is called different names. For example, the azimuth sampling rate is represented by the burst rate when the transmitted signal format is emphasized.

In section 3.5, it was shown that the maximum Doppler bandwidth

$$k_{dB} = \frac{1}{2\pi a} \left[ \left. \frac{d\phi}{d\theta} \right|_{\max} - \left. \frac{d\phi}{d\theta} \right|_{\min} \right] = 2k_0.$$

The maximum change in phase from one range profile to the next range profile (or called signature) is then

$$|\Delta\phi_{\max}| \cong \left. \frac{d\phi}{d\theta} \right|_{\max} \Delta\theta = 2\pi a k_0 \Delta\theta. \quad (4.2.1)$$

For sufficient sampling in the angular (azimuth) dimension the following criterion must be met.

Criterion 2: The maximum phase change between two consecutive range profiles (signatures) must be less than  $\pi$ . i.e.,

$$|\Delta\theta_{\max}| \leq \pi.$$

Hence

$$\Delta\theta \leq \frac{\pi}{2\pi a k_0} = \frac{1}{2a k_0}.$$

Since

$$\begin{aligned} N &= 2\pi/\Delta\theta, \\ N &\geq 4\pi a k_0. \end{aligned}$$

Therefore

$$\boxed{\begin{aligned} K &\geq 2a k_B \\ N &\geq 4\pi a k_0 \end{aligned}} \quad (4.2.2)$$

These are called the sufficient conditions that must be satisfied so that the target can be resolved to the best resolution achievable with the system without being



plagued by undersampling effects. They also give parameters with which preprocessors can be designed to bring down oversampled rates.

### Necessary Condition

Very often, because of practical limitations, sufficient sampling conditions in Eq. (4.2.2) cannot be met. In those cases the question that one needs to ask is what the necessary sampling rate should be if reconstruction is possible at all.

In general, the maximum unambiguous range is given by

$$2\rho_{\max} = \frac{K}{k_B}. \quad (4.2.3)$$

Again in general, from Eq. (3.5.2), it can be derived that

$$\frac{d\phi}{d\theta} = 2\pi a k_0 \sin\theta.$$

With  $\Delta\theta = 2\pi/N$ ,

$$|\Delta\phi| \approx 2\pi a k_0 \sin\theta \cdot \frac{2\pi}{N}.$$

Using criterion 2 for  $|\Delta\theta| \leq \pi$ ,

$$\frac{4\pi a k_0 \sin\theta}{N} \leq 1.$$

Hence

$$\theta \leq \sin^{-1} \left( \frac{N}{4\pi a k_0} \right). \quad (4.2.4)$$

Let

$$\theta_{\max} = \sin^{-1} \left( \frac{N}{4\pi a k_0} \right), \quad (4.2.5)$$

then the above inequality from criterion 2 becomes

$$\theta \leq \theta_{\max}. \quad (4.2.6)$$

Therefore suppose that range sampling is sufficient, then as long as we do not process the echo signal of a point target  $\sigma(\rho_0, \phi_0)$  for more than  $2\theta_{\max}$  across the zero Doppler aspect angle, the target reconstruction can be achieved without azimuth undersampling effects. The zero Doppler condition occurs when the aspect angle  $\theta = \phi_0$  and  $\theta = \phi_0 + \pi$ . Moreover, the maximum  $\theta$  aspect angle extent for unambiguous Doppler phase is  $\theta_{\max}$ . In order to unambiguously reconstruct the target, we use the following criterion which is also illustrated in Fig. 4.2.1.

Criterion 3: The contour of integration  $\ell = a \cos \theta$  for every target point should pass through the region of overlap constrained by these two conditions:

$$\begin{aligned} \ell &\leq \rho_{\max} \\ \theta &\leq \theta_{\max}. \end{aligned}$$

These criteria can also be rewritten as

$$\theta_{\max} \geq \theta_{Az} \quad (4.2.7)$$

where

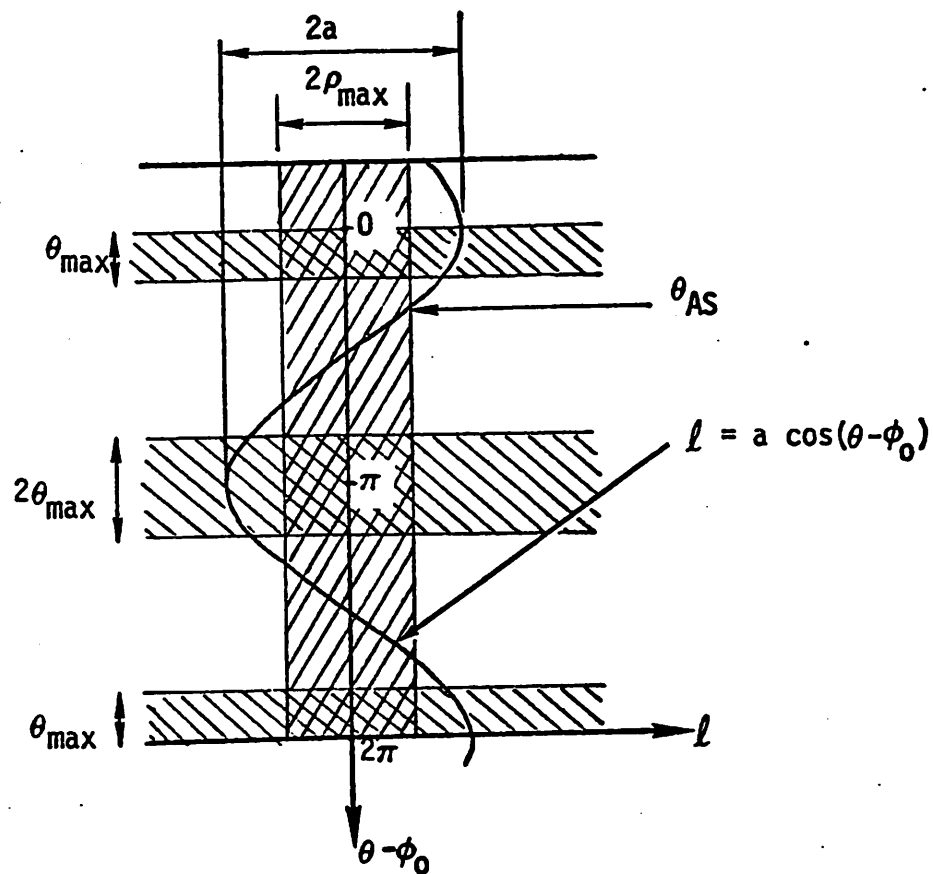


Figure 4.2.1.  $l = a \cos(\theta - \phi_0)$  is the contour of the signal from a point target  $\sigma(a, \phi_0)$  projected onto the line-of-sight as it rotates.

$$\begin{aligned}\theta_{Az} &= \cos^{-1} (\rho_{\max}/a) \\ &= \cos^{-1} (K/2ak_B).\end{aligned}$$

On simplification

$$\left(\frac{N}{4\pi ak_0}\right)^2 + \left(\frac{K}{2ak_B}\right)^2 \geq 1. \quad (4.2.8)$$

which is the necessary condition

Table 4.2.1 Summary of Sampling Requirements in Polar Coordinates

NECESSARY CONDITION	$\left(\frac{N}{N_s}\right)^2 + \left(\frac{K}{K_s}\right)^2 \geq 1$
SUFFICIENT CONDITION	$\begin{aligned}N &\geq N_s = 4\pi ak_0 \\ K &\geq K_s = 2ak_B\end{aligned}$

The necessary and sufficient conditions can easily be visualized if we plot the constraints in two dimensions. This is illustrated in Fig. 4.2.2. Note that Eq. (4.2.8) is in general an ellipse with major (minor) axis  $N_s$  or  $K_s$ .

#### 4.3 Sampling Requirements From the DOF Point of View

##### (A) Range Sampling

The DOF concept in one dimension is given by the "time bandwidth product." Hence, for a target of maximum extent  $2a$  and bandwidth  $k_B$  for the transmitted signal,

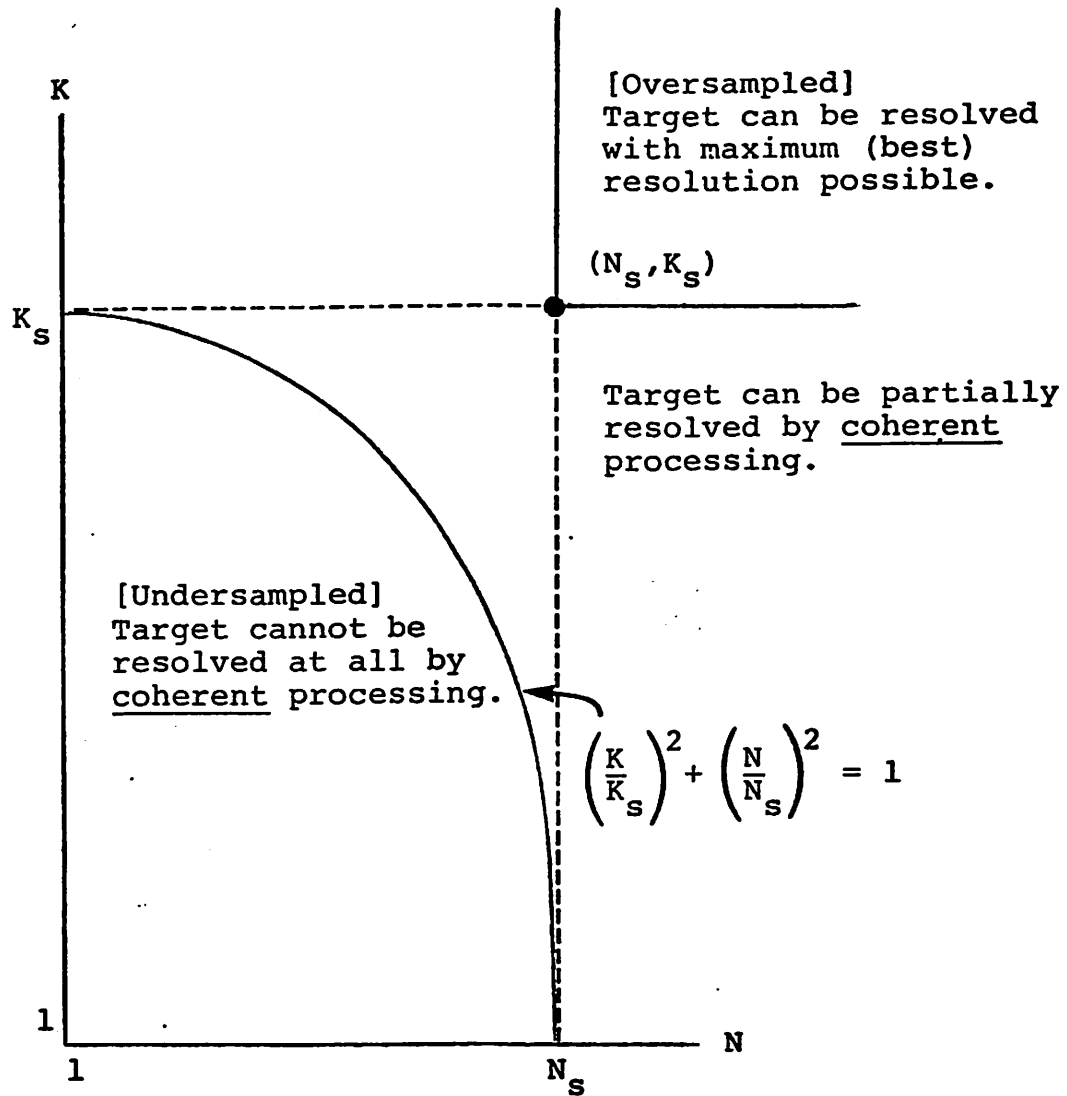


Figure 4.2.2. Regions of  $(N, K)$  which illustrate the sampling requirements.  $N, K$  are integers greater than 0.

the "time bandwidth product"

$$\begin{aligned}\text{TBWP} &= (\text{maximum spatial extent})(\text{signal bandwidth}) \\ &= 2ak_B \\ &= K_S .\end{aligned}$$

Since the TBWP represents the maximum number of samples of data that needs to be processed to give one reconstruction sample point, it also represents a sufficient sampling condition. Moreover, this number is identical to the range sampling requirement found from a slightly different point of view.

#### (B) Azimuth Sampling

The degrees-of-freedom (DOF) is defined as [15] the product of the target area with the Fourier domain pupil area. This number (an integer) represents the total number of linearly independent samples that can pass through the imaging system and therefore only DOF number of samples need be collected to sufficiently reconstruct the target. For the annula ring pupil,

$$\text{Target area} = \pi a^2$$

$$\text{Pupil area} = 2\pi k_0 k_B .$$

$$\begin{aligned}\text{Then the DOF of imaging system} &= (\pi a^2)(2\pi k_0 k_B) \\ &= 2\pi^2(ak_0)(ak_B) .\end{aligned}$$

The azimuth sampling requirement is

$$N = \frac{\text{DOF}}{\text{TBWP}} = \frac{2\pi^2 (ak_0)(ak_B)}{2(ak_B)} \\ = \pi^2 ak_0$$

Therefore

$$\boxed{\begin{aligned} K &= 2ak_B \\ N &= \pi^2 ak_0 \end{aligned}} \quad (4.3.1)$$

for sufficient sampling. Note that with the Doppler bandwidth approach, the sampling criterion was

$$NK \geq 8\pi (ak_0)(ak_B) \quad (4.3.2)$$

and with the DOF approach it was

$$NK \geq 2\pi^2 (ak_0)(ak_B) \quad (4.3.3)$$

which are very close in comparison. They are off only by a factor of 4:5.

#### 4.4 Conclusion

It was shown that the PSF corresponding to the discretely sampled data in the annula ring pupil function is different from the ideal PSF corresponding to the continuously sampled data in the same pupil function. The difference lies in the presence of more or less periodically recurring so called clutters along the radial dimension of the discrete PSF. The seemingly additive

nature of these clutter functions may provide some clues to their analytic structure.

Next, it was also shown that by using criteria 1 and 2, the sufficient sampling requirement was

$$K = K_S = 2ak_B$$

$$N = N_S = 4\pi ak_0.$$

From criterion 3, the necessary sampling requirement was

$$\left(\frac{N}{N_S}\right)^2 + \left(\frac{K}{K_S}\right)^2 \geq 1.$$

These sampling conditions were similar to those derived from the Degrees of Freedom concept which is a completely different approach.



## Chapter 5

### ERRORS IN POLAR COORDINATE SAMPLING

In many of the new imaging systems that are arising, more and more of these seem to collect their data samples with a polar coordinate format. Most of these systems involve obtaining projections of the object and reconstructing the image from these projections. Since only a finite number of projections can be taken and only a finite number of samples can be read from each projection, the polar coordinate sampling format is "built into" the system. Systems that use polar coordinate sampling include radio astronomy, electron microscopy, X-ray tomography, rotationally symmetrical array design, optical imaging, radar imaging and so on.

The first attempt to estimate the sampling requirements in polar coordinates appeared in 1967 [5] in which the maximum linear distance between any two adjacent samples in the Fourier transform domain was chosen so that its inverse was greater than the maximum diameter of the object. This intuitively obtained result was also discovered in section 4.1. Smith et al. [33] in 1973

computed the Fourier transform of a 2-D Gaussian function sampled in polar coordinates. It was found that besides another Gaussian function that was obtained after the Fourier transformation, a series of clutter terms associated with the function also appeared.

The objective of this chapter is to obtain an analytic expression for the errors or clutters associated with sampling in polar coordinate format and therefore try to determine exactly the necessary and sufficient sampling rate in both azimuth and radial dimensions. Our approach is as follows. We will sample a disc and an annula ring pupil in polar coordinates and compute their Fourier transforms which will be called "discrete" point spread functions. Since these functions are isotropic, we will mention the transformation as Fourier Bessel transformation. We will apply Poisson's Summation Formula to compute the discrete point spread function and get an expression for the difference between the discrete transform and continuous transform. This difference is the error associated with the sampling.

One very significant immediate application of the result is on the estimation of the azimuth and radial sampling intervals for X-ray tomographic systems. For many practical systems, experimentation was the method

used to find an "optimum" number of azimuth samples or projections. Since each projection exposes the patient with an extra dose of radiation it is extremely important to know the minimum number of projections that is needed to get a reconstruction that is free of sampling errors.

## 5.1 Poisson's Summation Formula

### 1. Fourier's Theorem

Let  $g(x)$  be a periodic function with period  $\Delta$ , with at most only a finite number of simple discontinuities (finite steps). Then for any  $\epsilon > 0$ ,

$$\lim_{\epsilon \rightarrow 0} \frac{g(x+\epsilon) + g(x-\epsilon)}{2} = \sum_{n=-\infty}^{\infty} g_n e^{-j \frac{2\pi}{\Delta} nx}$$

where

$$g_n = \frac{1}{\Delta} \int_0^{\Delta} g(x) e^{j \frac{2\pi}{\Delta} nx} dx.$$

This is Fourier's Theorem.

2. Now consider the integral  $\int_0^{N\Delta} f(x) e^{j \frac{2\pi}{\Delta} nx} dx$  where  $f(x)$  also has only a finite number of simple discontinuities.

$$\begin{aligned} \int_0^{N\Delta} f(x) e^{j \frac{2\pi}{\Delta} nx} dx &= \left[ \int_0^{\Delta} + \int_{\Delta}^{2\Delta} + \dots + \int_{(N-1)\Delta}^{N\Delta} \right] f(x) e^{j \frac{2\pi}{\Delta} nx} dx \\ &= \sum_{m=1}^{N-1} \int_{m\Delta}^{(m+1)\Delta} f(x) e^{j \frac{2\pi}{\Delta} nx} dx \\ &= \sum_{m=0}^{N-1} \int_0^{\Delta} f(t+m\Delta) e^{j \frac{2\pi}{\Delta} n(t+m\Delta)} dt \end{aligned}$$

Then

$$\int_0^{N\Delta} f(x) e^{j \frac{2\pi}{\Delta} nx} dx = \sum_{m=0}^{N-1} \int_0^{\Delta} f_m(t) e^{j \frac{2\pi}{\Delta} nt} dt \quad (5.1.1)$$

where  $f_m(t) = f(m\Delta + t)$ . From Fourier's Theorem,

$$\lim_{\epsilon \rightarrow 0} \frac{f_m(t+\epsilon) + f_m(t-\epsilon)}{2} = \frac{1}{\Delta} \sum_{n=-\infty}^{\infty} e^{j \frac{2\pi}{\Delta} nt} \left[ \int_0^{\Delta} f_m(\xi) e^{j \frac{2\pi}{\Delta} n\xi} d\xi \right].$$

At  $t = 0$ , the left hand side is

$$\lim_{\epsilon \rightarrow 0} \frac{f_m(+\epsilon) + f_m(-\epsilon)}{2} = \frac{1}{2} [f(m\Delta) + f(m+1)\Delta]$$

and the right hand side is

$$\frac{1}{\Delta} \sum_{n=-\infty}^{\infty} \int_0^{\Delta} f_m(\xi) e^{j \frac{2\pi}{\Delta} n\xi} d\xi.$$

Therefore

$$\frac{1}{\Delta} [f_m + f_{m+1}] = \frac{1}{\Delta} \sum_{n=-\infty}^{\infty} \int_0^{\Delta} f_m(\xi) e^{j \frac{2\pi}{\Delta} n\xi} d\xi$$

where  $f_m$  represents  $f_m(0)$ . Summing up both sides over all

$$\begin{aligned} \sum_{m=0}^{N-1} \frac{1}{2} [f_m + f_{m+1}] &= \frac{1}{\Delta} \sum_{m=0}^{N-1} \sum_{n=-\infty}^{\infty} \int_0^{\Delta} f_m(\xi) e^{j \frac{2\pi}{\Delta} n\xi} d\xi \\ &= \frac{1}{\Delta} \sum_{n=-\infty}^{\infty} \left[ \sum_{m=0}^{N-1} \int_0^{\Delta} f_m(\xi) e^{j \frac{2\pi}{\Delta} n\xi} d\xi \right]. \end{aligned}$$

Substituting Eq. (5.1.1) into the term in the square brackets,

$$\sum_{m=0}^{N-1} \frac{1}{2} [f_m + f_{m+1}] = \frac{1}{\Delta} \sum_{n=-\infty}^{\infty} \int_0^{N\Delta} f(x) e^{j \frac{2\pi}{\Delta} nx} dx.$$

On simplification,

$$\sum_{m=0}^{N-1} f_m = \frac{1}{\Delta} \int_0^{N\Delta} f(x) dx + \sum_{n=1}^{\infty} e_n + \frac{1}{2}[f_0 - f_N] \quad (5.1.2)$$

where

$$e_n = \frac{2}{\Delta} \int_0^{N\Delta} f(x) \cos\left(\frac{2\pi}{\Delta} nx\right) dx .$$

This is the Poisson's Summation Formula [5]. It says that if we approximate an integral  $\int_0^{N\Delta} f(x) dx$  with a linear sum of samples, the error incurred will be a (countably) infinite sum of error terms, the nth order of which being  $e_n$ . The residual error term  $\frac{1}{2}[f_0 - f_N]$  only depends on the end points of the function and is usually not consequential.

## 5.2 Angular Sampling

Consider the discrete Fourier Bessel transform of a unit circle discretely sampled in azimuth as in Fig. 5.2.1.

Let

$$f(\theta) = e^{j2\pi\rho\cos\theta} \quad \text{for } \theta = \frac{i}{N}2\pi, i=0,1,2,\dots,N-1$$

Let N be an even integer. Since  $f_0 = f_N$ , the residual term is

$$\frac{1}{2}[f_0 - f_N] = 0. \quad (5.2.1)$$

Using Poisson's Summation Formula in Eq. (5.1.2), the discrete F.T.

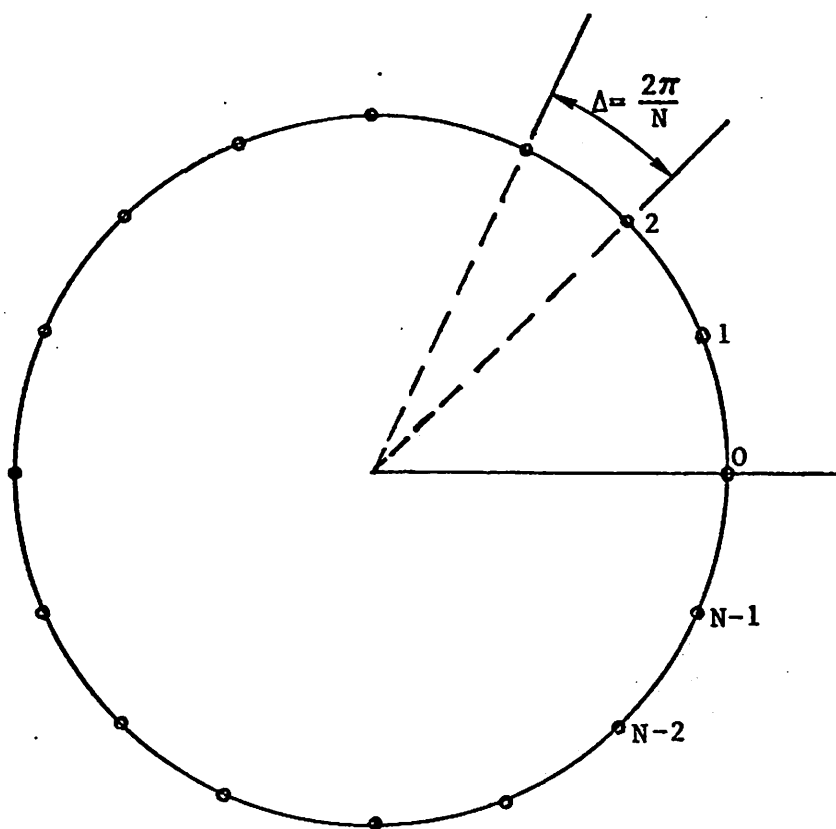


Figure 5.2.1. Angular sampling on a unit circle.

$$\frac{1}{N} \sum_{i=0}^{N-1} e^{j2\pi\rho\cos(\frac{2\pi}{N}i)} = \frac{1}{2\pi} \int_0^{2\pi} e^{j2\pi\rho\cos\theta} d\theta + \sum_{n=1}^{\infty} \frac{1}{\pi} \int_0^{2\pi} (5.2.2)$$

$$\cdot e^{j2\pi\rho\cos\theta} \cos(\frac{2\pi}{N}n\theta) d\theta$$

$$= J_0(2\pi\rho) + \sum_{n=1}^{\infty} e_n(\rho)$$

where

$$e_n(\rho) = \frac{1}{\pi} \int_0^{2\pi} e^{j2\pi\rho\cos\theta} \cos(nN\theta) d\theta. \quad (5.2.3)$$

From standard integral tables [1],

$$\frac{1}{\pi} \int_0^{\pi} e^{j2\pi\rho\cos\theta} \cos(nN\theta) d\theta = J_{nN}(2\pi\rho) e^{j(\frac{nN\pi}{2})}.$$

Because N is even say  $N = 2N'$ ,

$$\frac{1}{\pi} \int_{\pi}^{2\pi} e^{j2\pi\rho\cos\theta} \cos(nN\theta) d\theta = J_{nN}(2\pi\rho) e^{j\frac{nN\pi}{2}}.$$

Hence

$$e_n(\rho) = 2(-1)^{nN'} J_{nN}(2\pi\rho). \quad (5.2.4)$$

Note that if  $4|N$ ,  $(-1)^{nN'}$  is always positive and  $e_n(\rho)$  will always be positive. Finally substituting Eq. (5.2.3) into Eq. (5.2.2), the discrete Fourier Bessel transform of a unit circle is

$$\frac{1}{N} \sum_{i=0}^{N-1} e^{j2\pi\rho\cos(\frac{2\pi}{N}i)} = J_0(2\pi\rho) + 2 \sum_{n=1}^{\infty} (-1)^{nN'} J_{nN}(2\pi\rho) \quad (5.2.5)$$

If we call the left-hand side the Discrete Fourier Bessel transform of a circular ring, then the first term on the right-hand side is the continuous Fourier Bessel transform term while the terms  $J_{nN}(2\pi\rho)$  in the summation represents the  $n$ th order error due to the discrete approximation.

### Properties of $J_{nN}(2\pi\rho)$

Since discrete sampling is meaningful only when  $N$  is a large integer, we need only to study the properties of  $J_{nN}(2\pi\rho)$  for large orders  $nN$  [39].

From the properties of Bessel functions of the first kind and large orders,  $J_{nN}(z)$  is negligibly small compared to its first peak for  $0 \leq z \leq nN$ . The value of the first peak is also the most dominant one. Besides, over that interval  $J_{nN}(z)$  is a monotonically non-negative increasing function. We will therefore only be interested in knowing where the first peak occurs and how significant it is compared to the maximum value of  $J_0(2\pi\rho) = 1$  at  $\rho = 0$ . This will give us a concrete method to choose  $N$  (or the angular sampling interval  $\frac{2\pi}{N}$ ) depending on exactly how large an error one can tolerate on the discrete approximation.



Referring to G.N. Watson [39], the first peak of  $J_{nN}(2\pi\rho)$  for large  $N$  occurs at

$$\rho = P_n = \left(\frac{N}{2\pi}\right)n + \left(\frac{0.8086N^{1/3}}{2\pi}\right)n^{1/3} + O(nN)^{-1/3} \quad (5.2.6)$$

where  $O(\cdot)$  represents the order of the series truncation error. For large  $n$ ,  $P_n$  is approximately linearly proportional to  $n$  which means that the  $n$ th order error shows up at  $\rho \approx nP$  where  $P = N/2\pi$ . The series of  $n$ th order error will therefore appear like radially periodic clutters. In two dimensions, the errors appear as circular artifacts of radius given by  $P_n$  for  $n = 1, 2, 3, \dots$

Table 5.2.1 shows values of  $P_n$  computed for various values of  $n$  for  $N = 256$ . A linear approximation using only the first term in Eq. (5.2.6) is shown with the resulting percentage error. Notice that even without the linear approximation, values of  $P_n$  still show that  $P_n$  is very closely equal to  $nP$  but with  $P \approx 41.00$ . The radially periodic phenomenon and the value of the "period"  $P$  was already observed in section 4.1. This observation will be brought up again when we consider the PSF of the narrowband pupil.

The last column of Table 5.2.1 shows values of the first peak of the  $n$ th order error term  $e_n(\rho) = J_{nN}(2\pi\rho)$ .

TABLE 5.2.1  
PROPERTIES OF THE FIRST FIVE ANGULAR SAMPLING CLUTTER\*

n	$P_n = \left(\frac{N}{2\pi}\right) n + \left(\frac{0.8086N^2}{2\pi}\right) \frac{1}{n^3}$	Linear approx. $\frac{nN}{2\pi}$	Percentage error	Clutter $2J_{nN}(nN)$	Value of 1st peak $J_{nN}(P_n)$
1	41.561	40.74	2.0%	0.140	0.211
2	82.517	81.49	1.3%	0.112	0.168
3	123.410	122.23	1.0%	0.098	0.147
4	164.272	162.97	0.8%	0.088	0.134
5	205.116	203.72	0.7%	0.082	0.124

\*  $N = 256$   
 $J_0(0) = 1$

For  $N = 256$ , the first peak of the first order error  $J_N(2\pi\rho)$  is 0.211 (-6.76dB). This is a significant value compared to  $J_0(0)$ . If  $\rho_{\min}$  is the smallest radius of the first order error term  $J_N(2\pi\rho)$  that can be tolerated and  $\epsilon$  is the largest error allowed within the region of interest,  $N$  must be chosen such that

$$J_N(2\pi\rho_{\min}) \leq \frac{1}{2} \epsilon \quad (5.2.7)$$

As an illustration, Fig. 5.2.2a shows  $J_0(2\pi\rho)$  which is the exact Fourier Bessel transform of a circle of unit radius in Fig. 5.2.1.

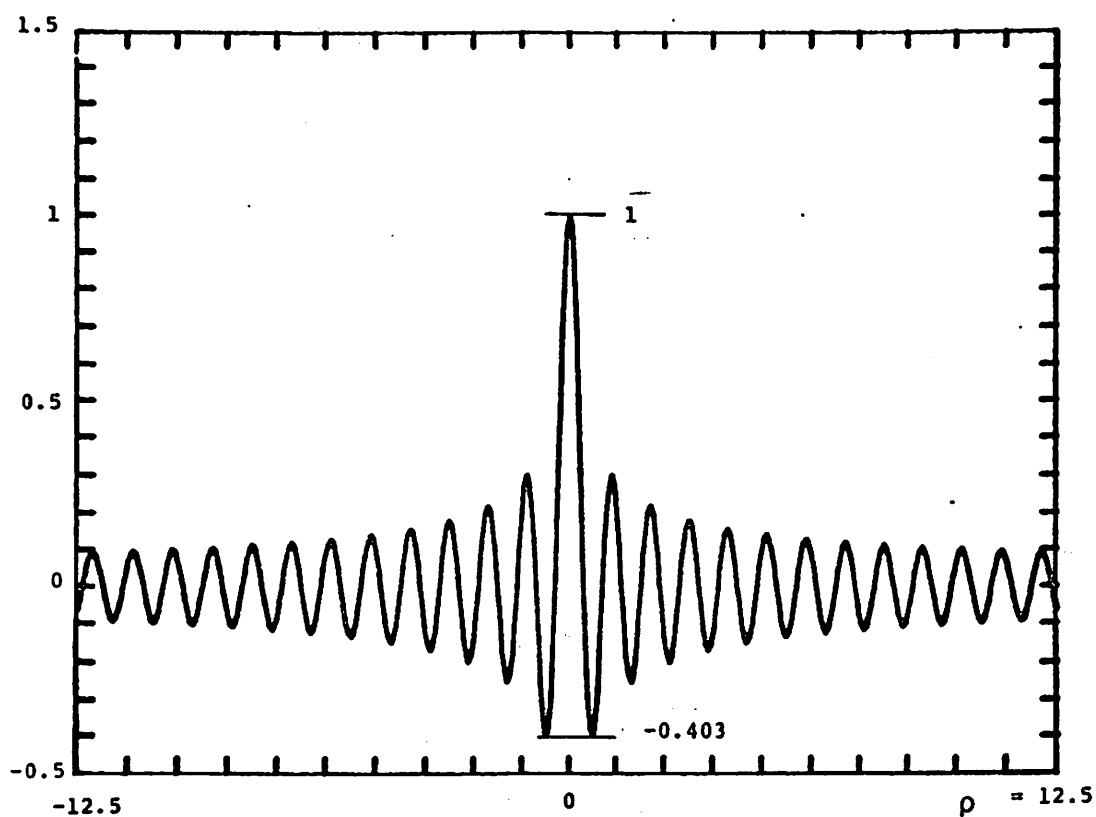
Figure 5.2.2b shows the discrete Fourier Bessel transform as given in Eq. (5.2.5) for  $P$  over  $[0, 200k_0^{-1}]$  where  $k_0 = 1$ . Figure 5.2.2c shows the exact Fourier Bessel transform and the independent error terms for  $n = 1, 2, 3, 4$ .

### 5.3 Radial Sampling

#### A. Over Full Disc Pupil Function

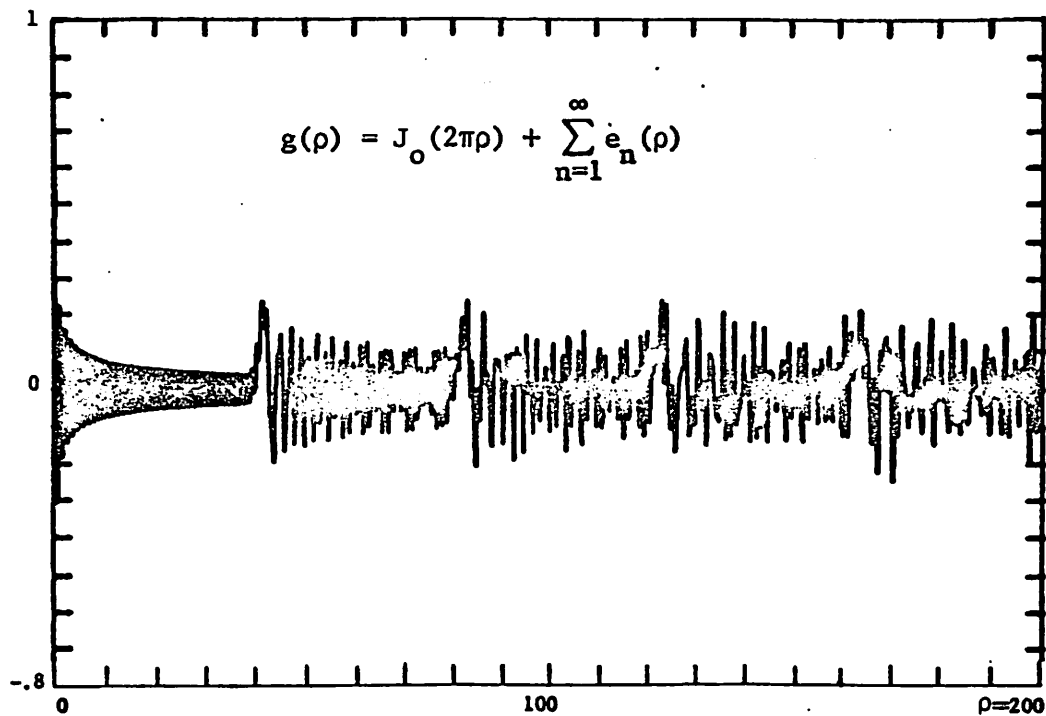
Suppose we have a series of  $K$  impulsive concentric circles shown in Fig. 5.3.1a as pupil function. Let the pupil function be

$$G(k) = \Delta k \sum_{j=0}^{K-1} \delta(k - j\Delta k) \quad (5.3.1)$$

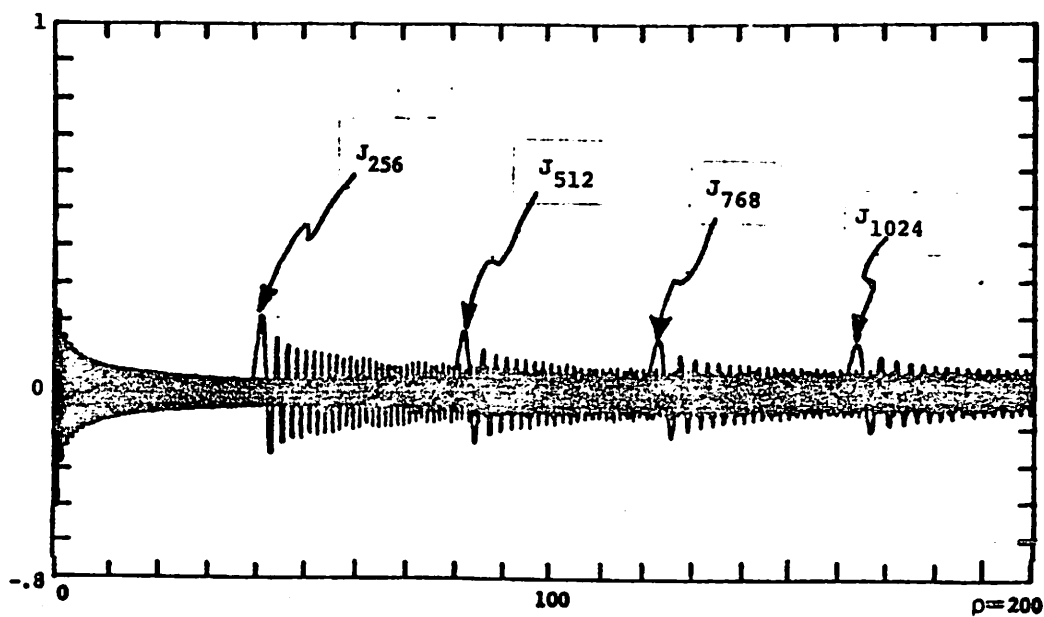


(a) The exact transform  $J_0(2\pi\rho)$  of a unit circle.

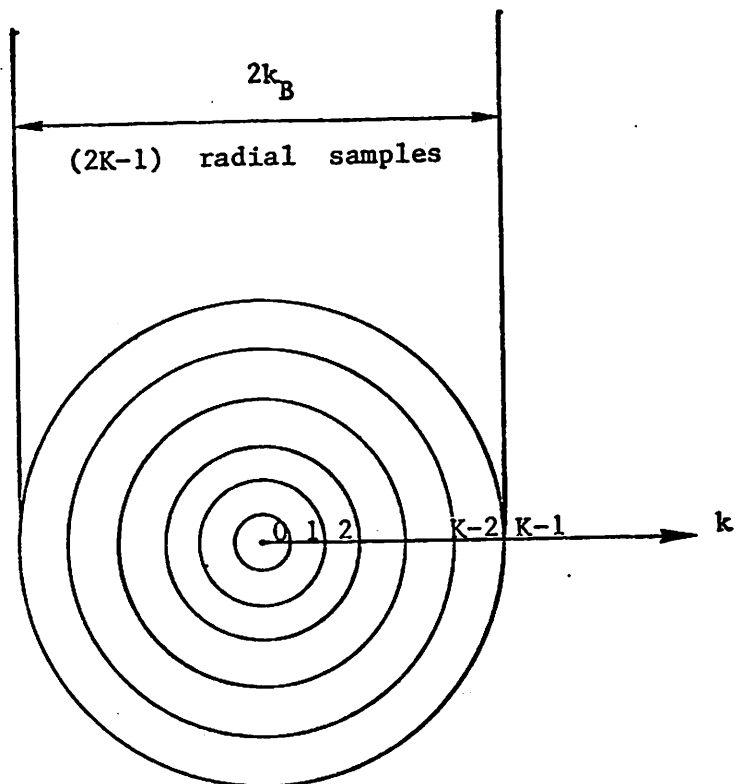
Figure 5.2.2. Fourier Bessel transform of a unit circle and its angular sampling effects.



(b) The Fourier Bessel transform  $g(\rho)$  of the unit circle with angular sampling interval  $2\pi/256$ .



(c) The exact transform  $J_0(2\pi\rho)$  and the independent error terms due to angular sampling.



Radial sampling index  $j=0,1,2,\dots, K-2, K-1$ .

Figure 5.3.1. Full disc pupil function, discrete in radial dimension but continuous in angular dimension.

where  $\Delta k = k_B / K-1$ . Since this is an isotropic function, the point spread function is also an isotropic function given by

$$\begin{aligned} g(\rho) &= \mathcal{B}\{G(k)\} \\ &= 2\pi \int_0^\infty k G(k) J_0(2\pi k \rho) dk \\ &= \left\{ \begin{aligned} &2\pi \Delta k \sum_{j=0}^{K-1} j J_0\left(\frac{2\pi}{K-1} k_B \rho j\right) \quad \text{or} \quad (5.3.2) \\ &\pi \Delta k \sum_{j=-K+1}^{K-1} |j| J_0\left(\frac{2\pi}{K-1} k_B \rho j\right) \quad (5.3.3) \end{aligned} \right. \end{aligned}$$

Here, two forms of the point spread function have been presented because depending on the application one or the other will become more handy to use.

For our purpose, we will use Eq. (5.3.3). Applying Poisson's Summation Formula from section 5.1 in a slightly modified version, it can readily be shown that the PSF of the multi-circle pupil function is

$$\begin{aligned} g(\rho) &= \pi \int_{-k_B}^{k_B} |k| J_0(2\pi \rho k) dk + 2\pi \sum_{n=1}^{\infty} \int_{-k_B}^{k_B} |k| J_0(2\pi \rho k) \cos\left(2\pi \frac{K-1}{k_B} n k\right) dk \\ &\quad + 2\pi k_B J_0(2\pi k_B \rho). \end{aligned} \quad (5.3.4)$$

### The First Term

The first term on the right hand side of Eq. (5.3.4) is the Fourier Bessel transform of a disc pupil of radius  $k_B$  and is given by

$$\pi \int_{-k_B}^{k_B} |k| J_0(2\pi \rho k) dk = k_B \frac{J_1(2\pi k_B \rho)}{\rho} \quad (5.3.5)$$

The first term therefore represents the exact point spread function of the continuous disc pupil.

### The Third Term

The third term represents an additive factor which modifies the main lobe of the exact point spread function of the disc pupil.

### The Second Term

The second term on the right hand side of Eq. (5.3.4) represents a series of nth order "radial sampling clutter" [39]. It is

$$\begin{array}{l} \text{radial} \\ \text{sampling} \\ \text{clutter} \end{array} = \sum_{n=1}^{\infty} e_n(\rho) \quad (5.3.6)$$



where

$$e_n(\rho) = 2\pi \int_{-\infty}^{\infty} [|k| J_0(2\pi\rho k)] [\text{rect}(k/2k_B)] \cos(2\pi \frac{K-1}{k_B} nk) dk \quad (5.3.7)$$

is the  $n$ th order radial sampling clutter. Equation (5.3.7) is a cosine transform and the convolution theorem can be used to study the behavior of  $e_n(\rho)$ . Let

$$\hat{e}_n(\rho, x) = 2\pi \int_{-\infty}^{\infty} |k| J_0(2\pi\rho k) \cos(2\pi x k) dk \quad (5.3.8)$$

and define a convolving function

$$w_1(x) = \int_{-\infty}^{\infty} \text{rect}(k/2k_B) \cos(2\pi x k) dk. \quad (5.3.9)$$

Let us first find  $\hat{e}_n(\rho, x)$ . Equation (5.3.8) can be simplified as

$$e_n(\rho, x) = 4\pi \int_0^{\infty} k J_0(2\pi\rho k) \cos(2\pi x k) dk, \quad (5.3.10)$$

From standard mathematical tables, [Abramowitz, Stegun][1] and a little manipulation, it can be shown that

$$\int_0^{\infty} k J_{\mu}(ak) \cos(bk) dk = \begin{cases} \frac{-a^{\mu} \cos(\frac{\pi}{2}\mu)}{\sqrt{b^2 - a^2} [b + \sqrt{b^2 - a^2}]^{\mu}} \left[ \frac{1}{b^2 - a^2} + \frac{\mu}{b^2 - a^2} \right] & b > a > 0 \\ 0 & 0 \leq b < a \end{cases} \quad (5.3.11)$$

which is not defined for  $b = a$ . By substituting  $\mu = 0$ ,  
 $a = 2\pi\rho$ ,  $b = 2\pi x$ ,

$$\hat{e}_n(\rho, x) = \begin{cases} \frac{1}{2\pi^2} [x^2 - \rho^2]^{-3/2} & x > \rho > 0 \\ 0 & \rho > x \geq 0 \end{cases} \quad (5.3.12)$$

Next,  $w_1(x)$  can be rewritten as

$$w_1(x) = 2k_B \text{sinc}(2k_B x)$$

By the convolution theorem

$$e_n(\rho) = \hat{e}_n(\rho, x) * w_1(x) \Big|_{x = \frac{n(K-1)}{k_B}} \quad (5.3.13)$$

Hence

$$\begin{aligned} e_n(\rho) &= \int_{-\infty}^{\infty} \hat{e}_n(\rho, x) w_1\left(\frac{n(K-1)}{k_B} - x\right) dx \\ &= \frac{k_B}{\pi} \int_{\rho}^{\infty} \left[ \frac{1}{x^2 - \rho^2} \right]^{3/2} \text{sinc}\left(2k_B \left(\frac{n(K-1)}{k_B} - x\right)\right) dx \quad \forall \rho > 0. \end{aligned} \quad (5.3.14)$$

$w_1\left(\frac{n(K-1)}{k_B} - x\right)$  peaks at  $x = \frac{n(K-1)}{k_B}$  while  $\hat{e}_n(\rho, x)$  blows up at  $x = \rho$ . Since  $\rho$  is a moving parameter, we will expect  $e_n(\rho)$  to peak at or near  $\rho = \frac{n(K-1)}{k_B}$  at which point the area of

overlap is maximal. The convolution process is illustrated in Fig. 5.3.2.

### B. Over Annula Ring Pupil Function

Suppose the annula ring pupil is discretely sampled in the radial dimension as shown in Fig. 5.3.3. Since the derivation of  $\hat{e}_n(\rho, x)$  is independent of the pupil function,  $\hat{e}_n(\rho, x)$  stays the same for the annula ring. But the convolving function is instead, the sum of the F.T. of two rectangular functions displaced by  $+k_0$ ,  $-k_0$ , from the origin. It is

$$\begin{aligned} w_2(x) &= \mathfrak{F}\left\{\text{rect}\left(\frac{k-k_0}{k_B}\right) + \text{rect}\left(\frac{k+k_0}{k_B}\right)\right\} \\ &= 2k_B \text{sinc}(k_B x) \cos(2\pi k_0 x) \end{aligned} \quad (5.3.15)$$

The nth order clutter for the annula is therefore

$$e_n(\rho) = w_2(x) * \hat{e}_n(\rho, x) \Big|_{x = \frac{n(K-1)}{k_B}}$$

An interesting result from looking at the radial sampling effect on both the full disc pupil and the annula ring (bandpass) pupil is that in both cases the radial sampling clutter becomes significant in the vicinity of  $\rho = \frac{n(K-1)}{k_B}$ . The mean frequency of the annula ring does not play a direct role in determining the position of the

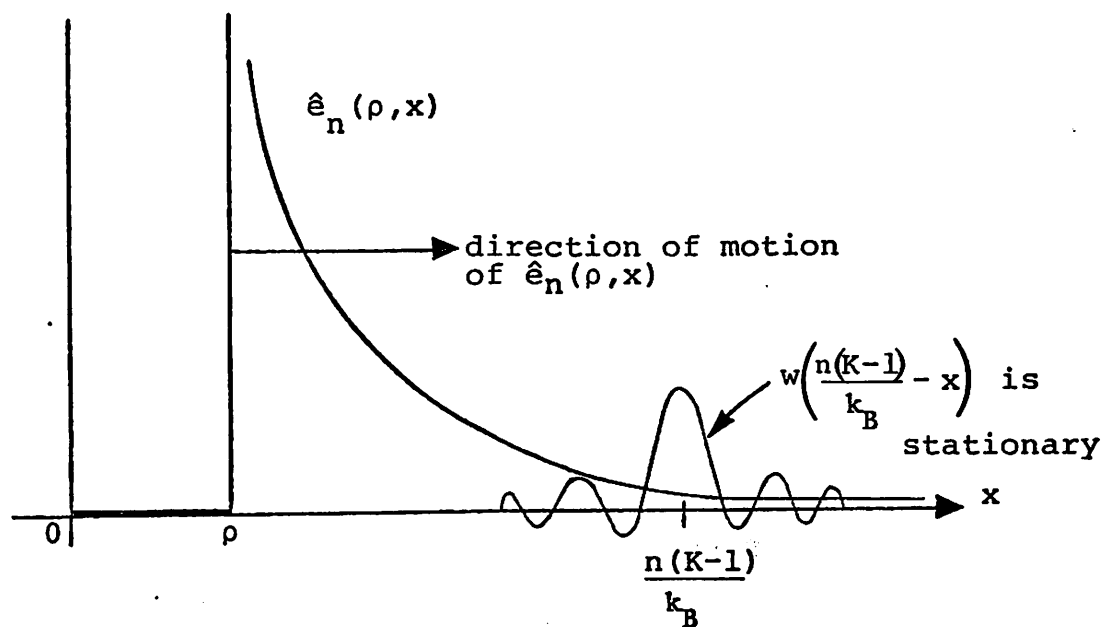


Figure 5.3.2. Convolution of  $\hat{e}_n(\rho, x)$  with  $w\left(\frac{n(K-1)}{k_B} - x\right)$ .

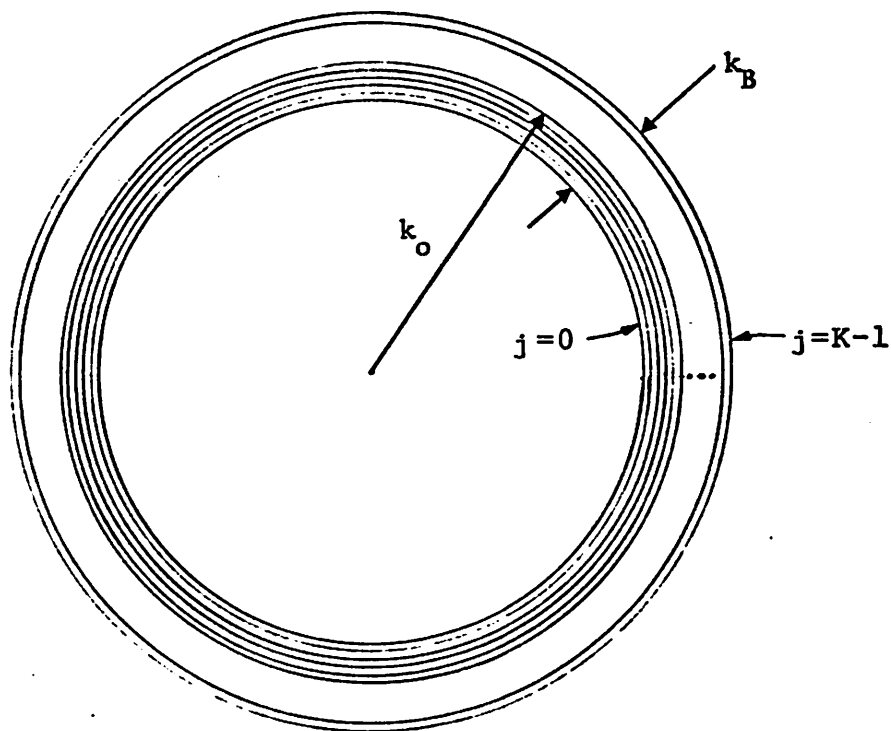


Figure 5.3.3. An annula ring pupil function, discretely sampled in radial dimension, but continuously sampled in angular dimension. ( $K$  radial samples.)

clutter. The minute details of the  $n$ th order clutter in each case will differ since they are determined by their individual convolving function  $w_i(x)$ . The gross behavior of the radial sampling clutters is essentially the same because they share the other common convolving function  $\hat{e}_n(\rho, x)$ .

The above results are illustrated in Fig. 5.3.4. Figure 5.3.4a shows the difference between the exact Fourier Bessel transform and the discrete Fourier Bessel transform of a circular disc pupil, with  $K = 20$ . Figure 5.3.2b shows the 1st order radial sampling clutter with a peak of 0.0875 at  $\rho = 19.27 \approx K-1$ . Figure 5.3.5a shows the exact Fourier Bessel transform of an annula ring with  $k_0 = 10k_B$ . Figure 5.3.5b shows the Fourier Bessel transform of the discrete annula pupil. Figure 5.3.5c is the isolated 1st order radial sampling clutter  $e_1(\rho)$  for the annula ring pupil. Figure 5.3.5d is a blown up view of the first order clutter which peaks with a value of 0.023 at  $\rho = 19.03 \approx K-1$ . Notice the similarities and difference in the 1st order clutters between the two systems.

#### 5.4 Simultaneous Radial and Angular Sampling

In section 5.2 it was shown that the Fourier Bessel transforms of the angular sampled circle and continuous

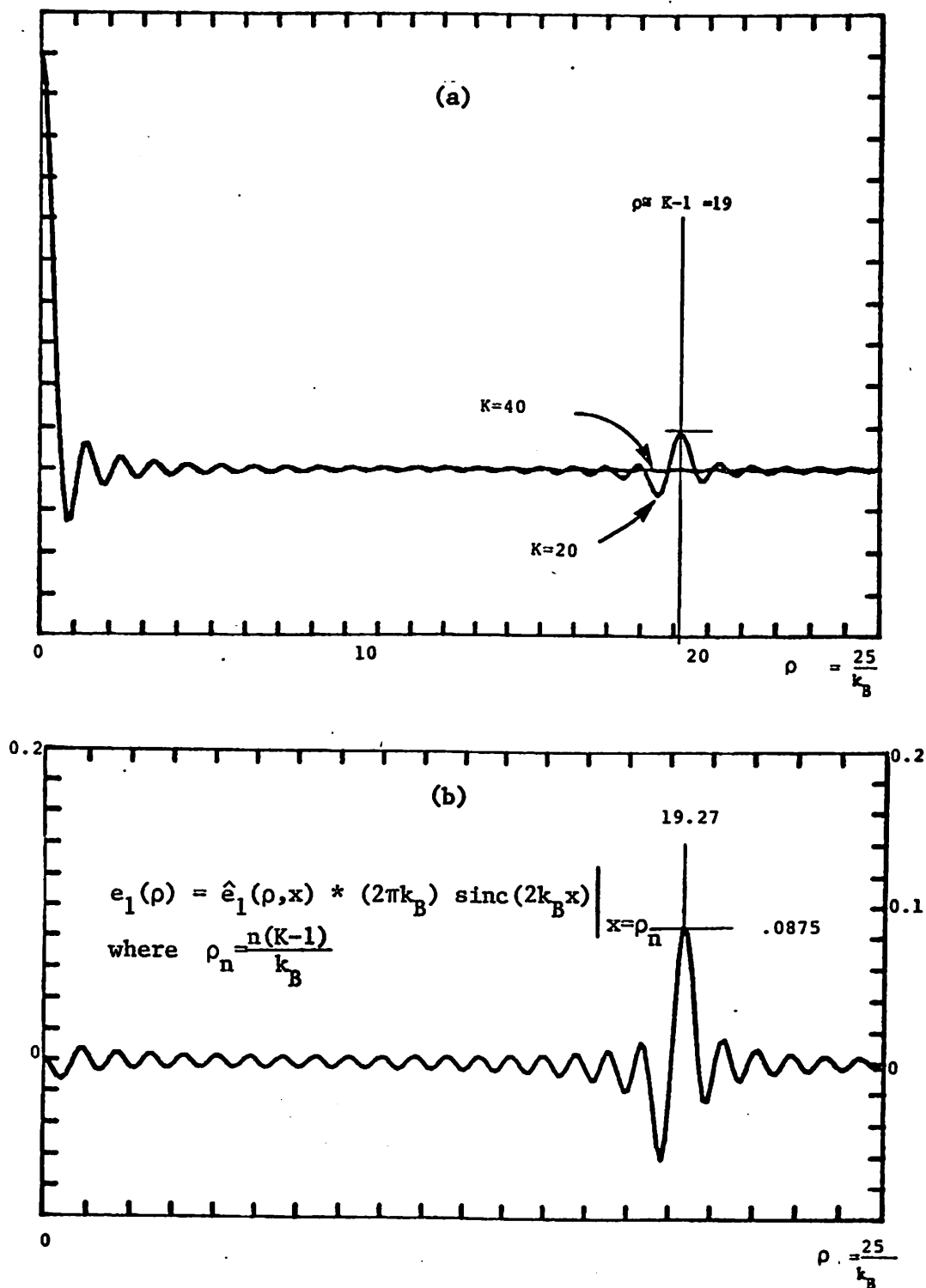


Figure 5.3.4. Fourier Bessel transform of a radially sampled disc function and its sampling effect. (a) Transform of the disc pupil function of radius  $k_B$ , with  $K=20$  and  $K=40$ . (Over the range of  $\rho$  shown in the graph, the curve for  $K=40$  can be taken as the exact transform.) (b) The first order radial sampling clutter term.

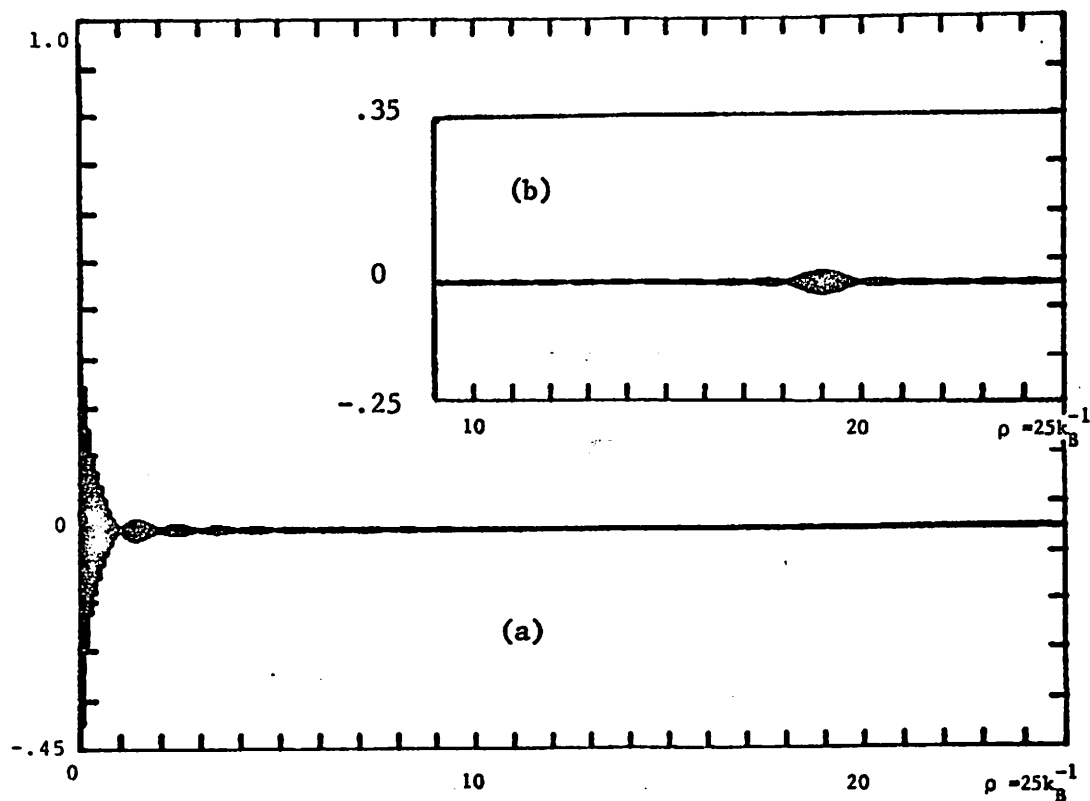
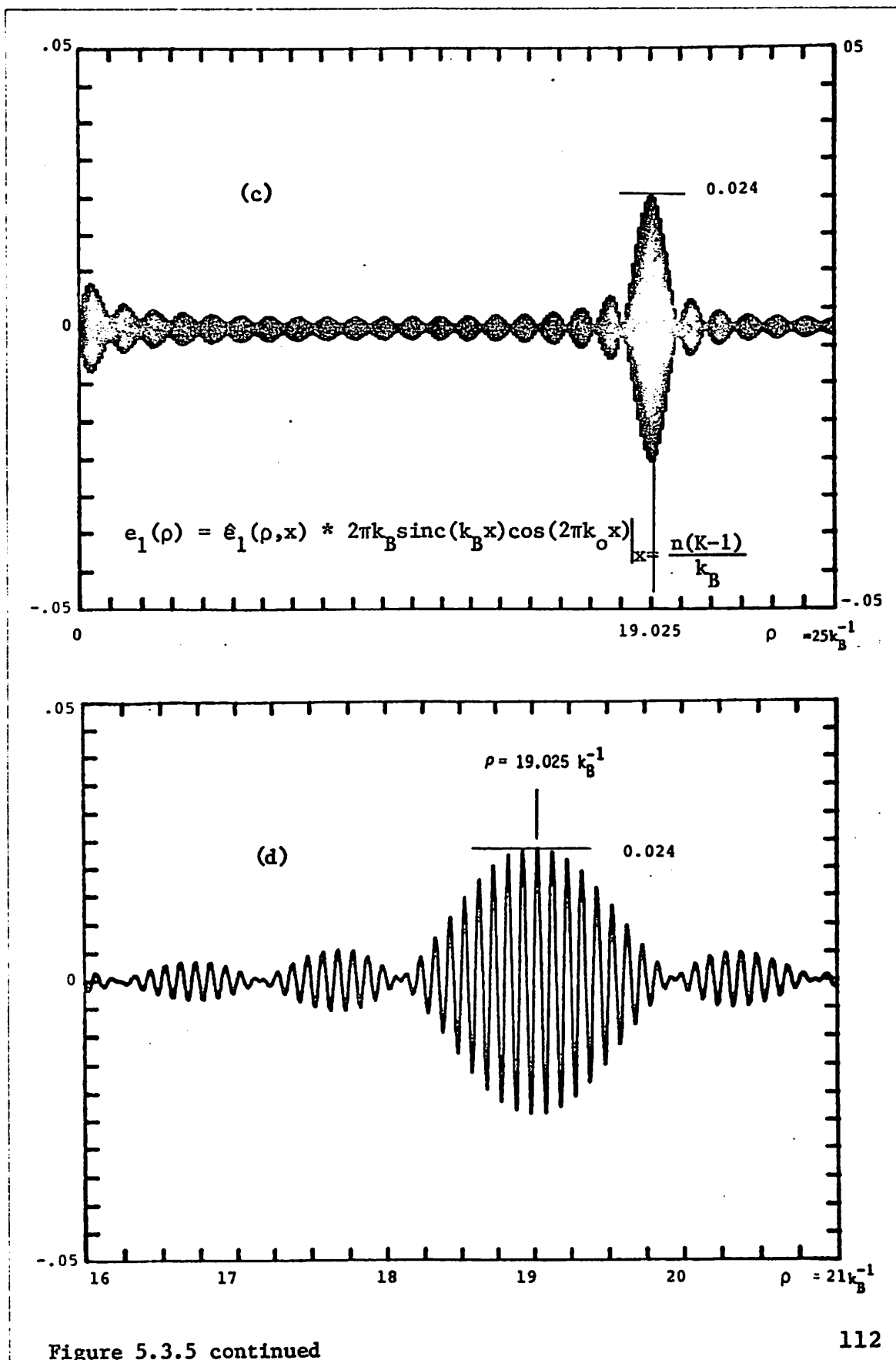


Figure 5.3.5. Fourier Bessel transform of a radially sampled annula ring pupil function ( $k = 10k_B$ ). (a) With  $K=35$ , over the range of  $\rho$  shown on the graph, it closely approximates the transform of the continuously sampled pupil function. (b) With  $K=20$ , the first order clutter occurs at approximately  $\rho \approx K-1 = 19$ . (c), (d) Finer details of the first order clutter. (Note the difference between  $e_1(\rho)$  here and the  $e_1(\rho)$  in Fig. 5.3.4b.)





circle were related by the following equation.

$$\frac{1}{N} \sum_{i=0}^{N-1} e^{j2\pi\rho\cos(\frac{2\pi}{N}i)} = J_0(2\pi\rho) + \sum_{n=1}^{\infty} (-1)^{\frac{N}{2}n} J_{nN}(2\pi\rho).$$

Let

$$G(k) = \frac{2\pi k}{N} \sum_{i=0}^{N-1} e^{j2\pi k\rho\cos(\frac{2\pi}{N}i)}.$$

Then

$$G(k) 2\pi k J_0(2\pi\rho k) + 2\pi k \sum_{n=1}^{\infty} (-1)^{\frac{N}{2}n} J_{nN}(2\pi\rho k) \quad (5.4.1)$$

and the PSF corresponding to the both radially and angularly sampled discrete pupil as shown in Fig. 5.4.1 is

$$g(\rho) = \frac{k_B}{K-1} \sum_{j=0}^{K-1} G(k_j) \quad (5.4.2)$$

where  $k_j = k_{\min} + j\Delta k$ ,  $\Delta k = k_B/(K-1)$ .  $k_{\min} = 0$  for full the disc pupil, and  $k_{\min} > 0$  for the annula ring pupil.  $G(k)$  can be split up into two terms. In particular

$$G(k) = G_1(k) + G_2(k)$$

where

$$G_1(k) \triangleq 2\pi k J_0(2\pi\rho k)$$

and

$$G_2(k) \triangleq 2\pi k \sum_{n=1}^{\infty} (-1)^{\frac{N}{2}n} J_{nN}(2\pi\rho k). \quad (5.4.3)$$

$G_2(k)$  is the clutter due to angular sampling called angular clutter.

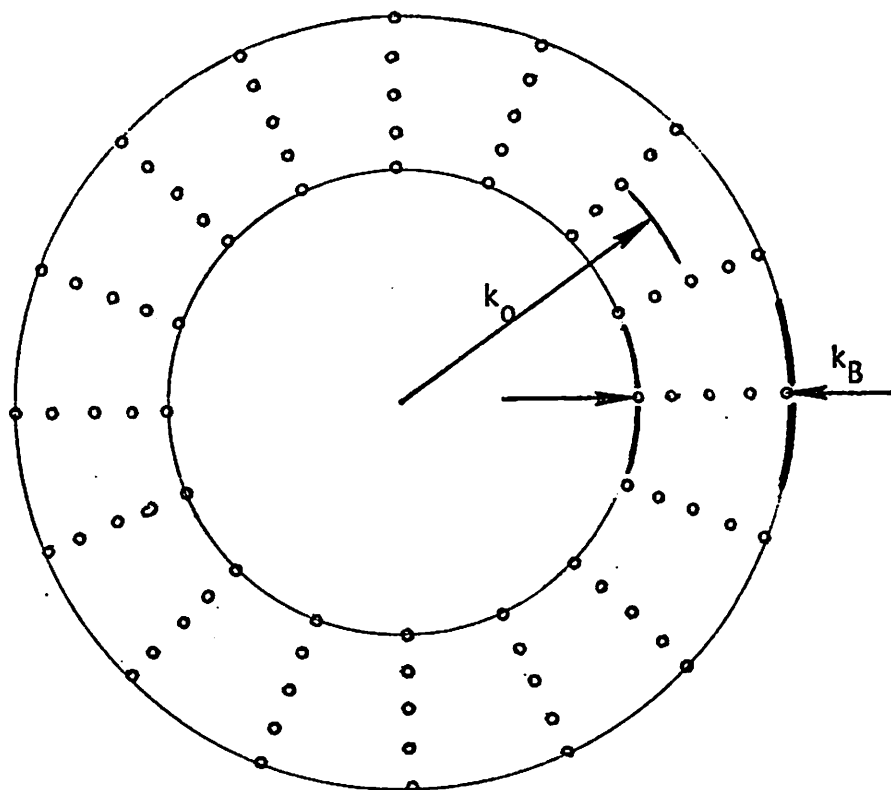


Figure 5.4.1. Polar format sampling in both radial and angular dimensions.

### A. Full Disc Pupil

$k_{\min} = 0, k_{\max} = k_B$ . The continuous system will give a PSF

$$g_c(\rho) = \int_0^{k_B} G(k) dk.$$

However, with discrete radial sampling, only the discrete PSF is available which is given by

$$\begin{aligned} g(\rho) &= \frac{k_B}{K-1} \sum_{j=0}^{K-1} G(k_j) \\ &= \frac{k_B}{K-1} \sum_{j=0}^{K-1} G_1(k_j) + \frac{k_B}{K-1} \sum_{j=0}^{K-1} G_2(k_j) \end{aligned} \quad (5.4.4)$$

Using Poisson's Summation Formula on  $G_1(k)$ ,

$$\begin{aligned} \frac{k_B}{K-1} \sum_{j=0}^{K-1} G_1(k_j) &= \int_0^{k_B} G_1(k) dk + 2 \sum_{m_1=1}^{\infty} \int_0^{k_B} G_1(k) \cos\left(\frac{2\pi}{\Delta k} m_1 k\right) dk \\ &\quad - \frac{k_B}{2(K-1)} G_1(k_B) \end{aligned} \quad (5.4.5)$$

The first term on the right side of Eq. (5.4.5) is

$$\begin{aligned} \int_0^{k_B} G_1(k) dk &= 2\pi \int_0^{k_B} k J_0(2\pi \rho k) dk \\ &= k_B \frac{J_1(2\pi k_B \rho)}{\rho} \end{aligned} \quad (5.4.6)$$

which is the exact PSF desired.

The second term on the right hand side of Eq. (5.4.5) is

$$\sum_{m_1=1}^{\infty} e_{m_1}(\rho) = 2 \sum_{m_1=1}^{\infty} \int_0^{k_B} G_1(k) \cos\left(\frac{2\pi}{\Delta k} m_1 k\right) dk \quad (5.4.7)$$

where upon simplification,

$$e_{m_1}(\rho) = 4\pi \int_0^{k_B} k J_0(2\pi \rho k) \cos\left(\frac{2\pi}{\Delta k} m_1 k\right) dk.$$

From Eqs. (5.3.7), (5.3.9), and (5.3.10), one can identify  $e_{m_1}(\rho)$  as the  $m_1^{\text{th}}$  order error corresponding to the error associated with radial sampling alone, as in Eq. (5.3.7). This term is therefore the clutter of the discrete system due solely to radial sampling alone. We will call this the "system radial sampling clutter."

The third term on the right hand side of Eq. (5.4.5) is

$$-\frac{k_B}{2(K-1)} G_1(k_B) = -\frac{\pi k_B^2}{K-1} J_0(2\pi k_B \rho)$$

which is the residual error term. This term does not introduce any clutter. It only modifies the exact PSF of the system.

Next, using Poisson's Summation Formula again on  $G_2(k)$ ,

$$\begin{aligned} & \frac{k_B}{K-1} \sum_{j=0}^{K-1} G_2(k_j) \\ &= \int_0^{k_B} G_2(k) dk + 2 \sum_{m_2=0}^{\infty} \int_0^{k_B} G_2(k) \cos\left(\frac{2\pi}{\Delta k} m_2 k\right) dk, \end{aligned} \quad (5.4.8)$$

In the same manner as with the function  $G_1(k)$ , the terms on the right hand side of Eq. (5.4.8) will be studied individually.

1st Term on the Right Hand Side of Equation (5.4.8)

Since  $G_2(k)$  is a linear sum of  $n$ th order angular clutter terms, the first term on the right hand side of Eq. (5.4.8) is the clutter of the system, due purely to discrete angular sampling alone; this is called the "system angular sampling clutter," and is equal to

$$\sum_{n=1}^{\infty} A_n(\rho) = \int_0^{k_B} G_2(k) dk \quad (5.4.9)$$

where

$$A_n(\rho) = (-1)^{\frac{1}{2}nN} \int_0^{k_B} k J_{nN}(2\pi\rho k) dk. \quad (5.4.10)$$

The  $n$ th order angular clutter term  $A_n(\rho)$  is insignificant for small  $\rho$  ( $|\rho| < 1/k_B$ ) because the linear summation should approximate the continuous integral well for small  $\rho$ . We know that  $J_{nN}(2\pi\rho k)$  is negligibly small for  $\rho \geq 0$  until  $2\pi\rho k \cong nN$ , i.e. when  $k \cong \frac{nN}{2\pi\rho}$ . However, for  $\rho$  small enough,  $\frac{nN}{2\pi\rho}$  may lie beyond the upper limit  $k_B$  of

the integral in Eq. (5.4.10), in which case  $A_n(\rho) \approx 0$ . This situation is depicted in the Fig. 5.4.2. Hence,  $A_n(\rho)$  is not significant until approximately

$$\rho = \frac{nN}{2\pi k_B} \quad (5.4.11)$$

and the first significant angular clutter will appear at  $\rho \approx \frac{N}{2\pi k_B}$ .  $A_n(\rho)$  peaks at the 1st zero of  $J_{nN}(2\pi\rho k)$ . If we insist on obtaining an expression for  $A_n(\rho)$  by carrying out the integration in Eq. (5.4.10), it can be shown that

$$A_n(\rho) = (-1)^{nN'} \left(\frac{1}{2}nN\right) \sum_{i'=0}^{\infty} \frac{(nN+1+2i')}{(nN'+1+i')(nN'+1')} \rho J_{nN+1+2i'}(2\pi k_B \rho)$$

by using standard integral tables. This resulting expression also predicts the same behavior of  $A_n(\rho)$  as in expression (5.4.10).

#### 2nd Term on the Right Hand Side of Equation (5.4.8)

The second term of Eq. (5.4.8) is the clutter due to radial and angular sampling simultaneously. It is

$$\sum_{m_2=1}^{\infty} \sum_{n=1}^{\infty} (-1)^{nN'} C_{nm_2}(\rho) \quad (5.4.12)$$

where

$$C_{nm_2}(\rho) = 2 \int_0^{k_B} k J_{nN}(2\pi\rho k) \cos(2\pi(K-1)m_2 k/k_B) dk. \quad (5.4.13)$$

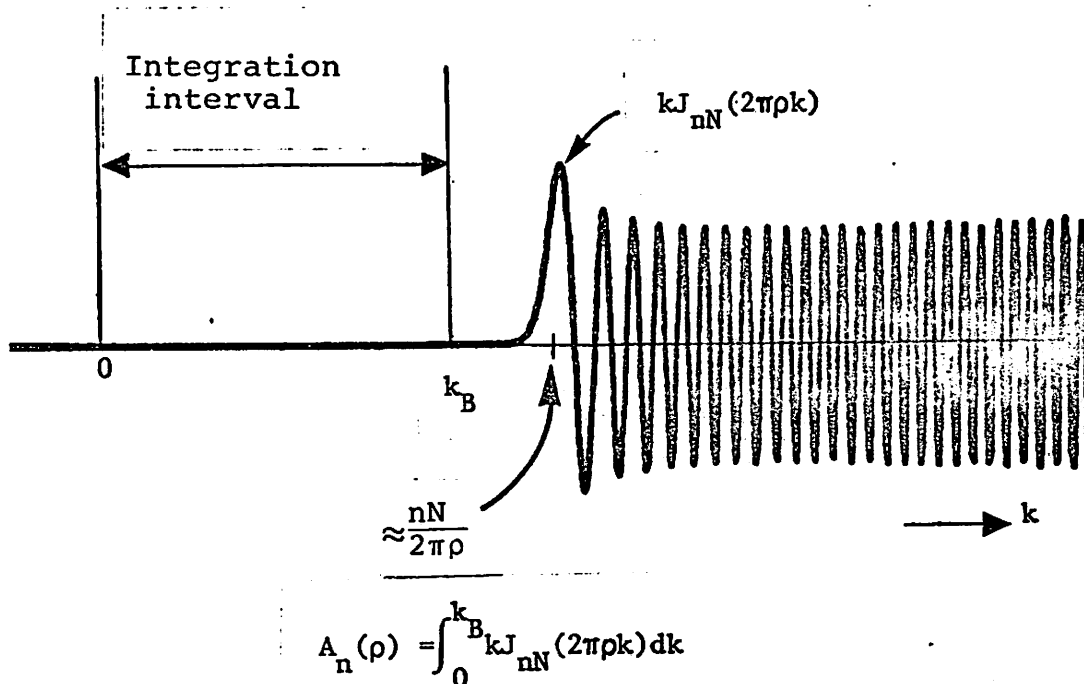


Figure 5.4.2. Integration process for the system angular sampling clutter  $A_n(\rho)$ . (Over the integration interval  $[0, k_B]$ ,  $kJ_{nN}(2\pi\rho k)$  has very little significance until  $k_B \approx \frac{nN}{2\pi\rho}$ . The first peak of  $A_n(\rho)$  occurs at the zero of the integrand  $kJ_{nN}(2\pi\rho k)$ , i.e. when

$$2\pi\rho k_B = nN + 1.86(nN)^{\frac{1}{3}} + 1.03(nN)^{-\frac{1}{3}} + \dots$$

Therefore  $A_n(\rho)$  becomes most significant when  $\rho \approx \rho_n = nN/2\pi k_B$ .)



$n$  corresponds to the  $n$ th order clutter due to angular sampling,  $m_2$  corresponds  $m_2$ th order clutter due to radial sampling. If we follow the same line of development as it was done in section 5.3,  $C_{nm_2}(\rho)$  can be rewritten as

$$C_{nm_2}(\rho) = \int_{-k_B}^{k_B} |k| J_{nN}(2\pi\rho k) \cos(2\pi K m_2 k / k_B) dk.$$

Again  $C_{nm_2}(\rho)$  is a convolution of two functions which are

$$\hat{C}_n(\rho, x) \triangleq \int_{-\infty}^{\infty} |k| J_{nN}(2\pi\rho k) \cos(2\pi x k) dk \quad (5.4.14)$$

and

$$\begin{aligned} w_3(x) &= \int_{-k_B}^{k_B} \cos(2\pi x k) dk \\ &= 2k_B \text{sinc}(2k_B x) \end{aligned} \quad (5.4.15)$$

such that

$$C_{nm_2}(\rho) = \hat{C}_n(\rho, x) * w_3(x) \Big|_{x = \frac{m_2(K-1)}{k_B}} \quad (5.4.16)$$

From Eq. (5.3.11)

$$\hat{C}_n(\rho, x) = \begin{cases} \frac{4}{(2\pi x)^{nN+1}} \frac{1}{\epsilon^2 [1+\epsilon]^{nN}} \left[ \frac{1}{\epsilon} + nN \right] & \text{for } x > \rho > 0 \\ 0 & \text{for } 0 \leq x < \rho \end{cases} \quad (5.4.17)$$

where  $\epsilon = \sqrt{x^2 - \rho^2}$ .

Figure 5.4.3 shows a plot of  $\hat{C}_n(\rho, x)$  for  $\rho = 0.1$ ,  $n = 1$  and for  $N = 0, 2, 4, 6, 8, 10$  and 100. Values of larger values of  $N$  cannot be computed on the computer (DEC 10) without arithmetic overflow. But one can see that it does not take  $N$  to be too large before  $\hat{C}_n(\rho, x)$  approaches to a delta function. Since for most polar coordinate sampling,  $N$  is in the order of at least  $10^2$ ,  $\hat{C}_n(\rho, x)$  is essentially a delta function given by

$$\hat{C}_n(\rho, x) \cong A_n \delta(\rho - x)$$

where  $A_n$  is some appropriate magnitude. Hence

$$\hat{C}_{nm_2}(\rho) \cong 4A_n k_B^2 \text{sinc} \left[ 2k_B \left( \rho - \frac{m_2(K-1)}{k_B} \right) \right]. \quad (5.4.18)$$

Now we can finally say this. By observing the limit of integration in Eq. (5.4.13),  $C_{nm_2}(\rho)$  cannot become significant until

$$\rho \cong \frac{N}{2\pi} k_B^{-1} \quad \text{for } n=1.$$

By observing Eq. (5.4.18),  $C_{nm_2}(\rho)$  cannot become significant until

$$\rho \cong (K-1)k_B^{-1} \quad \text{for } m_2=1.$$

Therefore, the simultaneous sampling clutter  $C_{nm_2}$  first becomes significant at

$$\rho \cong \text{Min} \left\{ \frac{N}{2\pi} k_B^{-1}, (K-1)k_B^{-1} \right\}.$$

This means that by considering the system radial sampling

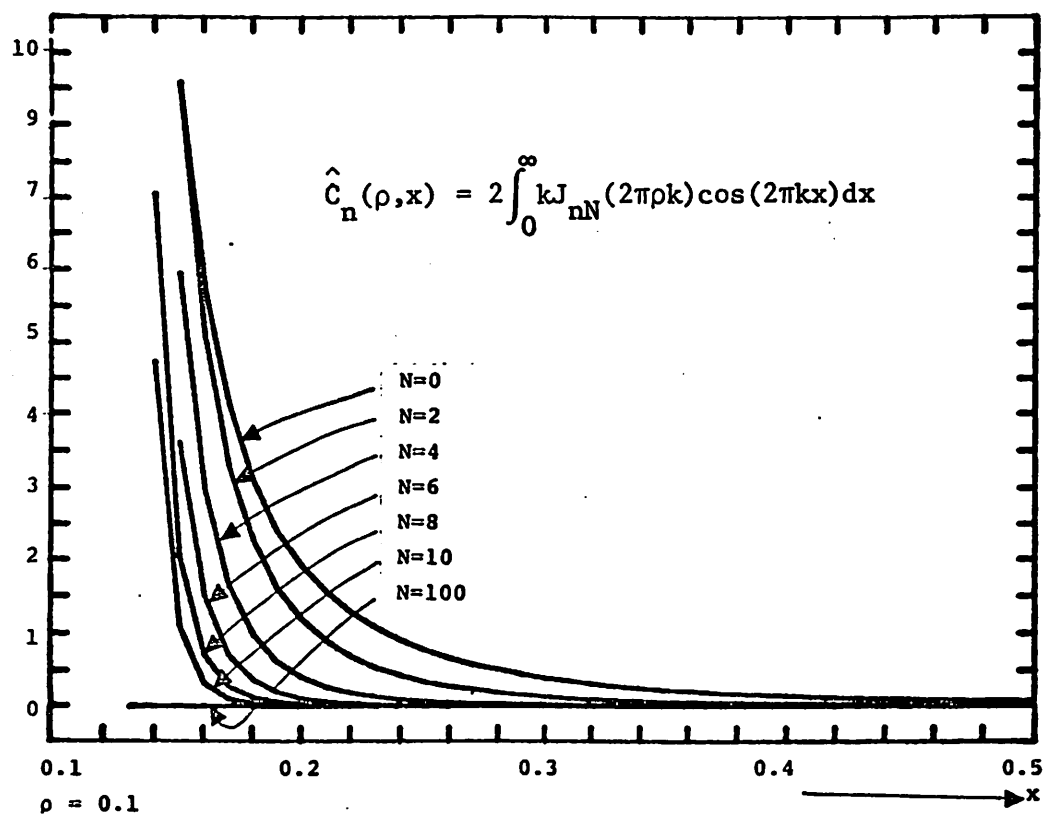


Figure 5.4.3. Plot of  $\hat{C}_n(\rho, x)$  for  $n=1$ ,  $N=0, 2, 4, 6, 8, 10, 100$ , and  $\rho = 0.1$ .

clutter of Eq. (5.4.7) and system angular sampling clutter of Eq. (5.4.10) independently, we will not have to worry about the simultaneous sampling clutter  $C_{nm_2}$ , unless  $\frac{N}{2\pi} = K-1$ . When this happens the three component clutters will be superimposed on top of each other around  $\rho \approx \frac{N}{2\pi} k_B^{-1} = (K-1)k_B^{-1}$  and their sum will determine the clutter level.

In short, the discrete sampling of a full disc pupil function in both the radial and angular dimensions gives a PSF which is a composite sum of 5 terms one of which being the exact PSF of the continuous pupil function. The 5 terms can be listed as follows.

1. Exact PSF:  $k_B \frac{J_1(2\pi k_B \rho)}{\rho}$

2. System radial sampling clutter:  $\sum_{m=1}^{\infty} e_m(\rho)$

where

$$e_m(\rho) = 4\pi \int_0^{k_B} k J_0(2\pi \rho k) \cos\left(\frac{2\pi}{\Delta k} mk\right) dk.$$

3. System angular sampling clutter:  $\sum_{n=1}^{\infty} A_n(\rho)$

where

$$A_n(\rho) = (-1)^{\frac{1}{2}nN} \int_0^{k_B} k J_{nN}(2\pi \rho k) dk.$$

4. Joint radial/angular sampling clutter:

$$\sum_{m=1}^{\infty} \sum_{n=1}^{\infty} (-1)^{nN'} C_{nm}(\rho)$$

$$\text{where } C_{nm}(\rho) = 2 \int_0^{k_B} k J_{nN}(2\pi \rho k) \cos(2\pi (K-1)mk/k_B) dk,$$

$$= \hat{C}_n(\rho, x) * w_1(x) \Big|_{x=m(K-1)/k_B}$$

$$W_1(x) = 2k_B \sin c(2k_B x)$$

$\hat{C}_n(\rho, x)$  is defined by Eq. (5.4.17).

$$N' = \frac{1}{2} N.$$

5. Residual error term:  $-\frac{\pi k_B^2}{K-1} J_0(2\pi k_B \rho).$

#### B. Annula Ring Pupil

$$k_{\min} \neq 0, \quad k_{\max} = k_{\min} + k_B$$

Using the above constraints on  $k$  and starting from Eqs. (5.4.2) and (5.4.3), one can go through the same derivations as in section 5.4A and obtain the following five components of the Fourier Bessel transform of the discrete annula ring pupil.

##### 1. Exact Fourier Bessel transform component:

$$k_{\max} \frac{J_1(2\pi k_{\max} \rho)}{\rho} - k_{\min} \frac{J_1(2\pi k_{\min} \rho)}{\rho}$$

##### 2. System radial sampling clutter (same as in section 5.3B):

$$\sum_{m_1=1}^{\infty} e_{m_1}(\rho)$$

where

$$e_{m_1}(\rho) = \hat{e}_{m_1}(\rho, x) * w_2(x) \Big|_{x = \frac{m_1(K-1)}{k_B}}$$

$$\hat{e}_{m_1}(\rho, x) = \begin{cases} \frac{1}{2\pi^2} [x^2 - \rho^2]^{-3/2} & x > \rho > 0 \\ 0 & \rho > x \geq 0 \end{cases}$$

$$w_2(x) = 2k_B \text{sinc}(k_B x) \cos(2\pi k_0 x).$$

This component is plotted in Figs. 5.3.5b and c.

3. System angular sampling clutter (same as in disc pupil):

$$\sum_{n=1} A_n(\rho)$$

where

$$A_n(\rho) = (-1)^{nN'} \int_{k_0 - \frac{1}{2}k_B}^{k_0 + \frac{1}{2}k_B} k J_{nN}(2\pi \rho k) dk.$$

This component is considerably different from the full disc case in section 5.4A. In particular, the integration interval here is centered at  $k_0$ . This is illustrated in Fig. 5.4.4. Again since  $k J_{nN}(2\pi \rho k)$  first peaks at approximately

$$k = \frac{nN}{2\pi\rho}.$$

$A_n(\rho)$  does not become significant until

$$k_0 + \frac{1}{2} k_B \approx \frac{nN}{2\pi\rho}.$$

4. Joint radial and angular sampling clutter

$$\sum_{m_2=1} \sum_{n=1} (-1)^{nN'} C_{nm_2}(\rho)$$

where

$$C_{nm_2}(\rho) = \hat{C}_n(\rho, x) * w_2(x) \Big|_{x = \frac{(K-1)m_2}{k_B}}$$

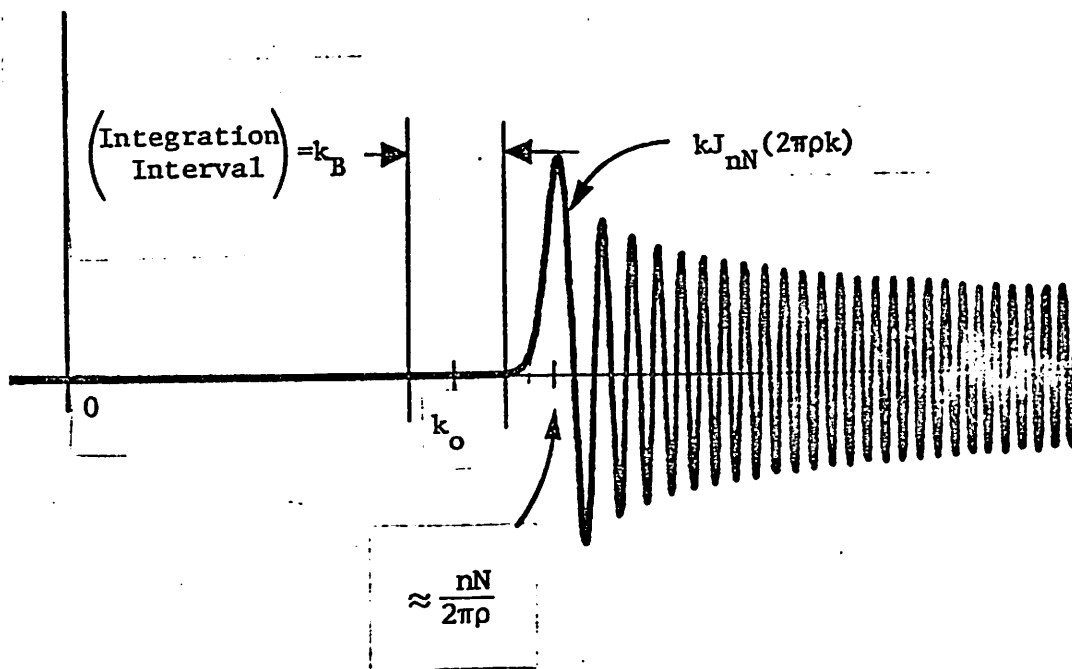


Figure 5.4.4. Integration interval for the annula ring case.

$$w_2(x) = 2k_B \text{sinc}(k_B x) \cos(2\pi k_0 x).$$

Again like in the case of the disc pupil,  $C_{nm_2}(\rho)$  does not become significant until

$$\rho \approx \text{Min} \left\{ \frac{N}{2} (k_0 + \frac{1}{2} k_B)^{-1}, (K-1) k_B^{-1} \right\}.$$

#### 5. Residual error term

$$\frac{\pi}{K-1} \left[ k_{\max}^2 J_0(2\pi k_{\max} \rho) - k_{\min}^2 J_0(2\pi k_{\min} \rho) \right]$$

The most important contrast between the disc and annula ring case is on the angular sampling clutter term  $A_n(\rho)$  and on the convolving functions  $w_1(x)$  and  $w_2(x)$  for the radial sampling clutter  $e_{m_1}(\rho)$ . For the disc case  $A_n(\rho)$  is insignificant until  $\rho \approx \frac{N}{2\pi} k_B^{-1}$  while for the annula ring case  $A_n(\rho)$  is insignificant until  $\rho \approx \frac{N}{2\pi} (k_0 + \frac{1}{2} k_B)^{-1}$ .  $w_1(x)$  for the disc pupil is  $1/2k_B$  "wide" but  $w_2(x)$  for the annula ring pupil is  $1/k_B$  "wide" and is modulated by a sinusoid of frequency  $k_0$ . Other than this, the two systems have essentially the same general features. For convenience of reference, Table 5.4.1 shows the components of the Fourier Bessel transform of the two discrete pupil functions.

#### 5.5 Conclusion

We have found exact analytic expressions for the artifacts that are generated by Fourier transforming a



Table 5.4.1 The Five Components of the Fourier Bessel Transform of the Discrete Pupil Function

	Disc Pupil	Annula Ring Pupil
Exact Transform	$k_B \frac{J_1(2\pi k_B \rho)}{\rho}$	$k_{\max} \frac{J_1(2\pi k_{\max} \rho)}{\rho} - k_{\min} \frac{J_1(2\pi k_{\min} \rho)}{\rho}$
$m^{\text{th}}$ order ( $m \neq 0$ ) Radial Sampling Clutter	$e_m(\rho) = \hat{e}_m(\rho, x) * w_1(x) \mid x = m(K-1)/k_B$	$e_m(\rho) = \hat{e}_m(\rho, x) * w_2(x) \mid x = m(K-1)/k_B$
$w_1(x)$	$w_1(x) = 2k_B \text{sinc}(2k_B x)$	$w_2(x) = 2\pi k_B \text{sinc}(k_B x) \cos(2\pi k_0 x)$
$\hat{e}_m(\rho, x)$	$\hat{e}_m(\rho, x) = \begin{cases} \frac{1}{2\pi^2} [x^2 - \rho^2]^{-3/2} & x > \rho > 0 \\ 0 & \rho > x \geq 0 \end{cases}$	
$e_m(\rho)$ is significant at	$\rho \approx (K-1)k_B^{-1}$	$\rho \approx (K-1)k_B^{-1}$
$n^{\text{th}}$ order ( $n \neq 0$ ) Angular Sampling Clutter	$A_n(\rho) = (-1)^{nN} \int_0^k k J_{nN}(2\pi \rho k) dk$	$A_n(\rho) = (-1)^{nN} \int_{k_{\min}}^k k J_{nN}(2\pi \rho k) dk$
$A_n(\rho)$ is significant at	$\rho \approx \frac{N}{2\pi} k_B^{-1}$	$\rho \approx \frac{N}{2\pi} (k_0 + \frac{1}{2}k_B)^{-1}$
Joint Sampling Clutter	$C_{nm}(\rho) = \hat{e}_n(\rho, x) * w_1(x) \mid x = m(K-1)/k_B$	$C_{nm}(\rho) = \hat{e}_n(\rho, x) * w_2(x) \mid x = m(K-1)/k_B$
$m^{\text{th}}$ order radial $n^{\text{th}}$ order angular ( $n \neq 0, m \neq 0$ )	$\hat{e}_n(\rho, x) = \begin{cases} \frac{4}{(2\pi x)^{nN+1}} \cdot \frac{1}{\epsilon^{2(1+\epsilon)}} \cdot \frac{1}{nN} \cdot \left[ \frac{1}{\epsilon} + nN \right] & \text{for } x > \rho > 0 \\ 0 & \text{for } \rho > x \geq 0 \end{cases}$ $\epsilon = \sqrt{x^2 - \rho^2}$	
Residual Sampling error	$\frac{\pi}{K-1} k_B^2 J_0(2\pi k_B \rho)$	$\frac{\pi}{K-1} \left[ k_{\max}^2 J_0(2\pi k_{\max} \rho) - k_{\min}^2 J_0(2\pi k_{\min} \rho) \right]$

polar coordinate sampled disc and annula ring pupil functions. This Fourier transform is therefore the point spread function of the corresponding imaging system which collects discrete samples of data in the Fourier transform domain. We have called these artifacts as clutters. The clutter terms can in general be put into three categories, viz.

1. Radial sampling clutter
2. Angular sampling clutter
3. Simultaneous sampling clutter

It turns out that the simultaneous sampling clutter does not become significant before either the radial sampling clutter or the angular sampling clutter does. A special case arises when

$$\begin{array}{ll}
 N = 2\pi(K-1) & \text{for disc pupil and} \\
 N = 2\pi(K-1)(k_0 + \frac{1}{2}k_B)/k_B & \text{for annula ring pupil}
 \end{array}$$

in which case all three components become significant simultaneously and henceforth their summation (joint clutter) must be considered. Otherwise, the radial and the angular sampling clutter can be considered independently.

Using the analytic expressions obtained for the clutters one can choose  $N$  and/or  $K$  exactly, given the

level of clutter that can be tolerated and the maximum diameter of the spatial region of interest. It is also found that both radial and angular sampling create artifacts that are isotropic in nature.

Finally, it is expected that a sampling theorem can be arrived at for polar coordinate sampling by extending the analysis to general 2-dimensional objects. It is also noted that if the first and the last radial sample is weighted by 0.5 in the (discrete) summations with respect to index  $j$ , the residual sampling error term will disappear.

## Chapter 6

### RECONSTRUCTION METHODS

In Chapter 2 it was shown that the signal data  $D(\theta, k)$  represented the two dimensional Fourier transform  $Z(\theta, k)$  of the target "reflectivity" function  $\sigma(\xi, \eta)$  if the target points were visible over the complete set of aspect angles (i.e. no shadowing) and if  $\sigma(\xi, \eta)$  was constant over the entire range of aspect angles of interest (i.e. no "reflectivity" change.) Reflectivity change problem will be considered as perturbation from the ideal situation, and will be considered later. Our reconstruction algorithms will be based on the above assumptions and result. Some more important assumptions are that the target rotation rate and the range of its center of rotation are known exactly. These may be unrealistic, but corrections can be made. Such corrections belong to the realm of motion compensation. Also, the collected data is narrowband in nature.

Reconstruction algorithms based on the above assumptions have been proposed but none seem to make use of the full potential resolution digitally. The optical

implementation of the high resolution reconstruction problem was achieved by J.L. Walker [37] by recording the data on a film in what is called the polar format. Here we are concerned with digital reconstruction and the problems associated with it.

The basic problem of reconstructing rotating targets is that of implementing the discrete version of the inverse transform relationship

$$\sigma(x,y) = \int_0^{2\pi} \int_{k_{\min}}^{k_{\max}} kD(\theta,k) e^{-j2\pi k(x\cos\theta+y\sin\theta)} dk d\theta. \quad (6.0.1)$$

Here we have implicitly assumed that  $360^\circ$  of data were available. The amount of data involved is usually so large that it poses a formidable computational and storage problem. Moreover, in practice the data is discretely sampled in azimuth and range, so that some form of interpolation will be needed somewhere in the reconstruction algorithm; for complex data, this becomes a difficult problem.

Radar reconstruction techniques for rotating targets can be classified as coherent processing, incoherent processing, and mixed processing. The way these are described here can be applied to both optical and digital processing, even though some aspects of the techniques may

be more difficult to implement optically than digitally.

### 6.1 Coherent Processing

Suppose we are given the target data  $D(\theta, k)$  for aspect angles within the range  $[\theta_{\min}, \theta_{\max}]$  over the spatial frequency  $[k_{\min}, k_{\max}]$ .

The reconstruction algorithm that makes use of the full Doppler frequency extent available in the data is called coherent processing. In effect, this means that the target reflectivity function is computed by the approximation

$$\sigma(\xi, \eta) = \int_{\theta_{\min}}^{\theta_{\max}} \int_{k_{\min}}^{k_{\max}} k D(\theta, k) e^{-j2\pi k(\xi \cos \theta + \eta \sin \theta)} dk d\theta. \quad (6.1.1)$$

Coherent processing amounts to implementing this equation in one form or another.

For most angularly symmetrical targets, the Fourier transform relationship is accurate enough to give good reconstructions since there will be minimal amount of shadowing and the target points will show the same reflectivity. J.L. Walker demonstrated this technique optically for either a collection of small point targets or a cylindrical object which is angularly symmetrical on the plane of rotation. For more realistic targets,

artifacts arising from shadowing and changing reflectivity will become significant problems.

The coherent processing technique can be understood if we implement Eq. (6.1.1) by integrating over frequency  $k$  first (range compression), and then contour integrate with respect to azimuth angle  $\theta$ . This was suggested in Chapter 3 as follows.

$$g_{RC}(\theta, \ell) = \int_{-\frac{1}{2}k_B}^{\frac{1}{2}k_B} D(\theta, k-k_0) e^{j2\pi k \ell} dk, \quad (6.1.2)$$

$$\sigma(\xi, \eta) \approx k_0 \int_{\theta_{\min}}^{\theta_{\max}} g_{RC}(\theta, \ell_\theta) e^{-j2\pi k_0 \ell_\theta} d\theta. \quad (6.1.3)$$

Since we integrate  $g_{RC}(\theta, \ell_\theta) \Big|_{\ell_\theta = \xi \cos \theta + \eta \sin \theta}$  over  $[\theta_{\min}, \theta_{\max}]$  to

get the image, the exponential term in Eq. (6.1.3) represents coherent phase compensation on each range compressed data point  $g_{RC}(\theta, \ell_\theta)$  and the entire integral represents what is called azimuth compression. Eqs. (6.1.2) and (6.1.3) together define the target reconstruction algorithm by coherent processing.

The physical interpretation of range compression is well understood [Skolnik][32]. From the signal processing point of view, consider a stationary point target

reflecting a continuous electromagnetic wave of effective spatial frequency  $k(=2/\lambda)$ . At this frequency the phase of the return signal is

$$\phi(k) = 2\pi k\ell \quad (6.1.4a)$$

where  $\ell$  is the distance along the line-of-sight of the point reflector from the antenna. The phase of the echo is a linear function of  $k$  as depicted in Fig. 6.1.1a. If we take  $k$  as a variable and regard  $\ell$  as the "frequency" with respect to that variable, then Fourier transforming the echo signals will give us a "sinc" function which peaks at a "frequency" equal to  $\ell$ ; the point target distance  $\ell$  can now be estimated. This process is called range compression and it is depicted in Fig. 6.1.1(b) which shows the compressed data.

The physical interpretation of azimuth compression as represented in Eq. (6.1.3) can also be understood by noting that after range compression, the azimuth phase  $e^{j\phi(\theta)}$  and hence the Doppler is determined by the mean frequency  $k_0$  and the distance  $\ell_\theta = \ell$ . This azimuth phase is illustrated in Fig. 6.1.2.

$$\phi(\theta) = 2\pi r_0 k_0 - 2\pi k\ell_\theta \quad (6.1.4b)$$

where

$r_0$  = distance between radar antenna and target center



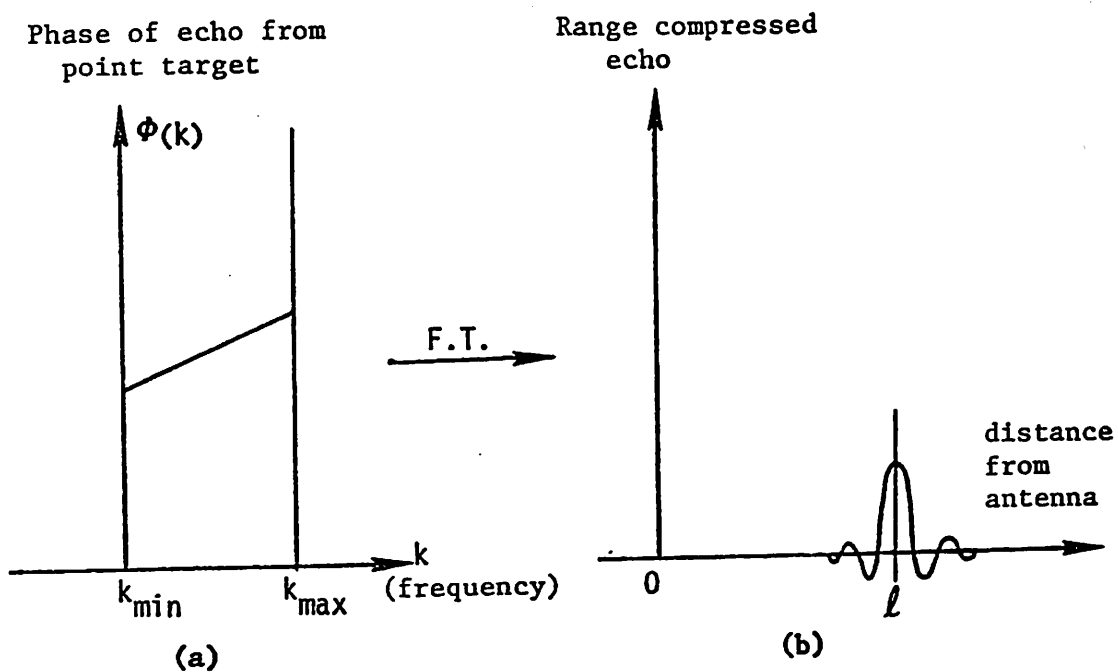


Figure 6.1.1. Range compression for MFS radar.

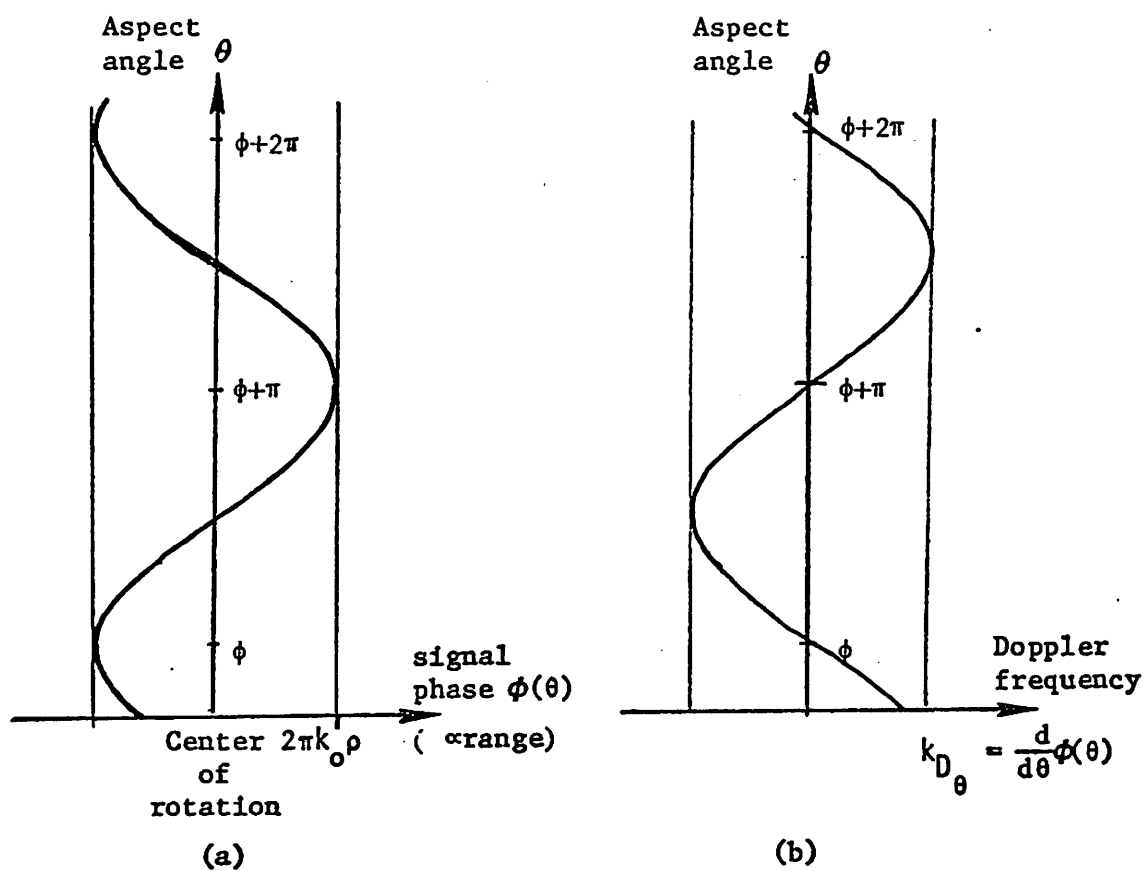


Figure 6.1.2. Phase and Doppler vs. aspect angle for point target at  $(\phi, \rho)$ .

of rotation,

$$l_{\theta} = \xi \cos \theta + \eta \sin \theta .$$

The first term in the phase is constant. The second term is linear in  $l_{\theta}$  but not linear in  $\theta$ , so that the Fourier transformation prescription will not apply. Instead, using a matched filter matched in phase with  $e^{-j\Phi(\theta)}$ , one gets

$$\sigma(\xi, \eta) = \int_{\theta_{\min}}^{\theta_{\max}} g_{RC}(\theta, l_{\theta}) e^{-j\Phi(\theta)} d\theta .$$

By substituting  $\Phi(\theta)$  into the above equation, it will become Eq. (6.1.3) except for a complex constant factor  $k_0 e^{j2\pi r_0 k_0}$

The Doppler time frequency can be obtained from the equation

$$f_D = \frac{d}{dt} \Phi(\theta) = \frac{d\theta}{dt} \frac{d}{dt} \Phi(\theta) = \omega f_{\theta}$$

where

$\omega$  = rate of rotation

$f_{\theta}$  = angular Doppler =  $\frac{d}{dt} \Phi(\theta)$  determined by  $k_0$  and the target coordinates.

In this form it becomes explicitly clear that the Doppler and hence the imaging property come as a result of target rotation.

Equations (6.1.2) and (6.1.3) are difficult to implement digitally because of the large number of computations they demand. Coherent processing can be implemented by segmenting the frequency plane into rectangular (or square) blocks, applying the the FFT on each block and coherently superimposing each block image. Because the data in the frequency plane are sampled in polar coordinates, interpolation will be required before the FFT can be applied. More importantly, most of the blocks will contain empty data. This unnecessarily increases the memory and computational requirement. Also, because the data are collected in azimuth sequence (one signature at a time), memory addressing will become very unwieldy. A different method of implementing coherent processing techniques can be developed.

Suppose we partition the  $[\theta_{\min}, \theta_{\max}]$  azimuth extent of the data into  $N_S$  equal segments of azimuth width  $\theta_W$ . For convenience let  $\theta_{\min} = 0$  and  $\theta_{\max} = 2\pi$ . Then each segment will be

$$\theta_W = \frac{2\pi}{N_S}$$

radians wide. How  $\theta_W$  and hence  $N_S$  are chosen will be mentioned later. Let us define (as illustrated in Fig. 6.1.3a )

$$\theta_n = n\theta_W = \text{Azimuth angle center of the } n^{\text{th}} \text{ segment.}$$

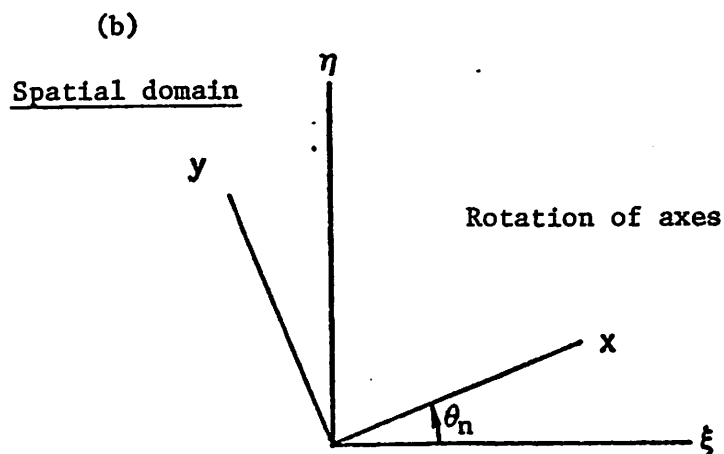
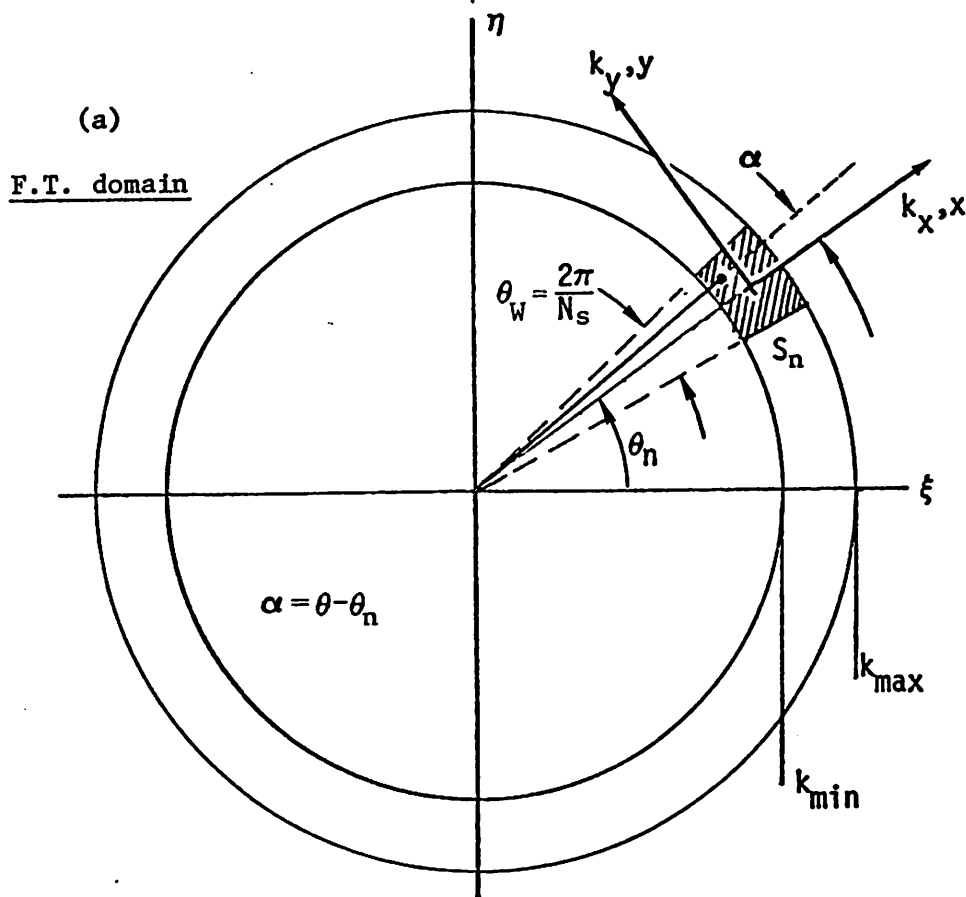


Figure 6.1.3. Angular (azimuth) partitioning of the radar data and the change in variables in coherent processing and mixed processing methods.

$$\alpha = \theta - \theta_n$$

$$S_n = \{(\theta, k) \mid \theta \in [\theta_n - \frac{1}{2}\theta_w, \theta_n + \frac{1}{2}\theta_w], k \in [k_{\min}, k_{\max}]\}.$$

The target reflectivity function from Eq. (6.1.1) is

$$\begin{aligned} \sigma(\xi, \eta) &= \int_0^{2\pi} \int_0^\infty k D(\theta, k) e^{j2\pi k(\xi \cos \theta + \eta \sin \theta)} d\theta dk \\ &= \sum_{n=0}^{N_S-1} \iint_{S_n} k D(\theta, k) e^{j2\pi k(\xi \cos \theta + \eta \sin \theta)} d\theta dk \\ &\approx \sum_{n=0}^{N_S-1} \iint_{S_n} D(\theta, k) e^{j2\pi k(\xi \cos \theta + \eta \sin \theta)} d\theta dk. \end{aligned} \quad (6.1.5)$$

Substitute  $\theta = n\theta_w + \alpha$  and make the following change of variables

$$\begin{aligned} k_x &= k - k_0 \\ k_y &= \alpha k_0 \end{aligned}$$

so that  $\alpha = k_x/k_0$  and  $k_0 d\alpha = dk_y$ . Then

$$D_n(k_x, k_y) = D(\theta, k)$$

where for convenience we have interchanged the variables.

Then

$$\begin{aligned} \sigma(\xi, \eta) &\approx \sum_{n=0}^{N_S-1} \iint_{S_n} D_n(k_x, k_y) \exp \left\{ j2\pi [k_0 + k_x] \right. \\ &\quad \cdot \left[ \xi \cos \left( n\theta_w + \frac{k_y}{k_x} \right) + \eta \sin \left( n\theta_w + \frac{k_y}{k_0} \right) \right] \left. \right\} dk_x dk_y \end{aligned} \quad (6.1.6)$$

$$= \sum_{n=0}^{N_S-1} I_n(\xi, \eta) \quad (6.1.7)$$

where  $I_n(\xi, \eta)$  is the integral in Eq. (6.1.6). By the rotation of axes as in Fig. 6.1.3b.

$$x = \xi \cos(n\theta_W) + \eta \sin(n\theta_W) \quad (6.1.8)$$

$$y = -\xi \sin(n\theta_W) + \eta \cos(n\theta_W)$$

$$I_n(\xi, \eta) = \iint_{S_n} D_n(k_x, k_y) e^{j2\pi(k_0 + k_x) \left[ x \cos\left(\frac{k_y}{k_0}\right) + y \sin\left(\frac{k_y}{k_0}\right) \right]} dk_x dk_y \quad (6.1.9)$$

$I_n(\xi, \eta)$  is the reconstruction from each segment, rotated by  $n\theta_W$ . Suppose  $\theta_W$  is sufficiently small so that one can make the approximations

$$\begin{aligned} \cos\left(\frac{k_y}{k_0}\right) &\approx 1 - \frac{1}{2}\left(\frac{k_y}{k_0}\right)^2 \\ \sin\left(\frac{k_y}{k_0}\right) &\approx \left(\frac{k_y}{k_0}\right) \end{aligned} \quad (6.1.10)$$

on the phase of the kernel in Eq. (6.1.9). Then

$$I_n(\xi, \eta) = \iint_{S_n} D_n(k_x, k_y) e^{j2\pi\phi} dk_x dk_y$$

where

$$\phi \approx xk_x + yk_y + xk_0 + \frac{yk_x k_y}{k_0} - \frac{xk_y^2}{2k_0} - \frac{xk_x k_y^2}{2k_0} \quad (6.1.11)$$

By keeping only the first three terms, one can further approximate  $I_n(\xi, \eta)$  by defining

$$\hat{I}_n(\xi, \eta) \triangleq \iint_{S_n} D_n(k_x, k_y) e^{j2\pi(xk_x + yk_y)} dk_x dk_y \quad (6.1.12)$$

such that

$$I_n(\xi, \eta) \cong e^{j2\pi k_0 x} \hat{I}_n(\xi, \eta) \quad (6.1.13)$$

$\hat{I}_n(\xi, \eta)$  now represents the 2-D Fourier transform of the  $n$ th segment and then rotated through  $n\theta_W$  by Eq. (6.1.8).

Hence

$$\sigma(\xi, \eta) \cong \sum_{n=0}^{N_S-1} e^{j2\pi k_0 (\xi \cos n\theta_W + \eta \sin n\theta_W)} \hat{I}_n(\xi, \eta) \quad (6.1.14)$$

Therefore, the target reconstruction algorithm involves taking the 2-D Fourier transform of each of the  $N$  segments, rotating them by their corresponding mean angle  $n\theta_W$  and then coherently summed according to Eq. (6.1.14).

It is not necessary to rotate the axes after Fourier transforming each segment.  $\hat{I}_n(\xi, \eta)$  can be obtained by first rotating the axes in the frequency plane of each segment and then carrying out the Fourier transform. However, because the phase of the target reflectivity  $\sigma(\xi, \eta)$  can change drastically from one range cell to another, or from one cross-range cell to the next, rotation of axes is recommended only in the frequency



plane where phase coherency is better preserved.

This method of implementation allows the use of the FFT and at the same time uses the minimal amount of memory.

Equation (6.1.14) can also have the following interpretation. It simply means splitting the integration interval of the contour integral Eq. (6.1.3) into  $N$  small segments, with each angular segment being so small that the curved contour in each segment can be approximated as a linear contour. At the same time, each segment is also small enough so that the contour within that segment does not migrate in down range (x-dimension) for more than one range cell width. The former limiting criterion is described in practice as "range dependent azimuth focus error" and the latter limiting criterion is described as the "range-walking" error. Both of these are described below.

Equation (6.1.14) was derived by making approximations in three different places:

1. no range curvature within target space,
2. narrowband assumption,
3. truncated Taylor's series expansion of Eq. (6.1.10).

The last approximation poses the most serious limitation. Two most significant aberrations are caused by neglecting the quadratic phases in Taylor's expansion. They are

$$\phi_1 = 2\pi y k_y k_x / k_0.$$

which causes "range walking"\* and

$$\phi_2 = -2\pi x k_y^2 / 2k_0$$

which causes what is called a "variable range rate" or "changing Doppler" or "range dependent azimuth focus error."<sup>□</sup> This is a classical problem in the processing of Strip mode SAR and is dealt with in detail by Leith, and Brown. The quadratic phases  $\phi_1$  and  $\phi_2$  can be dropped if they change less than  $\pi/2$  over each processing aperture  $S_n$ . Therefore, for negligible "range walking",  $|\Delta\phi_1| \leq \pi/2$ , and negligible "variable range rate",  $|\Delta\phi_2| \leq \pi/2$ . By applying the substitutions

$$|\Delta k_y| = \frac{1}{2} \theta_w k_0,$$

$$|\Delta k_x| = \frac{1}{2} k_B,$$

-----  
 \*Note that  $\phi_1 = 2\pi x' k_x$  where  $x' = y k_y$ . After range compression, the range of a point will be shifted by  $x'$  which is dependent upon the azimuth distance  $y$ .

□Note that  $\phi_2 = -\pi k_y^2 / \lambda F_y$  where  $F_y \propto \frac{1}{x}$  is the azimuth focal length.  $F_y$  changes with range  $x$ .

and  $|\Delta x| = |\Delta y| = a$ , one can show that

$$\theta_W \leq \frac{2}{ak_B} \quad (6.1.15)$$

for negligible range walking and

$$\theta_W \leq \sqrt{\frac{2}{ak_0}} \quad (6.1.16)$$

for negligible variable azimuth defocus blur. In practice, for example in Spotlight SAR,  $\theta_W$  is chosen such that range migration is less than 0.3 range bin width to avoid image degradation [6]. As an example, let  $k_0 = 200a^{-1}$ ,  $k_B = 10a^{-1}$  in normalized units. Then  $\theta_W \leq 0.1 \text{ rad} = 5.73^\circ$  for negligible range walking,  $\theta_W \leq 0.1 \text{ rad} = 5.73^\circ$  for negligible variable azimuth defocus blur. For those particular values of  $k_0, k_B$ , both limitations are the same. But for larger  $k_B$  (say  $k_B = 0.1k_0$ ), range walking becomes the limiting factor on the segment width  $\theta_W$  and for smaller  $k_B$ , the variable azimuth defocus blur becomes the limiting factor on  $\theta_W$ .

The narrowband assumption is common to both the mixed processing technique<sup>†</sup> and the coherent processing

<sup>†</sup>-----  
Mixed processing technique is described in Section 6.3.

technique. It affects the coherent processing technique more significantly because the "bandwidth" ( $k_{\max} - k_{\min}$ ) determines the sidelobe levels of the PSF, as was discussed before.

Only the range curvature approximation is common to all three processing techniques. For airborne targets, this approximation is accurate even when the best resolution is achieved with the coherent processing technique. But for ground mapping purposes, like in the case of the Spotlight SAR, range curvature ultimately determines the best achievable resolution. Based on this, the best possible resolution that is possible is given by

$$\delta = \frac{1}{\sqrt{2r_0 k_0}} a \quad (6.1.17)$$

where  $a$  = maximum radial extent of the target

$r_0$  = antenna - center of rotation distance

$k_0$  = mean spatial frequency ( $= \frac{2}{\lambda}$ )

which was derived by J.L. Walker.

For example with  $k_0 = 200a^{-1}$ ,  $k_B = 10a^{-1}$ ,  $\theta_W \leq 5.73^\circ$  for both negligible range walk and variable range rate aberrations. The resolution of this system is limited to approximately  $1/k_0 \theta_W = \frac{1}{20} a$ .

For the case when  $\theta_{\max} = 2\pi$ ,  $\theta_{\min} = 0$ , the point

spread function for the coherent processing technique is the point spread function of the system. This was derived earlier as

$$\text{PSF}(\rho) = k_{\max} \frac{J_1(2\pi k_{\max} \rho)}{\rho} - k_{\min} \frac{J_1(2\pi k_{\min} \rho)}{\rho}$$

## 6.2 Incoherent Processing

In conventional tracking radar systems, the Doppler phase information is usually lost at the output end. However, one might be able to reconstruct the target without Doppler phase at all. In contrast to coherent processing, a reconstruction algorithm which does not make use of the angle-to-angle Doppler phase variation of the echo is called incoherent processing. For this processing method the magnitude of range compressed data is assumed to be available. How the range compressed data is obtained does not matter at all.

From section 6.1 the range compressed data (range profile) is

$$g_{\text{RC}}(\theta, \ell) = k_B \left[ (g_r(\theta, \ell) e^{j2\pi k_0 \ell}) * (\text{sinc}(k_B \ell)) \right] \quad (6.2.1)$$

where  $g_r(\theta, \ell)$  is the true projection. Again we let

$$D(\theta, k) = \text{2-D Fourier Transform of } \sigma(\xi, \eta)$$

$$= \mathfrak{F}_{1D}\{g_r(\theta, \ell)\}.$$

where  $\mathfrak{F}_{1D}\{\cdot\}$  represents a one dimensional Fourier transformation. Suppose we approximate the projection of the target on to the line-of-sight by  $|g_{RC}(\theta, \ell)|^2$ , with

$$G(\theta, k) \triangleq \mathfrak{F}_{1D}\{|g_{RC}(\theta, \ell)|^2\} . \quad (6.2.2)$$

By the back projection theorem,  $G(\theta, k)$  is the spectrum of a hypothetical real object. The approximate magnitude of the target reflectivity function can therefore be obtained by 2-D Fourier transforming  $G(\theta, k)$ . The square of the magnitude of each range profile has been taken as representing the target's projection onto the line-of-sight because it is mathematically more tractable. In the SAR signal processing sense it is called incoherent processing.

Substituting Eq. (6.2.1) into Eq. (6.2.2) and using Appendix 6A

$$G(\theta, k) = \int_{-\infty}^{\infty} [D(\theta, k - [u - k_0]) D(\theta, -[u - k_0])] \cdot [\text{rect}(\frac{k-u}{k_B}) \text{rect}(\frac{u}{k_B})] du.$$

Then one can write

$$G(\theta, k) = \int_0^{\infty} D(\theta, k - [u - k_0]) D(\theta, -[u - k_0]) du \quad (6.2.3)$$

where  $0 =$  area of overlap between  $\text{rect}(\frac{k-u}{k_B})$  and  $\text{rect}(u/k_B)$ . The area of overlap is zero when  $|k| \geq k_B$ . Hence  $G(\theta, k) = 0$  for  $|k| \geq k_B$  which means that  $G(\theta, k)$  is a bandlimited spectrum with maximum spatial frequency component  $k_B$ . The correlation process in Eq. (6.2.3) is illustrated in Fig. 6.2.1.

The point spread function can be derived by substituting  $D(\theta, k) = 1$  in Eq. (6.2.3).

$$G(\theta, k) = \int_0^{\infty} du$$

Hence

$$G(\theta, k) = \Lambda\left(\frac{k}{k_B}\right) \quad (6.2.6)$$

where

$$\Lambda(x) = \begin{cases} 1 - |x| & -1 \leq x \leq 1 \\ 0 & \text{otherwise.} \end{cases}$$

The point spread function is therefore

$$\text{PSF}(\rho, \phi) = \int_0^{\infty} \int_0^{2\pi} k \Lambda\left(\frac{k}{k_B}\right) e^{j 2\pi k \rho \cos(\theta - \phi)} dk d\theta$$

By carrying out the resulting Fourier Bessel (or Hankel) transformation [Appendix 6B],

$$\text{PSF}(\rho, \phi) = \frac{1}{3} k_B \frac{J_1(2\pi k_B \rho)}{\rho} + \frac{k_B}{4} \sum_{j=1}^{\infty} \frac{c_j J_{2j+1}(2\pi k_B \rho)}{\rho} \quad (6.2.7)$$

where

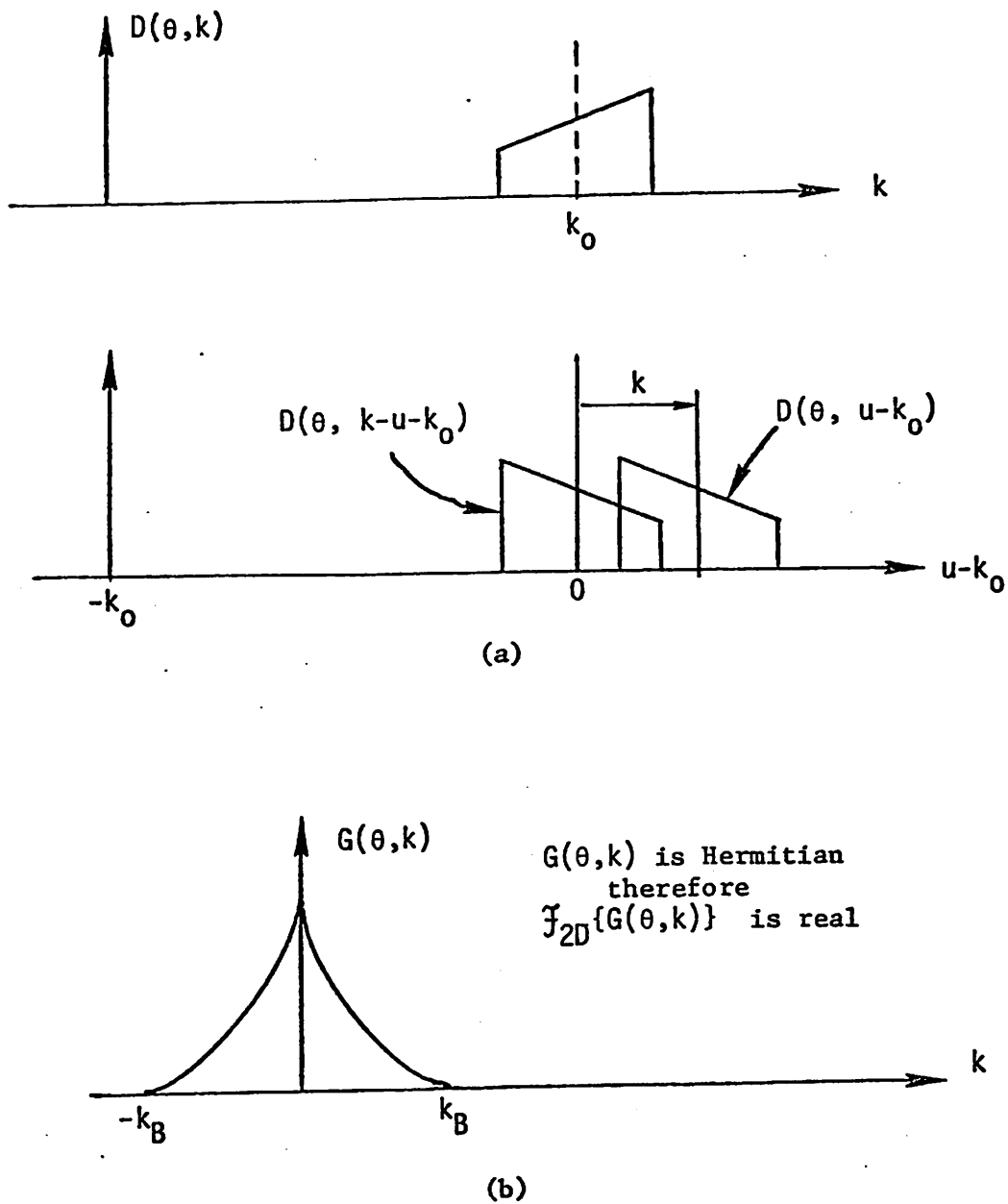


Figure 6.2.1. The correlation process of Eq. (6.2.3) for the incoherent PSF. (a) The correlation process. (b) The resulting PSF of the incoherent processing technique.



$$c_j = \frac{2j+1}{(j+\frac{3}{2})(j+\frac{1}{2})(j-\frac{1}{2})}.$$

The values of the coefficients  $c_j$  drop rapidly with  $j$  and a good approximation of the point spread function can be made by using up to only 5 terms in the expansion. The following are the first five values of  $c_j$ : 0.400, 0.095, 0.044, 0.026, 0.017.

The PSF of a full disc pupil of radius  $k_B$  is  $k_B \frac{J_1(2\pi k_B \rho)}{\rho}$ . This would have been the PSF of the system had the true projection  $g_r(\theta, \ell)$  of the target been available. If it were available, the system becomes identical to a parallel ray tomographic system. Since we only have  $|g_{RC}(\theta, \ell)|^2$ , the actual PSF will be different. Because  $|g_{RC}(\theta, \ell)|^2$  is a real function, reconstruction algorithms for tomographic systems can be used to reconstruct the target. The PSF of such a system is shown in Fig. 6.2.2 by plotting Eq. (6.2.7) and the corresponding PSF of a full disc pupil function is also plotted to show the difference.

The resolution of this incoherent system is essentially determined by  $1/2k_B$  which is much worse than the resolution of  $1/k_0$  theoretically achievable with the coherent processing technique.

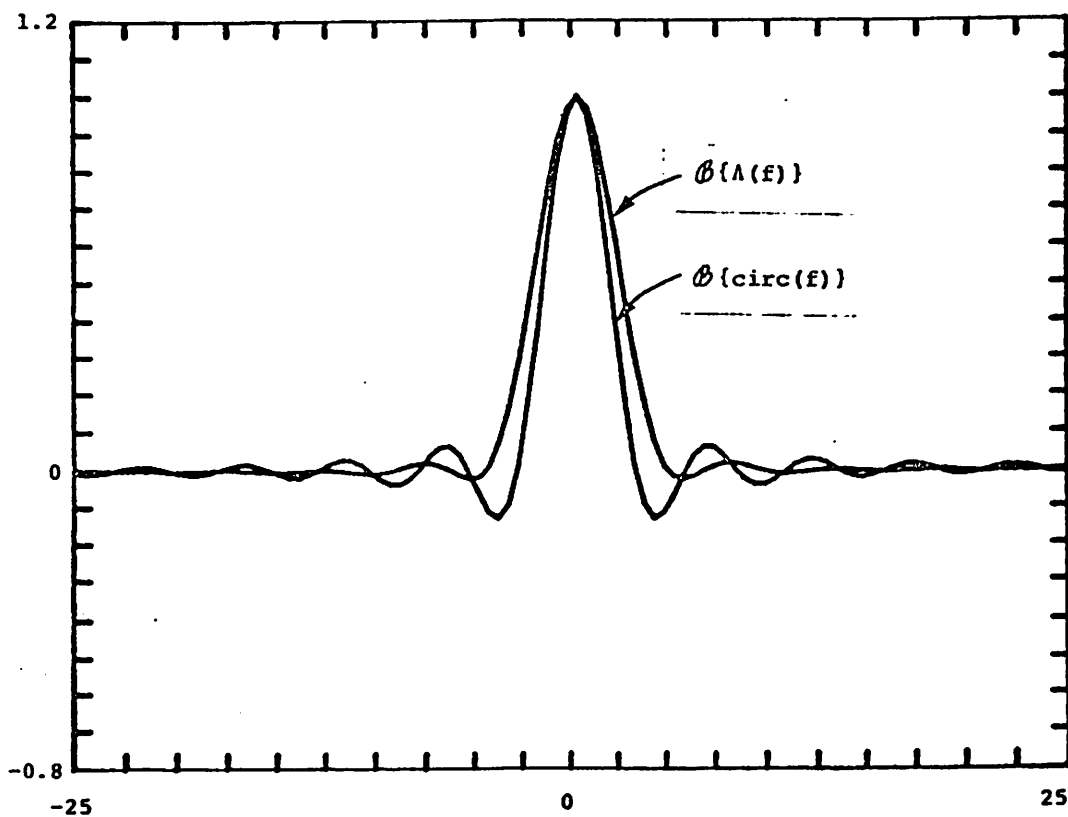


Figure 6.2.2. Point spread functions of a disc pupil function and a conical pupil function.  $\mathcal{B}\{.\}$  represents a Fourier Bessel transform or Hankel transform.

### 6.3 Mixed Processing

If Eq. (6.1.14) is replaced by an incoherent summation, we will have what we call "mixed processing" as follows:

$$\sigma(\xi, \eta) \approx \sum_{n=0}^{N_S-1} |\tilde{I}_n(\xi, \eta)|^2. \quad (6.3.1)$$

Therefore another way to reconstruct the target is to partition the data into  $N$  segments again. Each segment can be processed coherently and the magnitude of the results can be spatially rotated, interpolated, and summed up incoherently. Because of this the processing technique is called mixed processing. This method was used by Chen [11]. The width  $\theta_W$  of each segment of the data is subject to the same inequality as for the coherent processing case namely Eqs. (6.2.14) and (6.2.15).

The point spread function of each image frame is closely approximated by

$$\theta_W k_0 k_B \text{sinc}(k_B x) \text{sinc}(\theta_W k_0 y)$$

where  $x$  is the down-range dimension (along the line-of-sight) and  $y$  is the cross-range dimension. The point spread function for the mixed processing technique is therefore a superposition of the point spread functions of the  $N$  image frames. The resulting point spread

function is essentially given by

$$\text{PSF}(\rho) = \theta_W k_0 k_B \text{sinc}(k_m \rho)$$

where  $k_m = \min(k_B, \theta_W k_0)$ . The mixed processing technique has a resolution not better than one can expect from each segment reconstruction. But because of the shadowing problem in real objects, the incoherent summation in Eq. (6.3.1) serves to fill up the target space with points that cannot be seen from just one segment alone. Besides, the signal-to-noise ratio also improves with the summation.

Figure 6.3.1 gives a plot of the point-spread functions corresponding to the coherent processing technique and the mixed processing technique. An Airy function which corresponds to a full disc pupil function of radius  $k_B$  is also plotted to serve as a contrast to the incoherent processing point spread function.

#### 6.4 Digital Implementation

Digital processing is in most ways more practical than optical processing. For a list of the pros and cons see [3],[37]. Because it is now possible to make fast enough CCD correlators [2], real time digital processing becomes feasible. For this reason only digital implementation methods will be considered.

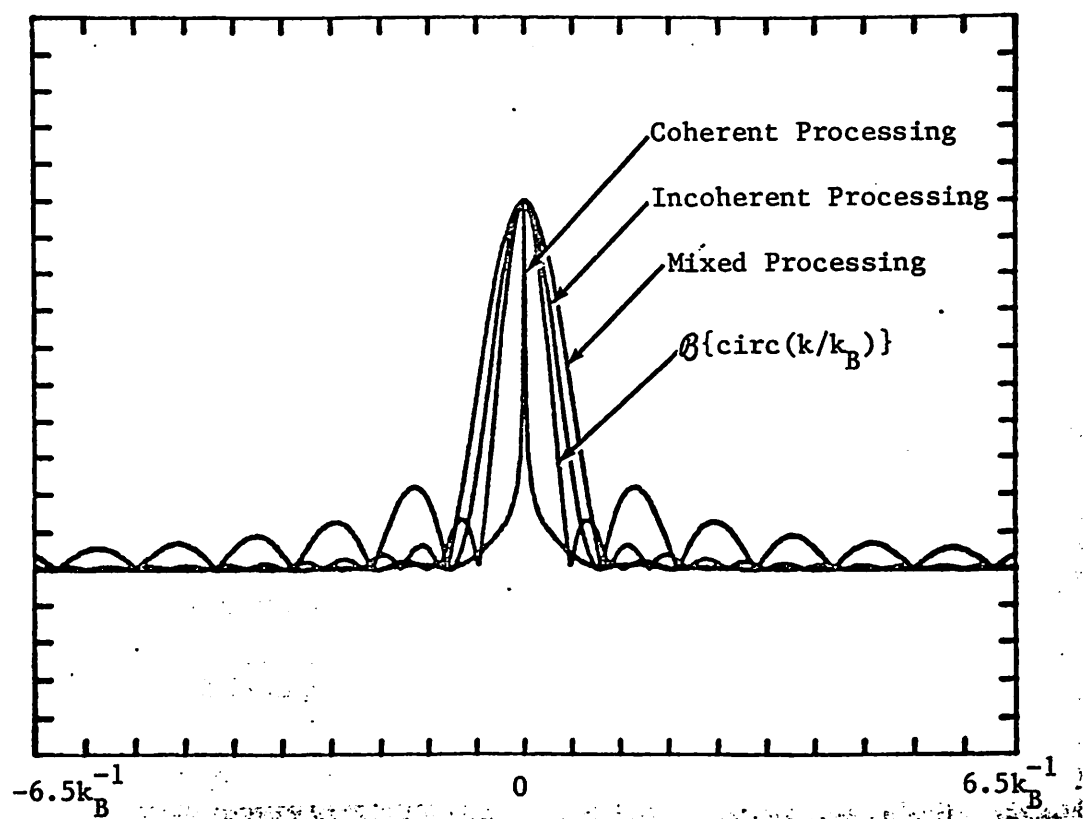


Figure 6.3.1. Plots of magnitudes of point spread functions related to the three processing techniques. ( $B\{\text{circ}(k/k_B)\}$  is plotted as a comparison to the incoherent processing case.)

## 1. Coherent Processing

A discrete version of Eq. (6.1.2) must be used for digital processing. Let range compressed data be

$$g_{RC}(i, n) = \frac{1}{K} \sum_{p=0}^{K-1} D(i, p) e^{j \frac{2\pi}{K} np} \quad (6.4.1)$$

where  $i = 0, 1, 2, \dots, N-1$

$n = 0, 1, 2, \dots, K-1$

$$g_{RC}(i, n) = g_{RC}\left(\frac{i}{N} 2\pi, \frac{n}{K_B}\right)$$

and  $D(i, p) = D\left(\frac{i}{N} 2\pi, k_{\min} + \frac{p}{K} k_B\right).$

To compute  $\sigma(\xi, \eta)$  we use a discrete version of Eq. (6.1.3):

$$\sigma(\xi, \eta) \approx \frac{K_0}{N} \sum_{i=0}^{N-1} \tilde{g}_{RC}(i) e^{-j2\pi k_{\min} \ell_i} \quad (6.4.2a)$$

where

$\tilde{g}_{RC}(i)$  = interpolated value of  $g_{RC}(\theta = \frac{i}{N} 2\pi, \ell_i)$

$$\ell_i = \cos\left(\frac{2\pi}{N} i\right) + \eta \sin\left(\frac{2\pi}{N} i\right). \quad (6.4.2b)$$

If the data is undersampled in azimuth, Eq. (6.4.2) can be modified so that for each point  $(\xi, \eta)$  being considered only the range profiles  $g_{RC}(i)$  that correspond to azimuth angles in  $[\phi_{\xi\eta} \pm \theta_c]$  will be integrated.

$$\begin{aligned}
\phi_{\xi\eta} &= \tan^{-1}(\pm\eta/\xi) \\
\theta_c &= \text{azimuth coherence interval} \\
&\leq \sin^{-1}(1/2\Delta\theta a k_0)
\end{aligned} \tag{6.4.4}$$

where  $\Delta\theta = \text{azimuth sampling interval} = \frac{2\pi}{N}$ .

This way high Doppler regions are avoided. In this case

$$\sigma(\xi, \eta) \cong \frac{k_0}{N} \sum_{i=0}^{N-1} \left\{ \tilde{g}_{RC}(i) e^{-j2\pi k_{\min} i} \right\} \text{rect} \frac{\frac{2\pi i}{N} - \phi_{\xi\eta}}{\theta_c} \tag{6.4.5}$$

If the range sampling rate is not sufficiently high, we can also use Eq. (6.4.5) but with

$$\theta_c \leq \cos^{-1} \left( \frac{K}{2ak_B} \right).$$

The point spread function for this modified algorithm is

$$\begin{aligned}
\text{PSF}(\rho) &= \frac{1}{4\theta_c k_0 k_B} \iint_{-\infty}^{\infty} \int_{k_{\min}}^{k_{\max}} k \left[ \text{rect} \left( \frac{\theta - \phi_{\xi\eta}}{\theta_c} \right) + \text{rect} \left( \frac{\theta - \phi_{\xi\eta} + \pi}{\theta_c} \right) \right] \\
&\quad \cdot e^{2\pi k \rho \cos(\theta - \phi_{\xi\eta})} d\theta dk
\end{aligned} \tag{6.4.6}$$

The constant  $1/4\theta_c k_0 k_B$  has been chosen so that  $\text{PSF}(0) = 1$ . From Appendix 6C,

$$\begin{aligned}
\text{PSF}(\rho) &= \frac{1}{2k_0 k_B} \int_{k_{\min}}^{k_{\max}} k J_0(2\pi k \rho) dk \\
&\quad + \frac{1}{k_0 k_B} \sum_{n=1}^{\infty} (-1)^n \text{sinc} \left( \frac{n\theta_c}{\pi} \right) \int_{k_{\min}}^{k_{\max}} k J_{2n}(2\pi k \rho) dk
\end{aligned} \tag{6.4.7}$$

The first integral in Eq. (6.4.7) is the original point spread function for the unmodified coherent processing

case. The integral in the weighted sum has the same form as the  $n^{\text{th}}$  order azimuth sampling clutter  $A_n(\rho)$  for  $N = 2$ .  $A_n(\rho)$  has a "main lobe" which peaks in the vicinity of  $\rho = \frac{n}{\pi k_{\max}}$ . Therefore the weighted sum in Eq. (6.4.7) can be interpreted as the term that decreases the "sharpness" of the original point spread function.

Figure 6.4.1 shows the point spread functions for the coherent processing case with modified and unmodified algorithms. A coherence interval of  $\theta_c = 60^\circ$  was arbitrarily chosen to illustrate modified algorithm. For computation, a simpler form of Eq. (6.4.6) exists by using the relationship in pp. 430 of [5].

The PSF can also be written in the form

$$\text{PSF}(\rho) = \frac{1}{2\theta_c k_0 k_B} \int_0^{\frac{1}{2}\theta_c} X_\rho(\theta) d\theta$$

where

$$\begin{aligned} X_\rho(\theta) = & 2[k_{\max}^2 \text{sinc}(2k_{\max}\rho \cos\theta) - k_{\min}^2 \text{sinc}(2k_{\min}\rho \cos\theta)] \\ & - k_{\max}^2 \text{sinc}^2(k_{\max}\rho \cos\theta) - k_{\min}^2 \text{sinc}^2(k_{\min}\rho \cos\theta). \end{aligned}$$

Figure 6.4.2 shows the half-power (3dB) width  $\rho_{\text{HP}}$  of the envelope of the point spread functions as a function of the azimuth coherence interval  $\theta_c$ . Twice the value of  $\rho$  when the magnitude square is equal to 0.5 is taken to be the half power width  $\rho_{\text{HP}}$  of the point spread function.



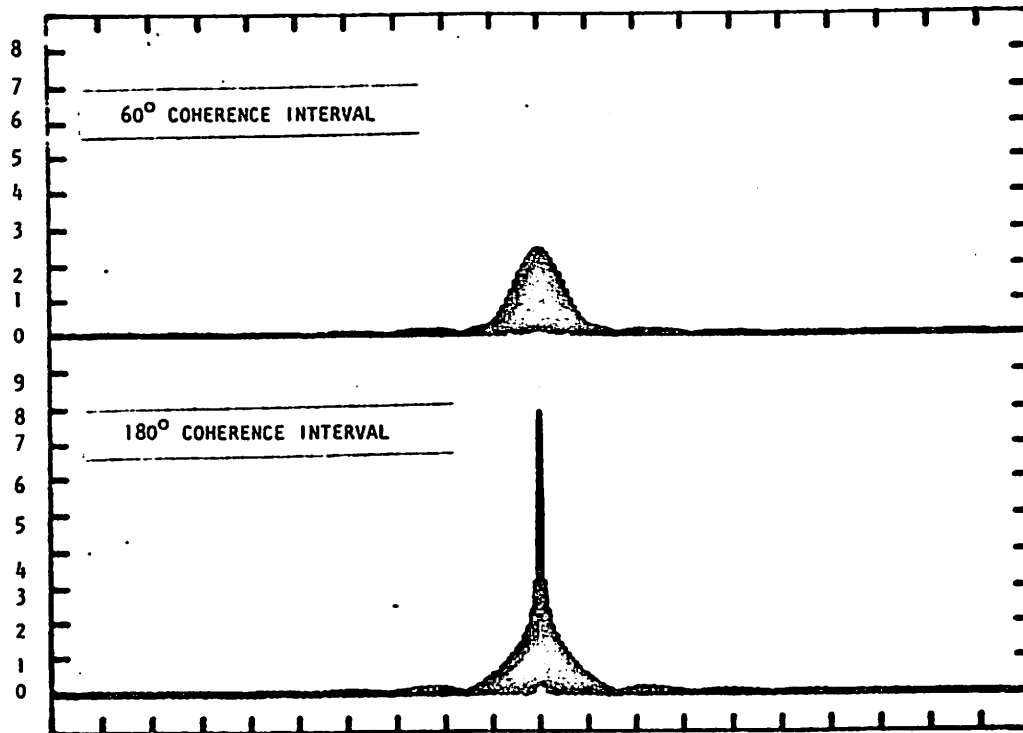


Figure 6.4.1. Magnitude of point spread functions with coherence intervals  $60^\circ$  and  $180^\circ$ . These are normalized such that the total energy is unity.

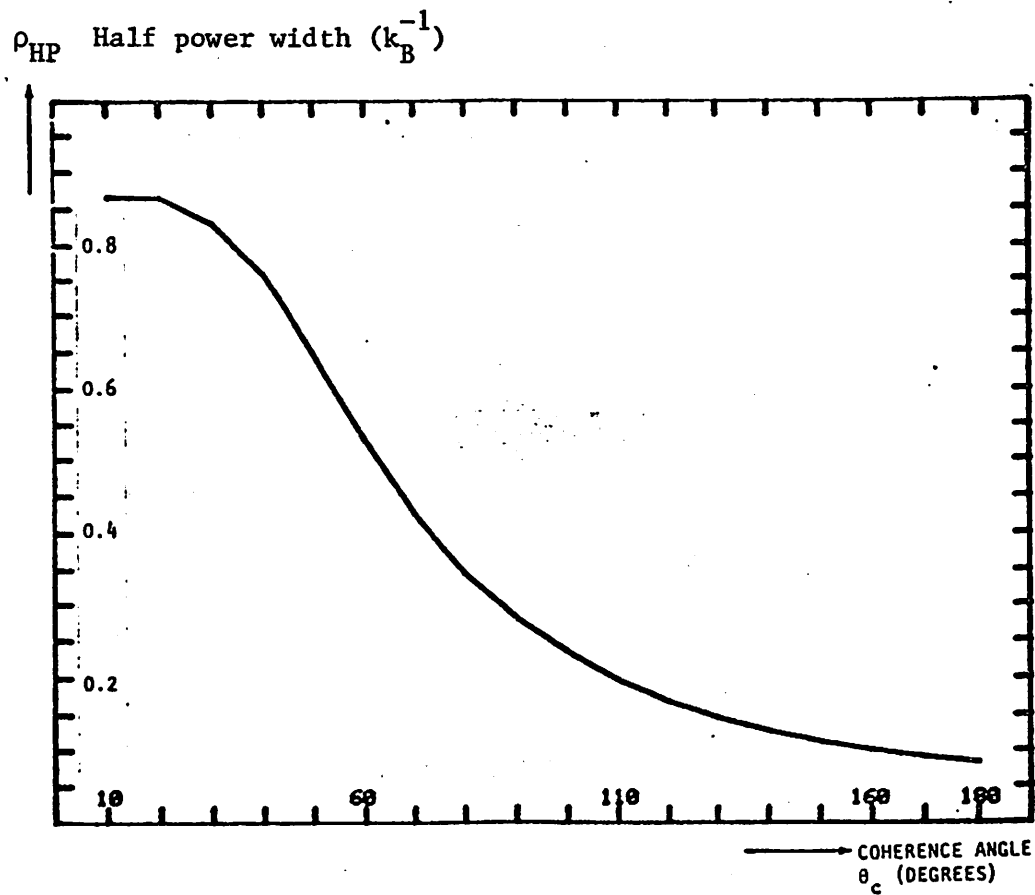


Figure 6.4.2. Variation of  $\rho_{HP}$  the half power (3dB) width of the point spread function with coherence angle  $\theta_c$ .

$\rho_{HP}$  is taken as a measure of resolution because of convenience and because it gives a reasonably good relative comparison of the resolution for various coherence angles  $\theta_c$ . The resolution stays about the same for  $\theta_c < 30^\circ$  and  $\theta_c > 100^\circ$ . Therefore, in designing the radar imaging system one may want to choose  $\theta_c$  to be not more than  $100^\circ$  because beyond that the law of diminishing returns takes over.

In choosing the actual computational algorithm, the batch-by-batch processing idea that led us to Eq. (6.1.14) is most attractive in both speed and storage because of the applicability of the FFT. Even in the case where the data are undersampled in azimuth, this batch-by-batch processing idea can be applied to the modified coherent processing technique by quantizing  $\theta_c$  so that  $\theta_c$  is equal to an integral multiple of  $\theta_w$ . Moreover, when speed is a crucial factor, one can apply the FFT on the initial segment of the data to obtain low resolution image frames and make initial assessments. As the target rotates through wider angles, the subsequent image frames can be rotated and coherently superimposed on the initial image frame to get better resolution. Because of the sequential nature in which the lumps of data are being processed, "lumped" pipeline architecture can potentially further speed up the processing time. Equation (6.1.14) therefore

represents a very practical algorithm.

Since we are interested more in the high resolution capability of the coherent processing technique, we will use the more easily implemented algorithm of range compression and contour integration as represented in Eqs. (6.4.1) and (6.4.2), respectively. One can think of the integration process of Eq. (6.4.2a) as spreading out the image information in each range profile onto the entire image. With the modified coherent processing case, an extra step is added. For a given range profile index  $i$ , expression (6.4.8) is added onto the image point  $(\xi, \eta)$  only if either

$$\left| \frac{2\pi}{N}i - \tan^{-1}(\xi/\eta) \right| \leq \frac{1}{2} \theta_c$$

or

$$\left| \frac{2\pi}{N}i - \tan^{-1}(\xi/\eta) - \pi \right| \leq \frac{1}{2} \theta_c$$

## 2. Incoherent Processing

Tomographic reconstruction schemes can be exploited to reconstruct the target. Many different tomographic computer reconstruction algorithms exist and they can, in general, be categorized into those which process in the spatial domain (e.g. convolution-back-projection algorithm [5], [27]) and those which process in the Fourier transform domain ([5], [30]). For a review on these algorithms see [29],[18].

The sampling requirement in azimuth and range is much less severe than that for the coherent processing technique. If the data is oversampled in azimuth, a processor which acts like a "fast-in/slow-out" filter may become necessary to azimuth-wise resample the data to the proper sampling rate.

For the sole purpose of illustrating this processing technique and for the reason of availability, we will use the Shepp and Logan [30] reconstruction algorithm to incoherently reconstruct the target.

### 3. Mixed Processing

Two-dimensional FFT techniques can be applied to each azimuth segment to get an image frame. Since only the magnitude of the resulting image frames are used, standard interpolation schemes can be used to rotate the image frames. The digital implementation of these techniques is expounded in detail in [10].

# APPENDIX 6A

$$\text{Statement } \mathfrak{F}_{1D}\{|x(t)*h(t)|^2\} = \int_{-\infty}^{\infty} [X(f-u)X(-u)] [H(f-u)H(-u)] du$$

$$\text{Proof} \quad \text{Let } y(t) = x(t)*h(t)$$

$$Y(f) = \mathfrak{F}_{1D}\{y(t)\}$$

$$X(f) = \mathfrak{F}_{1D}\{x(t)\}$$

$$H(f) = \mathfrak{F}_{1D}\{h(t)\}$$

$$\text{Then } Y(f) = X(f)H(f)$$

$$\begin{aligned} \mathfrak{F}_{1D}\{|x(t)*h(t)|^2\} &= \mathfrak{F}_{1D}\{y(t)y^*(t)\} \\ &= Y(f)*Y^*(-f) \quad (5A-1) \\ &= \int_{-\infty}^{\infty} Y(f-u)Y(-u) du \end{aligned}$$

$$\text{Using Eq. (5A-1)}$$

$$= \int_{-\infty}^{\infty} [X(f-u)X(-u)] [H(f-u)H(-u)] du.$$

This is a different version of the autocorrelation theorem.

# APPENDIX 6B

$$G(\theta, k) = \Lambda(k/k_B) = \begin{cases} 1 - \left| \frac{k}{k_B} \right| & |k| \leq k_B \\ 0 & \text{otherwise.} \end{cases}$$

Suppose  $G(\theta, k)$  is a pupil function. Then the corresponding point spread function is given by the Fourier transform of  $G(\theta, k)$ . The Fourier transform of  $G(\theta, k)$  becomes a Fourier Bessel transform (also called Hankel transform) when  $G(\theta, k)$  is independent of  $\theta$ . The point spread function is therefore

$$\begin{aligned} &= 2\pi \int_0^\infty k \Lambda\left(\frac{k}{k_B}\right) J_0(2\pi \rho k) dk \\ &= A(\rho) - B(\rho) \end{aligned}$$

where

$$\begin{aligned} A(\rho) &= 2\pi \int_0^{k_B} k J_0(2\pi \rho k) dk \\ &= k_B \frac{J_1(2\pi k_B \rho)}{\rho} \end{aligned}$$

and

$$B(\rho) = \frac{2\pi}{k_B} \int_0^{k_B} k^2 J_0(2\pi \rho k) dk.$$

From Abramowitz and Stegun, pp. 480, Eq. (11.1.1),

$$\int_0^z t^2 J_0(t) dt = \frac{2}{3} z^2 J_1(z) - \frac{z^2}{4} \sum_{j=1}^{\infty} c_j J_{2j+1}(z)$$

where

$$c_j = \frac{2j+1}{(j+\frac{3}{2})(j+\frac{1}{2})(j-\frac{1}{2})} \quad \text{for } j \geq 1$$

Then

$$\begin{aligned} B(\rho) &= \frac{2\pi}{k_B} \int_0^{k_B} k^2 J_0(2\pi k \rho) dk \\ &= \frac{2\pi}{(2\pi\rho)^3 k_B} \int_0^{2\pi\rho k_B} t^2 J_0(t) dt \\ &= \frac{2}{3} k_B \frac{J_1(2\pi k_B \rho)}{\rho} - \frac{1}{4} k_B \sum_{j=1}^{\infty} c_j \frac{J_{2j+1}(2\pi k_B \rho)}{\rho} . \end{aligned}$$

The point spread function is therefore

$$\begin{aligned} \text{PSF}(\rho) &= A(\rho) - B(\rho) \\ &= \frac{1}{3} k_B \frac{J_1(2\pi k_B \rho)}{\rho} + \frac{1}{4} k_B \sum_{j=1}^{\infty} c_j \frac{J_{2j+1}(2\pi k_B \rho)}{\rho} \end{aligned}$$

Each  $k$ th term in the series can be expanded in series form

$$\frac{J_{2j+1}(2\pi k_B \rho)}{\rho} = (\pi k_B)^{2j+1} \rho^{2j} \sum_{n=0}^{\infty} \frac{[-\frac{1}{4} \cdot (2\pi\rho k_B)^2]^j}{n! \Gamma(2j+2+n)}$$

which shows that it converges to 0 as  $\rho \rightarrow 0$ . Therefore we do not have any singularity problem with the series.



## APPENDIX 6C

The point spread function for the modified algorithm in the coherent case of Chapter 6 section 4 is

$$\text{PSF}(\rho) = \frac{1}{2\theta_0 k_0 k_B} \int_{-\infty}^{\infty} \int_{k_{\min}}^{k_{\max}} k \left[ \text{rect}\left(\frac{\theta - \phi_{\xi\eta}}{\theta_c}\right) + \text{rect}\left(\frac{\theta - \phi_{\xi\eta} + \pi}{\theta_c}\right) \right] \cdot e^{j2\pi\rho k \cos(\theta - \phi_{\xi\eta})} dk d\theta \quad (6c.1)$$

The constant  $1/2\theta_0 k_0 k_B$  has been chosen so that  $\text{PSF}(0) = 1$ . At the same time it turns out from Parseval's Theorem that

$$2\pi \int_0^{\infty} |\text{PSF}(\rho)|^2 \rho d\rho = 1.$$

Let  $\alpha = \theta - \phi_{\xi\eta}$ . Using the Bessel function expansion formulae (9.1.44) and (9.1.45) of [1],

$$e^{j2\pi\rho k \cos\alpha} = J_0(2\pi k\rho) + 2 \sum_{n=1}^{\infty} (j)^n J_n(2\pi k\rho) \cos(n\alpha). \quad (6c.2)$$

Also,

$$\int_{-\infty}^{\infty} \left[ \text{rect}\left(\frac{\alpha}{\theta_c}\right) + \text{rect}\left(\frac{\alpha + \pi}{\theta_c}\right) \right] \cos n\alpha d\alpha = \begin{cases} 2\theta_c \text{sinc}\left(\frac{n\theta_c}{2\pi}\right) & n \text{ even} \\ 0 & n \text{ odd} \end{cases} \quad (5c.3)$$

With a change in variable from  $\theta$  to  $\alpha$ , substituting Eq. (6c.2) into Eq. (6c.1) and using the result in Eq. (6c.3),

$$\begin{aligned} \text{PSF}(\rho) = & \frac{1}{k_0 k_B} \int_{k_{\min}}^{k_{\max}} k J_0(2\pi k \rho) dk \\ & + \frac{2}{k_0 k_B} \sum_{n=1}^{\infty} (-1)^n \text{sinc}\left(\frac{n\theta}{\pi}\right) \int_{k_{\min}}^{k_{\max}} k J_0(2\pi k \rho) dk \end{aligned} \quad (6c.4)$$

The last integral has the same form as the angular sampling error terms derived in Chapter 5.

## Chapter 7

### SOME PRACTICAL CONSIDERATIONS AND EXPERIMENTAL RESULTS

#### 7.1 RAT SCAT (RADar Target SCATtering site) Data

Two sets of data were collected on an experimental RCS measuring facility called the RAT SCAT located near Holloman AFB, New Mexico. A model F102 plane was used as the target and was mounted on top of a rotating turntable. Because of the operational difficulty in maintaining a coherent signal, a reference sphere located close to the line-of-sight between the turntable and the radar antenna was used to generate the reference signal. The recording geometry is described in Fig. 7.1.1.

The reference sphere S had a small diameter compared to the target size and therefore the echo from it could be taken to be the reference signal. Since it is closer to the radar antenna, its echo will return earlier than that from the target T. The reference echo was delayed by an amount which was controlled manually with the aid of an oscilloscope. Nominally, the delay should be equivalent to a round trip spatial distance of  $2r_1$ . In particular, the reference echo was delayed long enough so that its

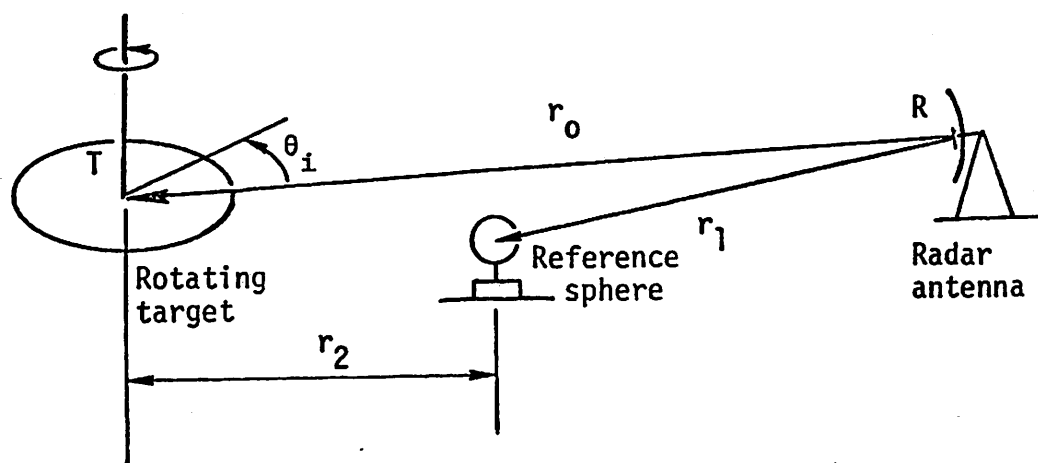


Figure 7.1.1. RAT-SCAT site recording geometry.

overlap with the target echo was maximal. The net effect of all this is that the estimation of the center of rotation (CR) distance can be off by a constant distance plus some incremental distance which is a random function of the azimuth angle. The rest is same as the imaging system described in Chapter 2.

Table 7.1.1 lists the imaging parameters for the F102 model plane. For convenience, the temporal frequencies are listed in the right column as spatial frequencies normalized against  $a = 10\text{ft}$ . ( $a =$  maximum radial extent of the target). When the actual data was collected, the center of rotation was centered at a point about 12ft. from one end of the plane so that the center of rotation is not at the target center.

The two sets of data are described as follows.

Set #1 = The model F102 plane is mounted right side up on the supporting pillars above the turntable. The data is collected over  $180^\circ$  azimuth angle with 0 degrees azimuth corresponding to the direction when the plane is facing head on towards the antenna.

Table 7.1.1 Parameters for Model F102-Plane Data  
 Model: 0.29 x actual plane dimensions  
 Plane dimension: 68 ft. (Nose-Tail), 38 ft. (Wing-Span)  
 Model dimension: 20 ft. (Nose-Tail), 11 ft. (Wing-Span)

Actual Physical Data	Normalized Data (against a=10 ft)
$r_0 = 1652 \text{ ft.}$	$r_0 = 165.2 \quad (a)$
$r_1 = 1112 \text{ ft.}$	$r_1 = 111.2 \quad (a)$
$r_2 = 540 \text{ ft.}$	$r_2 = 54.0 \quad (a)$
$f_{\min} = 9.130 \text{ GHz}$	$k_{\min} = 185.947 \quad (a^{-1})$
$f_{\max} = 9.997 \text{ GHz}$	$k_{\max} = 203.36 \quad (a^{-1})$
$f_0 = 9.5637 \text{ GHz}$	$k_0 = 194.478 \quad (a^{-1})$
$f_{\text{BW}} = 0.83 \text{ GHz}$	$k_B = 17.719 \quad (a^{-1})$
$\Delta f = 3.4 \text{ MHz}$	$\Delta k = 6.92 \times 10^{-2} \quad (a^{-1})$
$\Delta \theta = 0.2^\circ$	$\Delta \theta = 0.00349 \text{ radians}$
$K = 256$	$K = 256$
$N = 1800$	$N = 1800$

\* Conversion factors

$$f_{\text{(temporal)}} \xrightarrow{\times \frac{2}{c}} k_{\text{(spatial)}} \xrightarrow{\times 10 \text{ ft}} k_{\text{(normalized)}}$$

$$(\text{sec}^{-1}) \quad (\text{ft}^{-1}) \quad (a^{-1})$$

Set #2 = The same plane is mounted vertically (roll angle =  $90^\circ$ ) and data was collected over  $360^\circ$  azimuth angle.

For both sets of data, the nominal azimuth sampling interval was  $0.2^\circ$ . Using Eq. (4.2.5) with  $a = 10\text{ft}$  the coherence interval is approximately  $\theta_c = 47^\circ$ . Therefore, the data are undersampled in azimuth. In data set #2, the sampling interval varies from  $0.1^\circ$  to  $0.3^\circ$ . This corresponds to at best a coherence interval of  $29.4^\circ$  which is even worse. In the radial dimension, the unambiguous range interval (radial extent) is

$$\frac{1}{\Delta k} = \frac{1}{6.92 \times 10^{-3}} \approx 145 \text{ ft}$$

which is more than 7 times larger than the target size. Therefore, the data is oversampled in range. The range bin width in each range profile is

$$\Delta r = \frac{1}{k_B} \approx 0.56 \text{ ft,}$$

## 7.2 Range Compression

The two sets of data described in section 7.1 are recorded on a magnetic tape in blocks of 256 complex numbers, each block representing the 256 frequency samples for a given azimuth angle. Figure 7.2.1 shows the magnitude and phase of data set 1 in the format that it was recorded. Because of the large dynamic range,

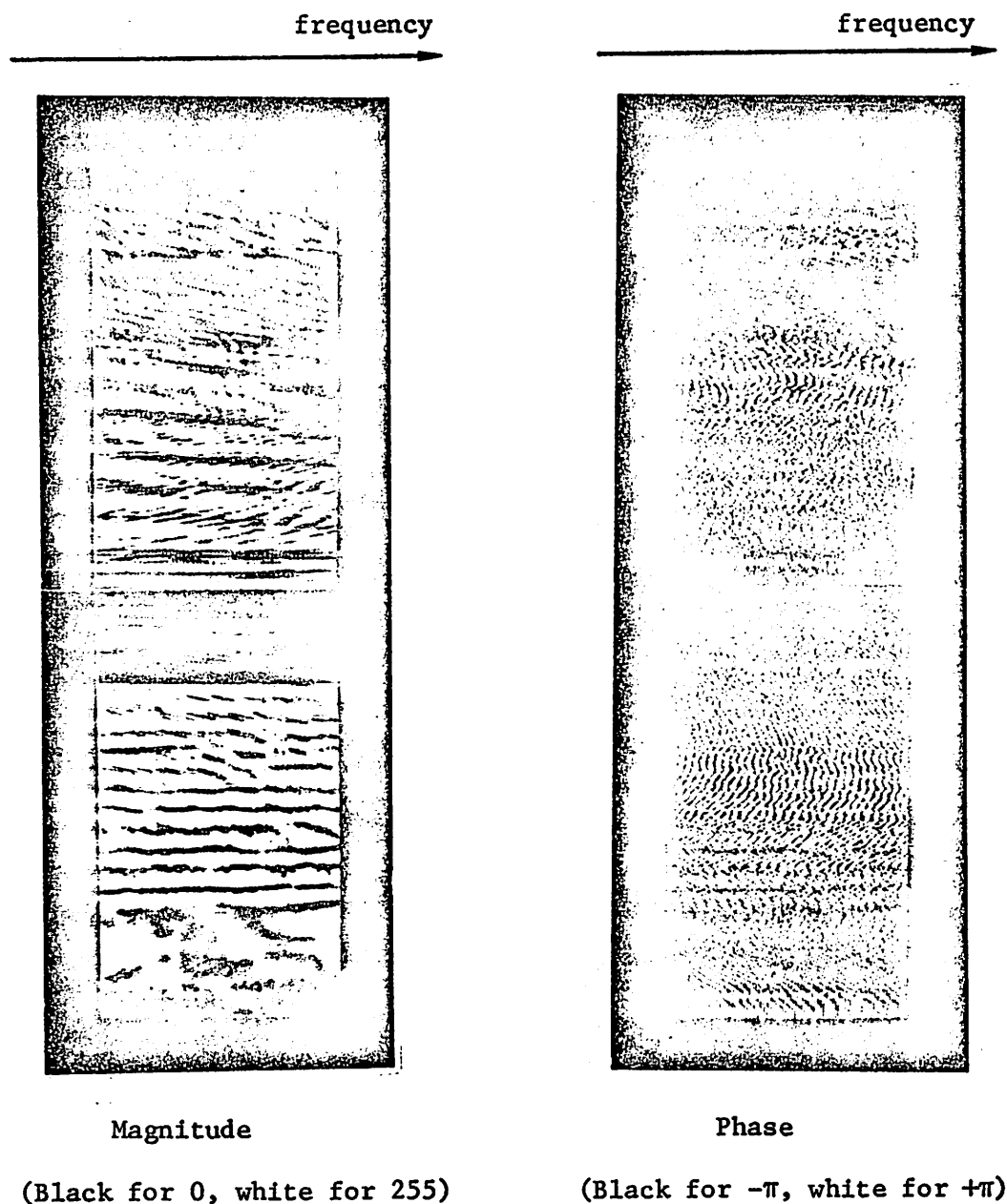


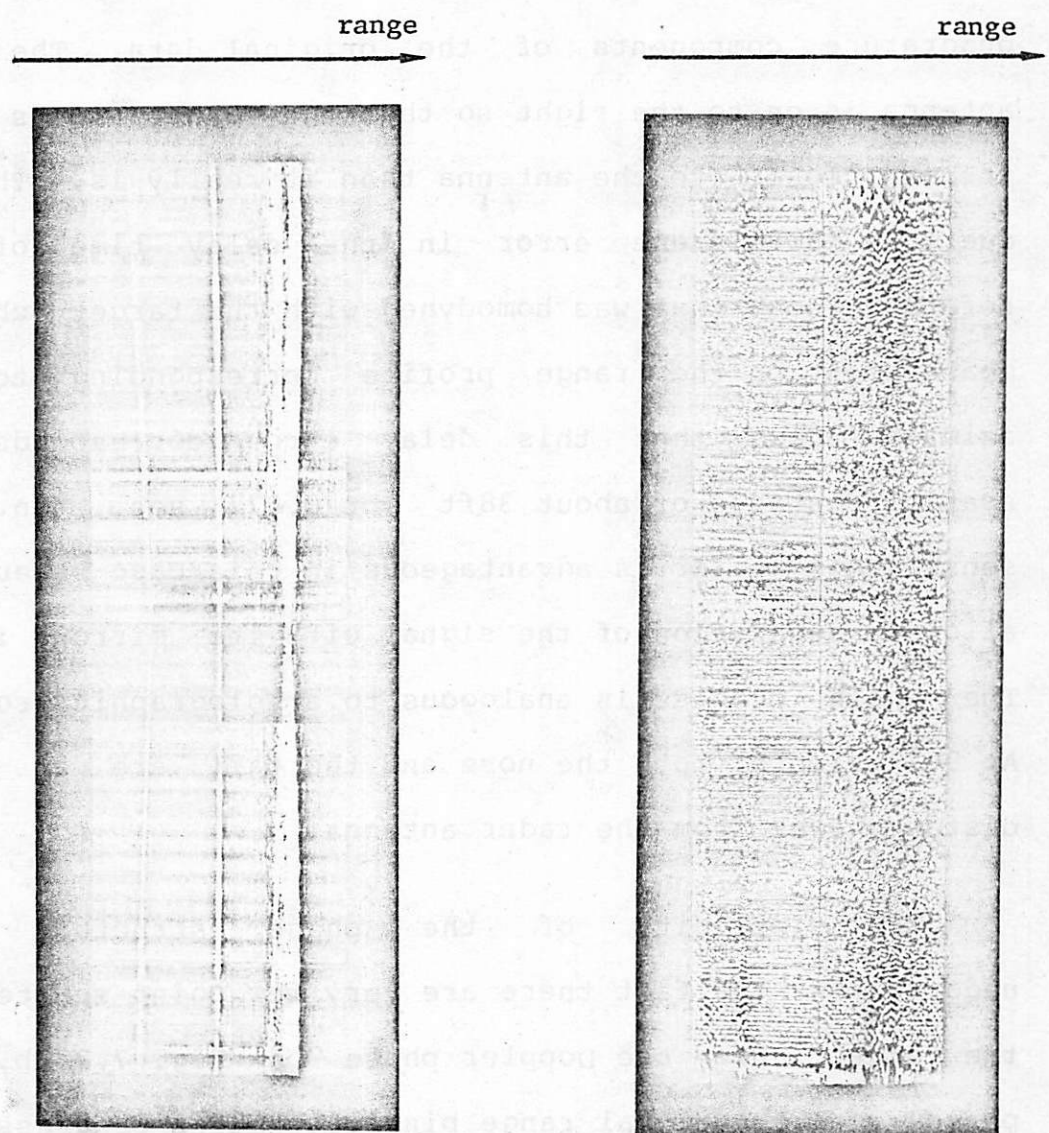
Figure 7.2.1. Phase and magnitude of experimental data set 1.  
 The horizontal axis represents frequency in steps of 3.4MHz (9.130MHz to 9.997MHz). The vertical axis represents aspect (azimuth) angles  $0^\circ$  (top) to  $180^\circ$  (bottom) in increments of a nominal  $0.2^\circ$ .



$\log(1 + \text{magnitude})$  is displayed instead of magnitude alone, so that some of the weaker signals become more visible. The horizontal dimension represents the radial frequency dimension from left to right ranging from 9.130GHz to 9.997GHz, in increments of 3.4MHz. The vertical dimension represents the azimuth angle from top to bottom,  $0^\circ$  to  $180^\circ$ . Each horizontal line of data will be called a signature. It is also referred to as an azimuth sample in the literature.

One-dimensional FFT was applied on data set #1, one signature at a time. The resulting projection space data is shown in Fig. 7.2.2. The magnitude of each signature is now the range profile which shows the intensity of the reflection coefficient in various range cells. Here again due to the large dynamic range, the log magnitude of each range profile is displayed in Fig. 7.2.2a. Figure 7.2.2b shows the composite Doppler phase of all the point scatterers of the target.

The strong signal along the center of the range profiles is the d.c. bias magnitude from the FFT. The strong signals to the right that look like cosine-shaped contours crossing at  $90^\circ$  azimuth are the range compressed signature of the target. The related mirror image on the left was found by Chen [10] to be caused by the unbalanced



Magnitude

(Normalized: black=0, white=1)

Phase

(Black for  $-\pi$ , white for  $+\pi$ )

Figure 7.2.2. Magnitude and phase of the range compressed data. The horizontal axis represents range (0 to 145ft.) and the vertical axis represents aspect angle (azimuth)  $0^\circ$  (top) to  $180^\circ$  (bottom). (Notice the decrease in Doppler frequency toward  $0^\circ$  and  $180^\circ$  aspect angles.)

amplification or attenuation on the in phase and quadrature components of the original data. The radar antenna is on to the right so that the target looks like it is closer to the antenna than it really is. This is due to a consistent error in the delay time of the reference echo that was homodyned with the target echo. A measurement on the range profile corresponding to  $90^{\circ}$  azimuth shows that this delay error corresponds to a spatial distance of about 38ft or 0.077 sec. In some sense this error is advantageous in this case because it allows a separation of the signal with its mirror image. The whole process is analogous to a holographic process. At  $90^{\circ}$  azimuth, both the nose and the tail are at equal distance away from the radar antenna.

The simplicity of the phase structure also underscores the fact there are very few point scatterers on the target. From the Doppler phase on Fig. 7.2.2b, the phase over the signal range bins fluctuates progressively slowly toward  $0^{\circ}$  and  $180^{\circ}$  azimuth. Such a Doppler phase history is typical of point scatterers at the nose and tail of the plane.

The magnitude and phase of the range compressed data for data set #2 is similar to Fig. 7.2.2.

From the range profiles, it is not difficult to see that the nose and the tail are consistently the dominant reflector. Notice how the nose and tail signals converge toward the same range cell at  $90^\circ$  azimuth.

### 7.3 Azimuth Compression, Coherent Processing

The azimuth compression step is basically a matched filtering process in which each point that is being reconstructed is associated with a unique filter function. It involves interpolation and coherent integration as expounded in Eqs. (6.1.2) and (6.1.3), respectively. This is how it was done. The reconstruction image was chosen to be  $256 \times 144$  with a scale of 200pixels: 20ft, so that it covered the entire target with a negligible amount of sampling clutter. Initially, the complex image was initialized to zero. Then the first signature ( $\theta_i = 0^\circ$  azimuth) was scanned. For each complex image point  $(\xi, \eta)$ , a two-neighbor interpolation generated a sample data as follows.

$$\tilde{g}_{RC}(i) = \frac{1}{2}\{g_{RC}(i, n_1) + g_{RC}(i, n_2)\}$$

with

$$n_1 = [\ell_i k_B]$$

$$n_2 = [\ell_i k_B]$$

$$\ell_i = \xi \cos \theta_i + \eta \sin \theta_i$$

$$\theta_i = (2\pi/1800)i \quad (i=0,1,2,\dots,N-1)$$

$\lceil x \rceil$  = smallest integer greater than  $x$

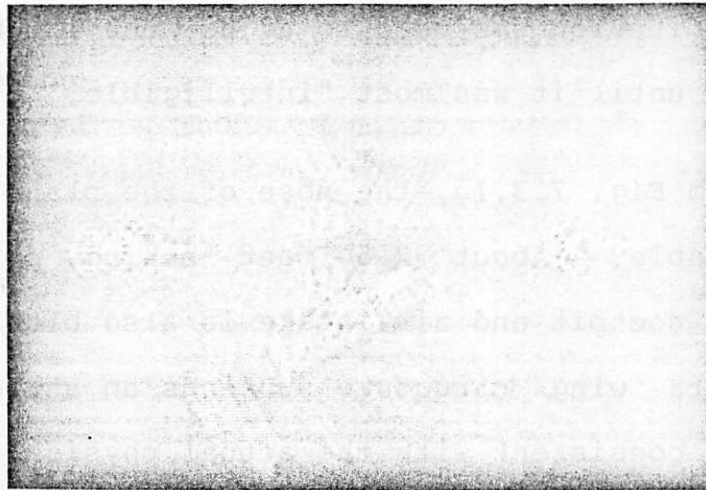
$\lfloor x \rfloor$  = largest integer smaller than  $x$ .

The final image point value was

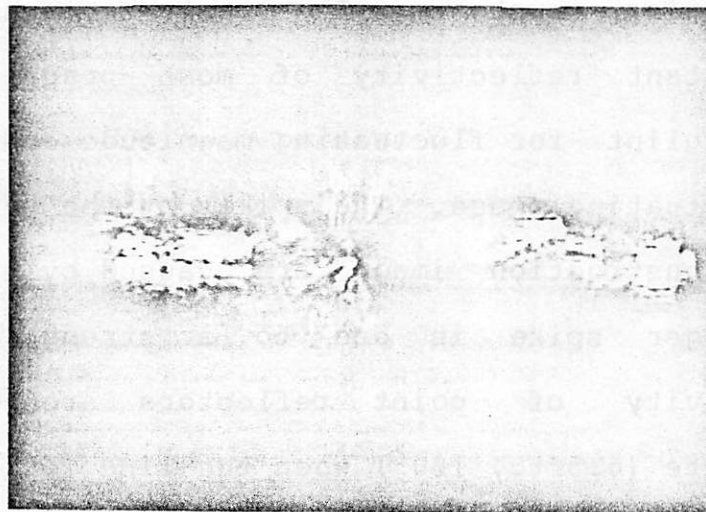
$$\sigma_{\text{coh}}(\xi, \eta) = \frac{k_0}{1800} \sum_{i=1}^{N-1} \tilde{g}_{\text{RC}}(i) e^{-j2\pi k_{\text{min}}^{\ell} i} v(\xi, \eta).$$

Because of azimuth undersampling, coherent integration is carried out only when  $\theta_i - \arctan(\eta/\xi)$  lay within  $0 \pm \theta_c$  or  $180 \pm \theta_c$ . For data set #1,  $\theta_c = 47^\circ$  and for data set #2,  $\theta_c = 29^\circ$ .

Figure 7.3.1a is a reconstruction from data set #1. Since the target was symmetrical about the horizontal axis, only the top half was reconstructed and the bottom half is its mirror image. The dynamic range of the magnitude of the reconstructed image is large so that weaker signals like the wing sections were not visible. The log magnitude is displayed instead. Figure 7.3.1b is the magnitude of the same reconstruction from data set #2, with no target symmetry assumed. The visual quality of the reconstruction does depend on the general intensity bias and contrast of the video display, but since our objective is to demonstrate the possibility of getting



(a)



(b)

Figure 7.3.1. Reconstruction by coherent processing technique. (a) Log magnitude of reconstruction from data set 1, with  $180^\circ$  of azimuth samples, and with  $\theta_c = 47^\circ$ . Target symmetry is assumed. Center R.B.<sup>c</sup> (range bin) # = 198. (b) Magnitude of reconstruction from data set 2, with  $360^\circ$  of azimuth samples,  $\theta_c = 29^\circ$ , and center R.B.# = 193.

high resolution radar images, we will not be concerned with that aspect of the problem. Instead, a subjective visual criterion was used to adjust the intensity bias and contrast until it was most "intelligible."

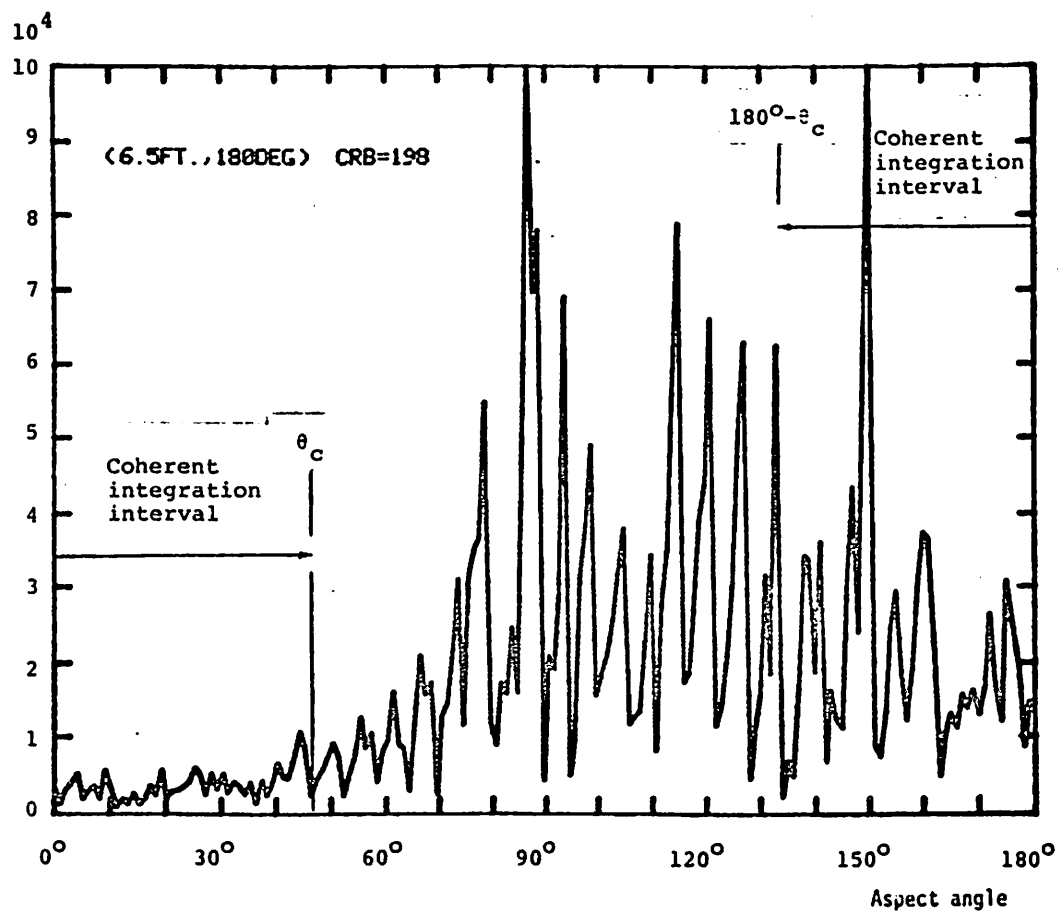
From Fig. 7.3.1a, the nose of the plane is distinctly identifiable. About 2.5 feet behind, point reflectors from the cockpit and air intake is also barely resolvable. The delta wing structure subtends an angle of about  $60^\circ$  which is consistent with the actual physical target. The entire length of the tail section can also be seen. However, there are serious problems inherent in this kind of imaging system. The most serious one is the non-constant reflectivity of most practical targets, called glint for fluctuating magnitude and scintillation for fluctuating phase. The spikes at the tail section of the reconstruction image are caused by such a problem. The longer spike is due to a strong surge in the reflectivity of point reflectors around the target coordinate (6.5ft.,  $180^\circ$ ) when the line of sight is at about  $150^\circ$  azimuth. The shorter and weaker spike is due to the same reason on a point reflector (7.2ft.,  $180^\circ$ ) when the line of sight is about  $20^\circ$  azimuth. This reasoning is supported by the evidence from plotting the magnitude of the range cells along the curves traced out on the projection space data by target points (6.5ft.,

180°) and (7.2ft., 180°). This is exactly what was done in Fig. 7.3.2a and Fig. 7.3.2b, respectively. The strong delta function like surge in reflectivity does occur at 150° for target point (6.4ft., 180°) and at 20° for target point (7.2ft., 180°). Note the glint along the azimuth dimension. Since the coherent integration interval is only  $\pm 47^\circ$ , most of the glint is not covered. Therefore, even if the data were sufficiently sampled, the glint problem will become a limiting factor on the quality of reconstructed image. As an illustration, a reconstruction result is shown in Fig. 7.3.3 with  $\pm 180^\circ$  coherent interval. Note the substantial increase in the number of spikes radiating from the tail end. The two arcs are azimuth sampling clutters described in Chapters 4 and 5.

The delta wing structure on the image from data set #1 is also a part of the glint phenomenon. The front sharp edge of the plane reflects strongly only to 90° incidence waves. Hence, the edge of the delta wing is at best resolved up to one range bin distance. This can be quantitatively described by the Geometrical Theory of Diffraction [20].

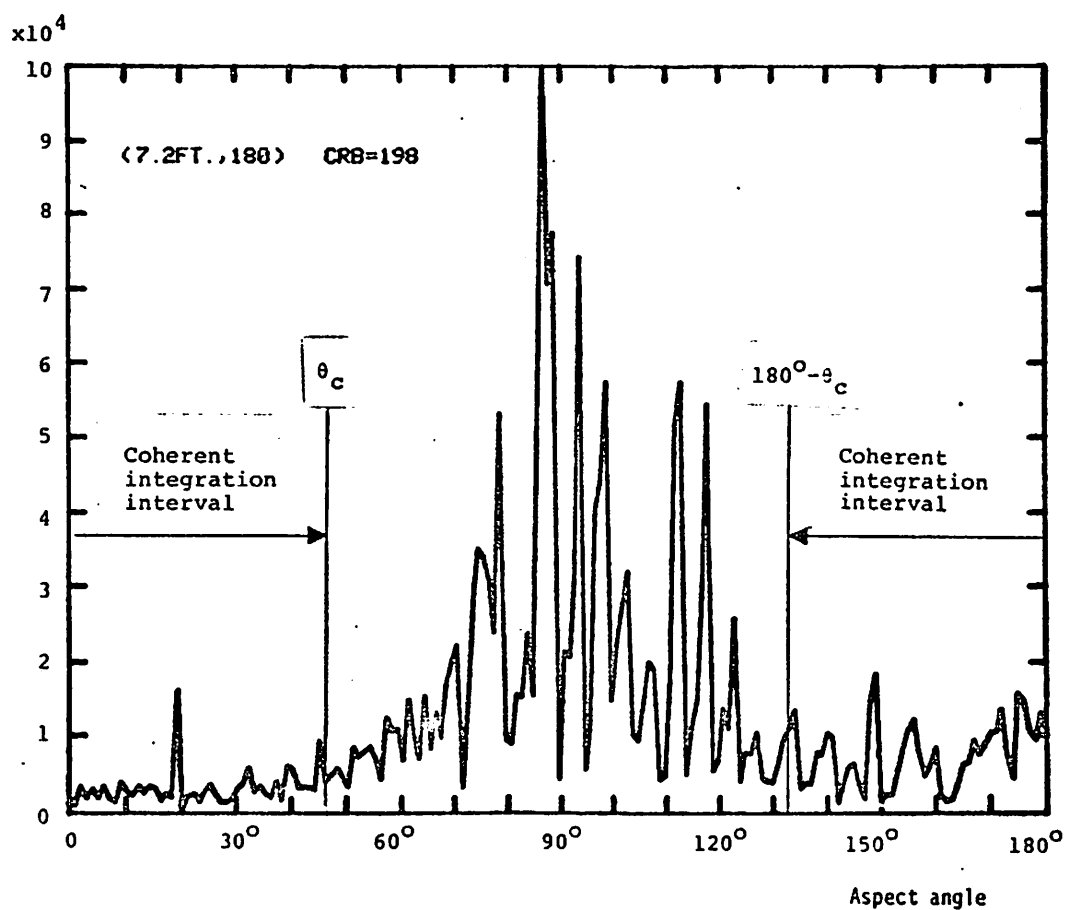
The glint problem can be described analytically. For all practical purposes, we can assume that a point target  $(r_0, \phi_0)$  is reflecting only when the line-of-sight is at an





(a) Target point (6.5ft., 180°) over (0, 180°) azimuth of data set 1. (Note the strong surge at 150° and the relatively weak reflectivity over (0, 90°) azimuth.)

Figure 7.3.2. Magnitude of the reflectivity of two tail end target points.



(b) Target point (7.2ft.,  $180^\circ$ ) over (0,  $180^\circ$ ) azimuth of data set 1. (Note the delta function type of reflectivity change at  $20^\circ$  azimuth.)

Figure 7.3.2 continued

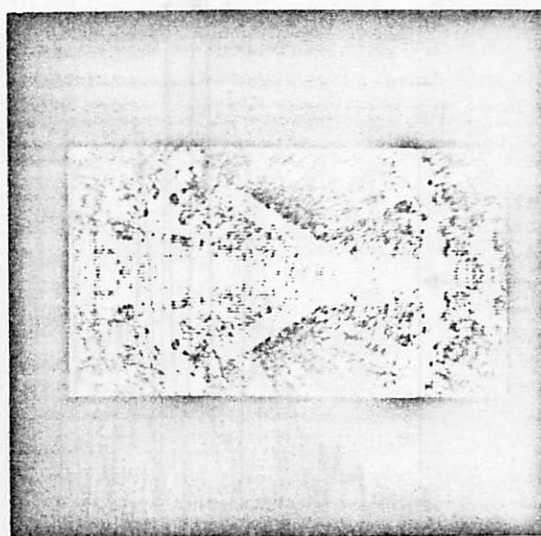


Figure 7.3.3. Reconstruction from experimental data set 1 using unmodified coherent reconstruction technique showing aspect (azimuth) angle undersampling effects due to non-constant target reflectivity function.

azimuth angle  $\phi_r$ . The line-of-sight dependent target reflectivity function can be written as

$$\sigma(r, \phi, \theta) = \sigma_0 \delta(r - r_0) \delta(\phi - \phi_0) \delta(\theta - \phi_r)$$

where  $\theta$  is the azimuth angle of the LOS.

The complex data from the radar imaging system will consequently be

$$D(\theta, k) = \sigma_0 r_0 e^{j2\pi r_0 k \cos(\theta - \phi_0)} \delta(\theta - \phi_r)$$

Using coherent processing, the reconstructed target will be

$$\begin{aligned} \sigma_{\text{coh}}(r, \phi) &= \iint k D(\theta, k) e^{-j2\pi k r \cos(\theta - \phi)} dk d\theta \\ &= \sigma_0 r_0 \iint k e^{j2\pi k [r_0 \cos(\theta - \phi_0) - r \cos(\theta - \phi)]} \delta(\theta - \phi_r) d\theta dk \\ &\approx \sigma_0 r_0 k_0 \text{sinc}(k_B x_1) e^{j2\pi k_0 x_1} \end{aligned} \quad (7.3.1)$$

where  $x_1 = r_0 \cos(\phi_r - \phi_0) - r \cos(\phi_r - \phi)$ .

Therefore the reconstructed image is a one-dimensional function of  $x_1$ . It will look like a line strip passing through the point  $(r_0, \phi_0)$  and extending out at an angle  $(\phi_r + 90^\circ)$ . These strips, which we called spikes are clearly obvious from Fig. 7.3.3.

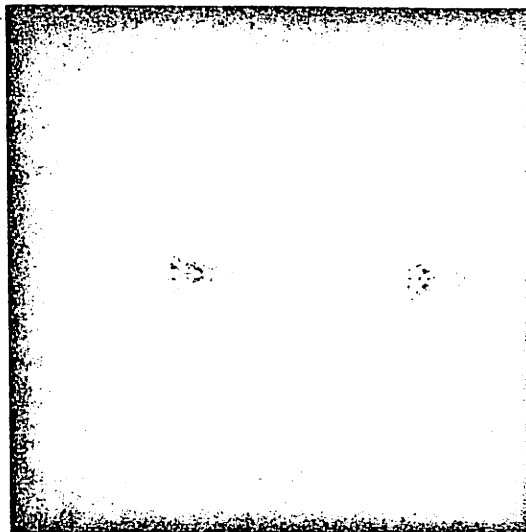
A second square of glint that is not so obvious here is the instability of the in-phase and quadrature signal amplifiers. This is apparent from the fluctuating bias on

the magnitude of the projection space data along the azimuth dimension. This is a problem in hardware technology.

The reconstruction from data set#2 is characterized by the glint problem too, but it is not as bad here because the coherence interval is only  $29^\circ$ . The bright spot near the center is the target center of rotation. It is put in for reference. In this reconstruction, the cockpit and the air intake of the fuselage are even better resolved. Part of the triangular shaped rudder, the tail and the wing edge can also be seen. A lot of signal noise appear near  $90^\circ$  and  $270^\circ$  azimuth. This is due to the fact that the projection data was very noisy around  $90^\circ$  and  $270^\circ$  azimuth. The angular discontinuity in the intensity of the reconstructed image is due to the concentration of signal like noise around the  $90^\circ$  and  $270^\circ$  azimuth region, and the small coherence interval being used.

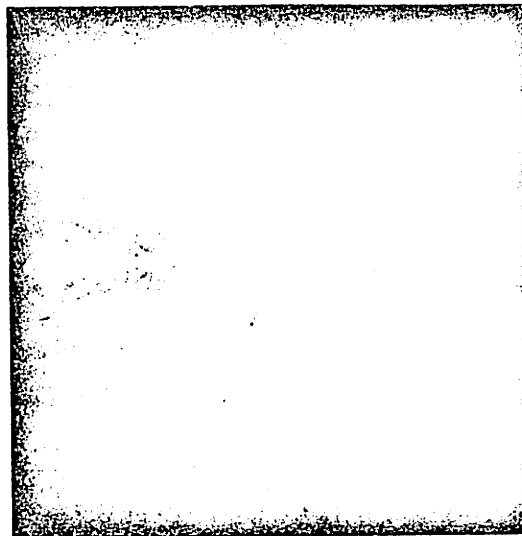
A logical step that follows is to de-emphasize the magnitude fluctuations in the projection data. One method is to reconstruct the image from the phase of the projection space data only. The result is shown in Fig. 7.3.4a. Another method is to replace the magnitude of the projection space data by its  $\log(1 + \text{magnitude})$  value. The resulting reconstructed image is shown in

Phase only reconstruction



(a)

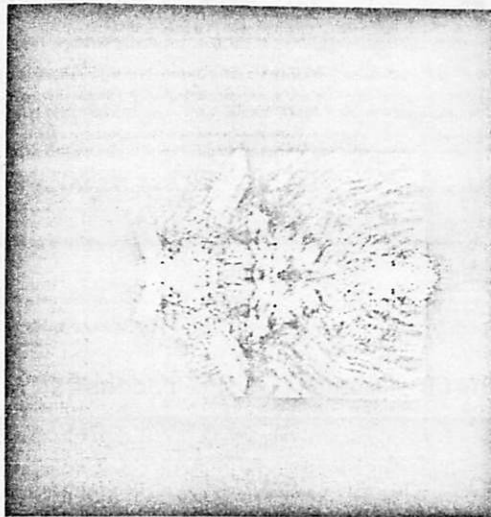
$\log(1 + \text{magnitude})$  reconstruction



(b)

Figure 7.3.4. Images from data set 2, reconstructed from modified range compressed data.  
(a) Phase only reconstruction.  
(b)  $\log(1 + \text{magnitude})$  reconstruction.  
(c) Reconstruction from range compressed data normalized in magnitude.

Reconstruction from normalized magnitude



(c)

Figure 7.3.4 continued

Fig. 7.3.4b. A third possible method is to normalize the projection space data so that the maximum magnitude in each signature is normalized to unity. The reconstructed image is shown in Fig. 7.3.4c.

Shadowing problem is potentially also a serious limitation to the imaging system. To illustrate this, data set #2 was reconstructed with no target symmetry assumed. This is shown in Fig. 7.3.5. The bottom half of the target cannot be seen since no data was collected over  $180^{\circ}$  to  $360^{\circ}$  azimuth. This problem can partially be overcome by taking  $360^{\circ}$  azimuth data. However, in practical situations this luxury is probably not available. Fortunately, the shadowing problem only becomes serious on  $0^{\circ}$  elevation. Since for most practical applications the elevation angle is non zero, shadowing is not expected to become a major handicap.

#### Error in Target Rotation Center Range

In practical situations, the range of the target center of rotation is never known exactly. Two types of errors are possible in the estimation of the range of the target center of rotation.





Figure 7.3.5. Reconstruction with  $180^\circ$  aspect (azimuth) angle extent from experimental data set 2, with no target symmetry assumed. The bottom half of the target is in the shadow region.

### 1) Constant Range Error

Suppose the reference signal was delayed by  $\frac{2\hat{r}_0}{c}$  instead of  $\frac{2r_0}{c}$  where  $\hat{r}_0$  is the estimated range. Then the collected data will have a range frequency carrier. Let  $r_\epsilon = \hat{r}_0 + r_0$ . Then

$$D(\theta, K) = e^{-j2\pi r_\epsilon k} G(\theta, k)$$

where the constant of proportionality has been omitted. The blurring function is an isotropic function  $h(r)$ .

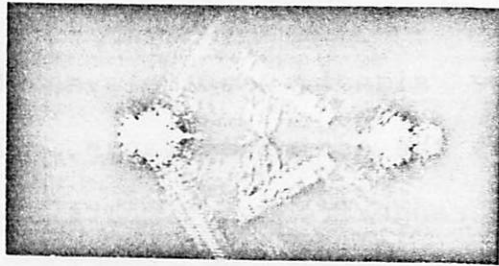
$$h(r) = \mathcal{B}\{e^{-j2\pi r_\epsilon k}\} = \hat{h}(r) * w_2(r)$$

$$\hat{h}(r) = \begin{cases} \frac{1}{2\pi^2} [r^2 - r_\epsilon^2]^{-3/2} & r > r_\epsilon > 0 \\ 0 & r_\epsilon > r \geq 0 \end{cases}$$

$$w_2 = 2\pi k_B \text{sinc}(k_B r) \cos(2\pi k_0 r).$$

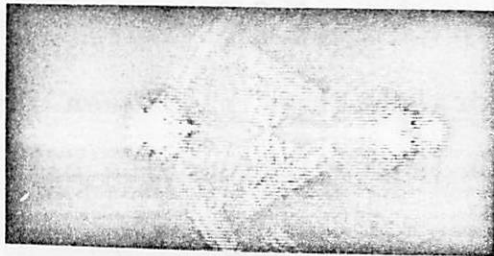
Since  $\hat{h}(r)$  is singular at  $r = r_\epsilon$ ,  $h(r)$  is a ring-like function with radius  $r_\epsilon$ . Besides the blurring, the reconstructed target image is also displaced in location by  $(\epsilon_x, \epsilon_y)$  where  $(\epsilon_x, \epsilon_y)$  is the  $(x, y)$  coordinate error in the center of rotation [page 144, 37].

Figure 7.3.6 shows a sequence of reconstruction from data set #2 using a sequence of estimates for the location of the target rotation center. The target rotation center is located around range bin number 198. The reconstructions are made with the center of rotation at range bin 197, 197.5, 198, 198.5, 199. Data set #2 is

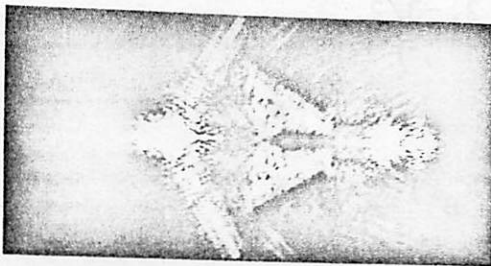


Center of rotation at

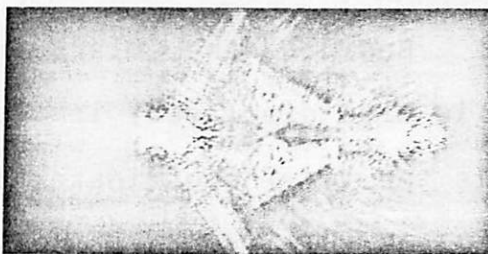
range bin # = 197.0



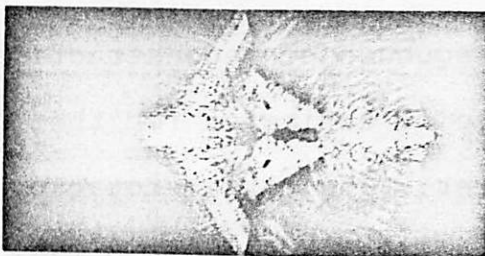
range bin # = 197.5



range bin # = 198.0



range bin # = 198.5



range bin # = 199.0

Figure 7.3.6. Reconstruction from data set 2, using coherence interval  $\theta_c = 47^\circ$ , mean (spatial) frequency  $k_o = 194.478$  but varying center (of rotation) range bin number. One range bin number corresponds to 0.56 ft.

used because it has a wider coherence interval and therefore the blurring effect can be more noticeable for center range 197 to 199. It should also be realized that the smaller the coherence interval, the less severe is the effect of constant range error.

## 2) Sinusoidal Range Error

Suppose  $\hat{r}_0 = r_0 + r_\epsilon \cos(\theta + \theta_\epsilon)$  where  $r_\epsilon, \theta_\epsilon$  are constant.

Then the gathered data will be

$$D(\theta, k) = e^{-j2\pi k r_\epsilon \cos(\theta + \theta_\epsilon)} G(\theta, k).$$

In Cartesian coordinates this can be rewritten as

$$D(k_x, k_y) = e^{-j2\pi(k_x x_\epsilon + k_y y_\epsilon)} G(k_x, k_y)$$

where

$$k_x = k \cos \theta$$

$$k_y = k \sin \theta$$

$$x_\epsilon = r_\epsilon \cos \theta_\epsilon$$

$$y_\epsilon = r_\epsilon \sin \theta_\epsilon.$$

The reconstructed image will simply be shifted by  $(x_\epsilon, y_\epsilon)$  and no blurring or distortion occurs.

This type of range error is very realistic because in practical situations  $r_0$  is more difficult to estimate than  $\hat{r}_0$ . For example,  $\hat{r}_0$  can be taken as the range of the most prominent point reflector or the closest point reflector.

### Error in Rotation Rate

In general, this error is time variant in nature and hence it is difficult to examine its effect over large azimuth coherence intervals. For small azimuth coherence intervals the problem has been solved [page 139, 37]. Suppose a small error exists in the rotation rate such that

$$\Delta\theta = \frac{\Delta\phi}{1-\epsilon_0}$$

where  $\Delta\phi$  is the actual target rotation in a given increment of time  $\Delta T$  and  $\Delta\theta$  is the azimuth increment in the same  $\Delta T$ . Assuming  $|\epsilon_0| = \text{constant} \ll 1$  and small azimuth coherent processing interval, the data over that interval is

$$D(k'_x, k_y) = e^{-j2\pi\epsilon_0 x \left(\frac{k_y^2}{k_0}\right)} \cdot G(k'_x, k_y(1+\epsilon_0))$$

where  $k'_x = k_x - k_0$

$k_x$  = down-range frequency

$k_y$  = cross-range frequency

Therefore the reconstructed image will suffer a scaling distortion in the azimuth dimension. This is known as a change in aspect ratio. Besides this, a range dependent defocus blur will also occur.

#### 7.4 Incoherent Processing

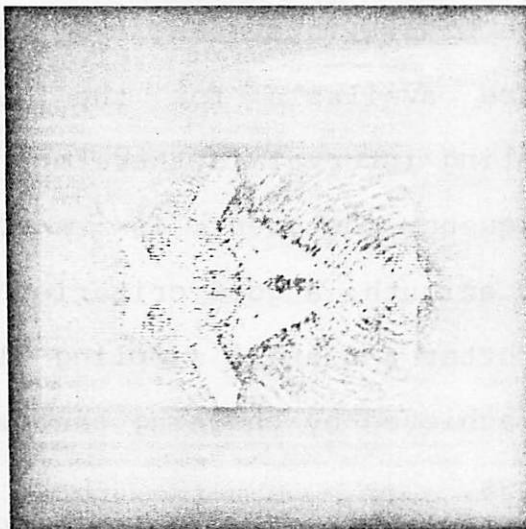
From the projection space data, the target signal extends over about 40 range bins. This means that only 40 radial frequency samples are available for the target. The radial frequency sampling interval is therefore  $k_B/40$  and the maximum radial frequency components is  $\frac{1}{2} k_B$ . In order not to oversample in azimuth, a good criterion is to let the radial sampling clutter and angle sampling clutter overlap. This can be achieved by choosing the azimuth sampling interval as follows.

$$\begin{aligned}\Delta\theta = \text{Azimuth sampling interval} &= \frac{\text{radial frequency sampling interval}}{\text{maximum radial frequency}} \\ &= \frac{k_B/40}{k_B/2} \\ &= 2.86^\circ\end{aligned}$$

Both data sets #1 and #2 are therefore oversampled in azimuth.

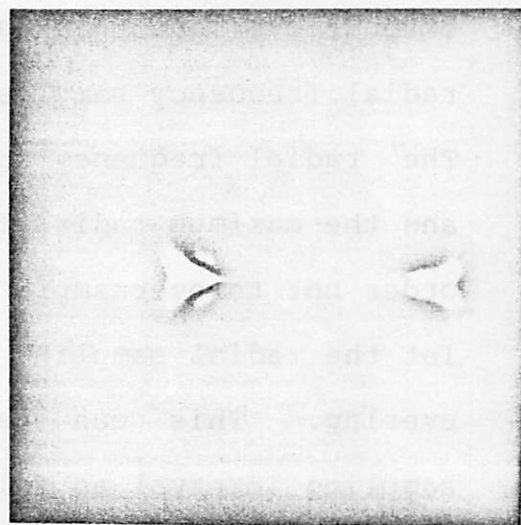
The data was resampled with  $\Delta\theta = 1^\circ$  by keeping one out of every five signatures. The magnitude square in the projection space was computed. From that point on the Shepp & Logan algorithm for CAT reconstruction was used to reconstruct the target. Figure 7.4.1b and Fig. 7.4.2b shows the result of incoherent processing from data sets #1 and #2, respectively. In Fig. 7.4.1b, target symmetry was assumed. Here the reconstruction is "unintelligible" other than to give a rough estimate on the length of the target. Since  $360^\circ$  data is available for data set #2,

Coherent Processing



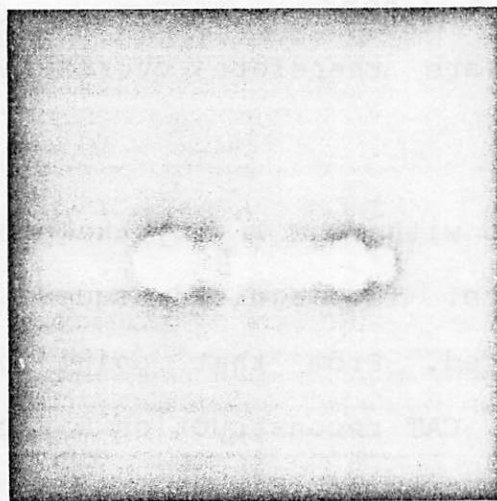
(a)

Incoherent Processing



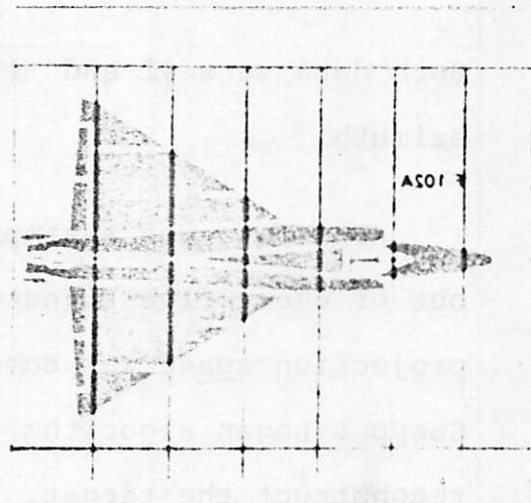
(b)

Mixed Processing



(c)

A Sketch Diagram



(d)

Figure 7.4.1. Reconstructions from data set 1, using the three reconstruction techniques.

(a) Coherent processing ( $47^\circ$  azimuth coherence).

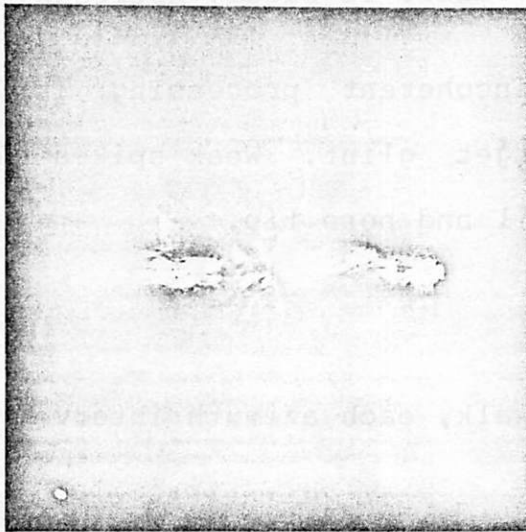
(b) Incoherent processing ( $180^\circ$  projections).

(c) Mixed processing.

(d) A sketch diagram of the F102A plane.

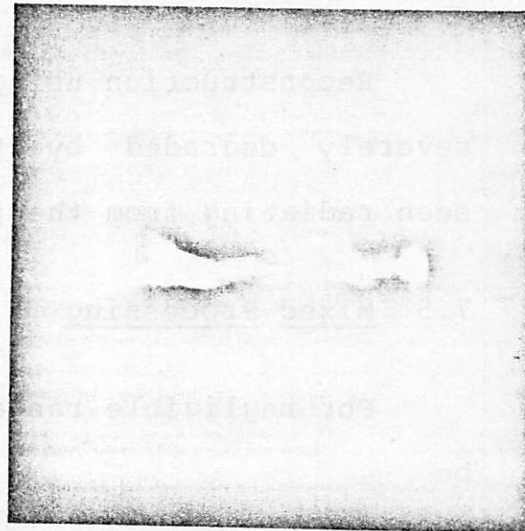


Coherent Processing



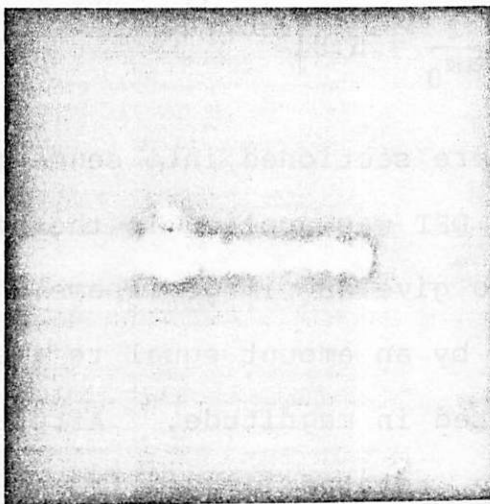
(a)

Incoherent Processing



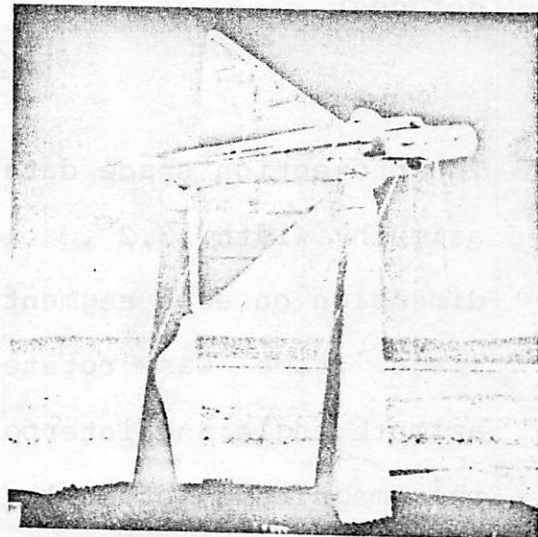
(b)

Mixed Processing



(c)

The Actual Setup



(d)

Figure 7.4.2. Reconstructions from data set 2 using the three reconstruction techniques.

(a) Coherent processing ( $29^\circ$  coherence).

(b) Incoherent processing (360 projections).

(c) Mixed processing.

(d) The actual model F102A plane setup at  $90^\circ$  roll on the rotating platform when data set 2 was collected.



Fig. 7.4.2b is much more intelligible. In particular, the nose, cockpit area and the rudder is barely noticeable.

Reconstruction using incoherent processing is also severely degraded by target glint. Weak spikes can be seen radiating from the tail and nose tip.

### 7.5 Mixed Processing

For negligible range walk, each azimuth interval must be

$$\theta_W \leq \frac{1}{ak_B} = 3.23^\circ$$

and for negligible change in Doppler (variable azimuth defocus)

$$\theta_W \leq \sqrt{\frac{2}{ak_0}} = 5.81^\circ$$

The projection space data were sectioned into segments of azimuth width  $3.2^\circ$ . 1-D DFT was applied in the azimuth dimension on each segment to give an image frame. Each image frame was rotated by an amount equal to its mean azimuth angle and interpolated in magnitude. After this the magnitude of all the rotated image frames were superimposed. Even though azimuth ambiguity exists in each frame, it gets averaged out in the final image. Figures 7.4.1c and 7.4.2c are reconstructions from data sets #1 and #2, respectively using this technique. In Fig. 7.4.1c, target symmetry was again assumed which means

that the upper half of the image is a flipped version of the lower half. For reference, a sketch of the actual F102A plane is shown in Fig. 7.4.1d and the actual model on the turntable in the testing grounds is shown in Fig. 7.4.2d.

Experiments [page 135, 10] have shown noticeable amounts of blurring when the target center of rotation is off by as little as 0.25 range bin width.

#### 7.6 Comparison of the Three Techniques

The first obvious observation is on the target resolution. As predicted earlier, the resolution achieved with coherent processing is best among all three techniques. The resolution with mixed processing is worse than that with incoherent processing for data set #2 but not so for data set #1. It is therefore inconclusive as to which latter two techniques gives better resolution. Because of target glint, the coherent processing technique will give non-uniform resolution in distinct directions. In practical cases, where only a fraction of the azimuth data is available coherent processing will again give non-uniform resolution. This problem is not serious with mixed processing. The effect on incoherent processing is not known.

As it is characteristic with any type of coherently processed image, speckle is also present with coherent processing technique. The image frames do have a lot of speckle but it is washed out through incoherent summation.

Sensitivity to glint is particularly strong for both coherent and incoherent processing. This is natural for the coherent technique because of the high resolution. But for incoherent technique, it is due to the lesser amount data averaging. Sensitivity to a constant error in the target center of rotation is strong for both coherent and mixed processing. It is also expected to be strong with incoherent processing.

Sampling requirement is least critical with incoherent processing whereas both the other two techniques demand greater sampling rate. Computation time required is also substantially less for incoherent processing. It was only 2 minutes CPU time while it took more than 90 minutes using coherent techniques.

## Chapter 8

### INVERSE SYNTHETIC APERTURE RADAR

#### 8.1 The General ISAR Doppler

In this chapter we will be concerned with applying the basic imaging process to Inverse Synthetic Aperture Radar (ISAR). The ordinary SAR geometry consists of an airborne radar platform illuminating the terrain below. In contrast ISAR geometry consists of a ground-based radar tracking moving target. The motion of the tracked target is, in general, composed of rotational motion and translational motion. Since only the target's rotation with respect to line-of-sight (LOS) contributes to the imaging property, the Doppler induced by the remaining components of the motion will have to be removed from the data before any further processing can be done.

Let us first derive an expression for the return phase and Doppler of a general target flying an arbitrary trajectory. The practical assumption here is that the front end of the target will always be pointing in the direction of the trajectory. A target reference point C will be taken as that point in space which the tracking

radar is locked on to. The instantaneous slant range vector of this target reference point C will be denoted as the gross range vector  $\bar{r}_0$ .

Let  $\bar{x}$  be a vector of an arbitrary point B on the target referenced to the target reference point C as shown in Fig. 8.1.1. The entire rigid body is moving with instantaneous velocity  $\bar{v}(t)$  and rotation vector  $\bar{\omega}_T(t)$ . Then the general range vector of B is

$$\bar{r} = \bar{r}_0 + \bar{x} \quad (8.1.1)$$

The phase return of a point reflector at B is

$$\phi = 2\pi \bar{k} \cdot \bar{r} \quad (8.1.2)$$

where  $\bar{k} = \frac{2}{\lambda} \bar{u}_{r_0}$  (propagation vector/ $\pi$ )

$$\bar{u}_{r_0} = \frac{\bar{r}_0}{r_0} \quad (\text{unit vector parallel to } \bar{r}_0)$$

$\lambda =$  mean wavelength of radar signal.

From here one  $\bar{u}$  will represent a unit vector in the direction of the vector indicated by its subscript.

Therefore

$$\begin{aligned} \frac{1}{2\pi k} \phi &= \bar{r} \cdot \bar{u}_{r_0} \\ &= \bar{r}_0 + \bar{x} \cdot \bar{u}_{r_0} \end{aligned}$$

Differentiating the left- and right-hand side of the above equation

$$\frac{1}{2\pi k} \frac{d\phi}{dt} = \frac{d\bar{r}_0}{dt} + \frac{d}{dt} (\bar{x} \cdot \bar{u}_{r_0})$$

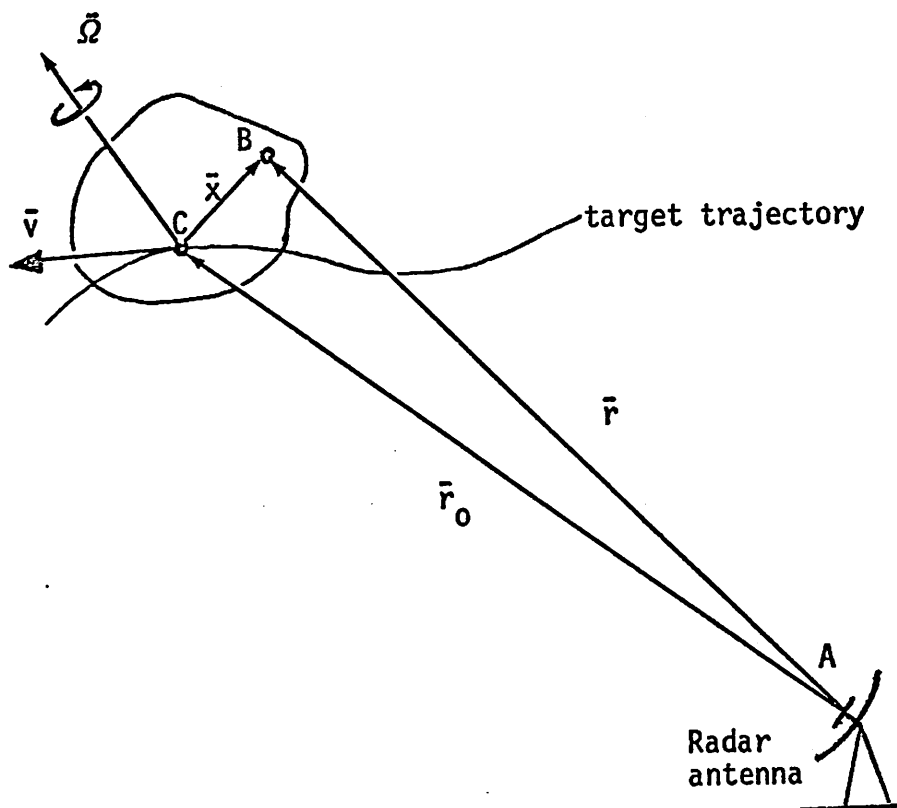


Figure 8.1.1. Inverse SAR geometry.

$$= \frac{dr_0}{dt} + \frac{d\bar{x}}{dt} \cdot \bar{u}_{r_0} + \bar{x} \cdot \frac{d\bar{u}_{r_0}}{dt} \quad (8.1.3)$$

$$= \frac{dr_0}{dt} + \bar{\omega}_T \bar{x} \cdot \bar{u}_{r_0} - \bar{\omega}_L \bar{x} \cdot \bar{u}_{r_0}$$

where

$$\bar{\omega}_L \triangleq \frac{\bar{r}_0 \times \bar{v}}{r_0^2}$$

= instantaneous angular velocity (rotational) of the LOS, due to its translational motion.

In deriving Eq. (8.1.3) we have used the following relationships.

Since  $\bar{x}$  is a vector on a rigid body, its tangential velocity ( $\bar{\omega} \times \bar{x}$ ) is the only velocity component it has.

Hence,  $\frac{d\bar{x}}{dt} = \bar{\omega}_T \times \bar{x}$ . Also from Appendix 8A,

$$\bar{x} \cdot \frac{d\bar{u}_{r_0}}{dt} = \bar{\omega}_L \bar{x} \cdot \bar{u}_{r_0}$$

where  $\bar{\omega}_L$  is defined as before.

Rearranging Eq. (8.1.3) and defining the time Doppler frequency as  $\frac{1}{2\pi} \frac{d\phi}{dt}$ , the Doppler of the return signal is

$$f_d = k \left[ \frac{dr_0}{dt} + (\bar{\omega}_T - \bar{\omega}_L) \bar{x} \cdot \bar{u}_{r_0} \right] \quad (8.1.4)$$

The Doppler frequency ( $f_d$ ) therefore has in general three components. The first component

$$f_1 = k \frac{dr_0}{dt} \quad (8.1.5)$$

is called the translational Doppler or the gross

range-rate of the target. This is the component that has no contribution to the imaging process. It must be isolated and subtracted from the overall Doppler in the tracking data.

The second component

$$f_2 = k(\bar{\omega}_T \times \bar{x} \cdot \bar{u}_{r_0}) \quad (8.1.6)$$

is that part of the rotational Doppler that is due to the actual rotation of the target.

The third component

$$f_3 = k(\bar{\omega}_L \times \bar{x} \cdot \bar{u}_{r_0}) \quad (8.1.7)$$

is that part of the rotational Doppler that is due to the rotational effect of the object with respect to the LOS and is contributed by the target's translational motion.

The difference of the last two components

$$f_2 - f_3 = k(\bar{\omega}_T - \bar{\omega}_L) \times \bar{x} \cdot \bar{u}_{r_0}$$

contributes to the imaging capability of the radar system and it is called the differential Doppler\* or the rotational Doppler.

-----  
\*The terms translational Doppler and differential Doppler were used by D.R. Wehner in [40].



The translational Doppler can be crudely approximated from the range rate in the tracking data. If the signatures are sampled at sufficiently high rate, this crude approximation can be fine tuned to a better accuracy by following the Doppler history of a small point object on the target. Examples of such points are the wing tip or the nose tip of an airplane.

$\bar{\omega}_T = 0$  when the target is flying a linear trajectory. In this case the  $f$  component of the differential Doppler is zero. When the aircraft makes a turn or maneuvers a non-linear trajectory,  $\bar{\omega}_T \neq 0$ ,  $f_2 \neq 0$ . Even though any yaw, pitch, or roll from air turbulence will create random errors in  $\bar{\omega}_T$ , such problems will not be of concern to us here.  $\bar{\omega}_T$  will in general be a linear combination of roll, pitch, and yaw;

$$\bar{\omega}_T = \bar{\omega}_r + \bar{\omega}_y + \bar{\omega}_p . \quad (8.1.8)$$

where  $\bar{\omega}_r, \bar{\omega}_y$ , and  $\bar{\omega}_p$  are respectively the roll, yaw, and pitch components of the target rotation. If an aircraft makes a turn,  $\bar{\omega}_r$  (roll component) will be the dominant component of  $\bar{\omega}_T$  for the initial moments of the turn. Then  $\bar{\omega}_r$  will drop to zero and  $\bar{\omega}_y$  will take over. Simulation results [38] point to the fact. However, for arbitrary maneuvers  $\bar{\omega}_r, \bar{\omega}_y$ , and  $\bar{\omega}_p$  will all be functions of time. Because  $(\bar{\omega}_T - \bar{\omega}_L)$  is normal to the projection plane, it

means that the projection plane will also be a function of time. It is very difficult to estimate  $\bar{\omega}_T$  in general simply from the phase return of the target. For simple flight trajectories however, gross estimations can be made from the tracking data.

Except for the linear trajectory case,  $\bar{\omega}_L$  is in most cases negligible.  $\bar{\omega}_L$  has two components as follows.

$$\bar{\omega}_L = \bar{\omega}_e + \bar{\omega}_a \quad (8.1.9)$$

where  $\bar{\omega}_e$  is the elevation angle scan rate and  $\bar{\omega}_a$  is the azimuth angle scan rate. For targets at small elevation angles,  $\bar{\omega}_e$  is usually negligible. Since  $\omega_e$  and  $\omega_a$  in practice do not fluctuate wildly, the elevation angle  $\theta_e$  and the azimuth angle  $\theta_a$  from the tracking data will probably give a sufficiently good estimate of  $\omega_L$ .

From here on, the problem cannot be developed further without further information or assumption. One such information is the flight trajectory. We will look into the pattern of the various Doppler components for two simple trajectories. the linear trajectory and the circular trajectory.

## 8.2 Linear Trajectory

To simplify the problem, let us look at the plane formed by the linear flight path and the antenna location A as in Fig. 8.2.1. Let  $y$  be the distance BC along the flight path between target reference center C and the point (B) of the closest slant range distance  $R_0$ .  $\theta$  is the aspect angle on the plane of interest and is given by

$$\theta = \sqrt{\theta_e^2 + \theta_a^2}$$

where  $\theta_e$  and  $\theta_a$  are elevation angle and azimuth angle, respectively.  $\theta_0$  is some initial reference angle such that when the LOS is broadside on the antenna,

$$\theta + \theta_0 = 0.$$

The translational Doppler frequency which arises from the velocity component along the LOS is

$$\begin{aligned} f_1 &= k \frac{dr_0}{dt} \\ &= kv \sin(\theta + \theta_0) \end{aligned} \quad (8.2.2a)$$

$$\text{or} \quad kv \frac{y}{\sqrt{R_0^2 + y^2}} \quad (8.2.2b)$$

By expanding the inverse square root term in Eq. (8.2.2b), one gets

$$f_1 \left\{ \begin{aligned} &= kv \left[ 1 - \frac{R_0^2}{2y^2} + \dots \right] \text{ for } y > R_0 \\ &\approx \frac{kv}{2} \left[ 1 + \frac{\epsilon}{R_0} - \frac{1}{8} \left( \frac{\epsilon}{R_0} \right)^2 + \dots \right] \text{ for } y = R_0 + \epsilon, |\epsilon| \ll R_0 \\ &= kv \left[ \frac{y}{R_0} - \frac{y^3}{2R_0^3} + \dots \right] \text{ for } y < R_0 \end{aligned} \right. \quad (8.2.3)$$

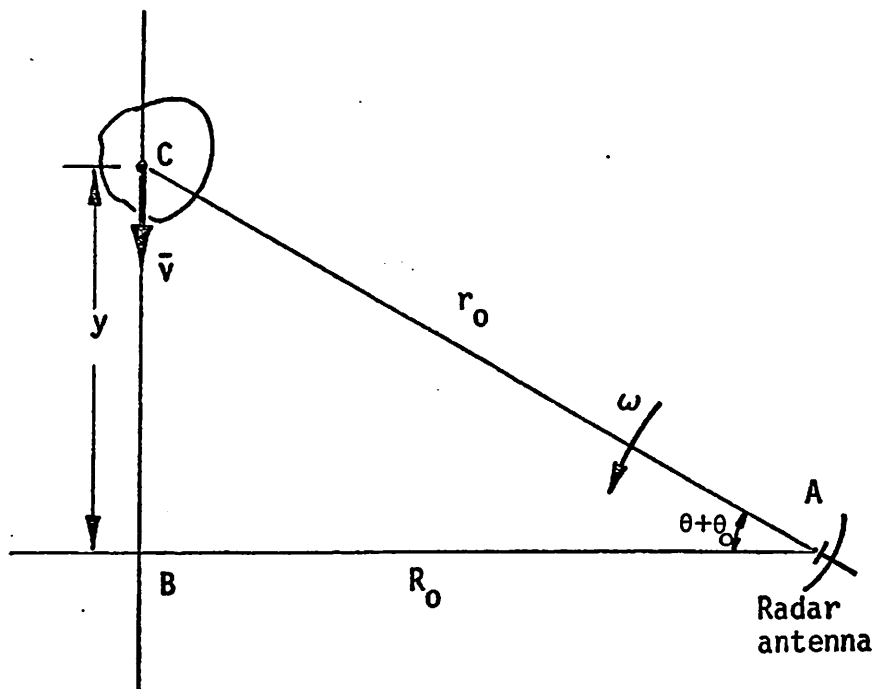


Figure 8.2.1. Linear flight path geometry.

By integrating  $f_1$  the translational Doppler phase from the target reference center is

$$\begin{aligned}
 &\text{constant} + kv[y + \frac{1}{2} \frac{R_0^2}{y} + \dots] && y > R_0 \\
 &\text{constant} + \frac{kv}{2} [\epsilon + \frac{1}{2} \frac{\epsilon^2}{R_0} - \frac{1}{24} \frac{\epsilon^3}{R_0^2} + \dots] && y = R_0 + \epsilon, |\epsilon| \ll R_0 \\
 &\text{constant} + \frac{kv}{2} [\frac{y^2}{R_0} - \frac{1}{4} \frac{y^4}{R_0^3} + \dots] && y < R_0
 \end{aligned} \tag{8.2.4}$$

Therefore for slant range distances much larger than the broadside range  $R_0$  (i.e.,  $y > R_0$  and  $y \approx R_0$ ), the Doppler phase  $\phi_1$  varies more or less linearly with  $y$  (or  $\epsilon$ ) except that when  $y \approx R_0$ , the quadratic phase term  $\frac{kv}{4} (\frac{\epsilon}{R_0})^2$  becomes significant. For  $y < R_0$ , the Doppler phase is a quadratic function of  $y$ . When the target velocity  $v$  is constant, the  $y$  dependence of the Doppler frequency and phase can be carried over to its time dependence. But when  $v$  is not constant with time, the time variation of the Doppler frequency and phase will be more complicated. For this reason we have chosen  $y$  instead of  $t$  for the independent variable in Eqs. (8.2.3) and (8.2.4). This is illustrated in Figs. 8.2.2a and 8.2.2b.

The target rotation  $\bar{\omega}_T$  does not exist for the linear trajectory as that the first component of the differential Doppler is

$$f_0 = 0.$$

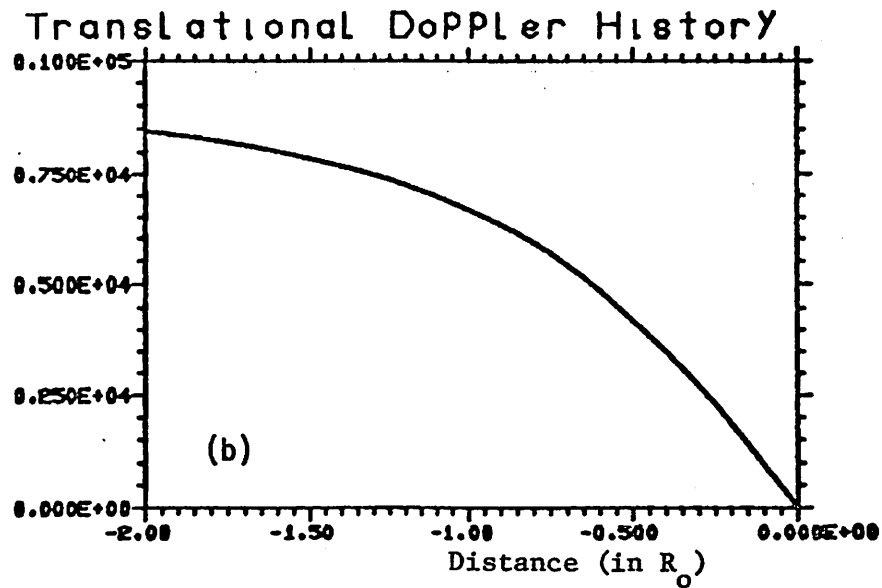
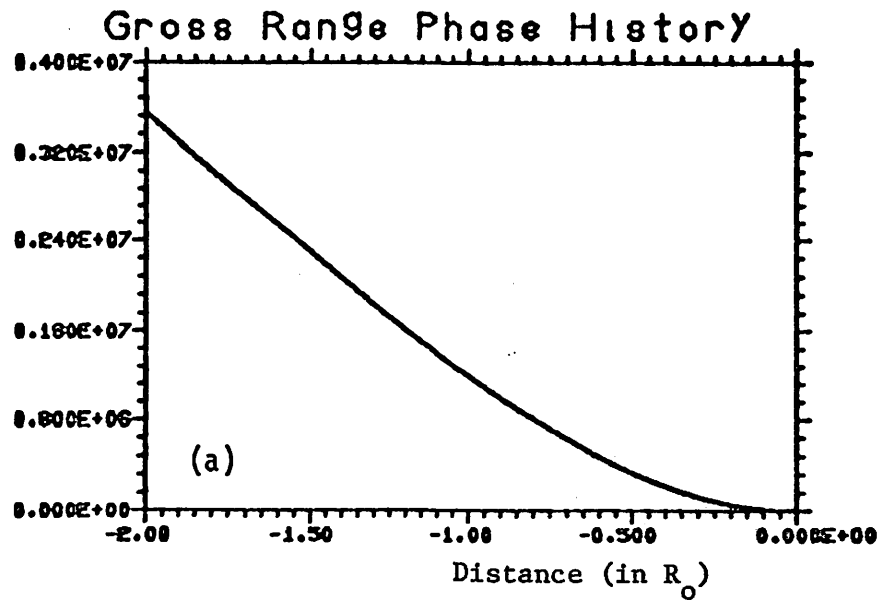


Figure 8.2.2. Computed flight parameters for linear trajectory vs. distance from the broadside position.

- (a) Phase (radians) from target center.
- (b) Translational Doppler (radians/sec).
- (c) Aspect angle (degrees).
- (d) Sweep rate (radians/sec) of the line of sight.

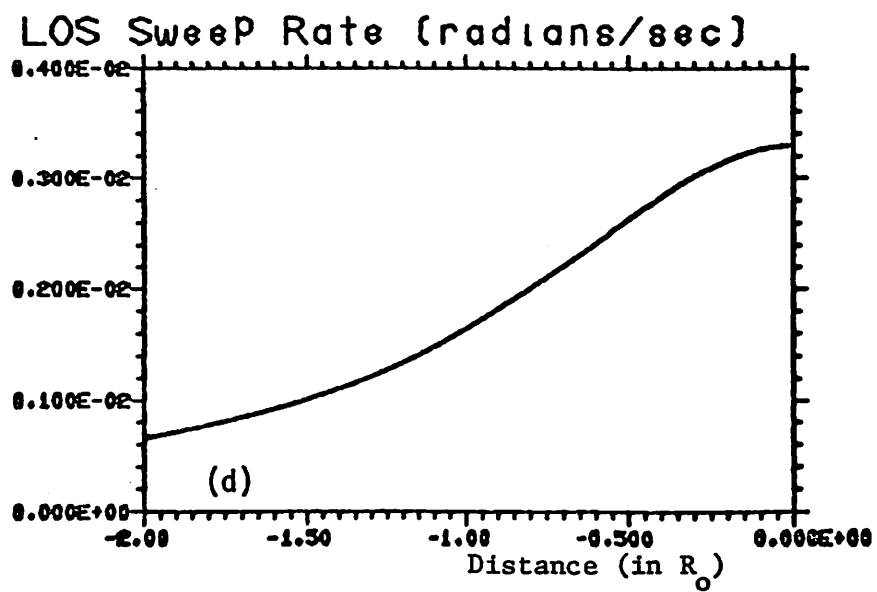
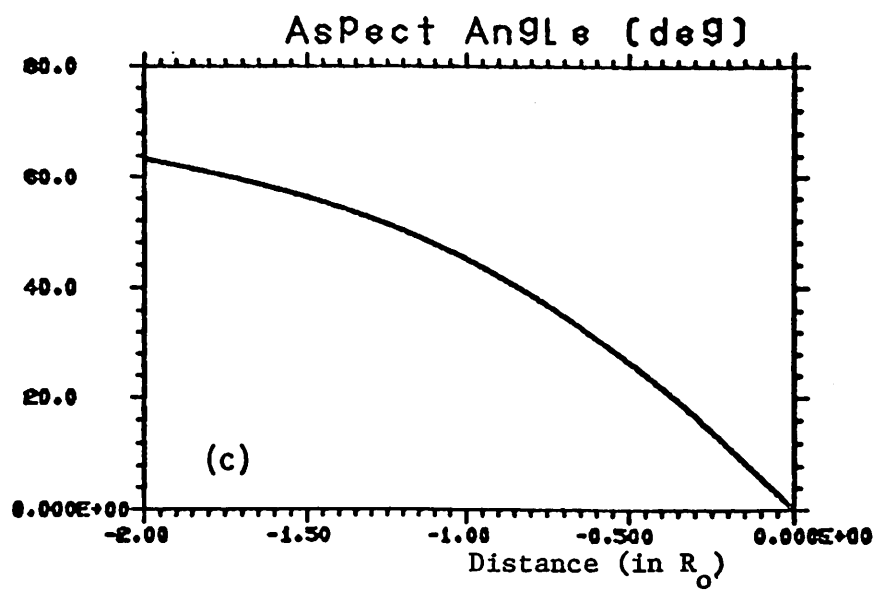


Figure 8.2.2 continued

The second component of the differential Doppler is  $f_3 = -k(\bar{\omega}_L \cdot \bar{x} \cdot \bar{u}_{r_0})$  where  $\omega_L = -\frac{d(\theta+\theta_0)}{dt}$ . Note that  $y = R_0 \tan(\theta+\theta_0)$ . Differentiating both sides of the above equation and rearranging the terms, one gets

$$\omega_L = \frac{v}{R_0} \cos^2(\theta+\theta_0) \quad \text{or} \quad \frac{v}{R_0} \frac{1}{1+(\frac{y}{R_0})^2} \quad (8.2.5)$$

$\omega_L$  is therefore maximum when the LOS is broadside and goes to zero in  $\cos^2(\theta+\theta_0)$ . Suppose the target is flying at a constant velocity toward the broadside position, and suppose the signature-to-signature time sampling interval is constant. As a result of Eq. (8.2.5) there will be an azimuth scale change between reconstructions from the far data and the near data. Far data means data collected far from the broadside aspect (i.e., large  $(\theta+\theta_0)$  or  $y$ ). Near data means data collected close to the broadside aspect (i.e., small  $(\theta+\theta_0)$  or  $y$ ). To correct this, the signature-to-signature sampling interval ( $\Delta t$ ) in time must be changed adaptively to

$$\Delta t \propto \omega_L^{-1} \quad (8.2.6)$$

provided that  $(\theta+\theta_0)$  can be estimated a priori. If the data is coherently processed over a wide aspect angle, this adaptive sampling correction is even more important because without it there will be not only a scale change



problem but also a defocusing effect.

Equation (8.2.5) is plotted in Fig. 8.2.2d with  $y/R_0$  as the independent variable. Notice how  $\omega_L$  (LOS sweep rate) changes by a ratio of 3:1 from broadside position ( $y=0$ ) to  $y = 2R_0$ . Figure 8.2.2c shows the aspect angle ( $\theta+\theta_0$ ) as a function of  $y$ . Figure 8.2.3 shows plots from actual tracking data on an F111 plane flying a linear path collected over approximately 50 seconds. The gross range ( $\propto$  gross-range phase) and the range-rate ( $\propto$  translational Doppler) are plotted in Fig. 8.2.3a and b, respectively. The aspect angle ( $\theta$ ) is plotted on Fig. 8.2.3c. Over the time interval when the data was collected, the aspect rate  $\omega_L$  is quite constant except for some local time fluctuations.

### 8.3 Circular Trajectory

A slightly more complicated case arises when the target traces out a circular trajectory of constant radius  $R$ . We will simplify the problem by assuming that the plane of the circular trajectory is the same as the plane formed by the LOS at all times. That is,  $\bar{v}$  and  $\bar{r}_0$  always lie on a same given plane. Furthermore, the vector  $\bar{R}_0$  corresponding to the center of the circular trajectory is constant. See Fig. 8.3.1.

The translational Doppler in this case is

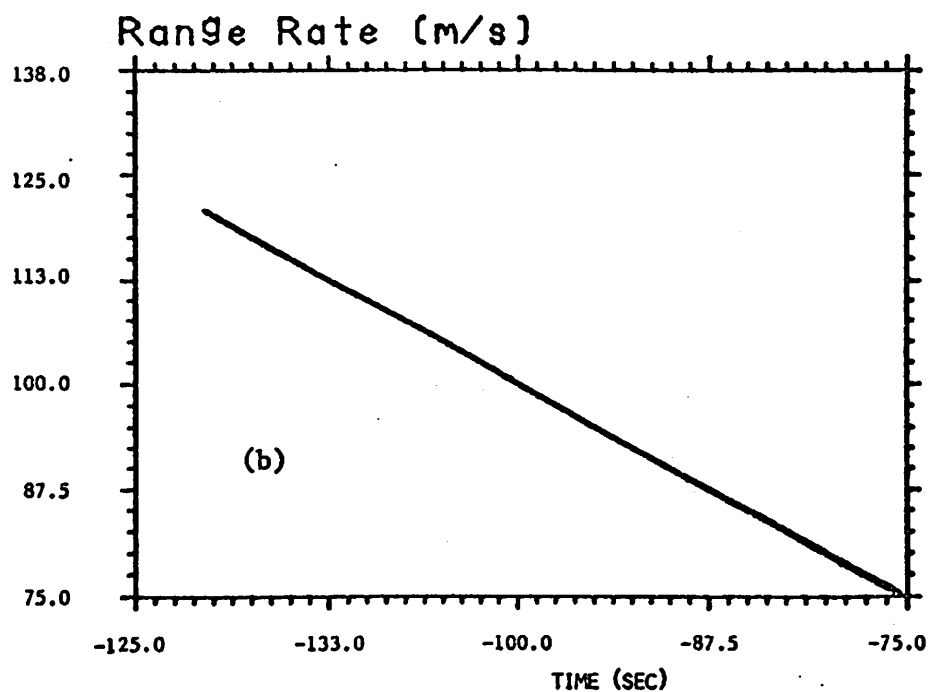
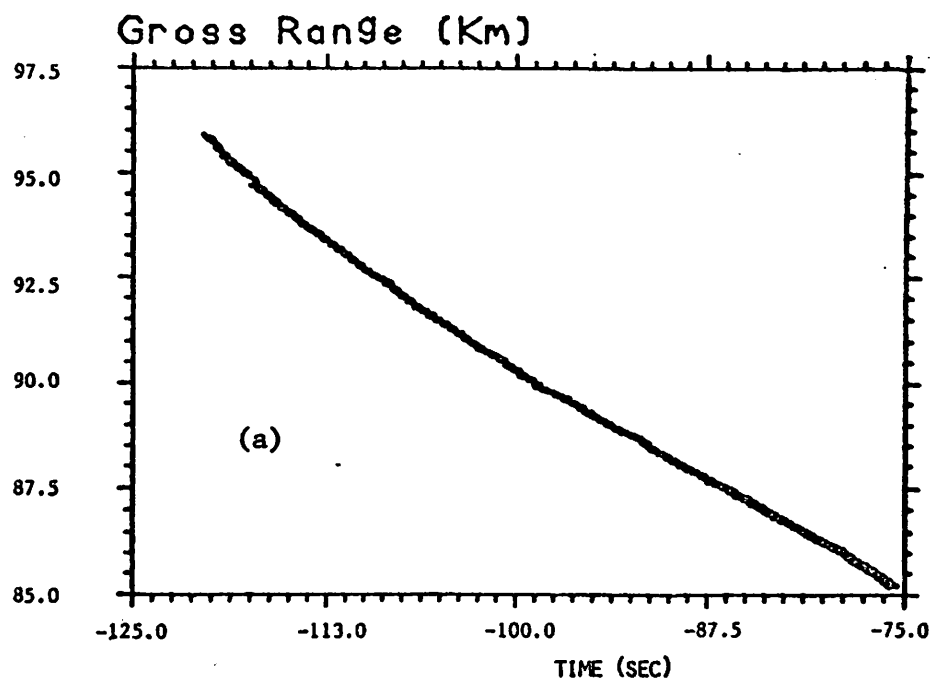


Figure 8.2.3. Flight parameter variation with time for a linear trajectory, plotted from actual tracking data of a F111 plane.  
(a) Gross range (km).  
(b) Range rate (m/s).  
(c) Aspect angle (degrees).

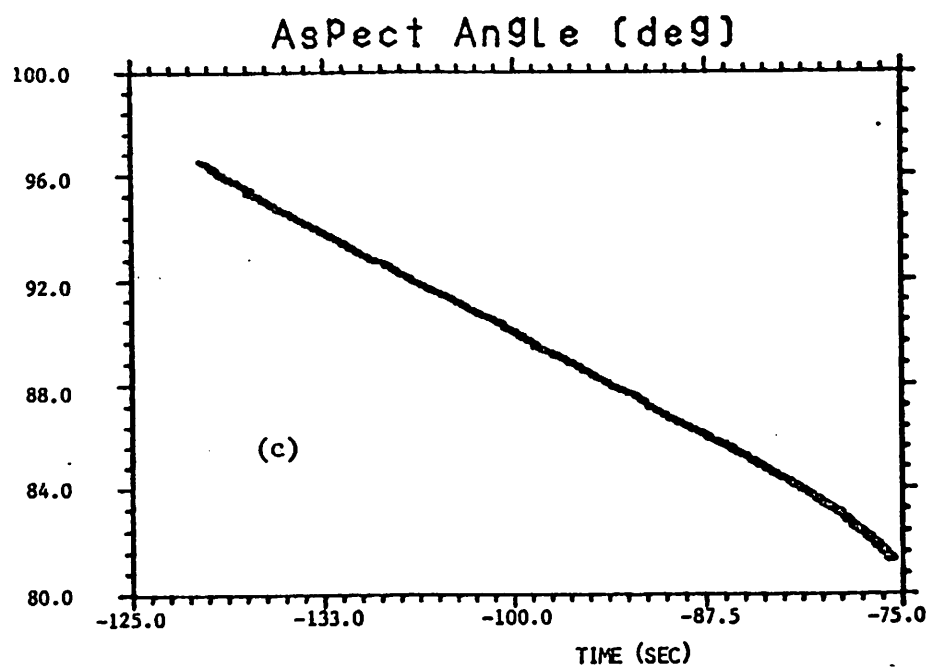


Figure 8.2.3 continued

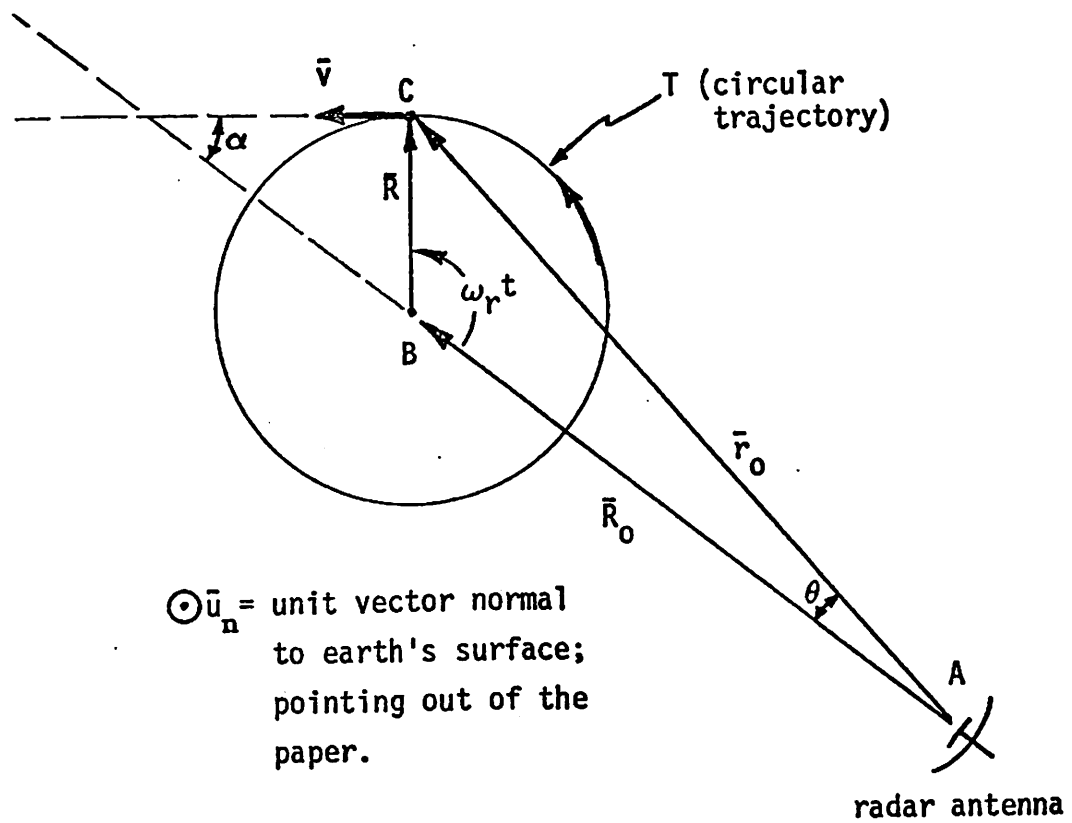


Figure 8.3.1. Imaging geometry for the circular trajectory case.

$$f_1 = \frac{kd r_0}{dt} = k(\bar{v} \cdot \bar{u}_{r_0}) = k\left(\frac{\bar{v} \cdot \bar{r}_0}{r_0}\right)$$

But  $\bar{r}_0 = \bar{R}_0 + \bar{R}$  and  $\bar{v} \cdot \bar{R} = 0$ . Therefore,  $f_1 = k\left(\frac{\bar{v} \cdot \bar{R}_0}{r_0}\right)$ .  
Letting  $\alpha$  being the angle between  $\bar{v}$  and  $\bar{R}_0$ ,

$$f_1 = (kR_0 v) \frac{\cos \alpha}{r_0} \quad (8.3.1)$$

This can also be rewritten as

$$f_1 = \frac{kv}{(1+\delta^2)^{1/2}} \frac{\sin \omega_T t}{(1-\gamma \cos \omega_T t)^{1/2}} \quad (8.3.2)$$

where  $\gamma = \frac{2RR_0}{R^2 + R_0^2}$ ,  $\delta = \frac{R}{R_0}$ .

Note that  $\alpha = \pi/2$  or  $3\pi/2$  when  $\bar{v}$  is normal to  $\bar{R}_0$  and  $\alpha = 0$  or  $\pi$  when  $\bar{v}$  is parallel to  $\bar{R}_0$ .

For the case when  $R_0 \gg R$  ( $\delta \ll 1$ ) such that  $r_0 \approx R_0 =$  constant, the translational Doppler is proportional to a sinusoidal function as follows.

$$f_1 \approx kv \cos \alpha. \quad (8.3.3)$$

If in addition  $v =$  constant,  $\alpha$  will be a linear function of time and the translational Doppler history will be a sinusoidal function of time

$$f_1 \approx kv \cos(\omega_T t), \quad (8.3.4)$$

In general  $\alpha$  is not known but if  $v$  is constant,  $\omega_T$  will also be constant and the least squares method can be used to estimate  $\omega_T$ . This will be shown in the following paragraph.  $f_1$  in Eq. (8.3.2) is plotted in Fig. 8.3.2b for  $\delta (= \frac{R}{R_0}) = 0.1, 0.3, 0.5, 0.7, 0.9$  and in Fig. 8.3.3b for  $\delta = 0.01, 0.02, 0.04, 0.08, 0.16$  with  $\omega_T = 1$ ,  $v = 250$  m/sec,  $k = \frac{2f_0}{c}$ ,  $f_0 = 5672$  MHz,  $c =$  velocity of light. Note that for  $\delta \ll 1$ ,  $f_1$  varies sinusoidally with time  $t$ . The gross-range phase  $\phi_1$  history is also plotted in Figs. 8.3.2a and 8.3.3a as follows:

$$\phi_1 = (kR_0\sqrt{1+\delta^2})\sqrt{1-\gamma\cos\omega_T t}$$

where  $R_0$  was taken to be 76 km. The gross range ( $\propto \phi_1$ ) and range-rate ( $\propto f_1$ ) for an F111 plane making a 0.9g turn are plotted in Figs. 8.3.4a,b, respectively.

The first component of the differential Doppler is

$$f_2 = k(\bar{\omega}_T \times \bar{x} \cdot \bar{u}_{r_0})$$

where  $\omega_T = vR$ . If  $\omega_T$  is constant, it can be estimated from the tracking data as follows. From Eq. (8.3.1), a slight modification will give

$$r_0 \frac{dr_0}{dt} = (R_0 v) \cos(\omega_T t + \alpha_0).$$

If  $R_0 v$  is constant, then the product of the range rate ( $\frac{dr_0}{dt}$ ) and slant range ( $r_0$ ) will be a sinusoidal function of  $t$  with some arbitrary error added to it. Let

$$\bar{y} = [y_0, y_1, \dots, y_{N-1}]^T$$

where

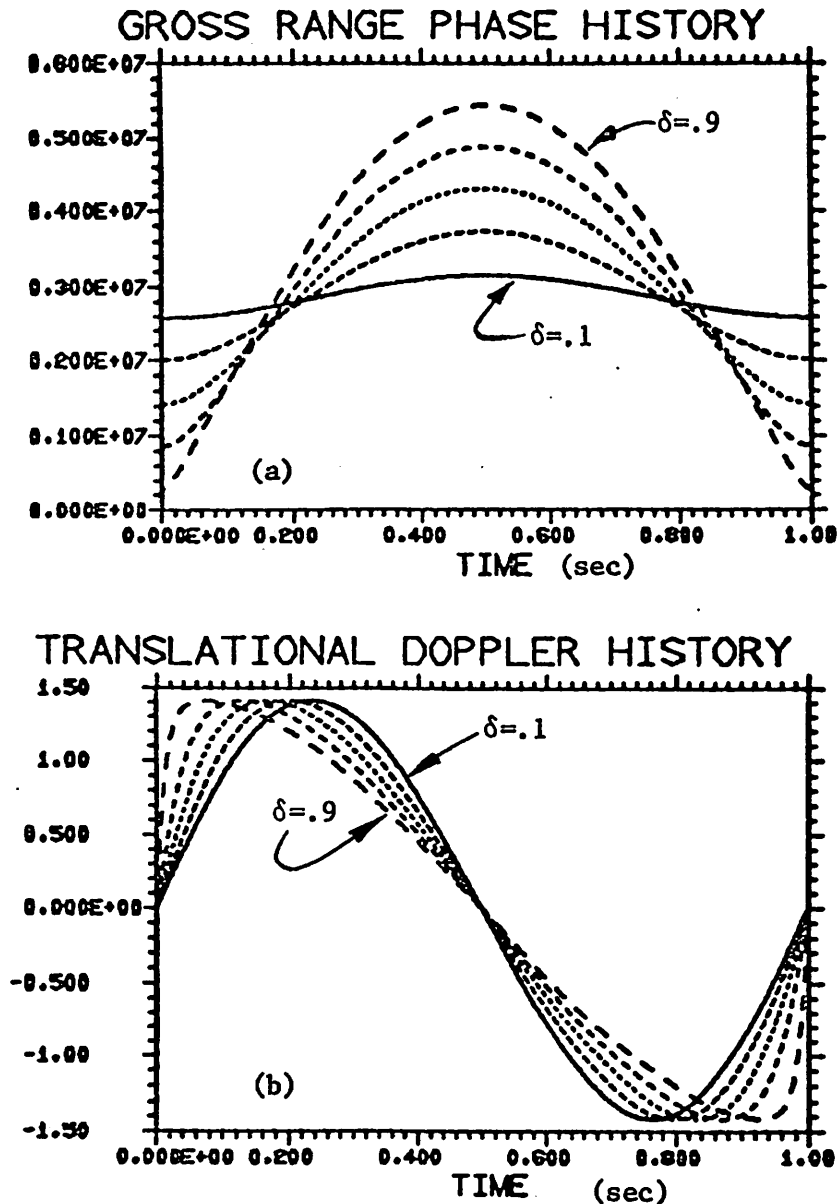


Figure 8.3.2. Computed time variation of flight parameters for a circular trajectory with values of  $\delta (=R/R_0)$  equal to .1, .3, .5, .7, and .9.

(a) Phase from the target center ( $\propto$  gross range).

(b) Translational Doppler (normalized to  $2v/\lambda$ ).

(c) Aspect angle ( $=\theta_e^2 + \theta_{az}^2$ ) radians.

(d) Sweep rate of the line of sight (in  $\omega_T$ ).

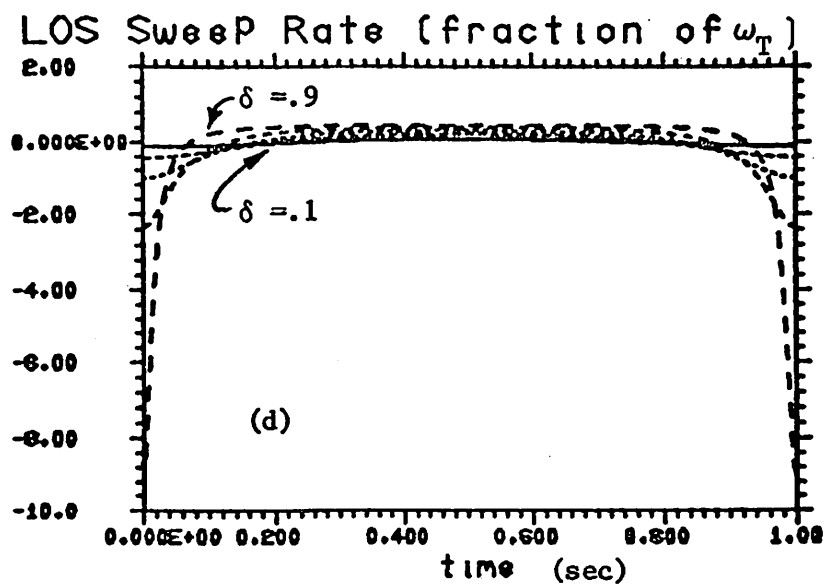
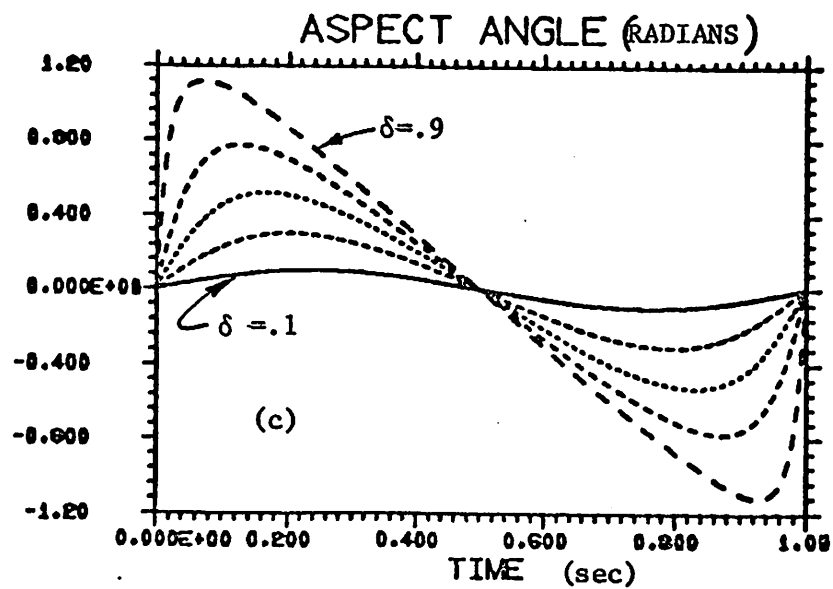


Figure 8.3.2 continued



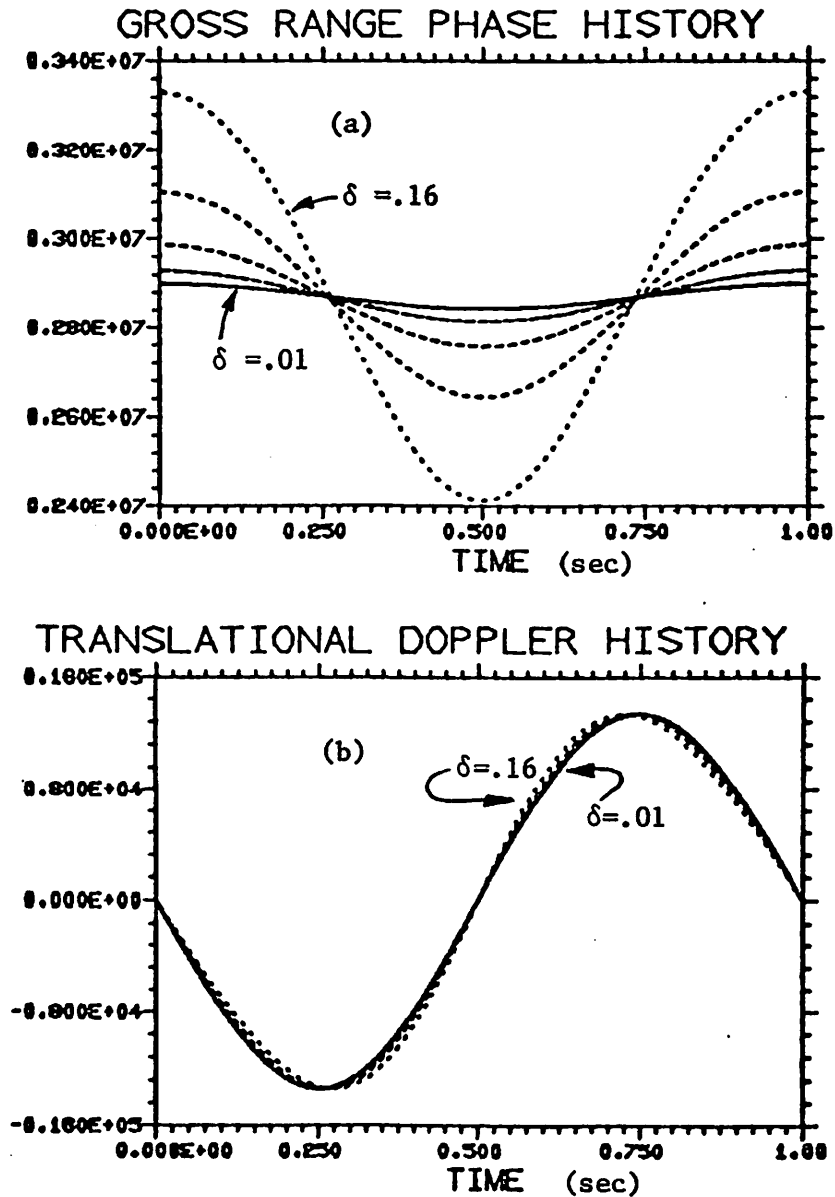


Figure 8.3.3. Computed time varying of flight parameters for a circular trajectory with values of  $\delta (=R/R_0)$  equal to .01, .02, .04, .08, .16.

(a) Phase from the target center ( $\alpha_{\text{gross range}}$ ).

(b) Translational Doppler (rad/sec).

(c) Aspect angle (degrees).

(d) Sweep rate of the line of sight (fraction of  $\omega_T$ ).

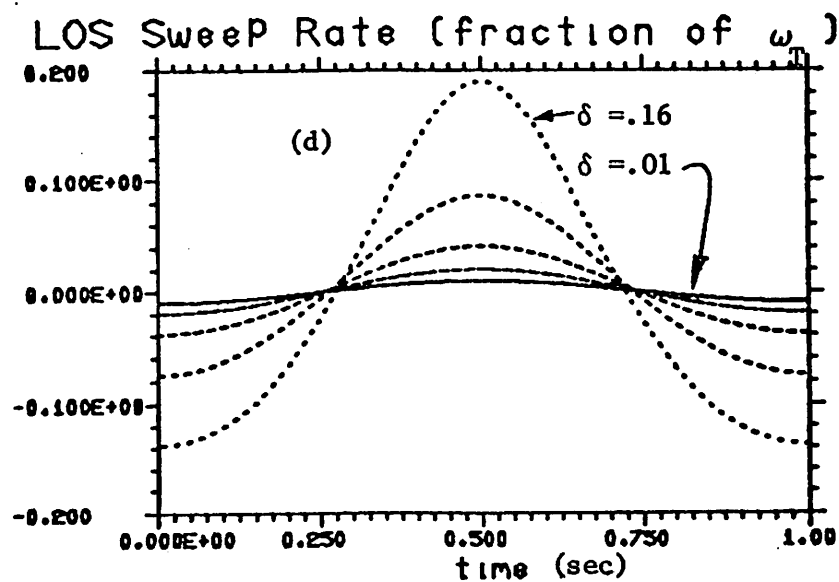
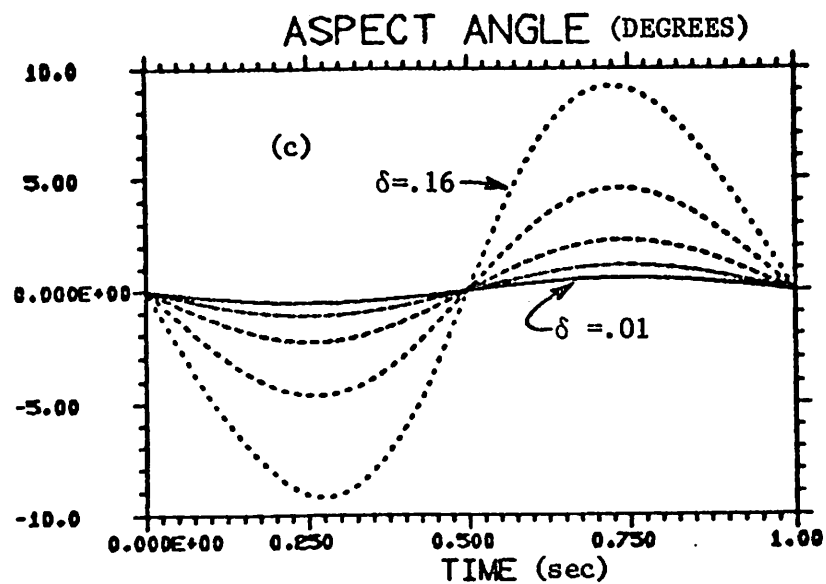


Figure 8.3.3 continued

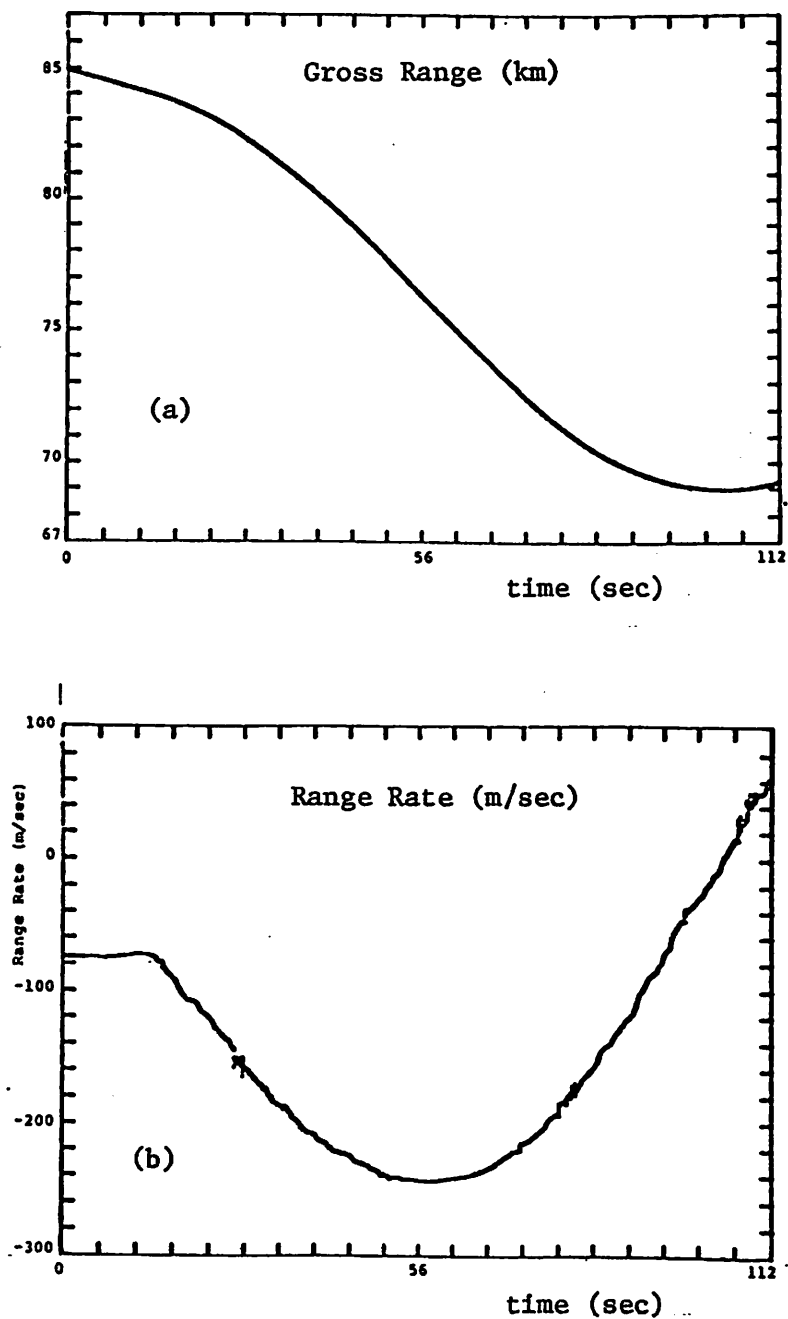


Figure 8.3.4. Flight parameters vs. time for a circular trajectory (approximately) plotted from actual tracking data on a F111 plane making a circular turn.

- (a) Gross range ( $\propto$  signal phase).
- (b) Range rate ( $\propto$  signal Doppler).
- (c) Aspect angle (degrees).
- (d) Sweep rate of the line of sight (or radar beam).

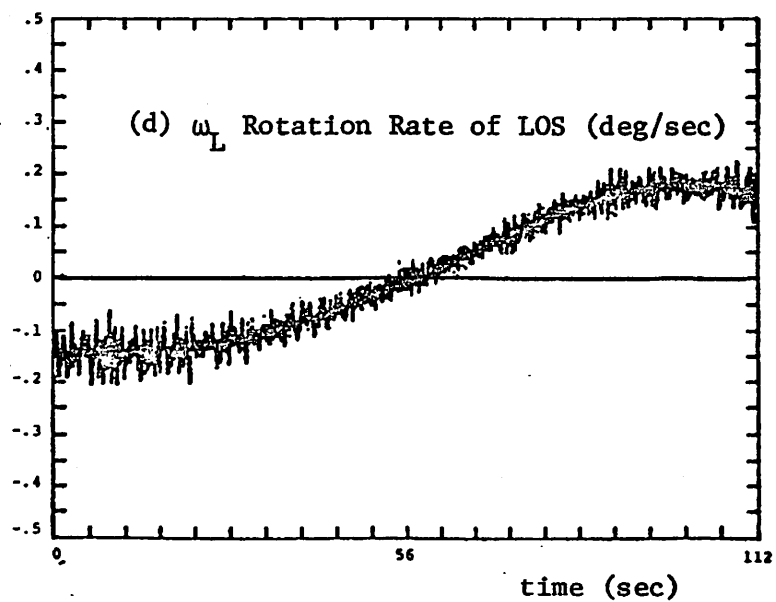
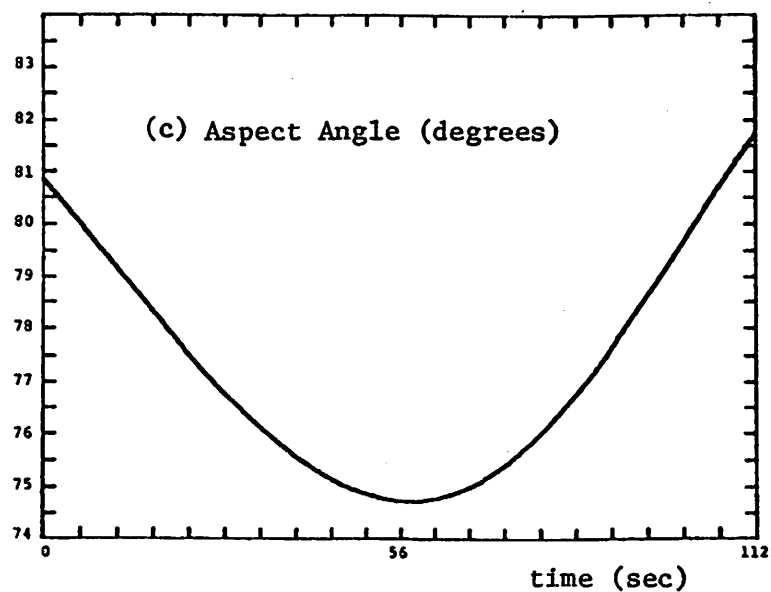


Figure 8.3.4 continued

$$y_1 = r_0(t_i) \frac{d}{dt} r_0(t_i)$$

$N$  = total number of signatures taken over the circular trajectory.

Also let

$$\bar{f} = [f_0, f_1, f_2, \dots, f_{N-2}]^T$$

$$f_i = R_0 v \cos(\omega_T t_i + \alpha_0)$$

Let  $\bar{x} = [R_0 v \ \omega_T \ \alpha_0]^T$  be the vector to be estimated. Then we can write

$$\bar{y} = \bar{f}(\bar{x}) + \bar{r}$$

where  $\bar{r}$  = error vector. Suppose  $\bar{x}_0$  is the initial guess for  $\bar{x}$ . Then  $\bar{x}$  can be iteratively estimated by minimizing the least squares error  $\bar{r}^T \bar{r}$  using the steepest gradient method as follows.

$$\bar{x}_{n+1} = \bar{x}_n - \frac{1}{|\bar{J}|} \left[ \frac{\partial \bar{f}(\bar{x})}{\partial \bar{x}} \right]^T (\bar{y} - \bar{f}(\bar{x})) \quad (8.3.5)$$

where

$$\bar{J} = \frac{d}{d\bar{x}} \left\{ \left[ \frac{\partial \bar{f}(\bar{x})}{\partial \bar{x}} \right]^T (\bar{y} - \bar{f}(\bar{x})) \right\}.$$

The second component of the differential Doppler is

$$f_3 = k(\omega_L \bar{x} \cdot \bar{u}_{r_0}).$$

$$\omega_L = - \frac{d\theta}{dt}$$

where  $\theta$  is the angle between  $\bar{R}_0$  and  $\bar{r}_0$ . Both  $\theta$  and  $\omega_L$  can be expressed as a function of time as

$$\theta = \tan^{-1} \left( \frac{\sin \omega_T t}{\frac{R_0}{R} - \cos \omega_T t} \right) \quad (8.3.6)$$

$$\omega_L = \left( \frac{1}{2} \gamma \right) \frac{\delta - \cos \omega_T t}{1 - \gamma \cos \omega_T t} \cdot \omega_T \quad (8.3.7)$$

where  $\gamma$  is defined in Eq. (8.3.2) and  $t = 0$  when the target is closest in range to the antenna.

Equations (8.3.6) and (8.3.7) are derived in Appendix 8B.  $\omega_L$  can also be approximated by smoothing the angle tracking data  $\sqrt{\theta_e^2 + \theta_a^2}$  over the entire aspect angle of interest.

Equation (8.3.7) indicates that  $\omega$  is a function of time with  $\omega_L$  increasing to its maximum around the trajectory points with zero range-rate.  $\omega_L/\omega_T$  is plotted in Figs. 8.3.2d and 8.3.3d with  $\delta = 0.10, 0.3, 0.5, 0.7, 0.9$  and with  $\delta = 0.01, 0.02, 0.04, 0.08, 0.16$ , respectively. Note that for  $\delta \ll 1$ ,  $|\omega_L|$  peaks at points of zero translational Doppler. Over the entire time interval (1 second) when the target makes a complete  $360^\circ$  turn, fluctuates as much as  $0.35\omega_T$  for  $\delta = 0.16$ . Also in the vicinity of maximum (or minimum) translational Doppler ( $T = 0.25$  and  $0.75$ ) the rate of change of  $\omega_L$  is most severe. Since the azimuth scale is directly proportional to  $\omega_L$ , it will go through its most drastic changes around points of maximum (or minimum) translational Doppler. If corrections for changing  $\omega_L$  is not made, the resulting image reconstruction will be most severely degraded in azimuth around points of maximum (minimum) translational Doppler.

The aspect angle pattern is plotted in Figs. 8.3.2c and 8.3.3c. The aspect angle  $\theta$  and the LOS sweep rate  $\omega_L$

from the same tracking data of a turning F111 plane are shown in Fig. 8.3.4c and d, respectively. Due to roundoff error and the inherent tracking loop estimation error in  $\theta$ ,  $\omega_L$  was computed by taking the derivative of the smoothed version of the angle ( $\theta$ ) tracking data.

The overall rotation rate ( $\omega_T - \omega_L$ ) will therefore not be constant even when  $v$  is constant. But if  $R_0 \gg R$ , then  $\omega_T \gg \omega_L$ . In this case, the effect of the time varying nature of  $\omega_L$  will be negligible over a reasonably small aspect angle interval.

In the analysis done so far, the surface scanned out by the LOS was isoplanar with the circular trajectory plane. In other words if  $u$  is a unit vector normal to the earth's surface and

$$\bar{u}_h \triangleq \frac{\bar{u}_n \times R_0}{|\bar{u}_n \times R_0|}$$

(subscript h corresponds to the direction of horizontal polarization), then the circular trajectory plane is the same as the  $(\bar{u}_h, \bar{R}_0)$  plane.

In general, that is not the case. The projection of the circular trajectory onto the  $(\bar{u}_h, \bar{R}_0)$  plane will be the effective trajectory. Within the limits of the far field assumption, this effective trajectory will be an ellipse with its major axis along the line of intersection between the trajectory plane and the  $(\bar{u}_h, \bar{R}_0)$  plane. This is

illustrated in Fig. 8.3.5.

Hence, if the circular trajectory gives rise to some appreciable change in elevation angle over the tracking interval, the effective trajectory (which is elliptical) should be considered instead.

#### 8.4 Conclusion

The time Doppler frequency associated with an airborne target flying an arbitrary trajectory has been mathematically formulated. It was shown that the Doppler frequency can be split into translational and rotational components. The rotational component is the Doppler induced by  $(\omega_T - \omega_L)$  where  $\omega_T$  is the rotation rate of the target itself and  $\omega_L$  is the rotational scanning rate of the radar line-of-sight. Two examples are given, one for a linear trajectory and the other for a circular trajectory. In both examples the pattern of the translational Doppler was derived, the time variation pattern of  $\omega_L$  was also derived and the least squares estimation of  $\omega_T$  was studied.

Finally, it should be noted that for the linear trajectory case, the rotational Doppler was induced by  $-\omega_L < 0$  while for the circular trajectory case it was induced by  $(\omega_T - \omega_L) > 0$ . Therefore, the rotational Doppler



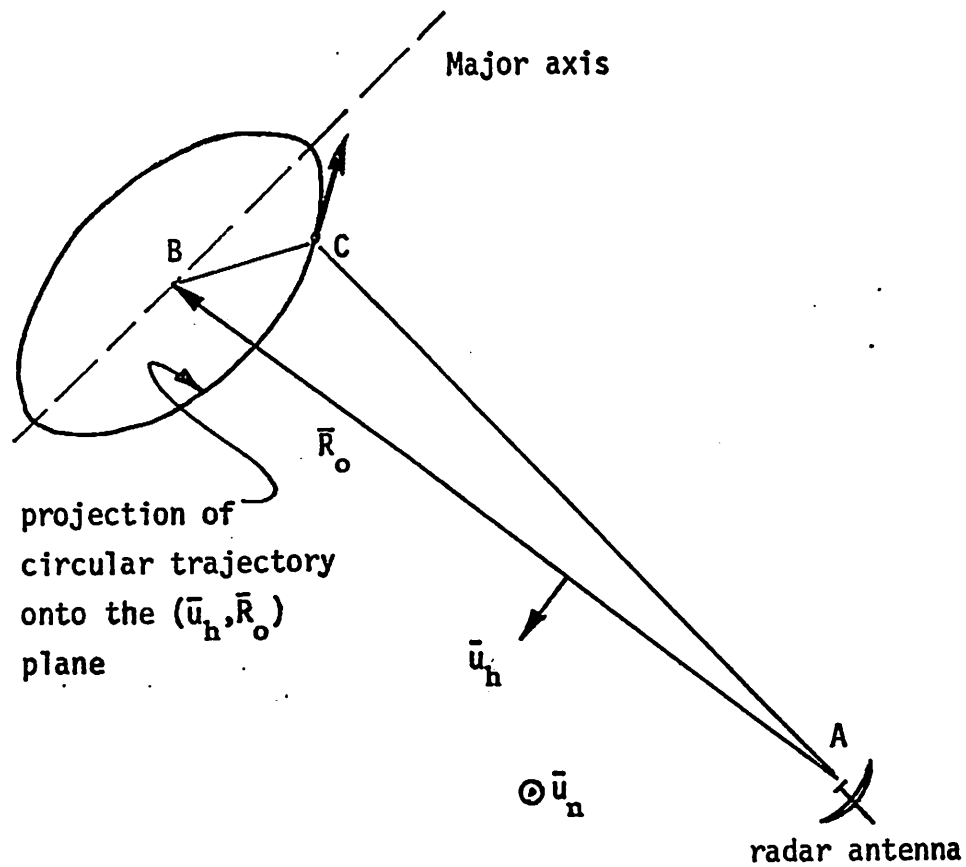


Figure 8.3.5. Elliptical effective trajectory for small angle of intersection between the circular trajectory plane and the  $(\bar{u}_h, \bar{R}_o)$  plane.

for the two cases have opposite signs. This means that if a small section of the data from both trajectories were range and azimuth compressed, the cross-range in the two reconstructed images will have opposite directions.

# APPENDIX 8A

Our objective is to show that  $\bar{x} \cdot \frac{d\bar{u}_{r_0}}{dt} = \bar{\omega}_L \times \bar{x} \cdot \bar{u}_{r_0}$ , where  $\bar{\omega}_L = (r_0 \times \bar{v}) / r_0^2$ . First of all note that

$$\bar{u}_{r_0} = \frac{\bar{r}_0}{r_0}$$

and  $\bar{v}_1 \times (\bar{v}_2 \times \bar{v}_3) = \bar{v}_2 (\bar{v}_1 \cdot \bar{v}_3) - \bar{v}_3 (\bar{v}_1 \cdot \bar{v}_2)$ . Hence,

$$\frac{d\bar{u}_{r_0}}{dt} = \frac{\bar{v}}{r_0} - \frac{\bar{r}_0}{r_0^2} \frac{dr_0}{dt}$$

Therefore

$$\begin{aligned} \bar{x} \cdot \frac{d\bar{u}_{r_0}}{dt} &= \frac{\bar{v}}{r_0} \cdot \bar{x} - \frac{\bar{r}_0}{r_0^2} \frac{dr_0}{dt} \cdot \bar{x} \\ &= \frac{1}{r_0} [\bar{v} \cdot \bar{x} - \bar{u}_{r_0} (\bar{v} \cdot \bar{x})] \\ &= \frac{1}{r_0} [\bar{v} \cdot \bar{x} - (\bar{x} \cdot \bar{u}_{r_0}) (\bar{v} \cdot \bar{x})] \\ &= \frac{1}{r_0} [(\bar{x} \cdot \bar{v}) \bar{u}_{r_0} - (\bar{x} \cdot \bar{u}_{r_0}) \bar{v}] \cdot \bar{x} \\ &= (\bar{x} \cdot \frac{\bar{v}}{r_0}) \bar{u}_{r_0} - \frac{\bar{v}}{r_0} (\bar{x} \cdot \bar{u}_{r_0}) \\ &= (\frac{\bar{v}}{r_0} \times \bar{u}_{r_0}) \times \bar{x} \cdot \bar{u}_{r_0} \\ &= (\frac{\bar{v} \times \bar{u}_{r_0}}{r_0^2}) \times \bar{x} \cdot \bar{u}_{r_0} \\ &= -\bar{\omega}_L \times \bar{x} \cdot \bar{u}_{r_0} \end{aligned}$$

QED

# APPENDIX 8B

To show that  $\theta = \tan^{-1} \left( \frac{\sin \omega_T t}{\frac{R_0}{R} - \cos \omega_T t} \right)$

$$\omega_L = \left( \frac{R^2}{R^2 + R_0^2} \right) \left( \frac{1 - \frac{R_0}{R} \cos \omega_T t}{1 - \gamma \cos \omega_T t} \right) \omega_T$$

where

$$\omega_T = \frac{v}{R}, \quad \gamma = 2R_0 R / (R_0^2 + R^2)$$

Proof. Referring to Fig. 8.3.1,

$$\begin{aligned} \frac{\sin \theta}{R} &= \frac{\sin(\pi - \omega_T t - \theta)}{R_0} = \frac{\sin(\omega_T t + \theta)}{R_0} \\ &= \frac{\sin \omega_T t \cos \theta + \sin \theta \cos \omega_T t}{R_0} \end{aligned}$$

On simplification,

$$\theta = \tan^{-1} \left( \frac{\sin \omega_T t}{\frac{R_0}{R} - \cos \omega_T t} \right) \quad (8B.1)$$

Since  $\omega_L = -\frac{d\theta}{dt}$ , by differentiating Eq. (8B.1) the rotation rate of the LOS will be

$$\begin{aligned} \omega_L &= \left( \frac{R^2}{R^2 + R_0^2} \right) \frac{1 - \frac{R_0}{R} \cos \omega_T t}{1 - \gamma \cos \omega_T t} \cdot \omega_T \\ &= \left( \frac{1}{2} \gamma \right) \frac{\delta - \cos \omega_T t}{1 - \gamma \cos \omega_T t} \cdot \omega_T \end{aligned}$$

where

$$\delta = R/R_0$$

$$\gamma = \frac{2RR_0}{R^2 + R_0^2}$$

## Chapter 9

### EXTENSION TO FURTHER STUDIES AND CONCLUSION

#### 9.1 Extension to Further Studies---Motion Compensation

We have addressed the problem of achieving high resolution 2-D digital reconstructions of radar targets from a multifrequency stepped radar. The first important criterion for such high resolution reconstructions is the requirement that the radar object be rotating at some constant or known angular rate. In practice, such rotational motion can be brought about from various sources. The first source of rotational motion can be generated from the translational motion of the radar target itself. One should keep in mind that it is the change in the aspect angle of the target with respect to the LOS which counts as the rotational motion. It was shown that this rotational motion is exactly the same rotational motion as that of the radar beam ( $\omega_L$ ) and therefore it can be estimated from the radar angle tracking data. This form of rotation is prevalent among non-maneuvering aircraft and ships moving along a linear trajectory over calm seas. The second source of

rotational motion is the true rotation of the radar object. Examples of this type of motion are the yaw and roll of a turning aircraft, the roll, pitch, and yaw of a ship on rough seas and the autonomous spinning and precessing motion of a space vehicle.

We have noted that the translational rotational motion can be estimated from the radar angle tracking data. Because the rotation rate determines the scale and the amount of distortion on the target reconstruction, it is important to be able to estimate the rotation rate to a high degree of accuracy. Unfortunately, because the target size to beam width ratios of most targets are much smaller than the beam splitting ratio ( $= \text{angle track resolution} / \text{beam angle}$ ), the tracking angle data are very crude in accuracy and usually some amount of smoothing would have to be done.

For the true rotational motion of the target, the rotation rate will not be readily available if the target is a non-cooperative target. In such cases the true rotation rate is difficult to estimate. Although further work has been done in the area of rotation rate estimation from radar signals, it is not within the scope of this dissertation. The important point to be made is that the true rotation rate of a target can be estimated from the

radar signals itself and therefore the angular scaling of the radar data can be adjusted.

Even though the rotational Doppler is responsible for the 2-D target reconstruction capability of the multifrequency stepped radar, it was shown that the data is a composite sum of two Doppler components, the rotational Doppler, and the translational Doppler which does not contribute to the 2-D target reconstruction process. Therefore with any realistic radar data, the translational Doppler must be removed from the raw radar data before any reconstruction procedures can follow. This step is called motion compensation. Since any translational Doppler not completely offset by motion compensation will easily degrade the quality of the radar object reconstruction, it becomes equally as important a task to be able to correctly carry out motion compensation.

Ideally, if one knows the exact motion of the target, one can carry out motion compensation on a target exactly without error. In the absence of such information, motion compensation becomes a difficult task. In the case when a reference target point scatterer stays within a single range resolution cell for a long period of time, one can completely motion compensate the data over that period of

time [10]. This is accomplished by subtracting the phase of the range compressed data over the entire range profile with the phase of the data in the range cell in which the reference target point resides. The criterion for choosing such reference range resolution cell is that only one scattering center should reside in that range resolution cell. If two scattering centers happen to stay within the same reference range resolution cell, the reconstructed radar object would appear as dual objects. Therefore, it is not difficult to identify such cases. Note that such motion compensation schemes will completely cancel out the phase in the reference range resolution cell.

To achieve higher resolution, a much more stringent motion compensation scheme is required. For one thing a given (or chosen) reference point scatterer will not always stay in the same resolution cell. Therefore, whenever the reference point scatterer migrates to the neighboring range cell, the entire range profile will have to be shifted by the same amount so that the reference point scatterer appears to be residing in the same range cell. This procedure is called range alignment. The difficult task is to be able to carry out the alignment procedure automatically over a long period of time (in the order of several minutes).



Another source of difficulty arises from the fact that any given scatterer will always share a common range cell with some other point scatterer at some target aspect angle. For the processing of radar data over a wide range of aspect angles, this situation is guaranteed to occur. When this occurs, it will be difficult to differentiate which of the two scatterers in the reference range cell is the reference scattering center.

A range alignment procedure was proposed by Chen [11]. The original purpose of this alignment procedure was to correct the range profile to range profile misalignment due to range tracking errors. The amount of range offset or misalignment between two adjacent range profiles was estimated by computing the amount of relative shift between two adjacent range profiles for which maximum cross-correlation is obtained. Only the magnitude of the complex range profile was used in the cross-correlation. Within a short period of time, such a procedure provided enough correction so that the remaining misalignment was noticeably within one range cell width. For longer periods of time however, such a procedure does not prevent the reference scatterer from drifting from range cell to another.

A new range alignment procedure that will prevent

long term drifting of a reference scatterer is needed. One method is to identify a point scatterer for the reference scatterer and track its long-term drifting behavior over the entire period of time in which coherent processing is desired. The method can be described as follows. First, the range profiles are range aligned to remove misalignment due to range tracking errors. Then a suitable point scatterer is chosen as the reference scatter center. When there is no other resident scatter center in the same range cell, this reference scatterer can be traced in range as it hops from one range cell to another. If the range profiles are sampled at small enough time intervals, so that there is no ambiguity in the phase change between adjacent range profiles, the range drift of the reference scatter center within any range cell can even be estimated to within a fraction of the signal wavelength.

Finally, when the ambiguity of two scattering centers residing within the same range cell arises, one can use Doppler measurements to resolve the two scattering centers. When Doppler measurements are needed to resolve ambiguous scattering centers, one must motion compensate the data first. However, since the objective is only to resolve two scatterers, a cruder motion compensation procedure is sufficient. This can be achieved by removing

the smoothed phase history of the range cell. Even though there is enough reason to believe that the above motion compensation procedure will sufficiently align the reference scattering center over a long term, much more work will be needed to show its performance.

## 9.2 Conclusion

A great deal of the current research activity centers around the problem of the target identification which hopefully will lead to automated target classification. The use of the term "target" implies that radar signals are used exclusively, which is misleading. In practice, target identification problems are also entertained by researchers in the infrared and optical regions of the electromagnetic wave spectrum.

One of the basic approaches to the problem of target identification using radar signals is to obtain faithful reconstructions of the target and then apply target identification algorithms on the reconstructed image of the target. This approach is followed in this dissertation except that we concentrate on only the reconstruction part of the problem.

In Chapter 2 we have described how a multifrequency step (MFS) radar represents the Fourier transform of the

target scattering coefficient distribution  $(x,y)$  of a rotating object. It was mentioned without proof that a similar relation holds for other coherent radars. The above relation holds as far correct as the following three important assumptions can be held true:

1. the radar signals can be motion compensated exactly;
2.  $(x,y)$  does not change with the aspect angle of the target relative to the line-of-sight;
3. the back scattering of radar signals is specular in nature.

(Atmospheric effects on the signals are less important.)

In general, the radar data represents the 3-D Fourier transform of the target scattering coefficient distribution. In the special case in which the rotation rate vector is constant in direction, the data represents the 2-D Fourier transform of the target scattering coefficient distribution. In this case, the signal frequency of the MFS radar represents the radial dimension in the Fourier domain, and the aspect angle represents the angular dimension in both the Fourier domain and the target space domain. This means that the radar data samples the Fourier transform domain of the target function  $(x,y)$  in polar coordinates.

The radar signal frequency has a maximum and minimum frequency limit defined by the burst of pulses in the MFS radar. If in principle the target aspect angle changes through  $360^\circ$ , then the radar data in the Fourier domain will be constrained to within an annula ring for the 2-D case. The frequency limits become a masking or filtering operation on the radar data. Since one can reconstruct the target simply by taking an inverse Fourier transform of the annula ring. The annula ring mask or filter is called the pupil function and its inverse transform is called the point spread function of the entire imaging system. It was shown that for narrowband systems (mean signal frequency signal bandwidth of the burst of pulses), the Rayleigh resolution was inversely proportional to the mean signal frequency only. The same conclusion was reached with the resolution problem when the Doppler bandwidth of the signal was studied. This is shown in Chapter 3.

Since the radar data is sampled discretely in polar coordinates in the Fourier domain of the target function  $(x,y)$ , it is important to understand the sampling requirements in both radial and angular dimensions. In Chapter 4, the effect of undersampling in either dimension was demonstrated. The necessary condition and the sufficient sampling condition were also derived and

summarized in Table 4.2.1. Sampling requirements from the DOF (Degrees of Freedom) [15] or time-bandwidth-product points of view also gave similar results. Moreover, a processing method was also suggested for cases in which the radar data was not sufficiently sampled but satisfies the necessary sampling condition.

In Chapter 5, an analytical approach is followed to solve the sampling requirement with polar format sampling in the Fourier domain. Poisson's summation formula was applied to the Fourier transform of the unit circle sampled in angle only. The same formula was applied to the Fourier transform of the annula ring pupil function sampled in radial dimension only. Then the process was repeated for the annula pupil function sampled in both radial and angular dimensions. It was shown that the polar coordinate sampling effects were drastically different from the well known sampling effects in rectangular coordinates. The most notable difference was in the absence of the main spectrum repeated periodically in a rectangular fashion. In contrast, the polar coordinate sampling gives rise to error terms (called clutter) which can accounted for as being the radial sampling effect, angular sampling effect, and simultaneous radial and angular sampling effect. The clutter from each sampling effect consists of an infinite number of terms (or

orders) and each term (say the  $n$ th order term) is an isotropic function whose value becomes significant only when the radial dimension of the spectrum is at  $n$  times some constant factor. This factor depends on the sampling interval of the corresponding dimension.

Besides the above three clutter terms, a fourth sampling effect term appears when there is radial sampling. The value of this term grows significant around the main lobe of the spectrum. It therefore does not behave the same way as the other three sampling effects in that it merely modifies the shape of the main lobe of the spectrum. Since its peak value is inversely proportional to the  $K-1$ , where  $K$  is the total number of radial samples, its effect becomes negligible when the radial sampling interval is small. The polar coordinate sampling effects were also studied with a disc pupil function (2-D circular low pass filter). The results are summarized in Table 5.4.2.

One should probably realize that Poisson's summation formula was a powerful tool in analyzing the polar coordinate sampling effects. Because of the limited scope of this dissertation, the subject was not pursued further. However, it is not difficult from here on to arrive at a sampling theorem corresponding to the polar format forming

a counter-part to the sampling theorem in rectangular coordinates. It is conceivable that the analytical tools developed using Poisson's summation formula will find a whole host of applications in areas where polar format sampling is a fact of life.

Based on the background developed in earlier chapters, three reconstruction methods are described in Chapter 6, namely the Coherent processing method, Incoherent processing method, and the Mixed processing method. An approximate coherent processing method was developed with the potential of achieving high resolution without the unduly increasing processing time and memory requirement. It is not unreasonable in practice to encounter sampling rates (especially aspect angle sampling rates) that do not satisfy the sufficient conditions showed in Chapter 4. Therefore, a method to process undersampled data was derived based on observations made in Chapter 4. The method is simply to process the portions of the data where sufficient sampling is expected. The resolution of such a modified coherent processing algorithm is also studied and summarized in Fig. 6.4.2

The incoherent processing method to reconstruct the target image without phase information in the range



profiles was shown to be similar to tomographic reconstruction systems. Therefore, tomographic reconstruction techniques can be applied to reconstruct the target from incoherent radar data. The mixed processing technique processes segments of the radar data coherently and then superimposes them incoherently. Finally, digital implementation problems relating to the above three reconstruction techniques are described.

Chapter 7 shows the results of applying the three reconstruction techniques on two sets of experimental data. The data is recorded off a static radar object which has only rotational motion. Motion compensation was therefore not necessary on the data. Results show that even though the data was undersampled in aspect angle, the modified coherent processing can provide reconstructions with resolution performance better than the other two reconstruction methods. The constant target reflectivity function assumption was found to be not very accurate and strong surges in backscattering showed up as bright stripes on the coherently reconstructed images. In this case, the modified coherent processing method was found to suppress a lot of these artifacts created by the non-constant behavior of the target reflectivity function. Shadowing problems did appear to shade out most of the "other" half of the target when less than 360 aspect

excursion was allowed on the rotated target. In practice since radar targets are usually observed at non-zero elevation (or depression) angles, shadowing problems will not become an important handicap.

As it was described earlier, one of the basic assumptions on the data is that the data can be motion compensated exactly. In practice this is not the case but one can hope to approach that assumption as close as possible. Towards this objective, an attempt is finally made in Chapter 8 to understand some of the basic components of the target motion that create Doppler phase shifts in the radar data. A simple model for the target motion was used, in which the target trajectory and the radar beam line-of-sight was coplanar. Two simple trajectories, namely the linear trajectory and the circular trajectory were used and the behavior of their translational Doppler was studied.

It is hoped that the work done in this dissertation provides some insight into the problems of high resolution radar imaging and other questions posed by the high resolution requirement. Much more work has to be done before one can establish the usefulness of the principles derived in this dissertation in practical applications.

## REFERENCES

- [1] Abramowitz, M., L. A. Stegun, Handbook of Mathematical Functions, National Bureau of Standard 1972 Edition.
- [2] Arens, W.E. , "Real-Time Synthetic Aperture Radar Data Processing for Space Applications," Proc. SPIE, Vol. 154, p. 14, Aug. 1978.
- [3] Ausherman, D.A., "Digital vs. Optical Techniques in SAR Data Processing," Proceedings of the International Optical Computing Conference, SPIE, Vol. 119, 1977.
- [4] Bojarski, N.N., "Three-Dimensional Electromagnetic Short Pulse Inverse Scattering," Report No. SPL-67-3, Syracuse University Research Corp., Syracuse, N.Y., Feb. 1967.
- [5] Bracewell, R.N., A.C. Riddle, "Inverse of Fan-Beam Scans in Radio Astronomy," Astrophys. J., Vol. 150, Nov. 1967.
- [6] Brookner, E., "Synthetic Aperture Radar Spotlight Mapper," Radar
- [7] Brown, W.M., R.J. Fredericks, "Range-Doppler Imaging with Motion Through Resolution Cells," IEEE Trans. on AES, Vol. AES-5, No. 1, pp. 98 102, Jan. 1969.
- [8] Brown, W.M., L.J. Porcello, "An Introduction to Synthetic Aperture Radar," IEEE Spectrum, Sept. 1969.
- [9] Brown, W.M., J.F. Riordan, "Resolution Limits with Propagation Phase Errors," IEEE Trans. on AES, Vol. AES-6, No. 5, Sept. 1970.
- [10] Chen, C.C., Imaging with Radar Returns, Ph.D. Dissertation, USCIPi Report No. 850, 1978.
- [11] Chen, C.C., H.C. Andrews, "Turntable Radar Imaging," USCIPi Report #800, Mar 31, 1978.

- [12] Cutrona, L.J., "Synthetic Aperture Radar," Radar Handbook, Edit. M.I. Skolnik, McGraw-Hill, 1970.
- [13] Elachi, C., W.E. Brown, "Models of Radar Imaging of the Ocean Surface Waves," IEEE Trans. on AP, Vol. AP-25, No. 1, Jan. 1977.
- [14] Elachi, C., D.D. Evans, "Effects of Random Phase Changes on the Formation of S.A.R.," IEEE Trans. on AP, Vol. AP-25, No. 1, p. 149, Jan. 1977.
- [15] Gori, F. and G. Guatarri, "Shannon Number and Degrees of Freedom of an Image," Optics Communications, Vol. 7, No. 2, Feb. 1973.
- [16] Graham, L.C., "Synthetic Interferometer Radar for Topographic Mapping," Proc. IEEE, Vol. 62, No. 6, June 1974.
- [17] Harger, Robert O., "Harmonic Radar Systems for Near-Ground In-Foliage Nonlinear Scatterers," IEEE Trans. on AES, Vol. AES-12, No. 2, Mar. 1976.
- [18] Horn, B.K.P., "Density Reconstruction Using Arbitrary Schemes," Proc. IEEE Vol. 66, No. 5, May 1978.
- [19] Keigo Iizuka, Hisanao Ogura, J.L. Yen, Van Khai Nguyen, and J. John Weedmark, "Performance of Hologram Matrix Radar," Proc. IEEE, Dec. 1974.
- [20] Keller, J.B., "Geometrical Theory of Diffraction," JOSA, 52, pp. 116-130, 1962.
- [21] Kirk, J.C., Jr., "A Discussion of Digital Processing In Synthetic Aperture Radar," IEEE Trans. on AES, Vol. AES-11, No. 3, May 1975.
- [22] Leith, E.N., "Quasi-Holographic Techniques in the Microwave Regions," Proc. IEEE, Vol. 59, No. 9, Sept. 1971.
- [23] Messereau, R.M., A.V. Oppenheim, "Digital Reconstruction of Multi-Dimensional Signals from Their Properties," Proc. IEEE, Vol. 62, No. 10, Oct. 1974.
- [24] Oppenheim, A.V., R.W. Schafer, Digital Signal Processing, Prentice-Hall, Englewood Cliffs, N.J. 1975.

- [25] Ormsby, J.K.A., N.M. Tomljanovich, H.S. Ostrowsky, M.R. Weiss, "Analytic Coherent Radar Techniques for Target Mapping," IEEE Trans. on AES, Vol. AES-6, No. 3, May 1970.
- [26] Porcello, J.F., "Turbulence-Induced Phase Errors in SAR," IEEE Trans. on AP, Vol. AP-6, No. 5, Sept. 1970.
- [27] Ramachandran, G.N., A.V. Laksmirnarayanan, "Three Dimensional Reconstruction from Radiographs and Electron Micrographs: Application of Convolution Instead of Fourier Transforms," Proc. National Academy of Science, Vol. 68, 1971.
- [28] Course notes from "Finite Field Transforms," Irving S. Reed, University of Southern California, Spring 1978.
- [29] Scudder, H.J., "Introduction to Computer Aided Tomography," Proc. IEEE, Vol. 66, No. 6, June 1968.
- [30] Shepp, L.A., B.F. Logan, "The Fourier Reconstruction of a Head Section," IEEE Trans. on Nuclear Science, Vol. NS-21, June 1974.
- [31] C.W. Sherwin, J.P. Ruina, and R.D. Rawcliffe, "Some Early Developments in Synthetic Aperture Radar Systems," IRE Trans. Mil. Electron, Vol. MIL-6, pp. 11-115, April 1962.
- [32] Skolnik, M.I., Radar Handbook, McGraw-Hill, 1970.
- [33] Smith, P.R., T.M. Peters, R.H.T. Bates, "Image Reconstruction from Finite Number of Projections," J. Phys. A: Math., Nucl. Gen., Vol. 6, March 1973.
- [34] Stremmler, F.G., W.M. Brown, "Phase Analysis in Multiple Sensor Receivers with High Signal-to-Noise Ratio," IEEE Trans. on AES, Vol. AES-5, No. 2, Mar. 1969.
- [35] Tomiyasu, Kiyo, "Tutorial Review of Synthetic Aperture Radar (SAR) with Applications to Imaging of the Ocean Surface," Proc. IEEE, Vol. 66, No. 5, May 1978, p. 563.
- [37] Walker, J.L., Range Doppler Imaging of Rotating Objects, Ph.D. Dissertation, U. of Michigan, 1974.

- [38] Wallenberg, R.F., Zenn Zenon, "Inverse SAR,"  
Proceedings of a Workshop on Applications of Image  
Understanding and Spatial Processing to Radar  
Signals for Automatic Ship Classification, sponsored  
by Naval Electronics Systems Command, 21-22 February  
1979.
- [39] Watson, G.E., Theory of Bessel Functions, Cambridge  
University Press, 1952.
- [40] Wehner, D.R., "Stepped Frequency Target Imaging,"  
Internal Rep., N.O.S.C., San Diego, June 1978.